SOFT CAPACITIVE FORCE SENSING SKIN: CHARACTERIZATION, OPERATION ON A CURVED SURFACE, AND INCREASED FORCE RANGE

by

Kieran Morton

B.Sc., University of British Columbia, Vancouver, 2019

A THESIS SUBMITTED IN PARTIAL FULFILLMENT OF

THE REQUIREMENTS FOR THE DEGREE OF

MASTER OF APPLIED SCIENCE

in

THE FACULTY OF GRADUATE AND POSTDOCTORAL STUDIES

(Biomedical Engineering)

THE UNIVERSITY OF BRITISH COLUMBIA

(Vancouver)

October 2021

The following individuals certify that they have read, and recommend to the Faculty of Graduate and Postdoctoral Studies for acceptance, the thesis entitled:

Soft capacitive force sensing skin: characterization, operation on a curved surface, and increased force range

submitted by Kieran Morton in partial fulfillment of the requirements for

the degree of Master of Applied Science

in Biomedical Engineering

Examining Committee:

John D. W. Madden, Professor, Electrical and Computer Engineering, UBC
Co-supervisor

Mirza Saquib us Sarwar, Postdoctoral Researcher, Electrical and Computer Engineering, UBC
Co-supervisor

Rizhi Wang, Professor, Materials Engineering, UBC
Supervisory Committee Member

Peyman Servati, Professor, Electrical and Computer Engineering, UBC
Additional Examiner

Abstract

Modern advances in medical robotics have brought them into many facets of day to day life, often directly interacting with humans. Some key applications of these robotics are human-interactive nursing robots and active prosthetics, where artificial ‘e-skins’ provide a soft interface with the environment. This thesis presents an investigation of long-term conductance stability for a flexible, stretchable conductive material, as well as two significant developments to a previously established flexible and stretchable combined pressure and shear sensor. The conductivity investigation was successful in reducing the resistance of flexible conductive elements by an order of magnitude, to approximately 1.8 kΩ. The two sensor development branches are aimed at creating a sensor that better resembles human skin in both form and function. Both sensors use a capacitive sensing approach to detect both pressure and shear using low-cost materials. The first area of development is exchanging the previously rigid and inflexible sensor base with a novel flexible one to allow for sensor function on surfaces with radii of curvature between 10 mm-100 mm, and updating the sensor characterization setup to accommodate curved devices. This work was successful in developing a sensor with a functional range of 0.1 N-1.6 N of normal force and 0-0.8 mm shear displacement at radii of curvature from 100 mm to 10 mm. The second is a novel sensor dielectric design which increases the functional range of the sensor to operate from a minimum functioning force of 0.05 N to a maximum functioning force of 50 N. This range increase is accomplished using a two-stage dielectric pillar shape, allowing the low normal force pressure and shear sensitivity of the original sensor design to be preserved while increasing the maximum allowable force significantly. Next steps in sensor design are integrating the high-force and flex designs, creating array-format sensors, and testing the device in practical environments such as basic robotic hands.

Lay Summary

From *Terminator* to *Star Wars*, artificial sensing skin has been acknowledged in pop culture as an important part of advanced humanoid robotics. The sense of touch allows us to identify, map, and grasp objects in our environment with relative ease. Devices such as modern prosthetics attempt to remedy this lack of touch sensation with other forms of feedback, such as visual. However, these methods cannot properly replicate the human sense of touch, a sensation that we consistently use in everyday life. This thesis presents a soft rubber sensor which mimics the properties of human skin while measuring forces in multiple directions. Different avenues for sensor development are explored, including increased ability for the sensor to flex around thin objects and increased force sensing range. Next steps in sensor development are combining the new designs presented in this thesis, and integrating the sensor into a device such as a robotic hand.

Preface

The research work presented in this thesis serves as an extension of the work previously conducted by Research Associate Dr. Mirza Saquib us Sarwar in soft capacitive sensing, and was conducted under the supervision of Professor John D. W. Madden and Dr. Mirza Saquib us Sarwar. The project is a collaboration with an industry partner in the area of human-interactive robotics, a relationship established by Dr. Sarwar and maintained by the author. The work presented in this thesis was conducted by the author, assisted by a graduate research associate and a team of undergraduate research assistants under the direct supervision and guidance of the author. Due to the industry connection and scope of the overall project from which this work is produced, a team consisting of the author, Zi Chen (UBC APSC, ECE), Bertille Dupont (Research Associate), Victor Mitchell (UVic APSC, MECH), Han Cat Nguyen (UBC APSC, BMEG), and Austin Weir (UVic ASPC, ELEC) worked as a team. Technical guidance and editorial feedback was provided by Dr. Sarwar and Dr. Madden.

In Chapter 2, the sensor design previously established by Dr. Sarwar is described, as are improvements to the characterization setup previously used (work conducted by Bertille Dupont with Dr. Sarwar), and an investigation of the sensor electrode material conductivity over time conducted by the author and Austin Weir. The author’s role in the conductivity investigation was experiment design, collection of data, and interpretation of data. The electronics and code described in this chapter are designed by Zi Chen and Austin Weir, under the guidance and supervision of the author, and serve as an extension of the hardware and software previously developed by Dr. Sarwar and his team. This supervision and guidance consisted of the author directly setting specifications for electronics design, regularly conducted design reviews, and provision of feedback based on results. A method for fabricating the sensors is also presented, created by the author and further developed by the author and Victor Mitchell. This fabrication method utilizing molds to build a sensor out of layers was solely created by the author to allow for precise sensor manufacturing. It was then later iterated upon by the author and Victor Mitchell to improve the process in terms of fabrication speed and precision, a collaboration in which the author provided direct design components, regular design review for iteration, and analysis of sensor data to determine factors such as improved fabrication precision.

In Chapter 3, the integration of a novel design for the base of the sensor to allow for bending is described, including design considerations and mechanical characterization. The design in this chapter involved a team led by the author, including Austin Weir, Han Cat Nguyen, and Zi Chen. In terms of design for this flexible sensor, the author contributed specifications for sensor design, methods to allow for the sensor to bend along a single axis of curvature while maintaining function, accommodations for characterization of sensors held to a single axis of curvature at given radii from 100 mm-10 mm, and regular design reviews for the novel sensor. Mechanical characterization of the sensor was conducted by the author and Austin Weir, under the author's supervision. Data analysis and interpretation was performed by the author.

In Chapter 4, the normal force sensing range of the sensor previously developed by Dr. Sarwar is increased. This was done through an exploration and redesign of the sensor dielectric architecture conducted by the author, Han Cat Nguyen, and Austin Weir. More specifically, the author contributed specifications for sensor design, novel sensor designs to increase normal force sensing range, and regular design reviews. Mechanical characterization of these high-range sensors was conducted by the author and Austin Weir. Data analysis and interpretation was performed by the author.

The contents of this thesis were written by the author, with editorial input from Dr. Madden, and suggestions on figure formatting and content from Dr. Sarwar.

Table of Contents

List of Tables

List of Figures

List of Abbreviations

CDC: Capacitance to Digital Converter

CNT: Carbon Nanotube

E-Skin: Electronic Skin (pressure and/or shear sensing)

MEMS: Micro-Electro-Mechanical Systems

MUX: Multiplexer

PCB: Printed Circuit Board

TENG: Triboelectric Nanogenerator

Acknowledgments

First and foremost, I would like to thank my supervisors Dr. John Madden and Dr. Mirza Saquib us Sarwar for their encouragement, support, and the vast number of opportunities they have provided for me. In addition, my thanks go to Ziqiang Chen, Bertille Dupont, Victor Mitchell, Han Nguyen, and Austin Weir, a team without whom this work would not have been possible. Thank you as well to the entirety of the Molecular Mechatronics lab at UBC, who welcomed me with open arms years ago and helped me pursue my goals. My final thanks go to Grace Lo, my parents, brother, and sister-in-law, who have all provided endless support through the last few years, without which I would not be where I am today.

Dedication

I dedicate this thesis to the love of my life Grace Lo and my family, who have all helped encourage my exploration of engineering and supported me throughout my journey. The contributions I hope to make to the field of prosthetics are all due to your undying support, and for that you have my gratitude.

Chapter 1: Introduction

This chapter explores a brief history of modern robotics through the lens of medical robotics, specifically soft, flexible artificial force-sensing skin for human-interfacing medical care robots and active prosthetics. A discussion of the human skin is first used to establish a biological baseline for artificial skin sensors such as those discussed in this thesis. A brief timeline of artificial e-skin is also presented to provide context for the work presented in this thesis, especially with regards to recent progress in the technology. The different sensing methods available for these flexible force sensors are discussed with a focus on capacitive sensing, the method of choice for this thesis; the previous iterations of these capacitive force sensors are also outlined in this chapter. Applications and motivation for these sensors are also established to provide context and impetus behind the technology being developed. Finally, the industry correspondent sponsoring the work presented here is described in terms of specifications outlined and general guidance for the thesis project.

Background

Over the years, the field of modern robotics has rapidly expanded from its original home in manual labor into many facets of our lives [1]. One particular region of interest is human-interactive robots, for uses such as social interactions and medical applications [2]. A primary challenge with robotics is their stiff nature, which makes it difficult to work with humans while minimizing risk; soft interfaces are a promising solution to bridge this boundary [3]. Common issues with conventional sensing methods range from technical issues such as the inability to exhibit sufficient dexterity and force control to sociological ones such as unwillingness to adopt new technologies due to the ‘uncanny valley’ effect often seen in humanoid robots [4]. Soft interfaces introduce soft, flexible, or stretchable (or some combination) materials and/or construction into traditional sensing elements which would normally be mostly composed of mostly rigid components. The result are sensors which are soft and allow for ready compliance with a variety of environmental impulses, such as human interaction. These sensors tend to provide significant immediate benefit in terms of user comfort due to their inherent similarity to skin or other biological components, especially compared to the rigid and outwardly mechanical appearance and feel of current widely used conventional sensors.

Humans use a wide variety of senses when they interact with the environment around them, ranging from sight and hearing to physical touch. In this wide array of sensations available to us, the ability to touch our surroundings is an important factor [5][6]. While the other senses provide huge amounts of information to us, there are several things only physical touch (and related aspects such as joint tension) may appropriately measure using only our biological perception. Surface roughness, slipperiness, and hardness are a few examples of the myriad of touch-related physical qualities that are partially or entirely touch-exclusive. Without our sense of touch, we quickly lose the ability to properly move in a stable and coordinated manner, let alone perform dexterous tasks vital to everyday life [6]. Lack of touch sensation results in extreme difficulty in interacting with both familiar and unfamiliar environments, resulting in spatial disorientation and a gap between the real world and how it is perceived. This dependence on touch translates strongly to robotic applications that seek to emulate human action, where the ability to process the environment in an adaptive and dynamic manner is a high priority for biomimicry.

Human skin is a highly elaborate, multifunctional organ that is our primary means of tactile perception, in addition to the identification of pressure, bending, and a wide variety of other stimuli [7]. Through an array of mechanoreceptors, thermoreceptors, and nociceptors, the skin allows for various degrees of body-wide mechanical, temperature, and pain sensing, respectively. The mechanoreceptors that permit this ability to feel our physical environment are split into four major types: Meissner’s corpuscles, Pacinian corpuscles, Merkel cells, and Ruffini corpuscles. Figure 1-1 displays the mechanoreceptors of human skin, including their general spatial placement and depth in the dermis and epidermis. These structures work together in the skin to form a complex weave of neurological signals that we interpret as vibration, appendage position, texture perception, and a wide array of other environmental stimuli. Human hands possess a large number of these receptors in comparison to the rest of the body, up to the order of hundreds per square centimeter at the fingertips, a densely populated area [1]. This high concentration heavily emphasizes the importance of sensation in the hands for the mechanical exploration of the environment, making fingertip-mounted sensing skin a reasonable priority for human-mimetic robotics such as active prosthetics and human-interactive nursing robots.

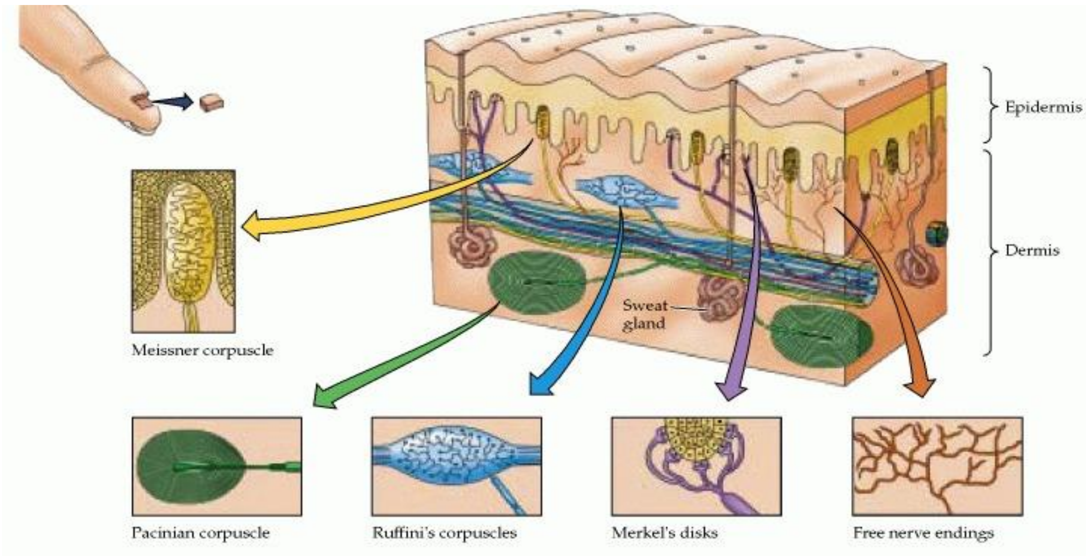

Figure 1-1: Force Sensing Components of Human Skin [8]

Due to this high importance of skin for everything ranging from limb placement perception to environmental mapping, artificial skin (or 'e-skin') for robotics has been an area of high activity for over 40 years [9]. These years of advancement are generally mapped out in Figure 1-2, including landmark technologies in the field and well-established cultural inspirations for the pursuit of e-skin technology. Early e-skins successfully used low-resolution (~5 cm) infrared sensors to provide proximity sensing to robotic arms for the purpose of obstacle avoidance and basic environmental mapping. This success produced a further push in the 1990's which resulted in printable shear-sensing MEMS sensors composed of silicon sensing 'islands' connected by flexible polyamide [9]. Since these major early advancements, investigation into artificial skin has accelerated due to an ever-increasing interest in flexible robotics for a huge variety of applications. Parallel advancements in related spheres have facilitated the continuous improvement of flexible sensing for artificial skin, particularly the areas of nanomaterials, microelectronics, and micromanufacturing. Other similar technologies of particular importance in the development of modern soft robotics include stretchable, flexible batteries and self-healing soft electronics.

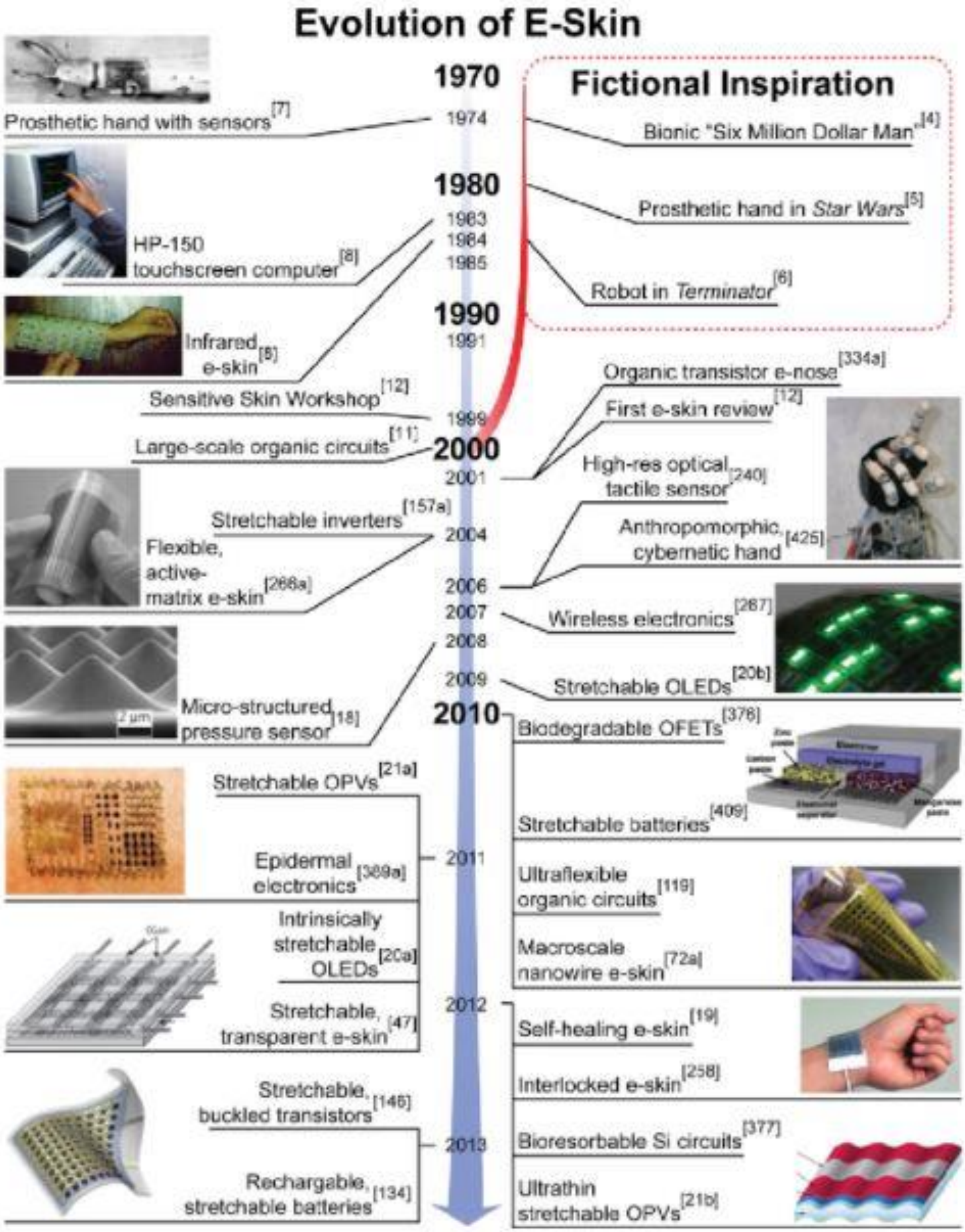

Figure 1-2: Artificial Skin Evolution from 1970-2013. Used with permission from John Wiley and Sons. [9]

Sensing Methods

It is established that providing skin-like soft sensing is an important and valuable component in producing human-mimetic robotics [9]. These ‘e-skins’ use a variety of novel materials to create stretchable, flexible sensors which may stand-in for biological skin in robotic contexts such as medical nursing robots and active prosthetics. Sensing methods are the core of novel e-skins, as different flexible skin applications may demand or allow for a wide variety of sensing methods which may preserve the desired physical parameters for skin. Several common sensing methods for these novel sensors are discussed in this section, particularly the capacitive sensing technique used for the sensors described later in this thesis.

A variety of sensing methods have been traditionally used for pressure and shear sensing in situations requiring soft sensors for applications in the biomedical field. The vital specifications for these sensing methods are the ability to flex and stretch, mechanical similarity to biological skin, high sensitivity potential, and a small minimum sensing footprint. The pros and cons of each sensing method are outlined in Table 1-1, with each method providing its own benefits; capacitive sensing is chosen for this project due to its high stability to time and the environment, consistent function under strain, and the straightforward design of the sensor architecture.

Sensing Method	**Pros**	**Cons**
Piezoresistive [9]	• Simple to implement • Straightforward stress/strain measurement • Low-cost materials	• Dependent on temperature • Highly sensitive to substrate material conductivity degradation
Capacitive [9]	• Highly temperature stable • High sensitivity • Good area coverage	• Sensitive to environmental electronic stimuli • High sensor crosstalk
Piezoelectric [10]	• High sensitivity • Fast response to changing force	• Highly material dependent • Overlap with pyroelectric materials can cause thermal interference • Incompatible with static or slower forces
Triboelectric [11]	• Self-powered • High sensitivity	• Restrictive in terms of materials • Signals only appear with dynamic force
Optical [12]	• Low interference with other electronic signals • Easy to implement in large-area applications	• Relatively difficult to implement
Electrochemical [13], [14]	• Functional at very small device sizes • Highly biocompatible	• Relatively complex implementation
Magnetic [15]	• Mass-producible • High 3-axis sensitivity	• Large area per sensor • Requires output amplification

Table 1-1: Sensing Methods, Pros and Cons [16][17][13][14][15]

Capacitive Force Sensing Principle

Capacitive sensors employ a parallel plate system in which the overall capacitance of the architecture – governed by the ideal capacitor equation $C = \varepsilon_0 \varepsilon_r A/d$, where ε_0 is the permittivity of air, ε_r is the equivalent overall permittivity of the dielectric, A is the parallel facing area of the capacitor plates, and d is the plate separation distance - is monitored for changes. This changing capacitance is mapped to force application through either change in plate separation distance d for normal force or area A for shear; depending on the material the sensor ε_r may also be utilized to measure either force application, but this generally requires a significant amount of specialized dielectric material design [9]. The sensors described in this thesis use the simple parallel-plate relationships, mapping the change in capacitor d or A to either applied normal or shear forces. These relationships are displayed in Figure 1-3, where normal force is related to plate separation distance d and shear force is related to one side of the capacitor parallel surface area A.

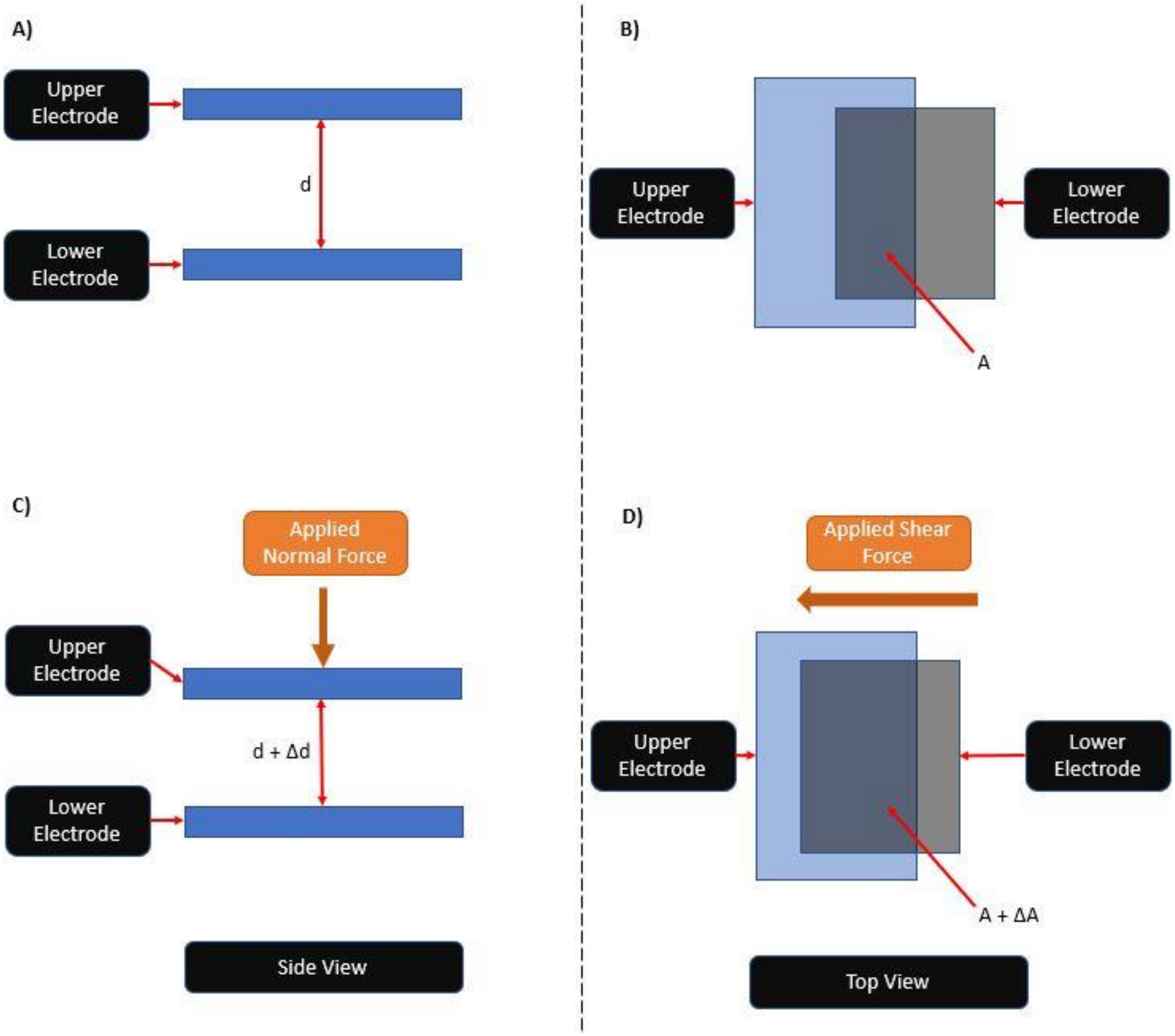

Figure 1-3: Capacitive Sensing Principle for Normal and Shear Forces A) Side View, No Force Applied, B) Top View, No Force Applied, C) Side View, Normal Force Applied, D) Top View, Shear Force Applied

Pressure and shear sensors with a capacitive basis are often designed using dielectric materials with a low Young's Modulus, allowing for particularly increased displacement of either the *A* or *d* described above. This material choice is also leveraged to produce sensors capable of stretch and flex, further requiring conductive electrode materials which have these characteristics. Previous work has used materials such as PDMS, Ecoflex^{TM} (*Smooth-On, Inc.*) silicone, or other similar low-modulus structural materials for the sensor dielectric, and conductive materials such as carbon nanotubes, metal nanowires, or thin film metals to fabricate electrodes [18]. The work described in this thesis focuses on Ecoflex™ 00-30 as the sensor dielectric material and a combination of carbon black and Ecoflex™ 00-30 for the sensor electrodes, to form a relatively homogenous stretchable and flexible sensor which provides high sensitivity to applied forces.

A key issue in the design of these elastomer-based flexible pressure and shear sensors is the force response of the soft dielectric. These soft materials produce devices that are highly stretchable and flexible, but are generally incompressible and susceptible to viscoelastic effects such as creep. To overcome these effects, a structured-material approach introducing air into the dielectric gap has a history of use [19][18]. This structuring facilitates the deformation of the sensor under force, but also reduces the effective dielectric constant of the material due to the introduction of air as a poor dielectric. The use of elastomers such as silicone rubber also provides a spring response, providing a returning force to maintain sensor structure after significant deformation in either the normal or shear directions. It also increases the complexity of sensor fabrication due to the difficulty of structure introduction, requiring techniques such as elastomer molding, photolithography, or foam curing. In this thesis, a molding process is used to fabricate mm-scale dielectric pillar structures which provide an elastomer:air ratio in the 0.3-0.4 range. Capacitive sensing also allows for the proximity sensing of certain materials by means of examining the localized electric fields outside of the inter-plate volume.

Other Sensing Principles

Piezoresistive sensors operate on the principle of changing material resistance with strain under applied forces. This may be accomplished through a variety of methods, such as changing geometries of sensing elements, semiconductor resistivity changes due to band structure changes, contact resistance alteration, or composite changing resistance due to interparticle separation changes [9]. These sensors are governed by the material resistance given by $\rho L/A$, with ρ as the material resistivity, L as the material length, and A as the cross-sectional area of the material examined. Previous groups have used materials such as Si, ZnO-coated conductive fibers, and CNTs to create sensing devices that work on a variety of mechanical principles to measure changing resistance with applied pressure or shear. Bending and strain has previously been enabled in these sensors through methods such as weaving together conductive fibers to form a piezoresistive material [20] or liquid metal [21], among other materials.

Piezoelectric sensing devices use materials that induce an electrical signal on deformation in specific directions, dependent on the material used [10]. The sensing principle of piezoelectric pressure and/or shear devices is based on the measurement of these electrical signals, often through a simple voltage measurement across terminals attached to the 'sensing' material itself. These sensors are generally self-powered, which poses a major advantage in many wearables or integrated devices, where power is already a significant bottleneck. The prominent disadvantages of piezoelectric pressure and shear sensors are material design and lack of stretchability. Piezoelectric sensors demand more complex material design due to the unique sensing method, as piezoelectricity often requires materials that are specifically engineered for this purpose or have relatively uncommon intrinsic properties. Additionally, piezoelectric materials are not commonly flexible or stretchable, which limits their ability to be integrated into the devices of interest outlined in this thesis. In addition, piezoelectric materials experience overlap with pyroelectric materials, which may make sensors less temperature stable than desired.

Triboelectric nanogenerators (TENGs) are sensors which use physical contact between two materials with different electronegativity to sense a variety of environmental impulses, such as motion [11]. As the plates are shifted by some outside mechanical force, a difference in electrical potential is established; this difference can then be translated into pressure or shear displacement through sensor structure design. TENG sensors generally have several advantages, such as being low-cost, lightweight, and self-powered. However, similar to piezoelectric sensors, the materials that are effective in TENG sensors are relatively limited, which may inhibit the ability of these sensors to stretch and flex appropriately for some applications. TENG sensors also often rely on dynamic forces for sensing, and are not as effective for sensing slower-applied static forces, such as slow device deformation over time.

Optical sensors convert light-based signals into mechanical information, often through inspection of changes in light intensity or wavelength of light in a fiber or optical waveguide [12]. Various architectures exist for this signal conversion, depending on the requirements of the sensing application such as sensitivity or flexibility. These sensors also have a distinct advantage against most other pressure and shear sensing methods due to an inherent lack of reliance on electrical signals, limiting crosstalk and interference with other nearby electronic signals. Optical signals also readily allow for much larger sensing areas than other methods, depending on device architecture. However, optical signal measurement for high spatial resolution combined pressure and shear measurements is difficult.

Electrochemical force sensors employ electrochemical impedance in a fluidic channel to measure forces, such as an electrolyte within a microstructure connecting electrodes [13]. As force is applied to the structured diaphragm or other similarly designed portion of the sensor, a measurable change in resistance is produced due to the change in ionic current flow path within the channel. This may then be mapped to applied forces depending on the architecture of the sensor. Electrochemical sensors have the benefit of high biocompatibility due to commonly used materials, and the lack of biologically dangerous materials in the fluid channel [14]. Due to the need for fluid-containing channels connected to readout elements, electrochemical sensors tend to be complex compared to other force sensing types.

Magnetic force sensors use changes in local magnetic fields generated by a magnet to measure applied force [15]. A magnet is placed within a piece of soft material such as an elastomer, with appropriate shielding to guard against outside field disturbances. The placement of this magnet creates a field within the sensor which varies depending on proximity to the field sensing element and walls of the sensor enclosure. A magnetometer or similar device is generally used to measure the local field, and output data for collection. The major advantages of magnetic force sensors are their high sensitivity and facilitation of mass manufacturing, due to the relative simplicity of the sensor itself. However, magnetic force sensors often require output signal amplification for use, which creates difficulties in readout circuit complexity and size.

Commercial Force Sensing Devices

A number of commercial devices exist that fit into the ‘e-skin’ sensing role that is the goal of the sensors presented in this thesis. Two of these devices are taken as examples in this section, Xela ‘uSkin’ by Xela Robotics [22] and the ‘BioTac®’ by SynTouch [23]. Both of these technologies have models aimed at incorporation into the curved surface of a finger for applications such as prosthetics with tactile feedback. The uSkin technology employs an array of electrodes incorporated onto a flexible substrate to provide sensing elements, with an overlaid elastomer layer creating a skin-like surface. BioTac® sensors use conductive fluid held over impedance-sensing electrodes by an encapsulating elastomer layer, using a small alternating current to measure the change in voltage across the fluid with applied force. These examples provide tri-axial force sensing on a curved finger-like base that is soft and skin-mimetic in terms of deformation and general aesthetic. A brief comparison of the general characteristics for the uSkin (model XR1944) and BioTac® is presented in Table 1-2, providing an example of the sensing methods and materials commonly used in modern e-skin sensors. Technical performance specifications for both the Xela uSkin (Model 1944) and SynTouch BioTac® are presented in Table 1-3 for comparison.

Both of these example sensors have unique advantages and disadvantages in comparison to the sensors presented in this thesis. Both sensor designs are capable of 3-axis force using different sensing techniques from the devices presented in this thesis, but the BioTac® does not produce directional data in response to applied shear. The uSkin sensor by Xela has a lower electrode density than the 12-taxel design described in Chapter 2 of this thesis, but all taxels in the uSkin produce 3-axis data. The BioTac® does not have a readily available specification for surface area or precise electrode distribution, but the overall system does compete in terms of number of sensing elements. The BioTac® sensor has a similar force range to the sensor design presented in Chapter 4 of this thesis, with a slightly higher force resolution (0.01 N for BioTac®, 0.05 N for the high-range sensor in this thesis); in comparison, the uSkin provides a much higher force resolution but less than half of the maximum normal force.

Sensor	Force Sensing Axes	Force Sensing Mechanism	Other Integrated Sensing	Material	Cost
Xela uSkin (Model XR1944)	3-Axis	Magnetic	None	Soft Elastomer (not flexible)	$2100 CAD (sensor with microcontroller)
SynTouch BioTac®	3-Axis (no directional information)	Impedance	Vibration, temperature	Soft Elastomer, Conductive Fluid	By quote

Table 1-2: Commercial Sensor Comparison, General Characteristics

Sensor	Spatial Resolution	Force Resolution	Force Range	Refresh Rate	Thickness	Electronics	Power Consumption
Xela uSkin (Model XR1944)	0.0238 taxels/mm^2	0.00098 N (shear), 0.0098 N (normal)	0-4.22 N (shear), 0-17.7 N (normal)	250 Hz	5.5 mm	Connects to external PC via microcontroller)	Not specified
SynTouch BioTac®	19 taxels per fingertip	10 mN	0-50 N	100 Hz	Not available	Connects to external device via microcontroller	Not specified

Table 1-3: Commercial Sensor Comparison, Technical Specifications

A major difficulty experienced by both sensors is the reliance on bulky circuitry connections for device function and data collection, requiring a connection to an external computer by means of an attached microcontroller. This is a common issue among 3-axis soft sensors in development, as they often have some combination of bulky circuitry or complex measurement designs [24]. The sensors described in this thesis experience a similar drawback, with significant readout circuitry required per sensor. The uSkin has a unique drawback in its lack of flexibility, as the sensor is flexible but documentation indicates that the magnetic field may not function properly if the sensor is used on a curved surface. Additionally, the lack of readily available directional information in the BioTac® sensor is a major disadvantage, as shear force is measured but may be difficult to interpret. Overall, each sensor has a variety of advantages and disadvantages, but serve as strong points of comparison across force sensing methods.

Academic Force Sensing Devices

The importance of sensing skin for many human-interfacing applications has lead to a significant focus on the development of soft, flexible devices that measure pressure and/or shear [24], [25], [15]. These sensors explore a variety of sensing mechanisms, including piezoresistive [24] and capacitive [25], [15]. Research has identified several key areas that require further development for the success of e-skins in providing tactile sensation for robotics applications. One of these regions of focus for improvement is complexity, as the circuitry or sensing array designs persistently pose a large problem for sensing element density and scalability of flexible sensors [24]. High conformability to stretch and curvature is also indicated a key factor of research in sensor design for humanoid robotics and similar applications, as previously developed high-sensing-density micromachined devices fabricated out of silicon tend to be too brittle for large deformations [25]. Other regions identified as important for soft flexible force sensors include cost and rapid real-time sensing of both pressure and shear [15].

Research Group	Force Sensing Axes	Force Sensing Mechanism	Spatial Resolution	Force Resolution	Force Range
Pang *et al.*	3-axis	Piezoresistive	0.016 taxels/mm^2	49 mN (normal), 1 mN (shear)	5-1500 Pa (normal), 0.001-1 N (shear)
Cheng *et al.*	3-axis	Capacitive	0.0625 taxels/mm^2	26 mN (normal, shear not specified)	0-0.812 N (normal)
Boutry *et al.*	3-axis	Capacitive	(Approx.) 2.78 taxels/mm^2	3.6E^{-4} %/N (normal), 2.7E^{-5} %/N (shear)	0-16.2 N (normal)

Table 1-4: Academic Soft Force Sensor Technical Specifications

Three academic sensors examined for comparison in this thesis, one piezoresistive sensor based on interlocking nanofibers (Pang *et al.* [24]) and two capacitive sensors with floating-electrode (Cheng *et al.* [25]) and active electrode (Boutry *et al.* [15]). The technical specifications for these sensors are presented in Table 1-4 for comparison. Cheng *et al.* present a sensor consisting of 4-taxel units which provides a similar sensing element density to the 12-taxel sensors presented in this thesis alongside a high normal force sensitivity, but functions in a much smaller force range than the sensors presented in this thesis. Additionally, the Cheng *et al.* sensor does not have a uniform upper surface which may conflict with the skin-like goal of the sensors in this thesis. The Boutry *et al.* sensor has a much higher taxel density and wider normal force range while maintaining a high sensitivity to force, but has a significantly nonlinear response to applied forces with sensitivity dependent on the force range. This sensor design also has a high density of signal-carrying wires, which may negatively effect the complexity of associated electronics. Compared to the sensors presented in this thesis, the Pang *et al.* sensor design has a lower sensing element density and smaller shear force range, but is functional up to large amounts of normal-direction pressure. Overall, the sensors presented in this thesis aim to present designs which allow for fully flexible sensors which are competitive with current research in terms of 3-axis taxel density, force resolution and force range.

Summary of Factors for Soft Force Sensor Design

Generally, the most important shared factor between these force sensor types is the ability to detect 3-axis forces with high sensitivity. Some desirable secondary characteristics that are shared between multiple of the common sensor types listed above include low-cost materials or straightforward fabrication, and high biocompatibility for applications such as artificial skin. The most prevalent drawback among sensing types is the complexity of the design, in particular the readout circuit components. In addition, several sensing methods commonly employed by soft force sensors are significantly sensitive to temperature, such as piezoresistive and piezoelectric. Temperature is also a concern for capacitive force sensing in devices where the conductivity of the electrode material is temperature-dependent, such as the elastomer-carbon black mixture described in this thesis. Both high circuit complexity and partial temperature dependence are very difficult factors to work with in the space of biomedical robotics and prosthetics, where sensing elements are limited in available volume and are expected to come into contact with warm surfaces, such as human beings, on a regular basis. Consideration of these limiting factors in the goal application of a sensor is very important when designing soft sensors.

Previous Sensor Design

The sensor architectures described in this thesis use capacitive sensing to detect the presence of pressure and shear; Figure 1-4 shows a simplified abstract construction of this combined pressure and shear sensor. The upper electrodes are formed out of a conductive, flexible, stretchable mixture of Carbon Black and Ecoflex™ 00-30 elastomer while the bottom electrodes are either the same material, or exposed copper on a commercial PCB. Capacitive sensing has previously been demonstrated to be relatively independent of temperature, as long as trace resistance and frequency are appropriately controlled [26]. This sensing mechanism allows for a temperature stable system that provides consistent measurements with relatively high sensitivity. Another potential electrode material that has been explored previously is ionic fluid, which would be injected into channels fabricated into the sensor body [27]. An elastomer, generally Ecoflex™ 00-30, is used as a structured dielectric layer to allow for increased unit sensitivity while still maintaining a skin-like surface structure. The specifications obtained for this previous sensor are presented in Table 1-5, and serve as a baseline for the sensor developed in this thesis.

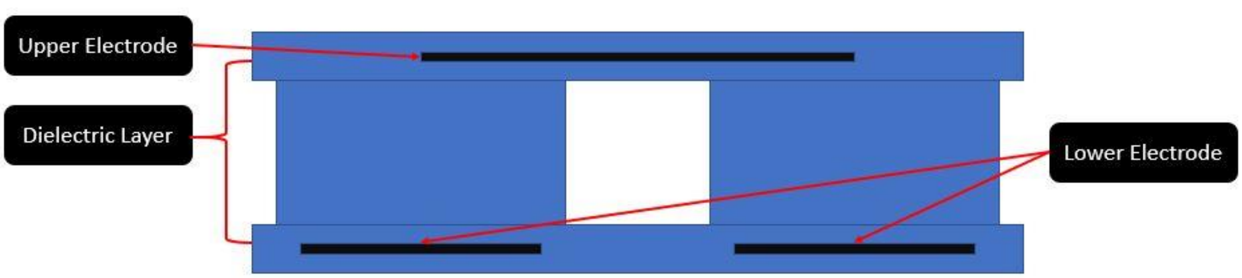

Figure 1-4: Combined Capacitive Pressure and Shear Sensor Basic Design Principle

Sensing Method	Shear			Normal	
	Range (N)	Resolution (N)	Max Displacement (mm)	Range (N)	Resolution (N)
Capacitive	1.5	0.02	1.5	12	0.1

Table 1-5: Previously Developed 4-Taxel Sensor Specifications [27]

Capacitive pressure sensing is achieved through measurement of charge differential between two parallel plate electrodes separated by a relatively pliable, often structured, dielectric material. This capacitor is ideally governed by the equation for an ideal parallel plate capacitor $C = \frac{\varepsilon_0 \varepsilon_r A}{d}$, where ε_0 is the vacuum permittivity, ε_r is the relative permittivity of the dielectric material, *A* is the plate overlap surface area, and *d* is the separation between plates. During normal force application, the separation *d* of the capacitor is reduced, increasing the capacitance between a given two plates. Similarly, under shear force application the in-line side lengths will increase or decrease depending on the direction of force. This can cause either an increase or decrease in capacitance, depending on the direction and the electrode overlap design.

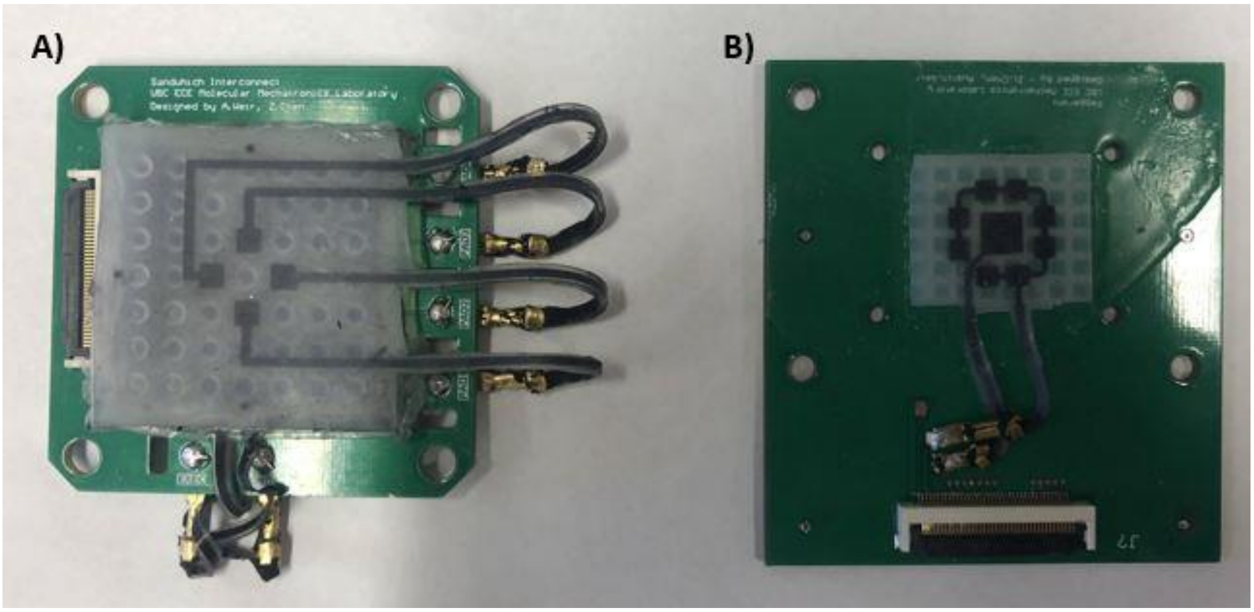

Figure 1-5: Previously Developed Sensor Designs A) 4-Taxel Sensor, B) 12-Taxel Sensor

Two distinct electrode architectures are described based on the work from *Sarwar et al.*; a base sensor with 4 lower electrodes and one upper electrode to allow for combined pressure and shear sensing, and a larger architecture which utilizes an additional 8 electrode pairs for enhanced pressure-only sensing. Figure 1-5 displays examples of both the base 4-electrode-pair architecture and 12-electrode-pair-architecture, using representative sensors for both developed by *Sarwar et al.* Both designs also implement an upper 'shield' electrode above the sensing layers, which provides both protection for the sensor from environmental electromagnetic interference and allow for basic proximity sensing. These sensors are fabricated from flexible and stretchable elastomers to allow for use as an artificial skin that accommodates for a variety of situations.

Elastomers have a history of use as artificial skin for various applications, such as medical robotics and skin grafts [28][29]. The elastomer used in the sensors for this thesis is Ecoflex^{TM} 00-30, a material which has previously been used in flexible sensors able to stretch to up to 460% original size while maintaining function [30]. This material is chosen over other elastomers due to its low Young's Modulus, low cost, and ease to work with in manufacturing. Ecoflex^{TM} also takes well to the incorporation of conductive elements to form a stretchable flexible conductor, such as Ag nanoflakes [31], acetylene black, carbon nanotubes, and graphene [32], making it an excellent material for the manufacturing of highly compliant pressure and shear sensors. In addition, the use of capacitive sensing allows for relatively straightforward readout electronics, with the only specialized component required being a readily-available capacitance to digital converter and enclosed systems which may be powered from a microcontroller 5 V output.

Overall, the combination of this electrode architecture, low-cost electrode material, and overall dielectric design allows for the fabrication of highly skin-like sensors that allows for multimodal sensing of touch, pressure and shear in one compact flexible and stretchable body [33].

Applications

Robotics in a variety of environments are a core application for soft artificial skin, especially human-interactive robotics [34]. These systems conventionally use stiff sensors in rigid systems, which experience issues in human interaction due to factors such as unintuitive action, dynamic environmental response, and even increased danger to the human [3]. In medical robotics this has been especially highlighted, due to consistent close interaction with humans and environments which are potentially sensitive to the rigid components of conventional robotics. In addition, the application of a dynamic tactile-sensing covering allows for better exploration of unmapped environments, allowing for human-mimetic robotics to operate without the explicit need to map the environment with other sensing methods [2]. Finally, sufficiently sophisticated tactile sensation is important for dexterous manipulation of objects in the hand without relying on other sensory features which may be more complicated or awkward to use in-situation.

Another primary area of continuous research where soft tactile sensing is highly utilizable is human-mimetic upper limb robotic prostheses. Humans rely strongly on their sense of touch for interaction with their environment, especially with manipulation of objects and other fine motions [6]. Even with all other senses available, it is difficult to maintain a steady grasp on objects, accurately perceive limb location, and even discern between the self and environmental objects. These prosthetics also have very high rejection rates associated with inability to properly perform the functions of the original limb due to feedback sensing limitations [35][36]. Conventionally used rigid sensors generally fail to provide an appropriate sensing schema for prosthetic limbs as well, in terms of both form and function. These sensors have high sensitivity to applied forces, but do not produce a dynamic response similar to human skin in addition to being difficult to aesthetically match to the missing limb.

Soft pressure and shear sensing have applications outside of artificial skin, particularly in the interface between people and wearable technology of various forms. These high-risk interfaces are unavoidable in a wide variety of wearables such as foot orthotics for plantar force monitoring, prosthetic leg sockets, pressure monitoring in joint braces, backpack-shoulder force application, and much more [37], [38]. These areas require monitoring of both pressure and shear for both comfort and safety, as locations with high sustained or repeated pressure and shear forces are at risk for ulcerification and other highly uncomfortable conditions. Comfort is extremely important for the uptake of wearables and prosthetics, remaining as a key factor in the continuing high rejection rate for prosthetics [39]. In addition, health conditions such as ulcers caused by pressure or shear can be extremely detrimental to user health with a variety of long-term wearable devices. To this end, the application of artificial ‘skin’ to the human-wearable interface could allow for important insight into the interfacial forces, and enhance the uptake rate for these technologies.

Motivation

In robotics an adaptive, environmentally-conforming, and low cost touch and pressure sensing is a key development for progression into unknown, unmapped environments [40]. While current robotics incorporate many different methods of exploring their environments, such as touch, vision, and even sound, a truly effective sensation of touch sensing remains out of reach. A human-mimetic artificial skin that can replicate some of the function of our somatosensory system by being able to sense a wide range of pressure and shear forces would greatly improve the ability of modern robots to move into and self-map unfamiliar environments, perform informed fine manipulation of objects, and other tasks generally ascribed to intelligent, autonomous life. In addition, a properly biomimetic skin would increase the aesthetic perception of robotics for social or medical purposes, such as in-home nursing robots or androids placed in human-interactive settings.

User rejection has long been an issue for upper limb prosthetics of various forms, limiting their effect on patient quality of life despite the enhanced functionality they provide. Over the last 25 years the mean rejection rate is as high as 45% for body-powered devices and 35% for electric ones in pediatric populations [41]. In these prostheses, hooks are generally preferred by users over hands due to factors such as ease of use, ability to perceive objects, and device weight. More modern electric prosthetic devices implement biomimetic features such as skin-like silicone gloves, high grip control, and increased finger articulation to increase user comfort, functionality, and overall successful adoption rate. A persistent design challenge that exists with all of these features is tactile feedback, which allows for better alignment of the prosthesis with user perception of their limb and effective use [42]. Tactile feedback allows for improved functionality of the limb due to reduced reliance on visual perception for object manipulation, in addition to increased user comfort for both passive and active upper limb prosthetics. When combined with an appropriate feedback communication system, an artificial pressure and shear sensing skin would enhance the functionality, user comfort, and aesthetic perception of robotic prosthetics, and potentially significantly decrease the persistently high user rejection rate.

Industry Correspondence

Literature exists outlining reasonable parameters for pressure and/or shear sensors seeking to provide artificial skin for various applications [9]. The specifications used for the sensor presented in this thesis are derived from those provided by an industry partner performing work in human-interfacing robotics. These specifications were divided into three major sections: improving sensor characterization, implementing the sensor on a curved surface, and increasing the range of the sensor designed by *Sarwar et al.* in terms of both sensitivity and upper max force. The industry collaboration project used as the basis for this thesis aims to implement the pressure and shear sensor on a robotic hand with a focus on sensing in the finger pads, a key area of work for both human-interactive robotics and active prosthetics. While these specifications provided in Table 1-6 do not encompass the final requirements for a real-world implementable soft pressure and shear sensor, they serve as a reasonable next step in sensor development towards this goal.

The curvature specifications described in Table 1-6 correspond to different parts of the body where sensing may be applied. Considering an example application of a hand, a 10 mm inner radius of curvature would correspond to a narrow part such as a large finger. Alternatively, the 100 mm inner radius of curvature would correspond to a much flatter part of the hand such as the ball of the hand. The maximum force of 50 N described in the specifications corresponds roughly to balancing a full 4 L jug of milk balanced on the fingertip, while a 0.03N force is slightly more than holding a penny flat in the palm of one's hand. These specifications would allow for the distribution of sensors throughout an example robotic hand, providing it with the ability to sense a wide range of common objects with a wide range of masses.

Category	Specifications Outlined
Implement on Curved Surfaces	● Minimum curvature radius of 10 mm ● Maximum curvature radius of 100 mm
Increased Dynamic Range	● Minimum detectable force of 0.03 N over a 14x14 mm area ● Maximum detectable force of 50 N over a 14x14 mm area

Table 1-6: Industry Correspondent Specifications for Sensor Development

The core focus in the continued development of *Sarwar et al.*'s sensor was in the areas of improved ability to characterize sensors, implementation of the sensor on curved surfaces using a flexible architecture, and increasing the range of the sensor in terms of both low force sensitivity and high force detection. These specifications focus on the industry partner's sensing area of 14x14 mm, the estimated surface area of each fingertip pad in their robotic application. Sensors of this area are expected to function on a variety of curvature radii in the range of 100-10 mm, measured from the inner surface of the sensor PCB. The industry partner also required the sensing range to operate in the 0.03N-50 N sensing range, an extended set of forces from the original sensor developed by *Sarwar et al.* (approximately 0.1-12 N).

In addition to the improved sensor specifications provided, improvements to the characterization setup previously utilized by *Sarwar et. Al.* were required for the further device characterization presented in this thesis. The basis of this characterization setup improvement was the replacement of components previously found to be unstable, such as the acrylic single-post frame and force-fit interconnects. The sensor specifications provided in Table 1-6 also necessitated further improvement to the previously used characterization setup, namely curved sensor and high force accommodations.

Thesis Outline

This thesis is divided into four chapters; in the first, the basic sensor developed by *Sarwar et al.* will be discussed including a detailed description of the sensor working principle, previous work on sensor architecture, and the established method of characterization. Here the improvements to the characterization setup previously used are described, headed by Bertille Dupont, a research engineer in the lab. In addition, a previously identified problem with the conductive material used in the sensor is described, which causes the resistance of the sensor leads to significantly increase over time. This difficulty is approached through analysis of a variety of alternative conductive materials which share the stretchable, flexible properties of the previously used carbon black-Ecoflex^{TM} blend. The second chapter covers the accommodation of this basic sensor architecture into a new flexible design through integration of a flexible PCB, as well as characterization on curved surfaces and discussion of this new sensor design. These flexible sensors were successfully characterized in a normal force range of 0.1 N-1.6 N, and shear displacements of 0.2 mm-0.8 mm. In the third chapter an enhancement to the basic sensor design is described, increasing the effective range of the sensor to accommodate a wider range of forces, particularly increasing the upper functional force range of the sensor. This is done by changing the dielectric architecture of the basic sensor architecture to create multiple distinct stiffness levels and allow for function on both ends of the force spectrum for the device. The sensor was successfully characterized in the increased force range, with an increase in the functional range of the sensor from 0.1 N-12 N to 0.05 N-50 N. Stress relaxation was observed at higher forces, making the precise identification of large forces less accurate. In the final chapter of the thesis, overarching conclusions are presented, based on the sensor characterization, design and performance, alongside a general discussion and suggestions for future work.

Chapter 2: Sensor Design and Characterization

The sensors described in this thesis are based on previous work by *Sarwar et al.* [33][27], which the author contributed to by improving the fabrication method and dielectric pillar design. In this chapter the relevant portions of this previous work are described, including sensor architecture, sensing principle, and fabrication methods. The fabrication method described in this chapter is an updated version of the fabrication originally designed by the author and previously described by *Sarwar et al.*, with refinements made by both the author and Victor Mitchell, an undergraduate research assistant under the guidance of the author. The characterization setup used for all of the data presented in this thesis is also described, with consideration for special circumstances required in high force sensing. This chapter also presents an exploration of the lifetime of the sensor electrode material, an elastomer-conductive nanoparticle blend. It was identified in previous work that the conductive nature of this material degrades over time in regular conditions, so identification of a method to stabilize the sensor electrode conductivity is vital for future sensor work.

The basis of the sensors described in this thesis is a 5-electrode capacitive structure that allows for the measurement of combined pressure and shear [27], described in further detail below. This sensor has previously been used to sense normal forces in the 0.1-15 N range on 12 taxels, and up to 1.2 mm displacement in the x-y shear directions. It traditionally is fabricated in one of two designs, either a full-elastomer sensor where the top and bottom are fabricated out of Ecoflex™ in addition to the dielectric or a partial-elastomer sensor where the bottom layer is replaced with a PCB. In both sensor designs, conductive-elastomer electrodes are connected to readout circuits using metal crimps which are soldered directly to exposed copper pads on the PCB surface. The base of each readout circuit is a capacitance-digital converter (the AD7745) connected to a microcontroller (the Arduino Uno or Nucleo L432KC) for readout and data storage.

Working Principle

The base principle behind the combined pressure and shear sensing unit described in this thesis can be explained using a parallel plate capacitive model. This model consists of two flat, parallel conductive plates (the electrodes) separated by a layer of insulating dielectric material (the dielectric). When connected to a voltage source, an electric field is induced between the plates, across the dielectric. Two portions exist in the electric field between the electrodes, both of which contribute to the overall capacitance: the straight, perpendicular field directly between the parallel plates, and the curved field outside of the parallel plates (known as the 'fringe field'). The perpendicular, straight field lines are governed by the ideal capacitor equation described in Chapter 1, which disregards fringe fields for simplicity. These fields induce opposing charge collections on the two electrode-dielectric contact areas, with charge direction dependent on the direction of applied voltage. By applying voltage and measuring this charge collection on these contact boundaries, devices such as capacitance-digital-converters (CDCs) may measure the total capacitance between the two sensor electrodes. The measured capacitance is a combination of the perpendicular and fringe fields.

This parallel plate capacitor is used to measure applied forces in the normal and shear direction through the integration of a soft, deformable dielectric. As the sensor dimensions (cross-sectional area A and plate separation d) are shifted due to applied force, the capacitance measured by the associated circuit will change accordingly. Capacitance is proportional to area A and inversely proportional to plate separation distance d, so shearing the two electrodes to have less overlap will decrease sensor capacitance, while shearing the two electrodes to have more overlap or applying pressure to decrease separation distance will increase sensor capacitance. This allows for the measurement of applied forces by mapping the sensor capacitance change (ΔC) to either shear or normal forces, depending on electrode architecture. A change in sensor area due to non-shear forces is also possible in situations such as lateral strain on the sensor, which may easily increase the electrode parallel surface area or decrease the plate separation, or both. Effort is taken in the sensors described in this thesis, primarily the attachment of sensors to PCBs or other rigid bases, to prevent this effect; therefore, this additional effect will be disregarded in the model of the sensor presented in this section. This simplification facilitates mathematical capacitive modeling of the sensor using the ideal capacitor equation, assuming fringe fields are limited and/or insignificant.

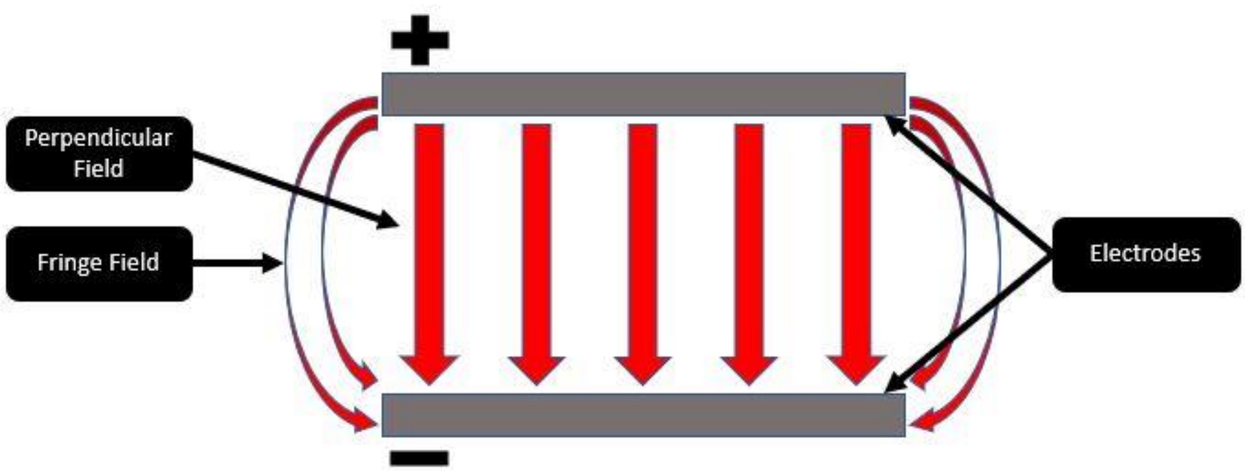

Figure 2-1: Parallel Plate Capacitor with Perpendicular and Fringe Electric Fields

Besides fringe fields, a major contributor to the sensor capacitance is influence from outside bodies, referred to in this thesis as the 'third body effect'. The model presented above assumes the two plates of the capacitor are undisturbed in an unchanging environment, so outside influences are ignored. However, in practical application it is highly likely that electrically interactive components will come close enough to influence the sensor capacitance.

The most common and significant source of this influence is the approach of a human, which acts like a large virtual ground to the sensor electrodes. This virtual ground, being much larger generally than the sensor ground electrode, will naturally attract or ‘decouple’ a significant amount of the electric field from the sensor itself. The result of this decoupling is the reduction of the sensor capacitance, as the inter-plate charge accumulation will be decreased in proportion to the amount of field strength ‘stolen’ by the approaching virtual ground. This poses a major problem for the applications described in this thesis, where robotic skin is likely to come into contact with people on a regular basis. To eliminate the majority of this unwanted third body effect, a ground shield layer is incorporated into the top layer of the sensor.

Sensor Body Design

The capacitive sensors used in this thesis are fabricated using Ecoflex™ 00-30, a soft silicone elastomer often used for custom cushioning, special effects fabrication, and simulated skin for applications such as prosthetics [43]. This material is naturally insulating, allowing for separation of the electrodes used in the construction of the sensor and providing a sensitive dielectric structure. Carbon particles can also be added to Ecoflex™ 00-30, allowing the creation of relatively conductive electrodes (approximately 0.131 S/m, or tens of kΩ in the sensor elements used in this work) while maintaining the ability to flex and stretch. This material is the same as was used by *Sarwar et al.* [27] in our lab’s previous work. The compatibility of this new Carbon Black infused Ecoflex™ with the non-carbon infused Ecoflex™ allows for good bonding, so the sensor may fabricated out of a material with similar structural properties using a method described later in this thesis.

To allow for significant change in capacitance via the methods described earlier, the dielectric must be soft enough to allow for significant change in plate separation and cross-sectional area (via side length change). While the Ecoflex™ 00-30 used is inherently a very soft material, the high sensitivity required by the industry partner of the project and artificial skin in general demands a structure with as much give to normal and shear force as possible. To accomplish this the dielectric is structured to introduce air gaps, a method used previously with architectures such as bubbles [27], squares, and pyramids [44], among other shapes. Dielectric shape is used to fine tune the sensor mechanical properties, including the height, side length, pillar-pillar pitch, and side wall angle of each pillar. The original sensor design used from *Sarwar et al.* used 2 mm x 2 mm squares in an 8 x 6 array with a 1 mm pitch, centered on the sensor electrodes. The specific dielectric dimensions for each sensor design are outlined in their given sections, due to the differing dielectrics required by the differing applications.

Alongside the dielectric architecture, electrode design is a key component for the function of the combined pressure and shear sensor. The core of each sensor is a 5-electrode shear sensor shown in Figure 2-2, with 4 small 3 mm x 1.5 mm rectangular electrodes on the bottom and one large square 6 mm x 6 mm one on the top. Under application of normal force, all of the sensing taxels will increase in capacitance due to the decreasing of capacitive plate separation distance, *d*, for each. The consistent increase of each sensing taxel at once allows for identification of the applied force as pressure rather than shear. Under applied shear the total surface area, *A*, of the two in-line taxels will change, while the out of line taxels will not experience any capacitive difference. The taxel in the direction of applied shear force will increase due to increasing surface area, while the opposite taxel will display an overall decrease in capacitance. Due to the two-taxel focus of the shear force detection, it is readily differentiable from applied pressure in an applied setting.

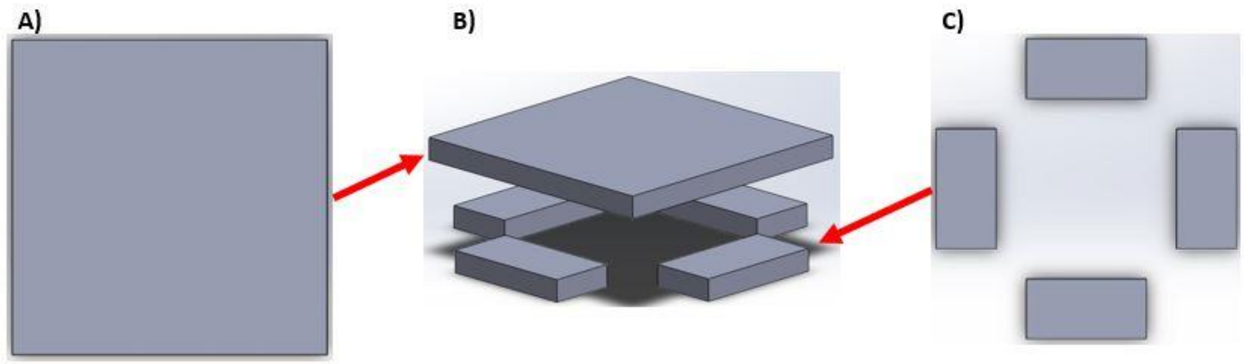

Figure 2-2: Combined Shear and Pressure Detection Sensor, A) Upper Electrode, B) Combined Sensor, C) Lower Electrodes

The major advantage of this electrode structure is the ability to readily differentiate between pressure and shear force applied, even when those forces are combined [33]. This is done through assessment of the capacitances formed between the lower electrodes and the large upper electrode in the structure depicted in Figure 2-2, labeled as C_1 through C_4 in a counterclockwise order starting with the electrode on the $+x$ direction (on the right in Figure 2-2 C)). It is assumed that the sensor is sufficiently shielded from any outside influences, such as an electrically grounded indenter which may have unwanted effects on the sensor capacitance. Under pressure, all four of these capacitances C_1-C_4 will increase simultaneously, in proportion to the applied force. If the upper layer is sheared in the $+x$ (right) direction, the overlap with C_1 will increase and C_3 will decrease, due to the changing parallel surface area of capacitive coupling. Due to the electrode architecture, the out of plane electrodes C_2 and C_4 are not expected to significantly change. This produces a change in capacitance of C_3-C_1 due to applied force, which is proportional to the expression

$$\frac{C_1C_3' - C_3C_1'}{C_1' + C_3'} \quad (1),$$

where C_1' and C_3' are the new capacitance values for the taxels after shear [33]. This equation may be used for shear in the y-direction by exchanging C_1 and C_3 with C_2 and C_4, respectively. Normal force may be calculated through the equation

$$\frac{\Delta C_1 + \Delta C_2 + \Delta C_3 + \Delta C_4}{C_1' + C_2' + C_3' + C_4'} \quad (2),$$

where each ΔC_i value represents the change in capacitance C_i-C_i'. The use of these equations in applications allows for pressure and shear imparted on the sensor to be readily differentiated, an important element of practical device usage.

It is notable that Equations 1 and 2 provide a reasonable theoretical approximation of sensor response to pressure and shear, the practical sensor values do not always follow idealized values. The primary deviations observed between the calculated and practical sensor responses take two forms: nonlinearity in calculated response to pressure or shear, and offset from zero in calculated response to shear. Nonlinearities generally appear due to either a nonlinear mechanical response of the sensor, or a disparity between the capacitive signal response between the two paired shear taxels measured (C_1 and C_3 in Equation 1). Offset from zero refers to calculated shear values using Equation 1 which do not cross zero at the same point as the actual applied shear displacement, indicating a nonzero calculated shear at rest. This offset may be caused by either a disparity between sensor taxel values or uneven sensor response to applied pressure. Both nonlinear response and offset are values which currently require sensor calibration to rectify for practical sensor application.

To enhance the sensing area of the architecture, an additional eight pressure-sensing taxels are integrated in a ring surrounding the central pressure unit described above. The extra electrodes are simple two-pad capacitors which measure force by means of change in plate separation *d* as the sensor is compressed. This expands the sensor functional area to a total of 14x14mm, with minimal dead space as permitted by the fabrication method precision.

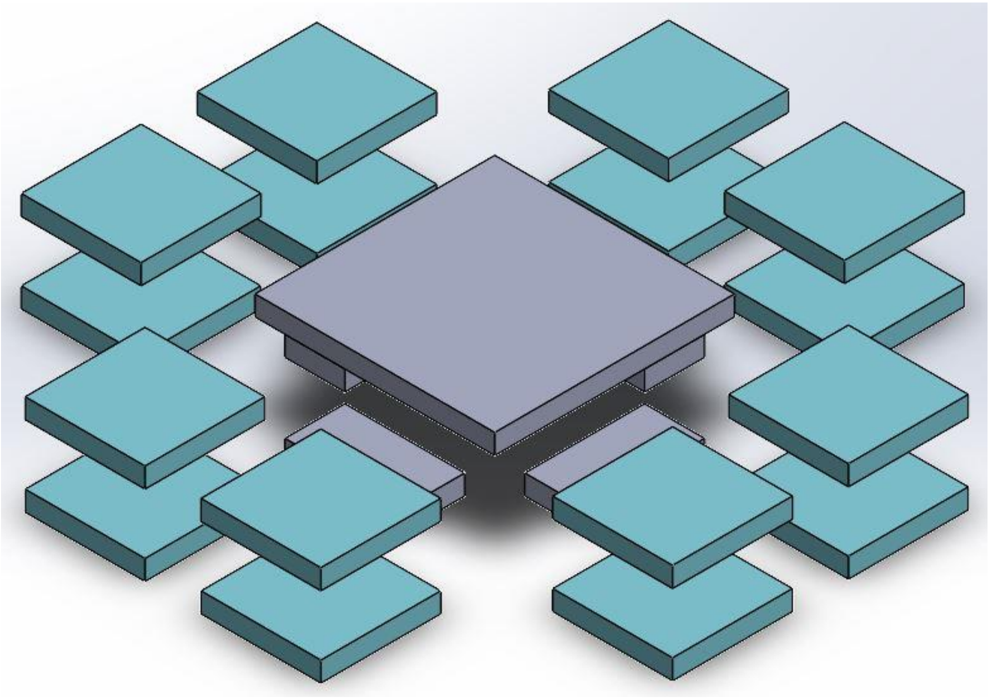

Figure 2-3: 12-Taxel Combined Pressure and Shear Sensor Electrode Layout, Combined Electrodes in Grey and Pressure-Only Electrodes in Blue. Upper Pressure-Only Electrodes Are Slightly Larger than Lower Ones (Not Reflected in Image) to Eliminate Effects of Shear.

Sensor Electronics Design

The hardware used to monitor the sensors presented in this thesis has four main components:

1. Sensor-hardware interconnect (metal crimps),
2. Electrode selection multiplexer (MUX),
3. Capacitance-digital converter (CDC),
4. Microcontroller,

Connection to the sensor PCB is established using metal crimps attached to the end of each trace, which are then soldered to exposed pads on the PCB surface. These crimps are used to create a robust connection between the flexible, stretchable conductive rubber used in the sensor and the metal of the PCB. This additional component is required due to the carbon black-Ecoflex™ material's inability to take up solder, which prevents a strong mechanical connection from being made to the readout circuit. Crimps are able to both pinch into the elastomer material and strongly solder to the exposed copper pads of the PCB, providing a bridge for the unconventional sensor material to the metal of the PCB traces. The lower electrodes of the sensor are incorporated into the PCB body, with exposed copper pads corresponding to the sensor design connected to the readout hardware using traces.

The center of the system is the AD7745, a 24-bit CDC which is used to read out the sensor capacitance signals. The AD7745 is equipped with a single 24-bit capacitance measurement system; to accommodate the large number of measurement points required for a single sensor (two for the upper portion electrode ring and large central plate, 12 for the lower portion smaller electrodes), 4:1 and 16:1 MUXes are used (ADG1434 and ADG1606, respectively). A combination of these multiplexers is used to increase the total number of channels available to the CDC through switching to monitor the entire sensor in quick succession. Switching the circuit and reading from the CDC is handled by an attached microcontroller, either an Arduino Uno (https://store.arduino.cc/usa/arduino-uno-rev3) or NUCLEO-L432KC (https://www.mouser.ca/ProductDetail/511-NUCLEO-L432KC). Power is provided to the entire circuit through the attached microcontroller, and all data is sent to storage on an attached laptop through the microcontroller serial communication port. An overall system diagram for the 12-taxel pressure and sear sensor system is presented in Figure 2-4.

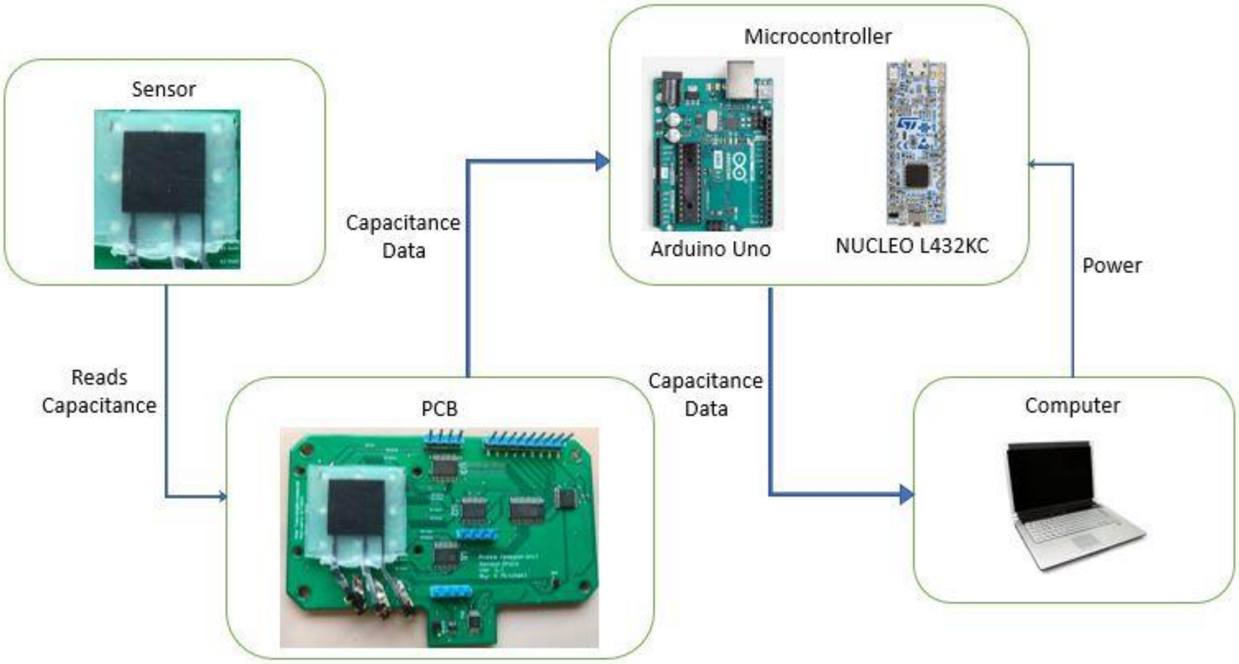

Figure 2-4: Sensor Readout Hardware System Diagram

Sensor Fabrication

A major component of the sensors described in this thesis is their fabrication, especially considering the reliance on flexible and stretchable unconventional sensor materials, such as Ecoflex™ 00-30 silicone rubber. To account for these materials, a molding method is used to fabricate the sensor in layers, which are then bonded together into a single body. Each sensor design described in this thesis is fabricated using the methods in this section, or some variation of these methods. This fabrication process consists of six main steps resulting in a single-piece sensor upper layer bonded to a rigid or flexible PCB to form the full sensor architecture described above. The sensor is fabricated using a combination of Ecoflex™ 00-30 and H30253 Carbon Black Super P Conductive [https://www.alfa.com/en/catalog/H30253/] to form flexible and stretchable insulating and conductive sensor components. An overview of this fabrication process is shown in Figure 2-5, with further details on the process presented below. The fabrication method described here was developed by Victor Mitchell and the author as an improvement on the method previously described by *Sarwar et al.* Compared to the previous fabrication method design, the process in this thesis allows for more consistent, closer alignment of sensor elements in a highly reproducible manner. The most significant advantage of this fabrication method over the previous design is the ability to blindly align elastomer-based sensor elements, facilitating the incorporation of the proximity shield in the design. This is due to the multi-part sensor molds designed by the author and Victor Mitchell, which uses layering and alignment components to precisely fabricate sensors with multiple different layers of electrodes.

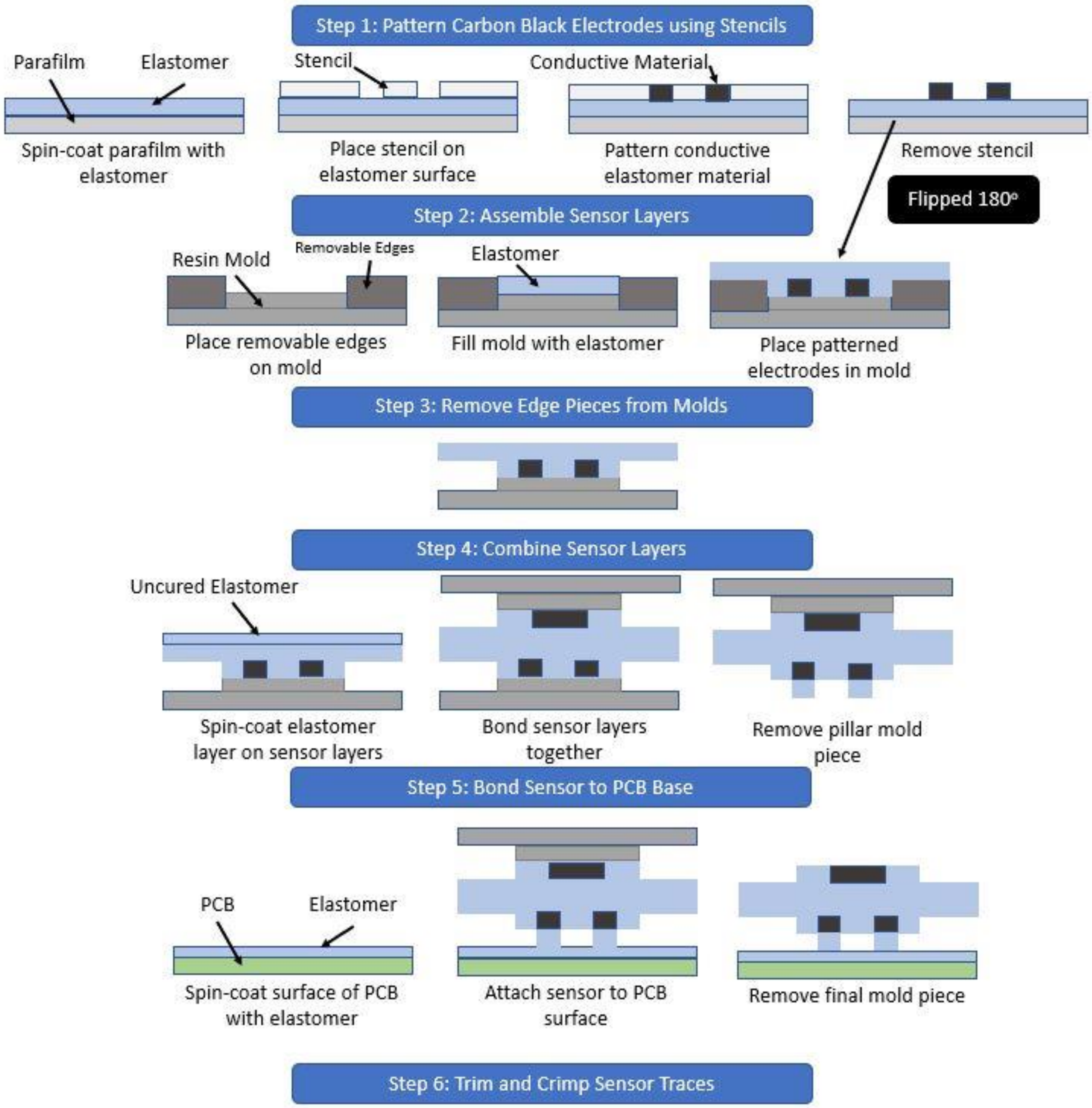

Figure 2-5: Sensor Fabrication Process Overview. In this Figure, light blue is Ecoflex™ 00-30, black is a carbon black-Ecoflex™ conductive mixture, white is acetate transparency, light grey is 3D printed resin mold base components, dark grey is 3D printed removable mold components, and green is the sensor PCB (flexible or rigid). Refer to text for details.

The first step in the fabrication process is the preparation of the sensor electrodes for attachment to the sensor body. Unless otherwise stated, the Ecoflex™ 00-30 in this section is prepared by measuring out equal parts Part A and Part B by mass into a weigh boat, as recommended by the manufacturer, then using a stir rod to mix manually for approximately 60 seconds. A thin layer of Ecoflex™ 00-30 (approximately 100 micrometers thick) is spin-coated onto a piece of Parafilm™ (https://www.tedpella.com/grids_html/807-2.htm) for 60 seconds at 800 rpm and allowed to cure at room temperature for 45 minutes. Electrodes are then patterned onto this Ecoflex™ 00-30 layer using a stencil cut out of acetate transparency material [45] and a mixture of Carbon Black and Ecoflex™ 00-30. Stencil cutting is done using laser machining, performed using a CO_2 laser engraver (*VersaLaser*). The mixed material is conductive when cured, with a resistance of approximately 10 kΩ for the electrode designs described in this thesis. The number of electrode patterns laid down on individual sheets of Parafilm™ vary based on sensor design, but generally two components are created in this step: a pressure and shear upper electrode layer, and above that an upper shield layer, separated from the patterned electrodes by a non-conductive Ecoflex™ layer. Once the electrodes are fully cured at room temperature, the final 2 cm of each sensor trace is masked with Scotch tape to allow for later electronic connection. Figure 2-6 displays a plastic petri dish with two upper electrode patterns stenciled in place, and the associated mask cut out of metal or acetate transparency material.

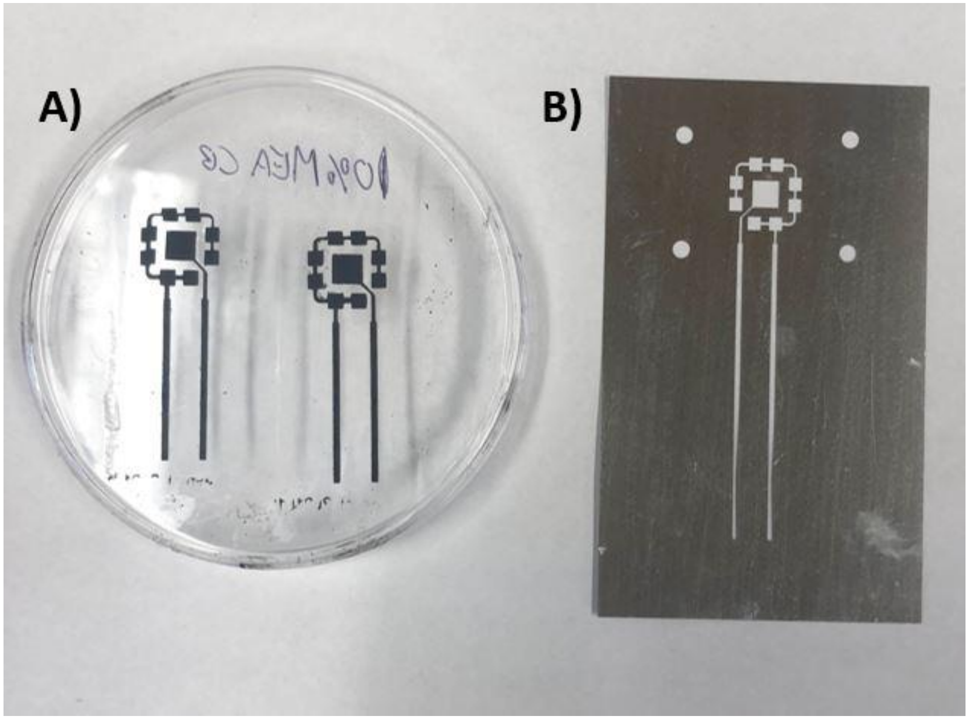

Figure 2-6: Sensor Fabrication Patterning Stage A) Upper Electrode Layer Stenciled Patterns, B) Upper Electrode Layer Stencil (Metal)

For the second step in the fabrication process, the sensor molds are prepared for formation of the sensor body layers that sit between the soft top electrodes and the electrodes on the PCB. This preparation includes cleaning the molds with isopropyl alcohol then coating each piece with a thin layer of Ease Release^{TM} 200 (*Smooth-On, Inc.*). The mold components in this step are shown in Figure 2-7, and consist of both pillar base and flat base components with their associated removable edges. Pillars are incorporated into the electrode layer mold to create an elastomer to air ratio, which softens the dielectric layer and allows for increased displacement due to normal or shear force. Once coated in Ease Release^{TM} 200, these component pairs are assembled to form a basin for Ecoflex^{TM} 00-30 shaping. Each assembled mold is then filled with Ecoflex^{TM} 00-30 and placed in a vacuum chamber for approximately two minutes to remove any excess air and ensure good compliance with the mold shape. The Parafilm-backed electrode layers are then placed Parafilm-outwards onto the uncured Ecoflex^{TM} to bond the electrodes down. A glass microscope slide is then used to gently scrape excess Ecoflex^{TM} 00-30 from under the electrode layer until the parafilm layer is flush with the mold edges. The two components are then cured in an oven at 60ºC for 20 minutes to ensure full curing of all Ecoflex^{TM} 00-30 in the mold.

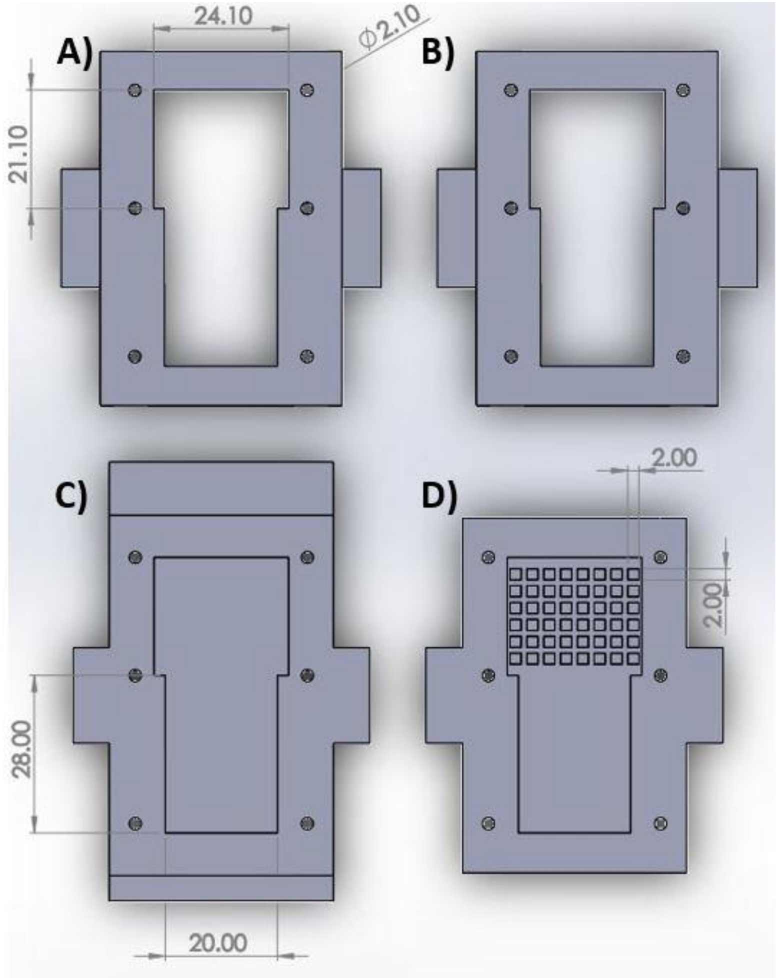

Figure 2-7: Sensor Fabrication Molds, A) Flat Base Removable Edge, B) Pillar Base Removable Edge, C) Flat Base, D) Pillar Base. Dimensions are in mm.

In the third step, the two electrode-base combined parts are trimmed down to the sensor area as defined by the removable edges of the mold. The Parafilm backing is removed from the sensor pieces and the contact area is gently cleaned using isopropyl alcohol. The edge pieces of the mold are then gently pried away, with care taken to ensure the sensor components stay firmly attached to their respective bases. Any excess Ecoflex™ material that seeped underneath the removable edges is also trimmed away at this stage, to ensure the final sensor is clean and free of excess silicone rubber.

The fourth step bonds the two sensor components together into a single component. A thin (~100 micrometer) layer of Ecoflex™ is spin-coated onto the surface of both pieces at 800rpm for one minute. The two pieces are then fitted into an alignment jig with the uncured Ecoflex™ layers facing one another, and pressed firmly together by hand for approximately 15 seconds to establish a strong connection. This conjoined sensor is then placed in a vacuum chamber for five minutes to remove any excess air introduced in the sandwiching process. The sensor is then cured in the oven at 60ºC for 30 minutes to ensure full curing of the elastomer and strong bonding between the pieces. Once the sensor is removed from the oven and cured, the pillar-side mold is gently removed from the overall piece using a spatula.

In the fifth step of fabrication, the sensor Ecoflex™ piece is bonded to the PCB base, either rigid or flexible. The PCB to be mounted has a ~100 micrometer layer of Ecoflex™ spun on it at 800 rpm, and is mounted in an alignment jig. The sensor, still attached to one of the mold bases, is then placed in the jig with the exposed pillars facing the PCB. Spacers built into the sensor mold base and alignment jig ensure the pillars maintain sufficient contact with the PCB Ecoflex™ layer without compressing them. The sensor is then cured in the oven at 60ºC for 20 minutes, and the mold base is pried from the attached sensor using a spatula.

The sixth and final step of the layered fabrication process consists of cleaning up the sensor traces and applying crimps to facilitate an electrical connection to the sensor PCB. A razor is used to cut away any excess material from the sensor, as well as excess elastomer from the surface of the PCB. The Ecoflex™ surrounding the conductive traces leading out from the sensor is carefully removed with the razor as well, minimizing the amount of extra material attached to the trace while maintaining structural integrity. Once as much excess material as possible is removed from the traces, they are individually crimped using a conventional electronics crimp as appropriate for the sensor being fabricated and are ready for use. The finished sensor product of this fabrication process is shown in Figure 2-8.

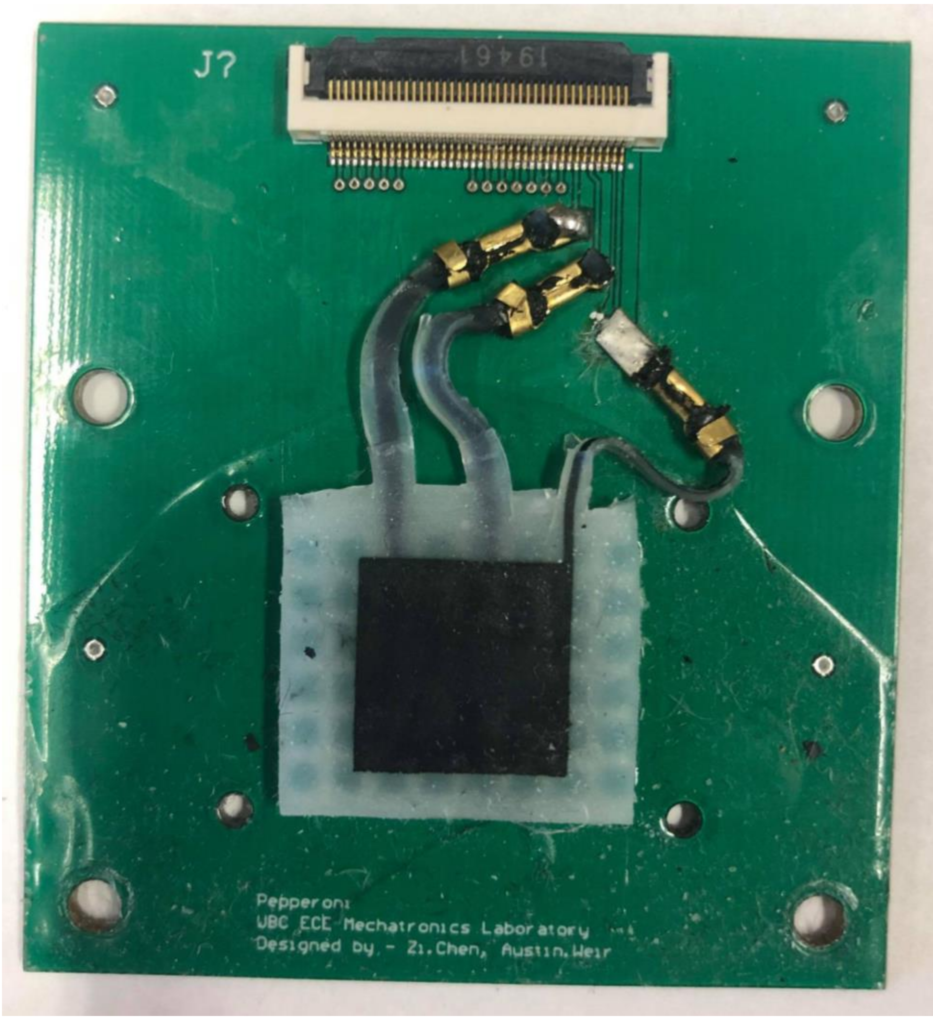

Figure 2-8: Completed 12-Taxel Sensor with Traces Crimped, Mounted on Rigid PCB

Characterization

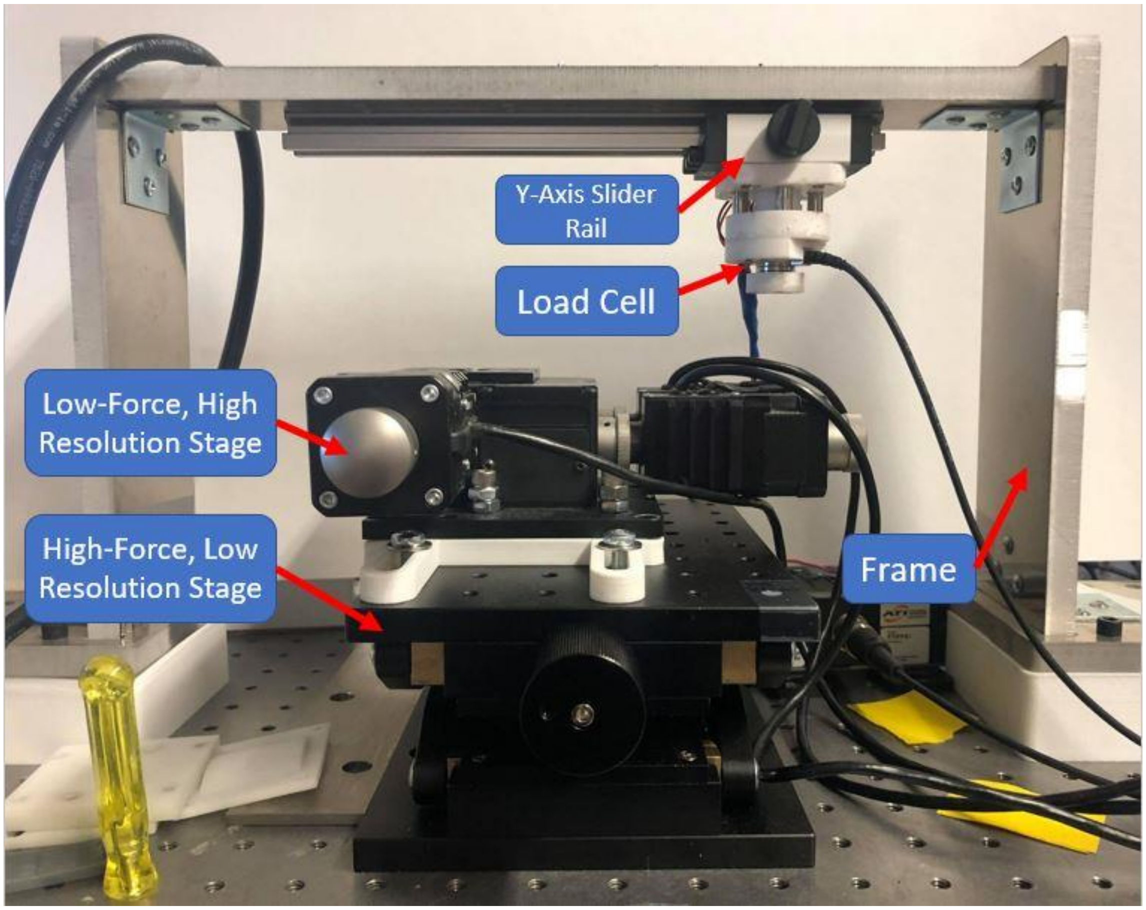

Figure 2-9: Characterization Setup, with Frame, y-Axis Slider Rail, Load Cell, and Stages Indicated

A primary concern for the development of soft sensors is an adequate method of characterization which allows for repeatable and precise measurement of both pressure and shear in sensors with unusual shapes or mechanical characteristics. The characterization setup described in this thesis, shown in Figure 2-9, was designed and fabricated by Bertille Dupont, Austin Weir, and the author. It employs a NanoMax 300 3-axis stage, an ATI SI-50-0.5 3-axis load cell, and BoliOptics SG02201211 lift to allow for total displacements of 4 mm in the x- and y-directions, and 124 mm in the z-direction; the specifications for these components are presented in Appendix A. These maximum displacements are governed by the NanoMax 300 stage maximum travel distance in the x- and y-directions, and both the NanoMax 300 and BoliOptics SG02201211 combined maximum travel distance in the z-direction (4 mm for the NanoMax 300 and 120 mm for the BoliOptics SG02201211). The setup is capable of force measurements of 50 N in the x- and y-directions, and 70 N in the z-direction with 1/80 N resolution, and torques of 500 Nmm in the x-, y-, and z-direction. This range of positions and forces is sufficient for all of the high-force sensing required by the industry partner of the partner, and all of the force sensing described in this thesis. The maximum force of the stage is approximately 10 N in any direction, so a substitute 3D printed stage stand-in shown in Figure 2-10 is used in place for the high-force (up to 50 N in the z-direction) force measurements described in Chapter 4 of this thesis. This stand-in is 3D printed out of ABS, and matches the dimensions of the Nanomax 300 3-axis stage to provide a replacement which will not be damaged at forces in the 10 N-50 N range. In these force ranges, the stand-in only functions for *z*-direction measurements using the manually controlled BoliOptics stage.

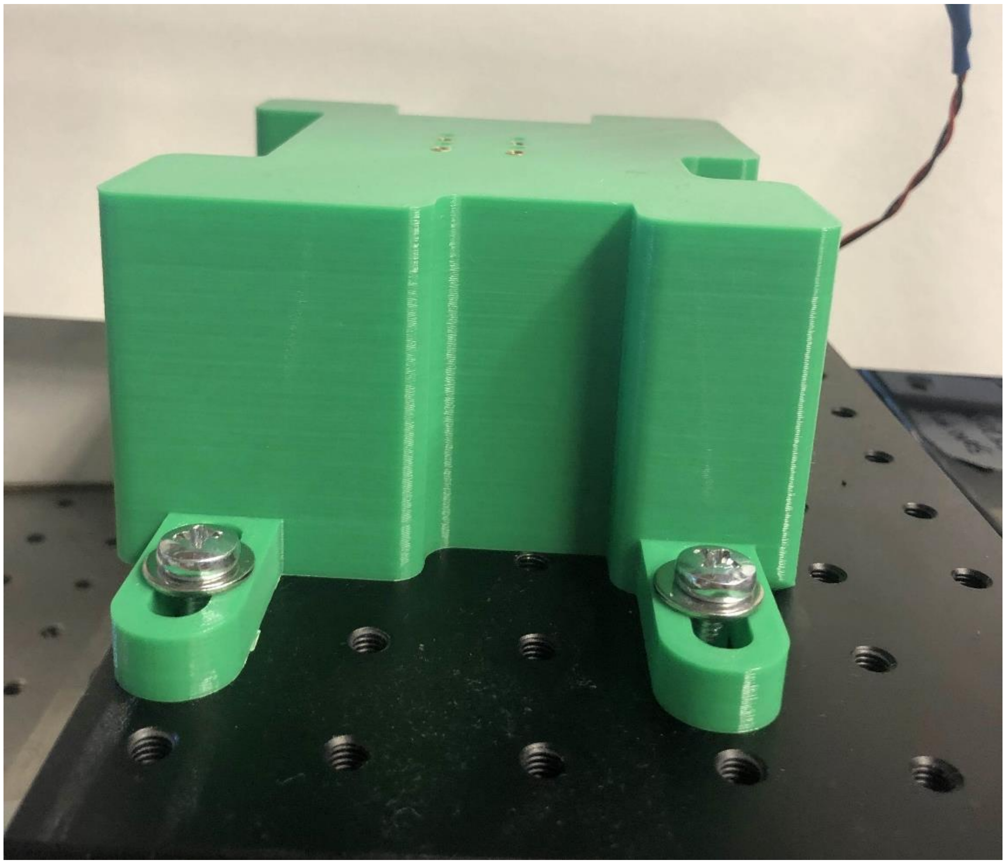

Figure 2-10: High-Force Characterization Stand-In for Nanomax 300 Low-Force Stage

The load cell is mounted in a fixed adapter that attaches to the metal frame of the stage via a sliding rail clamp, again as shown in Figure 2-9. It allows for lateral alignment of the load cell via attachment to a movable rail, and attachment of a variety of indenters as required by the characterization being performed. Major considerations for the design of the characterization setup load cell holder presented in this thesis are stability of the load cell during characterization, the flatness of the load cell, and the alignment of the sensor with the load cell. These three key parameters help in keeping the sensor characterization consistent, and mitigate potential factors which may interfere with accurate representations of the sensor such as loose components. It is imperative that the load cell holder apparatus is stable in both the normal and shear directions, as even small adjustments mid-characterization may have a large impact on the sensor signals recorded.

Displacements for both the normal and shear force applications are in the sub-mm range, so even small amounts of play (on the order of approximately 0.1mm) in any direction are significant. Load cell flatness is important to avoid a sensor ‘tilt effect’, shown in Figure 2-11 from occurring; this refers to a characterization in which the sensor and load cell were not parallel at their interface, causing an uneven distribution in force and unexpected torque. The introduction of these uneven distributions may pollute the sensor characterization data recorded. The most prominent effect of tilt effect on sensor data is an apparent shear mismatch between two opposing shear taxels, where one taxel signal changes and the other does not. This may produce apparent shear stress in the sensor even if no lateral displacement is applied by the characterization apparatus. Tilt effect has been observed in sensors at normal displacements as small as 0.1 mm, corresponding to an angular offset of only 0.41 degrees for a 14 mm x 14 mm sensor. Sensor-load cell alignment is also considered a core component of consistent and accurate characterizations. The sensor taxels are very fine in terms of manual alignment unassisted by any specialized alignment methods such as physical guides. If the sensor is misaligned even by amounts on the sub-mm range, it is highly likely that the effects will be visible in the sensor data recorded.

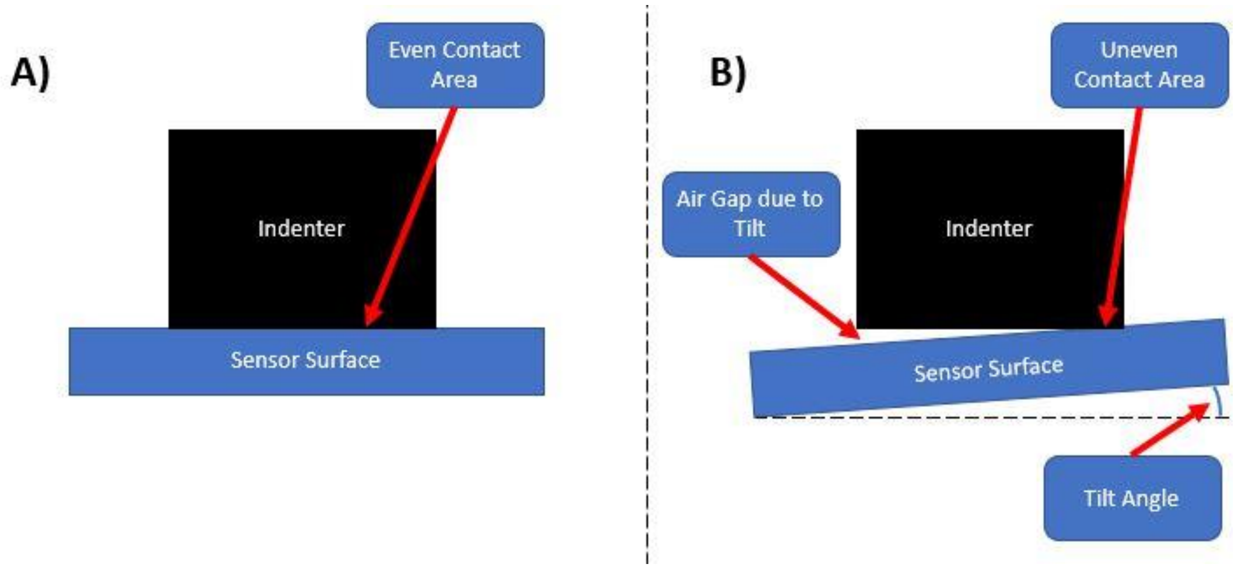

Figure 2-11: Tilt Effect Example Between Sensor and Indenter in Characterization, A) No Tilt, B) Tilt Present

The load cell holder has four main components, shown in Figure 2-12:

1. Rail attachment (not shown)
2. Alignment lasers (4x)
3. Holder body
4. Load cell

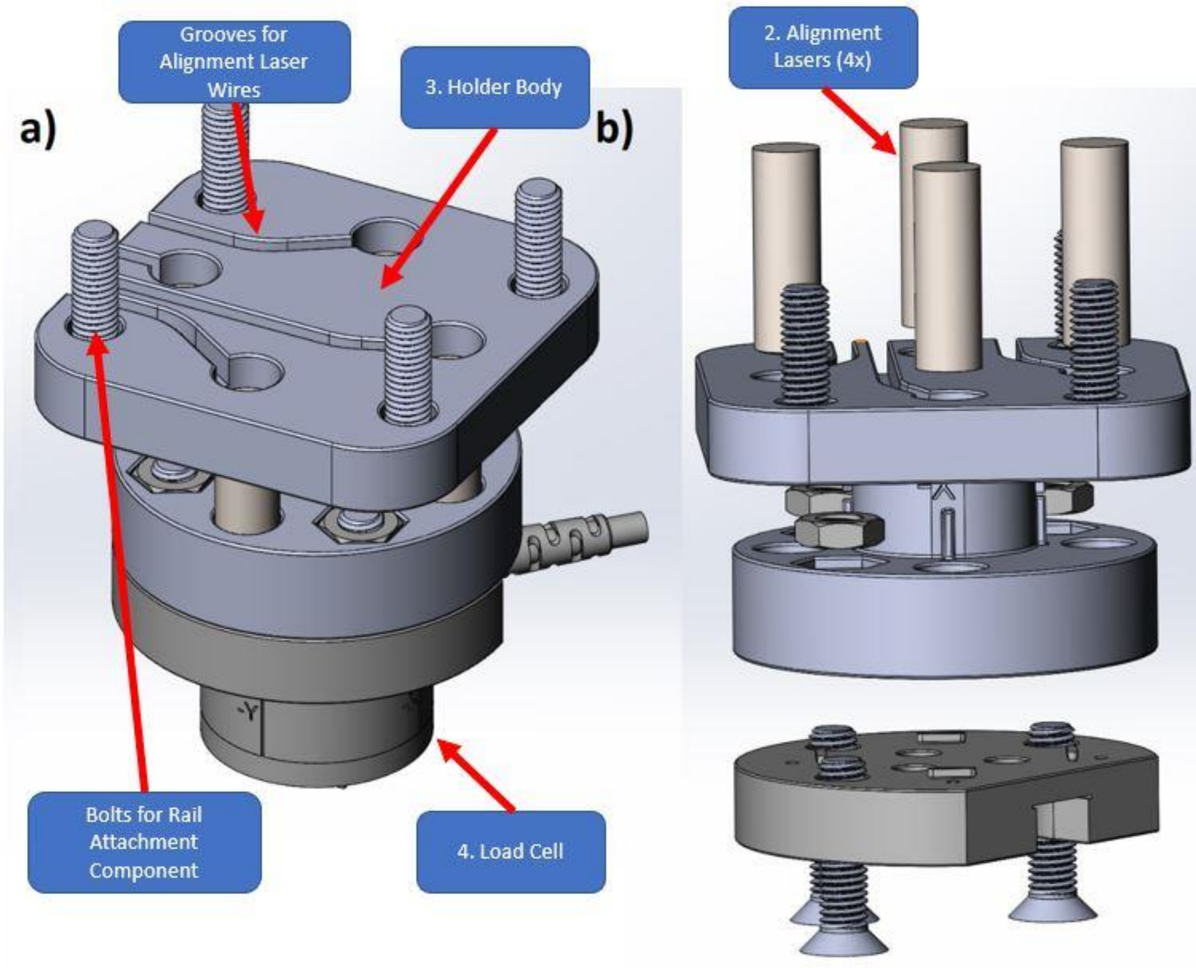

Figure 2-12: Load Cell Holder A) Assembled View, B) Exploded View (No Load Cell Attached)

The structure of the characterization setup portion is shown in Figure 2-12, including the load cell and alignment laser models. The three load cell holder body components are 3D printed out of SLA printer resin (*Formlabs* Grey, https://formlabs.com/materials/standard/#greyscale) using a Form 3 SLA printer (*Formlabs*), and connects to all of the other components in addition to holding the load cell. The layers of the load cell holder as a whole are held together with bolts to ensure flat and consistent marriage between the components, as indenter apparatus flatness is key to consistent sensor characterization. A threaded component in the bottom holds the load cell itself, to which an appropriately shaped indenter is attached with four screws. Four laser diodes are additionally inserted into the load cell apparatus to facilitate alignment of all sensor types by means of markers on the sensor surface.

This characterization setup is used in Chapter 3 and Chapter 4 of this thesis for analysis of the sensor designs presented.

Stretchable Electrode Conductivity Examination Conducted

An additional concern regarding sensor overall function is an observed increase in resistance of the stretchable electrode material over time. Keeping resistance of a capacitive sensor low is vital for accurate readings, as a high *RC* time constant will inhibit the ability to accurately measure the capacitance. As resistance of the sensor resistor-capacitor circuit increases it begins to dominate the sensor impedance and reduce the apparent capacitance being measured. This is due to the methodology the CDC used in sensor measurement employs; alternating current is applied to the electrode pairs of the sensor and charge accumulation on the plates is measured, a value which is then used alongside charging time to determine the capacitance of the pair. In the event that a sensor electrode has a high circuit resistance this charge accumulation is dampened, which is highly likely to result in inaccurate sensor readings. To allow the sensor full function under applied pressure and shear, a flexible and stretchable material with low resistance is required. For the sensors outlined in this thesis, 10% Carbon Black by volume is mixed with Ecoflex^{TM} 00-30, creating a material that can be patterned onto elastomer bodies and interfaced with electronics via PCB connections. Previous sensor work identified a significant trend of degradation in the conductive material, which occurred within time frames of weeks to months. Due to the dependence on capacitive measurement for detection of force and shear in this specific sensor architecture, large conductance decay poses a significant barrier to consistent sensor function in embedded applications, such as within the glove of a patient's prosthetic or in long-term functioning at home nursing robots.

To examine this resistive decay, sample strips of carbon black-elastomer materials were fabricated and monitored over the course of months. Several types and concentrations of carbon particles and elastomer host materials were tested in an effort to find a low resistance combination that is stable over time. The primary elastomers investigated were Ecoflex™ 00-30 and Dragon Skin™ FX-Pro due to their history of use in similar sensors [33] and similarity to previous materials used, respectively. Ecoflex™-PDMS mixtures are also investigated as PDMS may act has previously been used to form conductive materials with carbon black, but is relatively stiff and requires 'softening' through addition of Ecoflex™ [46][47]. Samples with copper or silver nanoparticles, or carbon nanofibers, are also fabricated; these additives are intended to increase the conductivity and/or conductive stability of the electrode material. These substrates and additives are summarized in Table 2-1.

Host Materials	Filler Additives
Ecoflex™ 00-30 (room light)	Copper Nanoparticles
Ecoflex™ 00-30 (darkness)	Silver Nanoparticles
Ecoflex™ 00-30 (room light, exposed to air)	Carbon Nanofibres
Dragon Skin™ FX Pro (room light)	
Dragon Skin™ FX Pro (darkness)	
Dragon Skin™ FX Pro (room light, exposed to air)	
25% Ecoflex™ 00-30, 75% PDMS 184	
50% Ecoflex™ 00-30, 50% PDMS 184	
75% Ecoflex™ 00-30, 25% PDMS 184	

Table 2-1: Durability Host Materials and Filler Additives Tested

These samples were fabricated using the same patterning and crimping methods as the electrodes incorporated into the sensors described in this thesis. Representative strips of conductive material were used instead of the sensor electrode patterns to allow for ready access for crimping to both ends of the sample, while maintaining encapsulation of the main sample body; the same crimping method described above for the sensors was used for these conductivity samples. Crimps are used for these resistance measurements due to the partial reliance of conductivity on the surface contact and strain in the material. Crimped traces provide a consistent point from which to measure the sample resistance, in an effort to maintain repeatability in electrical contact similar to the sensor solder joints. In order to compare the conductivities and time stabilities of sample strips with different compositions, they are mounted onto plastic petri dishes using the ~100 micrometer thick layers of the same substrate used for mixing each sample's conductive material, and encapsulated with a similar layer covering the traces, leaving the crimps exposed. An example of a resistance measurement trace is presented in Figure 2-13, with an Ecoflex™ substrate and Carbon Black/20% Cu conductive material filler. The resistive decay testing samples were fabricated in pairs on the same base to provide multiple sources of data from samples in very similar environments, in the event that there are interactions with the nonconductive substrate which may affect the conductivity over time.

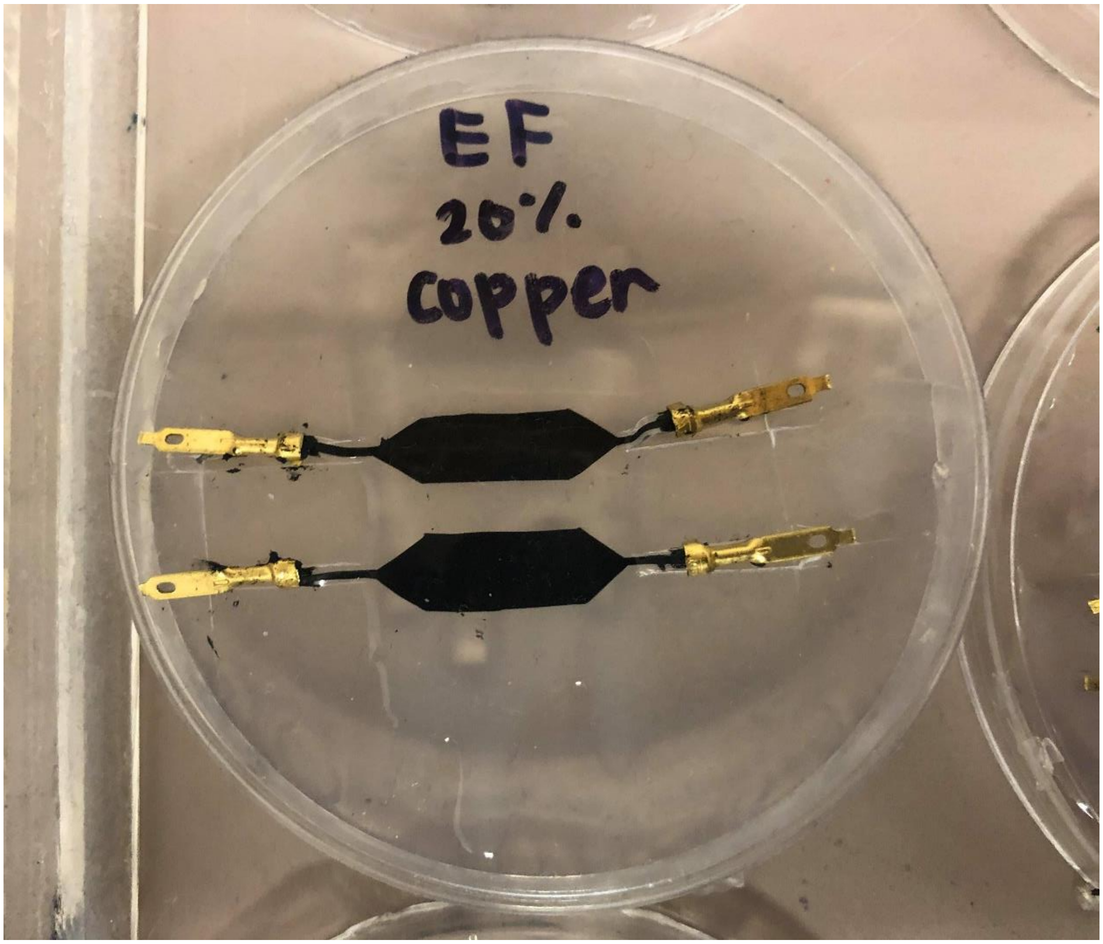

Figure 2-13: Resistance Measurement Trace Samples, 10% Carbon Black/20% Cu, Mounted on Plastic Petri Dish

This conductive decay is demonstrated in Figure 2-14, which displays the resistance of control samples of Carbon Black mixed with either Ecoflex™ 00-30 or Dragon Skin™ FX Pro. All of the samples tested exhibited significant initial resistance, and at least a doubling in resistance over the 238-day measurement period, with the values presented in Table 2-2. One of the Ecoflex™ 00-30 samples experienced a much larger change in resistance than any other sample, with an almost 20x increase in resistance - an order of magnitude larger than the others. Due to this, it is omitted as an outlier from the plot in Figure 2-14. Considering this outlier, the average daily increase in resistance was approximately 0.33 kΩ/day for the conductive Ecoflex™ 00-30 mixture and approximately 0.24 kΩ/day for the conductive Dragon Skin™ FX-

Pro mixtures. Overall, this increase in resistance represents too much degradation over even smaller frames of time such as months, as it will continuously increase the *RC* time constant of the sensor and inhibit proper and accurate function.

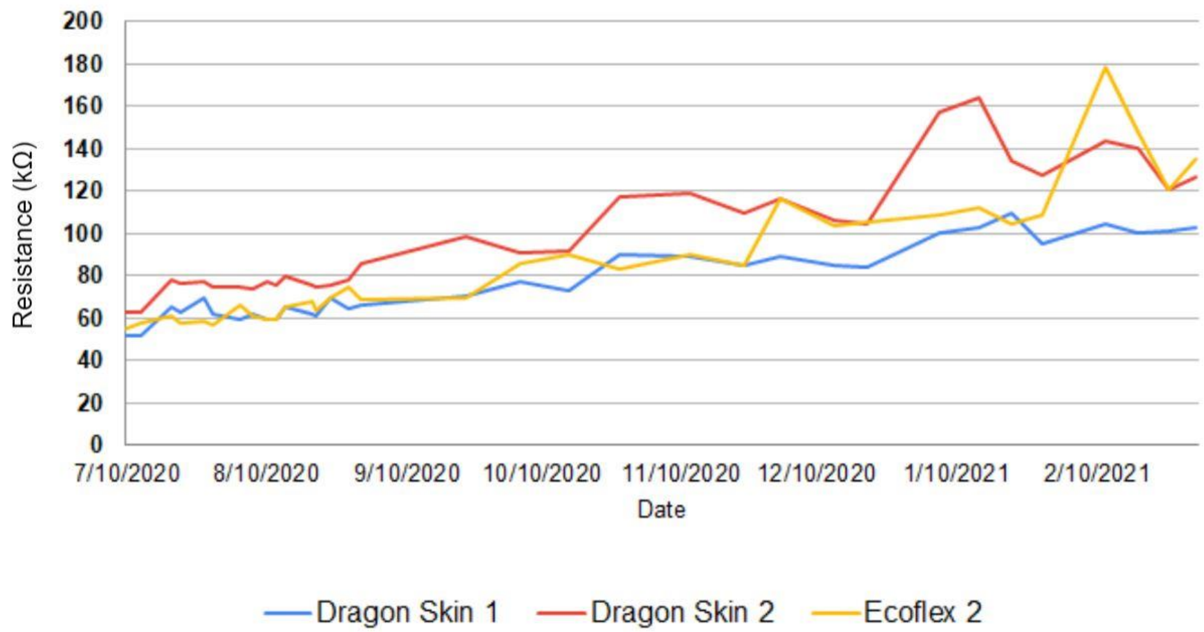

Figure 2-14: Dragon Skin™ FX-Pro, Ecoflex™ 00-30 Control Sample Resistance Over Time

Host Material	Starting Resistance (kΩ)	Day 238 Resistance (kΩ)
Ecoflex™ 00-30	79.7	1570
Ecoflex™ 00-30	54.9	135
Dragon Skin FX Pro	51.7	103
Dragon Skin FX Pro	62.5	127

Table 2-2: Ecoflex™ 00-30, Dragon Skin™ FX-Pro – Carbon Black Material, Start and 238-Day Values

The materials examined exhibited a wide range of both day-one and day-238 resistance values, as shown in Figure 2-15. Many of the samples experienced an increase in resistance of well over 100%, with some reaching the order of MΩ by the end of the measurement period

(Dragon Skin™ with 10% and 20% Ag nanoparticles). The average end resistance value was 159.38 kΩ, with the largest increase experienced by Ecoflex™ mixed with 10% carbon black and 20% Ag. A significant amount of variance was seen within many of the sample pairs in terms of both day one and day 238 values; it is expected that this variance is due to a combination of the material mixing homogeneity and the crimping of the samples. While efforts are taken to mitigate these factors in the samples such as mixing using a centrifugal mixer (*Thinky* ARE-310) to maximize mixing consistency and crimping the conductive material leads to provide a readily accessible measurement point, the samples are still likely to be sensitive to resistance-altering effects. This is due primarily to the tendency of carbon black-elastomer mixtures to be piezoresistive [48] and form 'islands' of conductive material when mixed with elastomers [49].

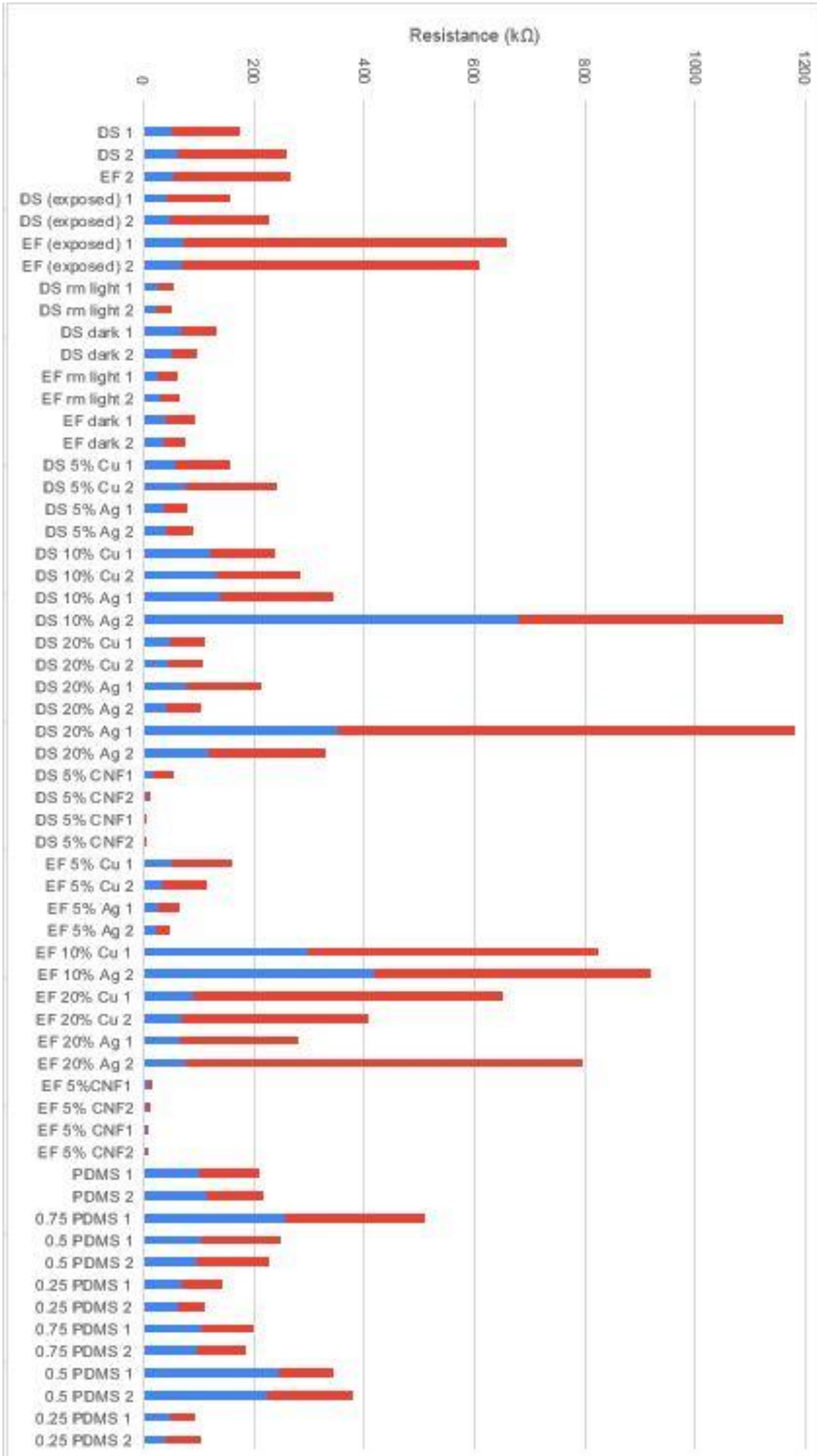

Figure 2-15: Stability of Sample Resistance Values, Day 1 (Blue) and Day 238 (Red). DS: Dragon Skin^{TM} FX-Pro, EF: Ecoflex^{TM} 00-30, CNF: Carbon Nanofiber, PDMS: Polydimethylsiloxane. It shows that the use of carbon nanofibers can help reduce and stabilize resistance.

To improve the temporal stability of the sensor electrode material a wide variety of conductive fillers were assessed in conjunction with carbon black. These materials were chosen due to their inherent conductivity, and compatibility with Carbon Black in terms of size (nanoparticles) or a history of combined usage (carbon nanofibers) [49], [50], ensuring a more homogeneous and even mixture and reducing the likelihood of mixture-dependent resistive differences. These additional conductive materials will help form structures within the material that are more conductive and/or more stable than those formed out of carbon black alone. Host materials examined are chosen based on historical usage by *Sarwar et al.*, or similarity to previously used silicone rubbers with regard to mechanical properties and material basis. Two conditions are tested for Ecoflex™ 00-30 and Dragon Skin™ FX-Pro, either full exposure to the lighting present in the lab or relatively full darkness (concealed within a desk drawer, only exposed to significant amounts of light for resistivity measurement). These conditions are chosen for investigation due to previous observations of potential UV dependence of the carbon black-Ecoflex™ conductive material. It is hypothesized that consistent exposure to light causes oil seepage out of the material, which may be causing intra-material structural changes that apply strain to the conductive structures.

A mixture of 10% Carbon Black and 5% Carbon Nanofibers by mass produced the best results in terms of both initial resistance and change in resistivity over time when mixed with either Ecoflex™ 00-30 and Dragon Skin™ FX-Pro. Both materials showed an order of magnitude reduction in initial resistance, compared to the carbon black-only mixtures for either host, with an average of 1.76 kΩ for Dragon Skin™ FX-Pro and 3.84 kΩ for Ecoflex™ 00-30. Dragon Skin™ FX-Pro also produced the smallest percentage change in resistance over time with a 9% predicted yearly change (down from 155% with carbon black only); Ecoflex™ 00-30 produced strong results as well with a 22% predicted yearly change (down from 223% with carbon black only).

The addition of the one-dimensional carbon nanofibers to the material aid the carbon black in forming a stronger structural scaffolding within the elastomer, maintaining higher conductivity even when the host material experiences degradation over time. Carbon black is known to agglomerate within materials, reducing intra-material connectivity and potentially limiting the conductivity of these conductors [49]. Carbon nanofibers are also often used to create conductive materials, but often suffer from agglomeration issues similar to carbon black even in lower concentrations by mass, due to their incompatibility with organic matrices [49]. It has previously been found that the addition of low percentage carbon nanofiber to materials with high percentage carbon black by mass mitigates the agglomeration of either material. The most likely cause for this mitigation is a bridging effect by the carbon nanofibers between the ‘islands’ formed by carbon black agglomeration in the material, where interconnecting fiber structures ensure sufficient electronic connections within the material [49].

It is likely that this scaffolding effect is the most prominent underlying mechanism for the reduced change in material conductivity over time. With carbon black alone, a significant amount of material is agglomerating while the rest is dispersed through the material. This results in a less robust connection between the conductive particles within the material, as mechanical strain or ageing-related shifts to the material structure may more easily separate the dispersed particles and isolate islands from the conductive regions of the mixed material. The bridges formed by non-agglomerated carbon nanofibers help prevent this shift in intra-material connections, creating a more robust framework for the conductive material.

The other material additives tested provided significantly less enhancement of both initial conductivity and conductivity over time for the hosts tested. These additive tests were performed using both Ecoflex^{TM} 00-30 and Dragon Skin^{TM} FX-Pro due to the similarity between these elastomers and the materials previously used in sensor fabrication. Addition of either Ag or Cu nanoparticles produced materials with high variance in conductivity compared to any other additive. This is most likely due to difficulties with consistency in mixing for these additives, as the particles are much denser than the other nanoparticles or elastomers used. After fabrication, significant amounts of either metal nanoparticle could be readily found within the mold used; the amount recovered indicates that little of the metal was retained by the sensor electrodes. This issue was consistent across all of the metal nanoparticles examined, and a solution was not found by the time of completion for the sensors described in this thesis. In total, no additive tested came within an order of magnitude of the performance produced by the Carbon Nanofibers, either in terms of initial conductivity or conductivity degradation over time.

The host used also had a significant effect on material conductivity, both initial and over time. Ecoflex^{TM} 00-30, Dragon Skin^{TM} FX Pro, and mixtures of Ecoflex^{TM} and PDMS ranging from 25:75 to 0:100 were tested with Carbon Black and no other additives, separate from the additive tests described above. This was done to isolate the host material as the controlled variable, as it was predicted that both the material and additive may have a significant effect on conductivity. It was found that increasing percentages of PDMS compared to Ecoflex^{TM} by mass created a material with a higher average initial conductivity, and a more stable conductivity over time when considered as a percentage increase on the initial conductivity. Dragon Skin^{TM} and Ecoflex^{TM} both produced sensors with very low initial resistance but tended to have higher percentage decay over time, with Dragon Skin^{TM} performing slightly better than Ecoflex^{TM} in both regards. From these results, Dragon Skin™ was identified as the most promising host material for the base conductive additive of carbon black.

From the 238-day period measured, it was found that the most promising host material-additive combination for the sensors described in this thesis is Dragon Skin™ mixed with a carbon black/CNF mixture. The starting sample resistance of this material was 1.759 ± 0.072 kΩ and the average end of period resistance was 1.8 ± 0.03 kΩ, for an average increase of 0.041 ± 0.042 kΩ for an approximate 2.33% increase. Ecoflex™ 00-30 and Carbon Black/CNF material exhibited a higher average starting resistance of 3.84 ± 0.09 kΩ and end of period average resistance of 4.7 ± 0.5 kΩ, an increase of 0.86 ± 0.41 kΩ or approximately 22.4%. Due to the overlap in timing of the information gathered in this study and the development of the sensors described in this thesis, these durability results are not reflected in the sensor results described. The obstacles described in this section are only expected to significantly obstruct sensor function in the long term due to conductance decay, and is not expected to affect the results gathered for this thesis due to the relatively rapid prototyping-characterization cycle.

The results obtained allow for an estimated maximum trace length to be obtained, establishing the effective maximum refresh rate of the sensor. To determine this refresh rate, the RC time constant τ is examined, as it establishes the minimum time required for the capacitor to charge appropriately for measurement; in this analysis, a safety margin of 10 will be used (total charge time of 10τ). This assessment will focus on the most distant taxel from the sensor crimp-PCB contact as it experiences the highest trace resistance, and will therefore act as a limiting factor for the overall sensor refresh rate. The maximum frequency f_{max} is then given by

$$f_{max} = \frac{1}{2\pi * 10\tau} = \frac{1}{2\pi * 10RC} \quad (3),$$

and the resistance R of the trace portion is given by

$$R = \frac{\rho L}{A} \; (4),$$

where C is the taxel capacitance, ρ is the resistivity of the conducting composite material, L is the approximate length between the crimp connection and sensing taxel, and A is the cross-sectional area of the trace. The total resistance seen by the most distant taxel is a combination of three trace elements: the crimp trace, preceding electrodes, and inter-electrode connections. Crimp traces refer to the length of conductive material between the metal crimps and the sensor body, preceding electrodes refer to the conductive material electrodes preceding the electrode of interest, and inter-electrode connections refer to the conductive material between electrodes. The resistance then becomes

$$R_T = R_{crimp} + R_{electrode} + R_{connect} \; (5), \text{ and}$$

$$R_T = \rho \frac{L_{crimp}}{A_{crimp}} + \rho \frac{L_{electrode}}{A_{electrode}} + \rho \frac{L_{connect}}{A_{connect}} \; (6),$$

After calculations, the R_T seen by the most distant taxel in the sensor architecture shown in Figure 1-5 B) is estimated as 1.2 kΩ for the Dragon Skin™ FX-Pro/Carbon Black-Carbon Nanofiber blend, the most promising material tested for resistivity in this section. This is considered the maximal resistance seen by any given electrode in the sensor as it will have the greatest length of resistive material, and therefore the limiting factor in the maximum measurement frequency. Assuming a per-taxel capacitance of 1 pF based on average sensor (a safety margin of approximately 30 based on the approximate values seen with the sensor taxels), the estimated maximum frequency without resistive decay is approximately 1.3 MHz. Considering a sensor system with 12 total taxels, the maximum per-sensor frequency is approximately 110 kHz. This frequency is significantly faster than the current sensor hardware allows, and combined with the reduced resistive decay of the new material is considered sufficient for the durability examination presented in this chapter.

Summary

In this chapter, a combined pressure and shear detecting sensor established by *Sarwar et al.* was described. This sensor allows for detection of pressure across 12 taxels in an approximate 14 mm x 14 mm area, and shear across 4 taxels total in an approximate 7.5 mm x 7.5 mm area. It is fabricated out of Ecoflex™ 00-30 and carbon black to form an elastomer body with enclosed flexible and stretchable conductive electrodes. The sensor detects pressure and/or shear using capacitive sensing, which examines the charge distribution on paired electrodes in the sensor architecture, with each pair referred to as a taxel. The device is read using a circuit mounted on a rigid PCB which employs a combination of multiplexers, capacitance-digital-converters, and a microcontroller to collect data. A previously used characterization setup was also described, allowing for 3-axis low force sensor testing and single-axis (normal direction) high force sensor testing.

In addition to this previous work, a new examination of the elastomer-based electrode material conductivity is presented, with a focus on the change in conductivity of the material over time. Several materials are tested for both initial conductivity and conductive stability over time, with carbon nanofibers identified as a strong agent for both increasing and stabilizing conductivity in both Ecoflex™- and Dragon Skin™-carbon black based conductive elastomer material. In the samples with a carbon black-carbon nanofiber blend, the approximate average resistance after the 238-day measurement period was reduced in Ecoflex™ from 135 kΩ to to 4.7 kΩ, and in Dragon Skin™ from 115 kΩ to 1.8 kΩ. This reduction in resistance is sufficient for measurement frequencies up to 100 kHz on a 12-taxel sensor design, which is much higher than the current sensor scan rates and should be sufficient for the foreseeable future.

In the following two chapters, two specific improvements to this previously developed sensor design are explored. The first is a change of the PCB base to a flexible design, allowing for the conformation of the sensor to curvatures ranging from flat to a 10 mm internal radius of curvature. This involves designing a new hardware integrating the flexible PCB, and characterizing this new flexible sensor at inner radius curvatures of 100 mm, 30 mm, and 10 mm to assess the effect of curvature on the sensor. The next chapter focuses on another novel sensor design aimed at increasing the overall normal force sensing of the device by integration of dielectric layers with differing stiffness. This creates a multimodal sensor which functions similarly to the previous sensor described here at low forces (up to the previous sensor's maximum force of 12 N, while maintaining normal force function up to 50 N). Characterization is performed on this novel sensor at both low and high forces to verify sensor function in both the prescribed shear and normal directions.

Chapter 3: Curvature-Accommodating Sensor

One primary goal for the advancement of the combined pressure and shear sensor is accommodation of curved surfaces. This specification is important to a wide variety of advanced soft sensors such as those found in human-interactive robotics and wearables [44]. This is especially true for artificial skin technologies, which require conformation to unusual and irregular surfaces such as finger pads or joints. In addition, artificial skin sensors are expected to be compliant and respond to environmental intrusion in a similar manner to regular skin. The sensors previously developed by *Sarwar et al.* demonstrated either poorer function under curvature for full elastomer structures, or were mounted on rigid PCBs that prevent any bending. By removing the sensors from PCBs the required flexibility may be achieved, but the higher dependence on carbon black-Ecoflex^{TM} material limits the overall functionality of the sensor. This is particularly the case for the 12-taxel sensor described above, where the lower electrodes are conventionally indexed individually in the PCB and only two high-resistance upper carbon black-Ecoflex^{TM} electrodes are required. In a full-elastomer design the number of high resistance traces would increase from two to fourteen, with related ramifications to device parameters such as maximum sensing frequency or mechanical and electrical durability. Due to these limitations, a flex-PCB-mounted sensor design is the only one pursued, and a full-elastomer design is not considered.

In this chapter, a sensor is presented that combines the architecture created by *Sarwar et al.* and a custom-fabricated flexible PCB to enable consistent device function at significant range of different curvatures. The work done in this chapter was done by the author and two undergraduate research assistants, Zi Chen and Austin Weir, under the author's supervision. The sensors in this section use the same dielectric layer dimensions as the sensors described in

Chapter 2. These sensors functioned at a variety of curvatures from flat to 10 mm inner radius, while continuously providing strong sensitivity to both pressure and shear forces. These sensors are characterized under these curvature radii at normal forces ranging from 0.1-1.6 N, and shear displacements of up to 0.8 mm in the x- and y-directions. A flat indenter was used down to the 10 mm inner radius of curvature, while cylindrical and spherical indenters were used down to a 30 mm inner radius of curvature. It was found that decreasing inner radii of curvature significantly increased the peak sensor signal response for both pressure and shear, and the differing indenters produced distinctly different peak signal and torque responses. The results presented in this chapter correspond to the first row of industry partner specifications provided in Table 1-6. They concern the ability to implement the sensors on a variety of inner curvatures, and meet the specifications described.

The primary challenge in this chapter is the implementation of the flexible PCB itself; associated design considerations include adjusting the previously established rigid PCB design by *Sarwar et Al.* and creating a robust mechanical interface between the sensor elastomer body and the flexible PCB. These are solved using a novel cable-connected flex-to-rigid design and the integration of a hatched ground plane design, respectively.

Need for Curvature

A key feature of human skin is the ability to flex and deform physically in response to environmental mechanical stimuli [9]. When a physical stimulus is applied to skin, the upper surface stretches and bends to accommodate the applied force and impart it to mechanical receptors for translation into sensory signals. While modern sensing methods provide very precise measurements of pressure and shear, they have difficulty providing a convincing replication of human skin to biomedical applications such as prosthetics or human-interfaced robotics. The measurement of pressure and shear while maintaining a skin-like exterior and ability to conform to environmental impulses is a key part of sensor development for these applications [44]. This involves creating devices capable of full function even under duress which may cause localized deformations to the sensor, including those which cause through-body deformation.

An additional advantage to the development of fully flexible and deformable sensors is the ability to better conform to a variety of body shapes and placement locations. The human body and human-mimetic designs such as prosthetics have a wide range of curved areas, as well as joints where the skin is required to dynamically deform as a result of motion. These areas demand sensors which may conform to these motions on at least one axis of flex, to facilitate mounting of pressure and shear sensing devices which continue to function regardless of limb position. This is especially true in areas of specific interest such as robotic hands, which produce a consistent overlap of these two factors and exacerbate the need for fully flexible sensors for pressure and shear detection.

Flexible Sensor

A vital component of an effective artificial sensing skin is compliance to not only the environment, but also potentially nonuniform sensor mounting locations such as rounded edges or joints [44]. For capacitive sensors, this includes compliance with potential deformation of both the upper and lower electrode regions, depending on placement of the sensor on the robotic body. Of particular concern for the full-flexible force sensor are the elements of force and signal cross-talk which may greatly decrease the effectiveness and accuracy of the sensor. To account for this limitation in the sensor previously, *Sarwar et al.* designed the sensor to be mounted on a rigid commercial PCB. This limited the cross-talk related signal distortion of the sensor, but limited it to single-plane implementation [33]. In this section of the thesis a lab-manufactured flexible PCB is integrated into the sensor design; this change resulted in a sensor with full functionality, able to conform to curvature radii from 100mm to 10mm.

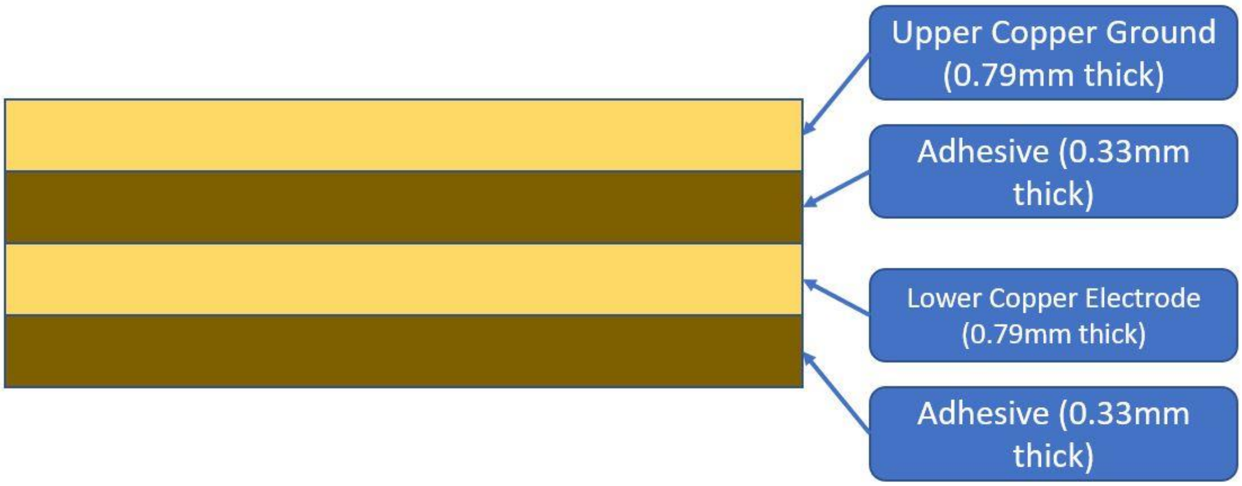

Figure 3-1: Flexible PCB Layer Diagram Cross-Section 2-Layer Design, Copper Tape Adhered with 3M Double-Sided Tape. The bottom layer of tape is left adhered to the original tape backing, or attached to another type of flexible backing.

The flex PCB used for all of the flexible designs presented in this chapter is made up of layers of thin copper sheet and adhesive, with a layer cross-section shown in Figure 3-1. These PCBs are fabricated in-lab using a laminator (Prolam Photo 6-Roller) and printer (LaserJet Pro MFP M227fdn) for photolithography patterning and an iron chloride solution for etching. The resultant flexible PCBs are highly compliant to curvatures, able to easily be mounted on cylindrical bases down to 10 mm in diameter without significant permanent bending or damage to traces. Using this method trace resolutions of 0.3 mm were achieved, which were fine enough to fully accommodate the sensor-area PCB designs established previously by *Sarwar et al.* In addition, the copper traces of these flexible PCBs provide a similar resistive characteristic to conventional PCB traces even under curvature due to the high conductivity of the trace material.

A major disadvantage of the new sensor reliance on flexible PCBs for sensor implementation is the incompatibility of a flexible substrate with the effective attachment of surface-mounted components. Due to this a two-PCB design is used, where the flexible PCB houses the sensor itself and the electronics are placed on a rigid PCB. A 40-lead cable is used to connect the two via low-force pressure mounts; to reduce signal noise, excess grounded wires separate the traffic-carrying wires (40 wires total to accommodate 14 traffic ones). An assembled sensor system with this interconnect is displayed in Figure 3-2, with the NUCLEO-L432KC microcontroller and 12-taxel sensor. This more distanced wired connection produces no significant change in sensor signal or noise when compared to the previous rigid designs, potentially allowing for further separation between the sensor and accompanying electronics than previously.

Another issue that arose from the integration of a copper-based flexible PCB as the sensor base is the adhesion of the sensor to the PCB material. Ecoflex™ has previously been observed to not readily adhere to the copper facing after the flexible PCB has been fabricated. This produced sensors that were too easily removed from the base through application of shear, rapidly de-adhering during the characterization process. To counteract this effect, a crosshatched pattern was introduced into the upper ground plane of the flexible PCB. This crosshatched pattern can be seen around the edges of the sensor in Figure 3-5, and is incorporated into all of the flexible sensors presented in this thesis. This exposes parts of the double-sided 3M tape used to sandwich the PCB layers together, which easily adheres to the Ecoflex™ elastomer used in sensor fabrication. The amount of adhesion created using this method was sufficient to eliminate any sensor adhesion issues in general use and characterization.

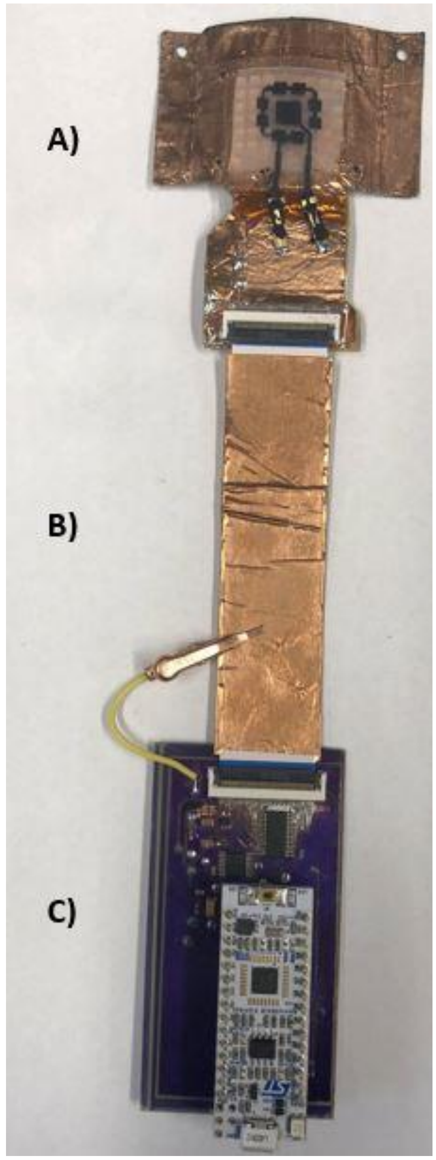

Figure 3-2: Flex-PCB to Rigid PCB Connection Setup, A) Flexible Sensor, B) Wire Interconnect, C) Microcontroller on Rigid PCB

Curved Characterization Data

The functionality and sensor characteristics for the flexible combined pressure and shear sensor was done using the characterization setup described previously. The sensor was attached to the 3-axis stage using a specialized clamping mechanism, which was able to provide curvature for the sensor to conform to. It is notable that while careful measures were taken to align the sensor, the curvature given to the sensor as part of the characterization work introduces some difficulty in precisely aligning the sensor with the load cell; due to this, some human error is inevitable and may be visible in the data. To demonstrate the ability of the sensor to function despite being flexed, curvatures of 100 mm, 30 mm, and 10 mm are used for this characterization. The curvature radii chosen are informed by both the industry partner expectations for the project, and biological structures, with the curvature of 100 mm representing a wide body part such as the shoulder and the 10 mm curvature representing a fingertip or some similar thin body part.

To emulate a variety of objects that may be encountered in robotics applications different indenter shapes, shown in Figure 3-3, are used to apply the characterization forces. These indenters include three unique shapes: a flat square, a sphere, and a cylinder mounted in-line and opposite of the curvature applied to the sensor. The characterization setup allows for easy exchange between the indenters, so each unique shape is characterized using the same setup described previously in this thesis. When characterizing with the cylindrical indenter, the spine of the indenter curvature is positioned in-line with the spine of the sensor curvature. The motivation behind these varying indenters is to expand the known functional range of the flexible sensor in preparation for real-world applications, as previous sensor characterization only focused on a flat, square indenter surface. The flat indenter corresponds to shapes such as the sides of boxes being picked up, spherical represents round or round-adjacent objects such as marbles, and the cylinder could represent items being picked up such as pencils or pens. The flat indenter is a 14mm x 14 mm square, the spherical indenter is a hemisphere with a radius of 7.5 mm, and the cylindrical indenter is a horizontal-cut cylinder with a radius of 7.4 mm.

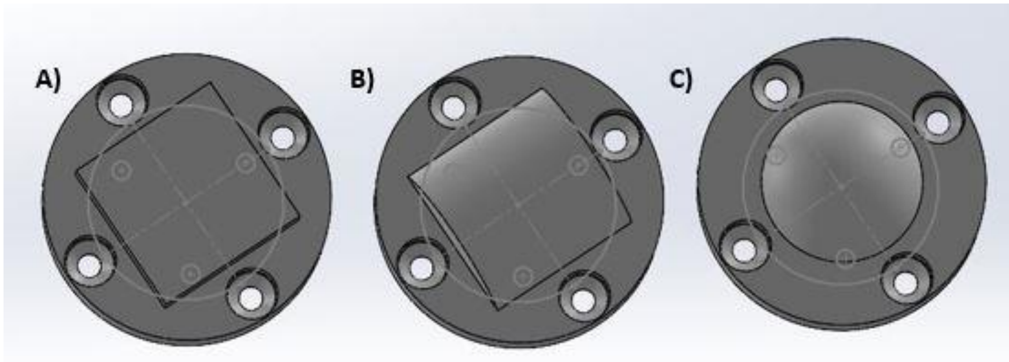

Figure 3-3: Indenter Types for Characterization, A) Flat, B) Cylindrical, C) Spherical

The sensor layout for the curved surface sensor focuses on the central four sensor taxels, which are used to measure both pressure and shear. The lower-upper electrode pairs are labeled taxels 1-4 in the analyses presented in this chapter, with the labeled PCB electrodes shown in Figure 3-4. These electrodes are paired with a single large electrode in the sensor body, as in the sensor shown in Figure 1-5 A). The electrode ring shown in Figure 1-5 B) are included in the sensor, but are not the focus of the curved surface characterization. It is expected that the curvature of the sensor as a whole will shift the signals seen from these taxel pairs, due to the introduced flexing forces pushing the sensor architecture away from an ideal parallel-plate capacitor.

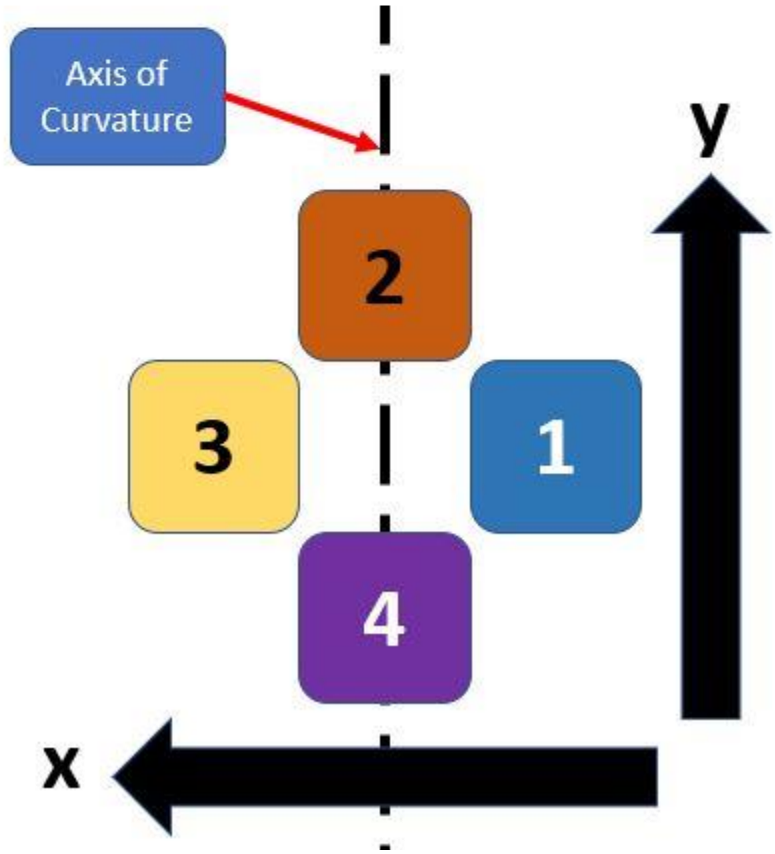

Figure 3-4: Central Four Taxel Labeling for Raw Capacitance Measurements, x-y Axis and Axis of Curvature for Mount and Cylindrical Indenter Labeled

The characterization apparatus for the curved surface sensors is the same as the one described in Chapter 2, with the exception of the alternative indenters shown in Figure 3-4 and curved sensor mounts such as the one shown in Figure 3-5. The curved mounts are printed in Formlabs Rigid 4k resin using a Form 3 SLA printer (*Formlabs*), with inner curvature radii of 100 mm, 30 mm, and 10 mm. To firmly mount the flexible sensor to the characterization setup a pair of SLA-printed clamps, which are bolted through holes cut in the corners of the sensor PCB, are used. These clamps are used in addition to the bolts normally used with rigid PCBs to protect the softer and more tear-prone flexible material, and provide additional tension to the PCB to prevent shifting of the sensor during characterization.

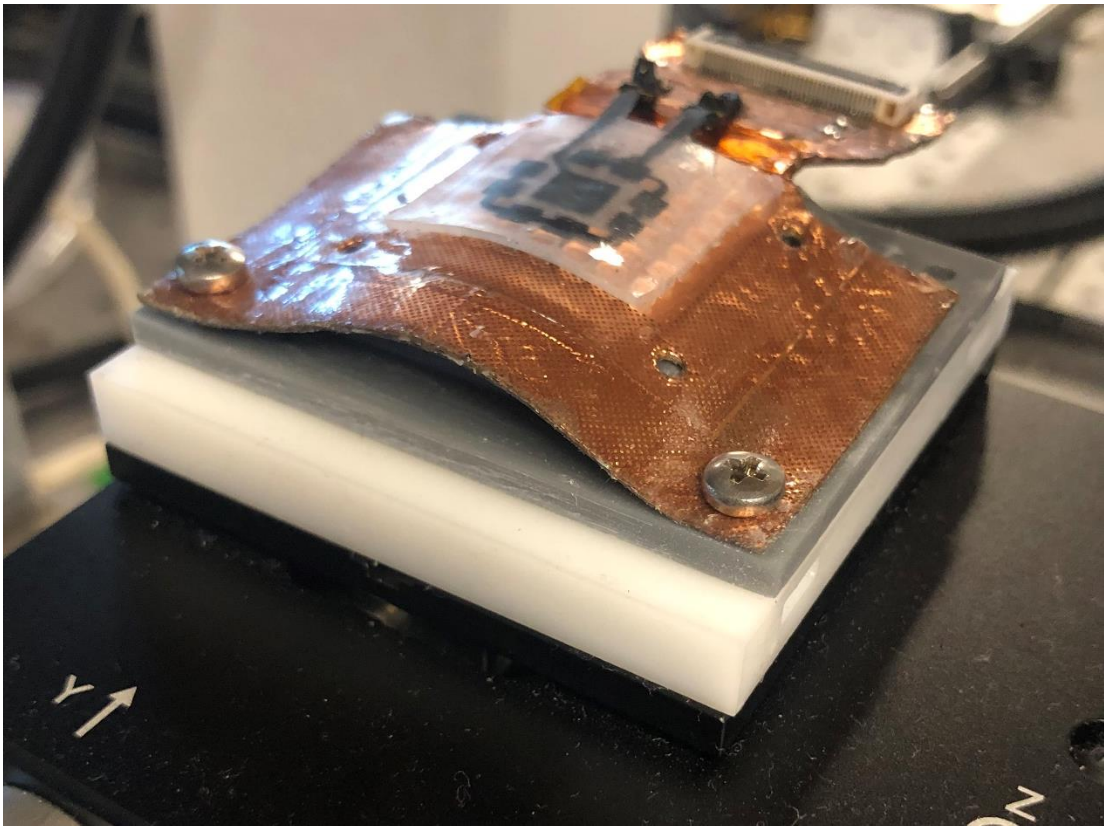

Figure 3-5: Flexible Sensor Attached to Curved Surface with 100 mm Inner Radius

Flat Sensor Characterization

To confirm the basic functionality of the new flexible combined pressure and shear sensor was attached to the characterization setup in a flat configuration, similar to the previous rigid-base sensor characterization setup described in Chapter 2. This is an important stage in the development of this new sensor to confirm that the newly fabricated flexible PCB does not significantly impede the functionality of the sensor, including shifting baselines or sensor behavior. When constrained to lay flat as shown in Figure 3-6 and characterized using the flat indenter, the flexible-PCB pressure and shear sensor demonstrated an approximate 4-6 fF change in capacitance under 1N of applied force, with baselines in the range of 34 fF (32 fF, 33 fF, 33.5 fF, 36 fF). This capacitive response is consistent throughout the 4 repeated force steps applied, which had an exertion period of 10 seconds and rest period of 10 seconds each.

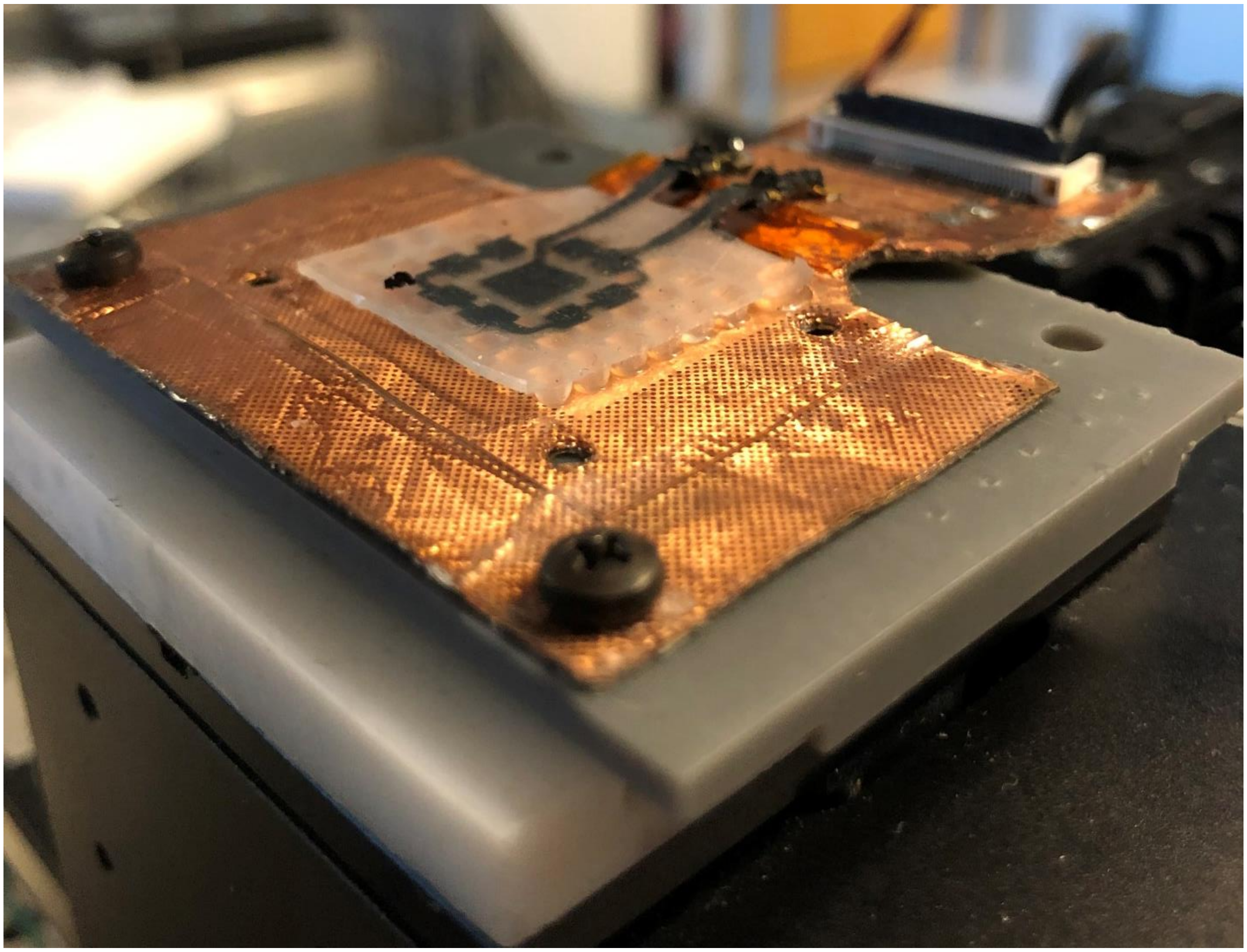

Figure 3-6: Flexible 12-Taxel (No Shield Layer) Pressure and Shear Sensor Mounted on Flat Characterization Surface

It is notable that some separation in baseline capacitance and change in capacitance is expected, based on the normal behavior of the sensors previously characterized by *Sarwar et al.* The raw capacitance values of the central four combined pressure and shear taxels are shown in Figure 3-7, with a repeated 1.6 N force applied for four cycles. Also, the baseline and 1.6 N applied force capacitance values of each taxel do not agree despite the sensor architecture being uniform. This disagreement in signal values is mostly likely caused by a combination of three factors which contribute to parasitic capacitance: PCB trace length, trace proximity to high-traffic system components, and outside electrical interference from nearby devices. Hysteresis of the sensor signal in the curved design was also minimal over this repeated pulse period, with a <1 fF maximum shift in capacitive signal for any individual channel - below or similar to the noise threshold. This is similar to the change in capacitance exhibited by previous versions of the sensor mounted on rigid PCBs [27], with consistently lower baseline capacitance values (34 fF average vs. a 40 fF average). The results indicate that the curve-facilitating enhancement to the sensor does not reduce capability significantly from the original rigid design when constrained to the same physical conditions (single flat plane placement on a rigid base). This similarity is vital both for analysis and function, as the custom fabricated PCB is shown to not produce any distinct abnormalities in sensor function and is readily comparable in signal response to previous work done.

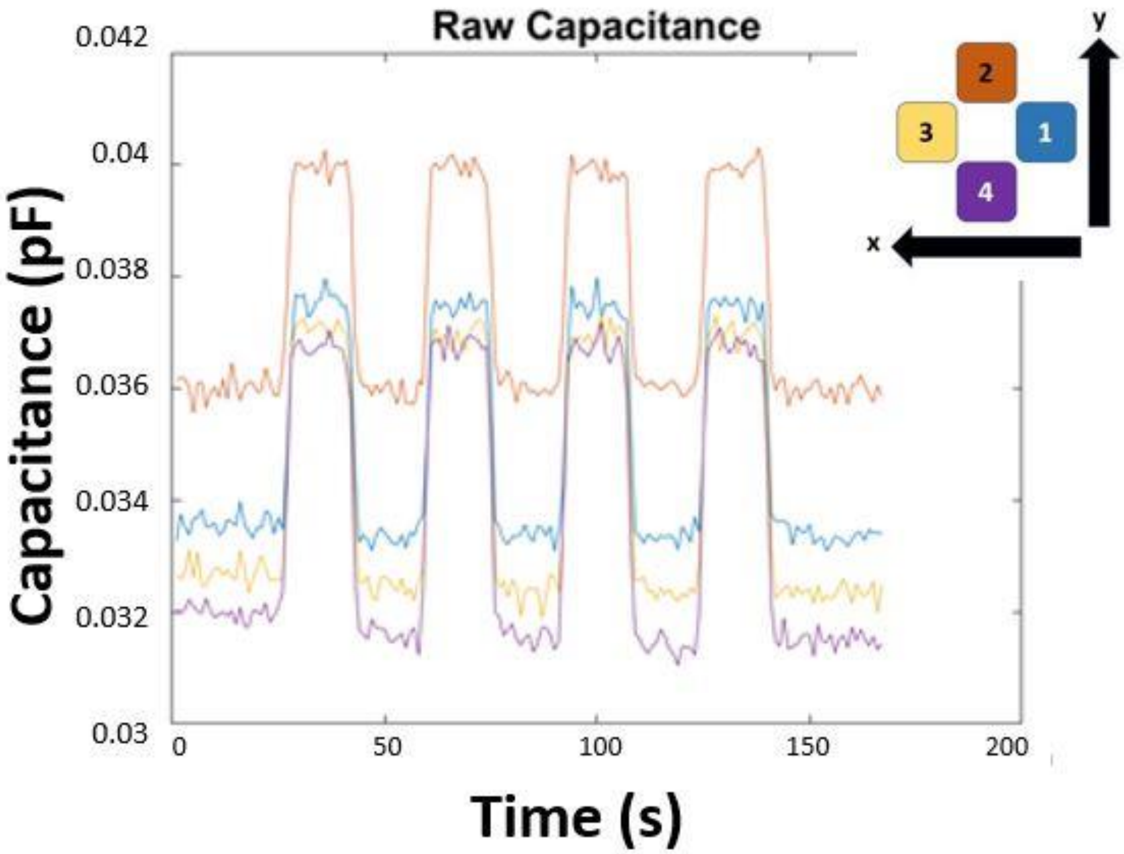

Figure 3-7: Flexible Pressure and Shear Sensor, 1 N Normal Force Flat Characterization Raw Capacitance Values. Baseline Value Disagreement between Taxels is due to a Combination of PCB Trace Length, Trace Proximity to High-Traffic Components, or Other Forms of Electrical Interference.

100 mm Radius of Curvature

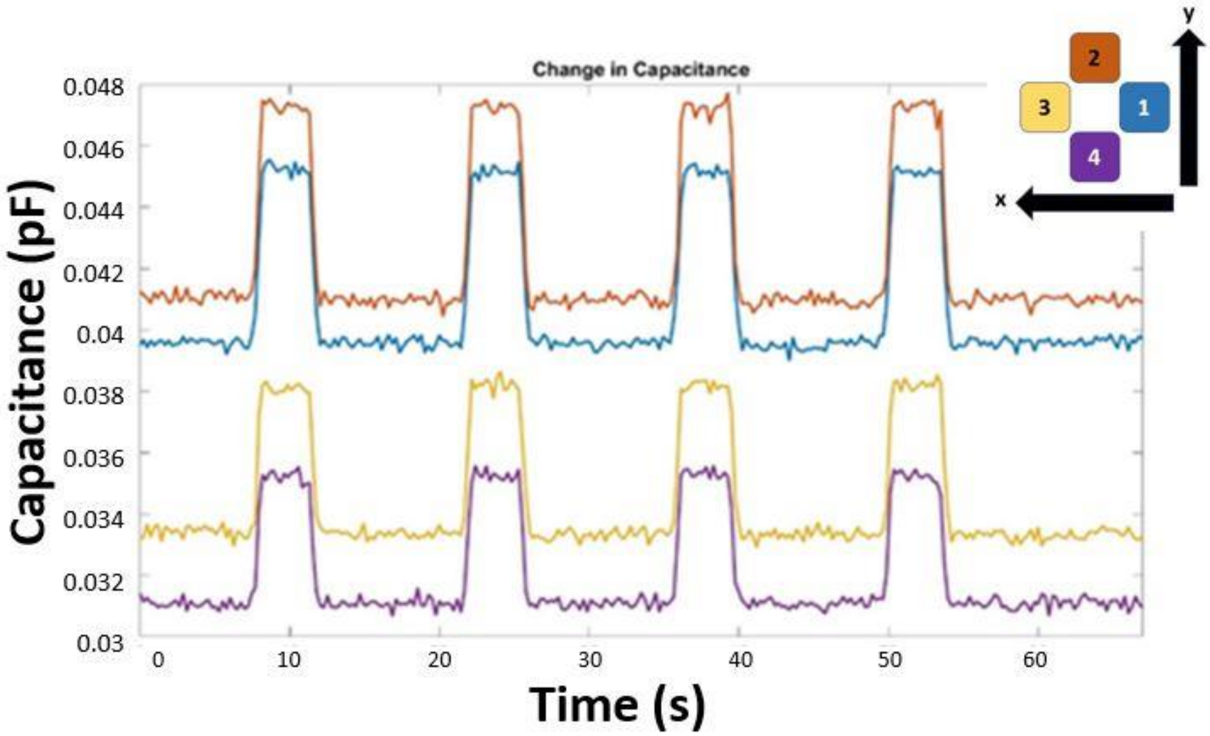

Figure 3-8: Flexible Pressure and Shear Sensor, 1 N Normal Force with 100 mm Radius of Curvature. Differing Baseline Values are Due to Parasitic Capacitance and Stretch Nonuniformities From Curvature. Axis of curvature is through taxels 2 and 4.

In the subsequent characterization experiment, a gentle curvature of 100 mm is applied to the sensor that was previously measured flat. The flexible PCB is constrained to the curved base by a clamping system, with no air gap allowed between the base and the PCB. This curvature causes the upper layer of the sensor to stretch, notably applying strain to the Carbon Black-Ecoflex^{TM} electrodes and increasing their effective capacitive surface area with respect to the lower PCB-based electrodes. The same repeated steps of 1N are applied to the sensor surface using the flat indenter with an application time of 5 seconds and relaxation time of 10 seconds, presented in Figure 3-8. The ratio of force to relaxation is increased compared to the prior flat test to reduce the potential effect of curvature-induced increases in hysteresis, due to the lateral stretching of the sensor body.

As a curvature is applied to the sensor body, both the flexible PCB and sensor body experience a stretching force lateral to the spine of curvature. The materials of the flexible PCB (copper tape and 3M double-sided tape) are both expected to be much stiffer than the attached elastomer sensor, so the resulting strain due to an increase in circumference from applied curvature is expected to be primarily focused in the sensor body. Assuming the total volume of the sensor remains unchanged during bending, the length of the elastomer body will increase while the thickness decreases. Both of these factors may have a significant effect on the capacitance seen at each taxel; lateral strain in each taxel, both those in-plane and out-of-plane to the bending, will increase the total upper electrode size and consequently the capacitor area A, while a decrease in sensor thickness will decrease the separation between the sensor electrodes d. The combination of these factors predicts that the baseline capacitance of each taxel should increase with decreasing inner radius of curvature, which is seen on average in Figure 3-8 and Table 3-1.

The lateral stretching and resultant vertical compression of the sensor may be approximated through assessment of the PCB as a rigid body which experiences minimal strain in any given direction compared to the elastomer. The original length of the sensor when held flat is the same as the original length of the PCB portion, as the considered area of the PCB is directly under the sensor. To simplify the approach, it is assumed that the thickness change of the sensor due to lateral strain is insignificant when considering the change in sensor length due to the applied radius, and that the entire sensor body (pillars and electrode layer) may be considered as one overall body. Using the center of the PCB as the base for sensor strain, the new sensor length at a given radius of curvature may be described as

$$L_s' = \theta\left(R + \frac{a}{2} + t_s\right) = \frac{L_{PCB}}{R}\left(R + \frac{a}{2} + t_s\right) \quad (7)$$

where L_s' is the new sensor length after bending ($L_s+\Delta L_s$), θ is the angle measured from the origin of the radius, R is the radius of curvature to the flexible PCB midpoint, a is the total PCB thickness, t_s is the total thickness of the sensor, and L_{PCB} is the length of the PCB. As the angle increases, the R and a will remain approximately static due to the relative rigidity of the PCB, and the t_s will decrease minimally compared to the lateral strain. This indicates that the sensor will experience lateral strain as a function of applied radius of curvature, as a decreasing radius of curvature will cause an increased lateral sensor strain.

The elastomer used is also assumed to be incompressible, so it may be assumed that the overall volume of the sensor will not change as the aforementioned strain is applied. The curvature is only applied in one axis, so it may be assumed that the overall width of the sensor is static throughout any theoretical applied curvatures. Taking the sensor body (pillars and electrode layer) as one overall piece, the new sensor thickness may be taken as

$$t_s' = \frac{t_s L_s}{L_s'} \quad (8),$$

where t_s' is the new sensor thickness. As the sensor is strained outwards and the L_s' increases in magnitude, the overall sensor thickness will decrease according to this relationship. Combined with the lateral sensor strain, it is expected that the overall raw capacitance of each taxel will increase as the inner radius of curvature is decreased throughout characterization.

This stretching can be seen in the shift in baseline capacitances between the flat and 100 mm curvature recorded data, with this shift shown in Table 3-1, and the change in capacitance values due to the 1 N applied normal force in Table 3-2. An average shift in baseline capacitance of approximately 2.69 fF, or approximately a 9.4% increase from the original C_0 values, is seen across all of the taxels measured, with taxels 1 and 2 experiencing a significant (5+ fF increase), 4 experiencing a small increase, and 3 decreasing slightly. This indicates some misalignment or other lack of symmetry in the sensor itself, as the change is unexpectedly nonsymmetrical across the peak of the curvature.

Taxel	Approx. Flat C0 (fF)	Approx. 100 mm C0 (fF)	% Change in C0
1	33.5	39.75	18.66%
2	36	41	13.89%
3	33	33.5	1.493%
4	32	31	-3.125%

Table 3-1: Shift in Flexible Sensor C_0 Values, Flat to 100 mm Inner Radius of Curvature

Taxel	Approx. Flat ΔC (fF)	Approx. 100 mm ΔC (fF)
1	4	6
2	4	6
3	4	5
4	5	4

Table 3-2: Shift in Flexible Sensor ΔC Values, Flat to 100 mm Inner Radius of Curvature

The change in capacitance also follows this shifting trend in the sensor, with noticeable increases in approximate peak capacitive change for taxels 1 and 2, no shift in taxel 4, and a slight decrease in capacitive change for taxel 3. It was not clearly visible through examination of the sensor precisely where this asymmetry originated on the sensor, and whether it was an issue inherent to the sensor tested or was being caused by an external component such as the sensor mount. Based on the significant difference in response to curvature between taxels 1-2 and 3-4, it is most likely that the indenter central point of contact is shifted from the expected contact area in the center. Based on the difference in capacitive shift between the taxels, a proposed actual center of contact is shown in Figure 3-9; it is difficult to verify this misalignment due to the structure of the characterization setup, and the relatively small distances involved (on the mm scale). This capacitive shift is consistent and does not impede the sensor, meaning the newly integrated flexible PCB does not introduce functional issues to the device under small strains. Overall, while the introduced curvature does significantly affect the signals read from the sensor, these differences can be accounted for and do not inhibit sensor use for large-radius curvatures such as the upper arm or shoulder of a human-mimetic medical robot.

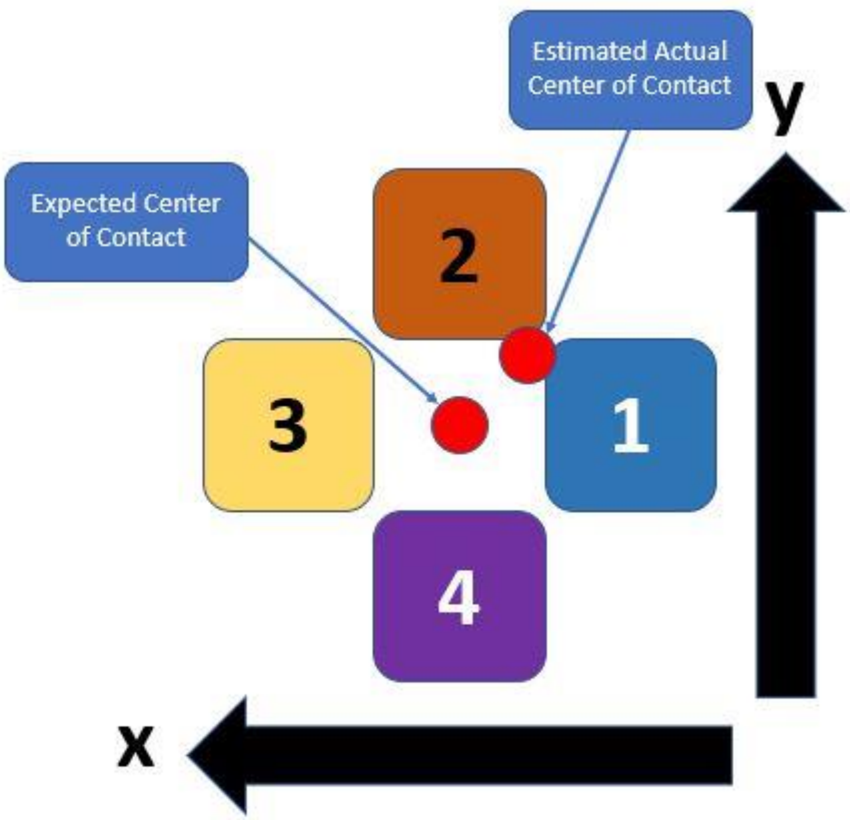

Figure 3-9: Expected vs. Estimated Actual Center of Sensor-Indenter Contact for Curved Sensor Characterization. Axis of curvature is through taxels 2 and 4.

10 mm Radius of Curvature

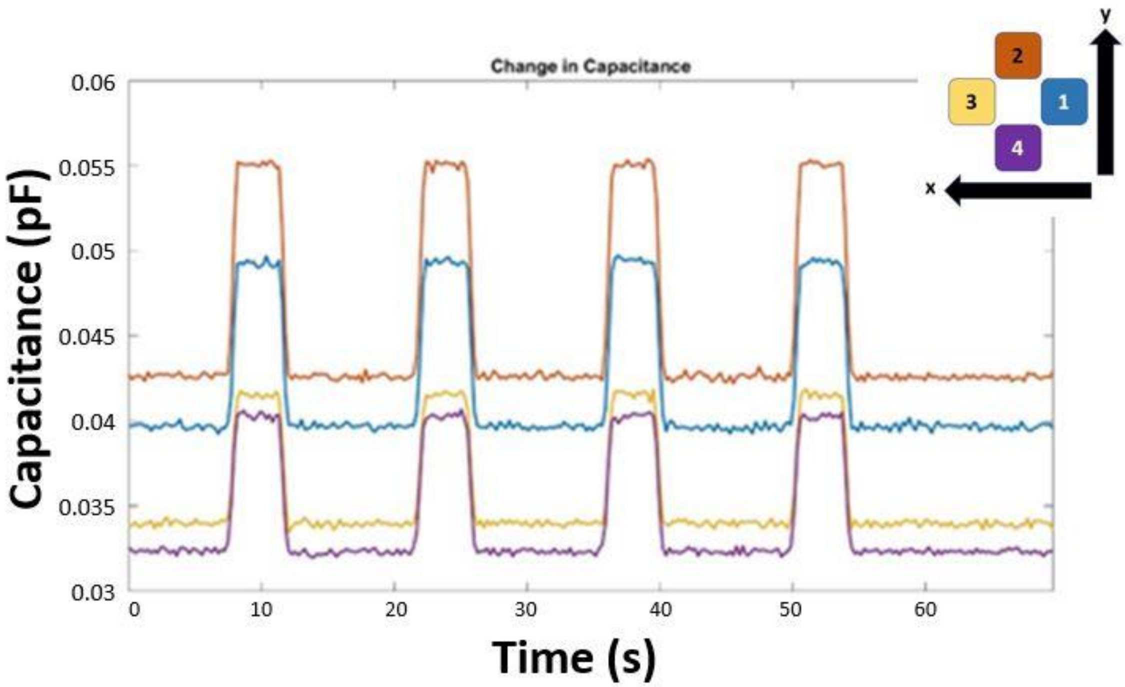

Figure 3-10: Flexible Pressure and Shear Sensor, 1 N Normal Force with 10 mm Radius of Curvature. Differing Baseline Values are Due to Parasitic Capacitance and Stretch Nonuniformities From Curvature. Axis of curvature is through taxels 2 and 4.

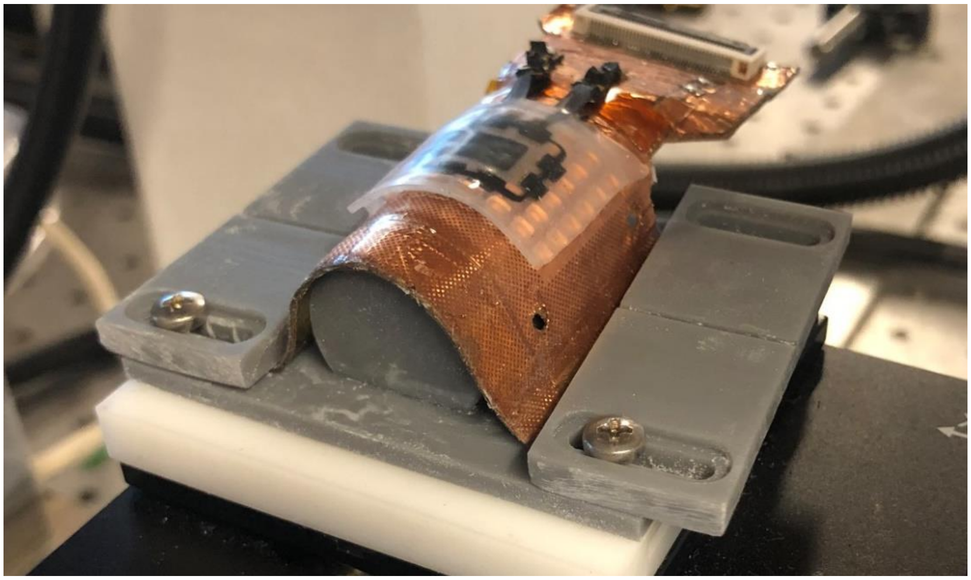

Figure 3-11: Flexible Combined Pressure and Shear Sensor on 10 mm Radius Mount

The change to a 10 mm radius curvature further affected the baseline capacitance values as shown in Figure 3-10, shifting them away from the flat baselines more than the 100 mm radius curvature. The start and end values for the sensor C_0 values are presented in Table 3-3, with the change in capacitance due to the 1 N applied force in Table 3-4. These shifts also do not align with the trends seen in the much more gradual 100mm curvature, with Taxel 2 experiencing an almost 7% further increase compared to Taxel 1's sub-1% increase in baseline when compared to the 100 mm values. Furthermore, the behavior of Taxel 4 has inverted, increasing by approximately 1 fF compared to its flat baseline capacitance. The most likely causes of this behavior are mounting or sensor fabrication asymmetries, which could be pronounced due to the high amount of curvature exerted on the sensor body. The sensor mounted to the 10 mm radius mount is shown in Figure 3-11 to display the strain on the elastomer body. Regardless of these inconsistencies in sensor signals over the range of curvatures there is no core concern with the function of the curved sensor, as none of the shifts are extreme and the general device behavior appears to remain the same.

Taxel	Approx. Flat C0 (fF)	Approx. 10mm C0 (fF)	% Change in C0
1	33.5	40	19.4
2	36	43.5	20.8
3	33	34	3.03
4	32	33	3.125

Table 3-3: Shift in Flexible Sensor C_0 Values, Flat to 10 mm Inner Radius of Curvature

Taxel	Approx. Flat ΔC (fF)	Approx. 10mm ΔC (fF)
1	4	10
2	4	11.5
3	4	8
4	5	7

Table 3-4: Shift in Flexible Sensor ΔC Values due to 1 N Applied Force, Flat to 10 mm Inner Radius of Curvature

The general trend of the baseline capacitance values and change in capacitance values tend to increase with smaller curvatures. This increasing trend is consistent throughout all of the central four taxels of the curved sensor, with a wide variance of effect across the different taxels for both 100 mm and 10 mm curvature implementation. The most likely cause for this increase is the stretching of both the upper elastomer layer and the elastomer-based structured dielectric, as the PCB remains largely structurally unchanged throughout the shift in curvature. As the sensor is curved, the upper layer is strained laterally to match the new radius as the elastomer is much softer than the strength of the material binding to the flexible PCB, as shown in Figure 3-12; in addition, the structure dielectric will also feel inward strain due to the changing effective circumference of the upper layer. A combination of these two physical strains causes the key sensor parameters of plate separation distance d (due to the pillar tension) and the upper electrode effective area A (due to lateral stretching changing side lengths) to decrease and increase, respectively. Significant asymmetry is observed in these taxels despite the evenly applied force, most likely caused by either a persistent sensor-load cell alignment issue or a fabrication inconsistency causing some pillars to experience strain differently.

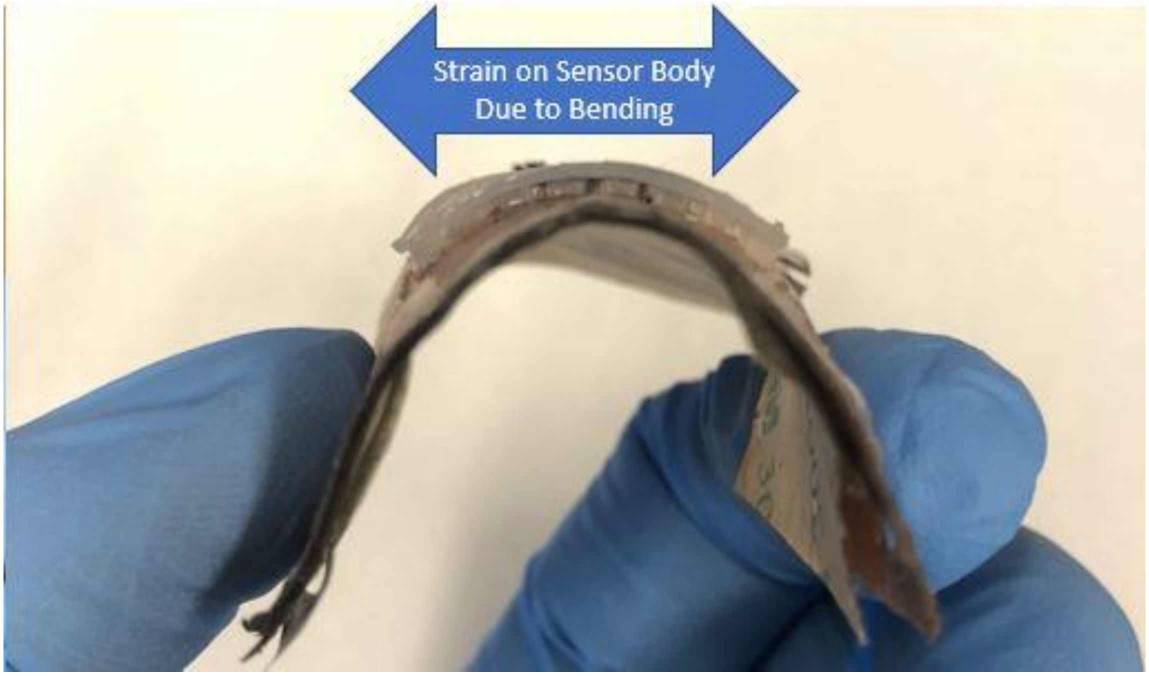

Figure 3-12: Lateral Force Exerted on Elastomer Sensor due to Bending (Photograph Example Only, Data is Taken with Uniform Curvature Applied using Sensor Mounts)

In the following sections, a normal force and shear displacement characterization is performed on the flexible sensor. For brevity only part of the data collected for each characterization scenario is presented in this chapter, with the rest of the data presented in Appendix B.

Normal Force Investigation

The first mode of characterization performed on the curved combined pressure and shear sensors is in the normal direction to the plane tangent to the peak of the applied curvature. The force for characterization was applied using the characterization setup presented in Chapter 2 of this thesis.

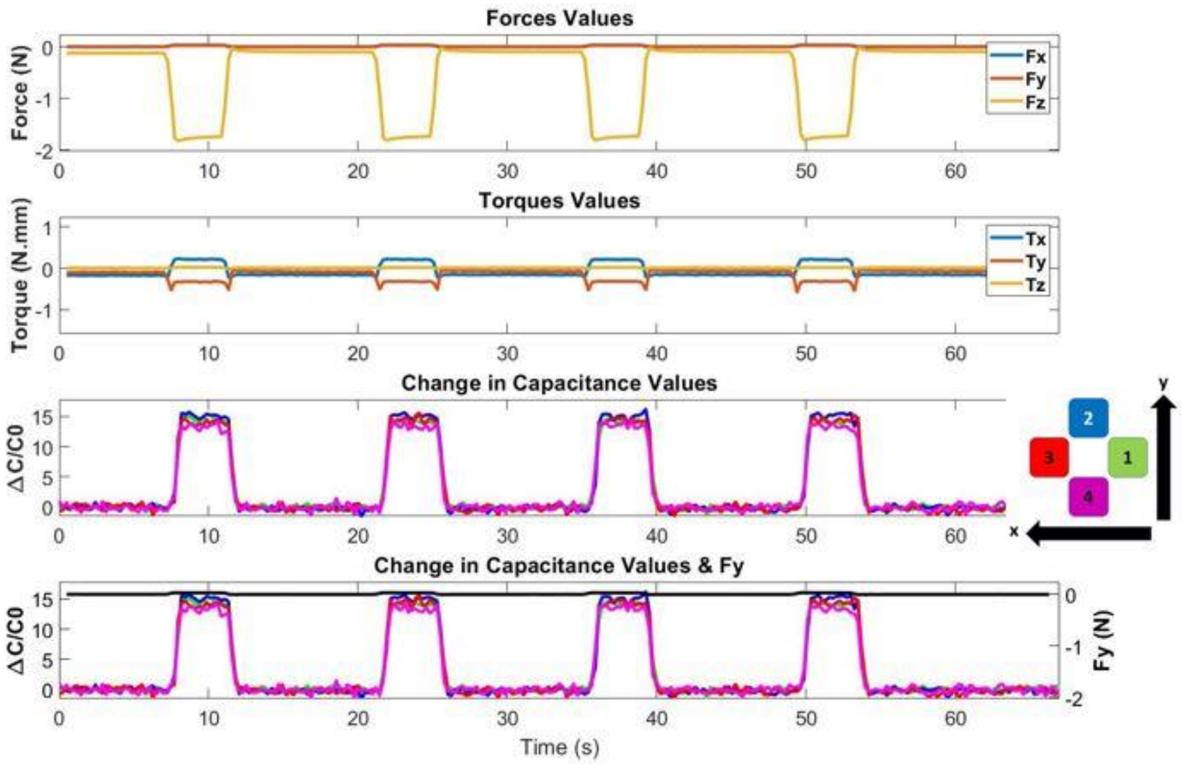

Figure 3-13: Normal Force Characterization at 100 mm Radius of Curvature with Flat Indenter, 1.6 N Repeated Normal Force Applied. Axis of curvature is through taxels 2 and 4.

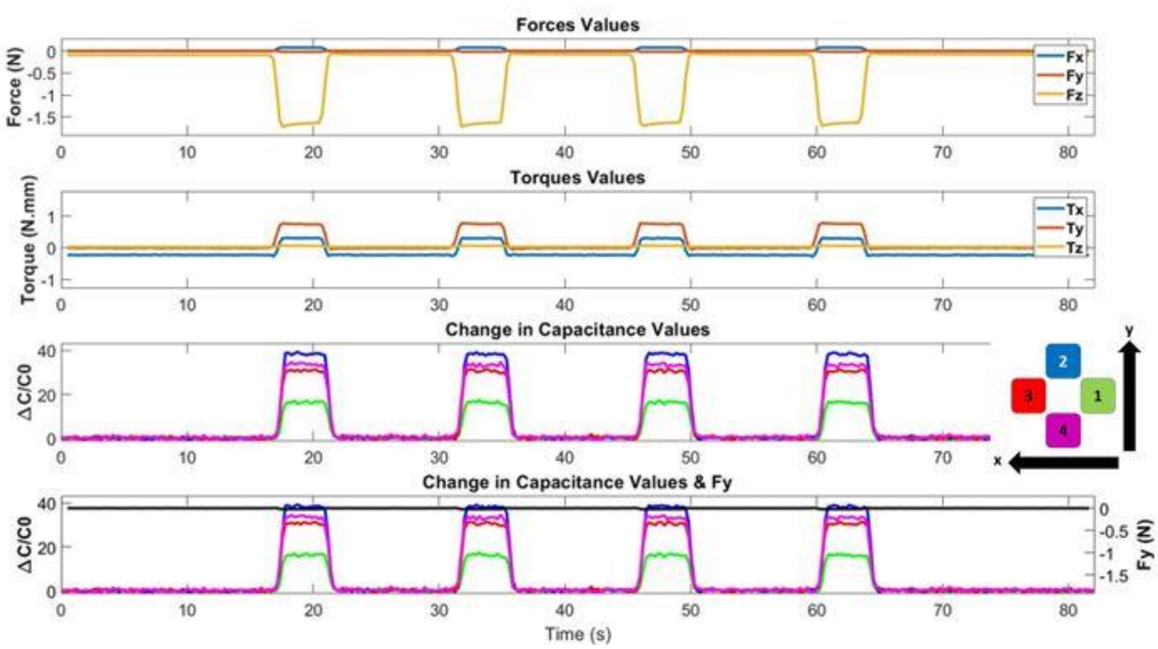

Figure 3-14: Normal Force Characterization at 100 mm Radius of Curvature with Cylindrical Indenter, 1.6 N Repeated Normal Force. Axis of curvature is through taxels 2 and 4.

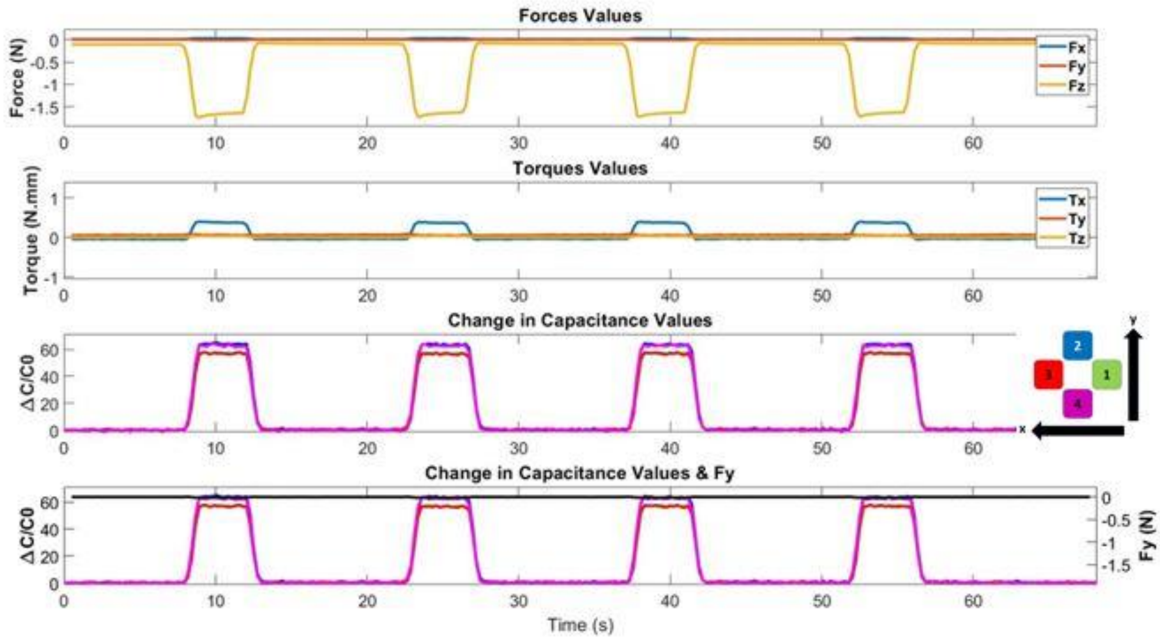

Figure 3-15: Normal Force Characterization at 100 mm Radius of Curvature with Spherical Indenter, 1.6 N Repeated Normal Force. Axis of curvature is through taxels 2 and 4.

The sensor produces a significant and consistent response to a repeated 1.6 N normal force. The flat-indenter response shown in Figure 3-13 is similar to that previously demonstrated by conventional flat sensors of a similar design, indicating that the sensor function is not significantly altered by the application of this curvature. Despite this resilience to slight applied curvatures, the device does exhibit a significantly different signal response when different indenters are used. The approximate peak $\Delta C/C_0$ signal for the flat indenter was 15%, while the cylindrical indenter produced a signal of approximately 34%, shown in Figure 3-14, (omitting the outlier green taxel, which is likely due to a small misalignment) and the spherical indenter approximately 60%, shown in Figure 3-15. A variety of factors may contribute to this shift in peak values, but the most likely dominant factor is the differing distribution of applied pressure between each indenter shape. The flat indenter applies pressure evenly across the sensor surface, which in turn causes a more horizontally constrained response in the incompressible elastomer material between the sensor electrodes. With the cylindrical and spherical indenters, a horizontal component is introduced to the force imparted onto the sensor upper electrode. This means the incompressible elastomer pillars have an additional axis along which to shift in response to the applied normal force, increasing the relative displacement per force applied.

An additional component of the shift in sensor response with differing indenters is the effect of indenter shape on the deformation of the upper electrode itself. The flat indenter produces a more distributed displacement of the sensor upper electrode compared to the other two indenters, with what is estimated to be minimal shape deformation vertically or horizontally. This is not the case for the other two indenters characterized, where uniform contact with the sensor surface is not achieved. It is highly likely that in a force-controlled characterization measurement such as those performed in the normal direction, this difference in distribution is causing some effect on the overall sensor deformation. This results in higher ‘equivalent’ pressure on the sensor taxels due to the centralized application area in the cylindrical and spherical indenters, with less dead space absorbing applied force. This unevenness in application can be most clearly seen in the cylindrical indenter, which exhibits much less sensor electrode agreement than the other two tests, primarily as a result of the lack of diagonal symmetry in the indenter.

An additional component to the normal force characterization is the out of plane force and torque experienced by the sensor. It is expected that, in normal force characterization, no forces outside of the normal axis (F_z) or torques will be observed. This is because in an ideal characterization situation, the sensor and indenter will be perfectly parallel and aligned; however, in practical characterization there will be nonidealities in both of these parameters that will contribute to the characterization. Best effort is taken to address these factors, described further in Chapter 2, as they are highly likely to cause some noticeable pollution of the sensor signal, such as increased noise or taxel signal separation. This can be seen in Figure 3-13 - Figure 3-15, where each dataset includes significant torques and some small out of plane force. This torque and out-of-plane force is taken into consideration in discussion of the sensor results, as the data analyzed represents the best-case characterization results in terms of torque.

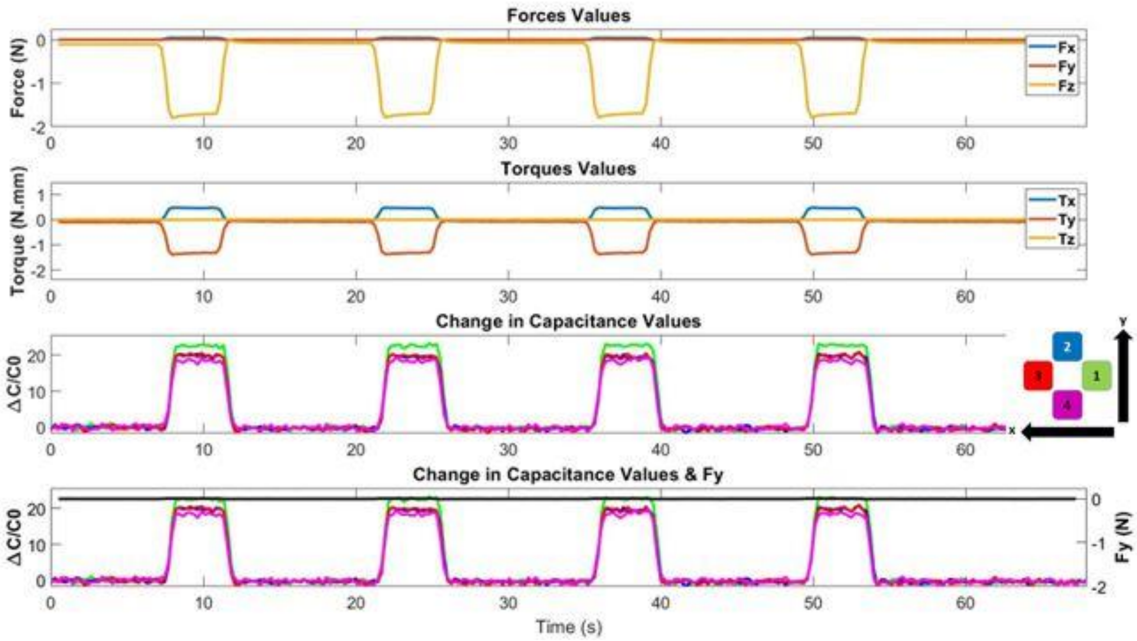

Figure 3-16: Normal Force Characterization at 30 mm Radius of Curvature with Flat Indenter, 1.6 N Repeated Normal Force. Axis of curvature is through taxels 2 and 4.

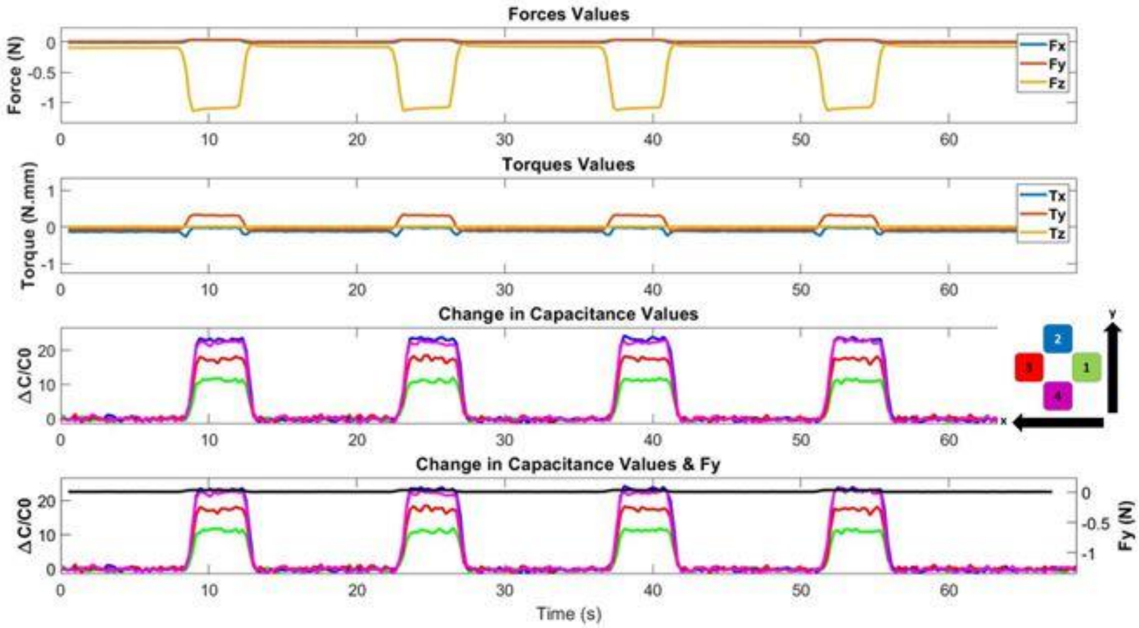

Figure 3-17: Normal Force Characterization at 30 mm Radius of Curvature with Cylindrical Indenter, 1.6 N Repeated Normal Force. Axis of curvature is through taxels 2 and 4.

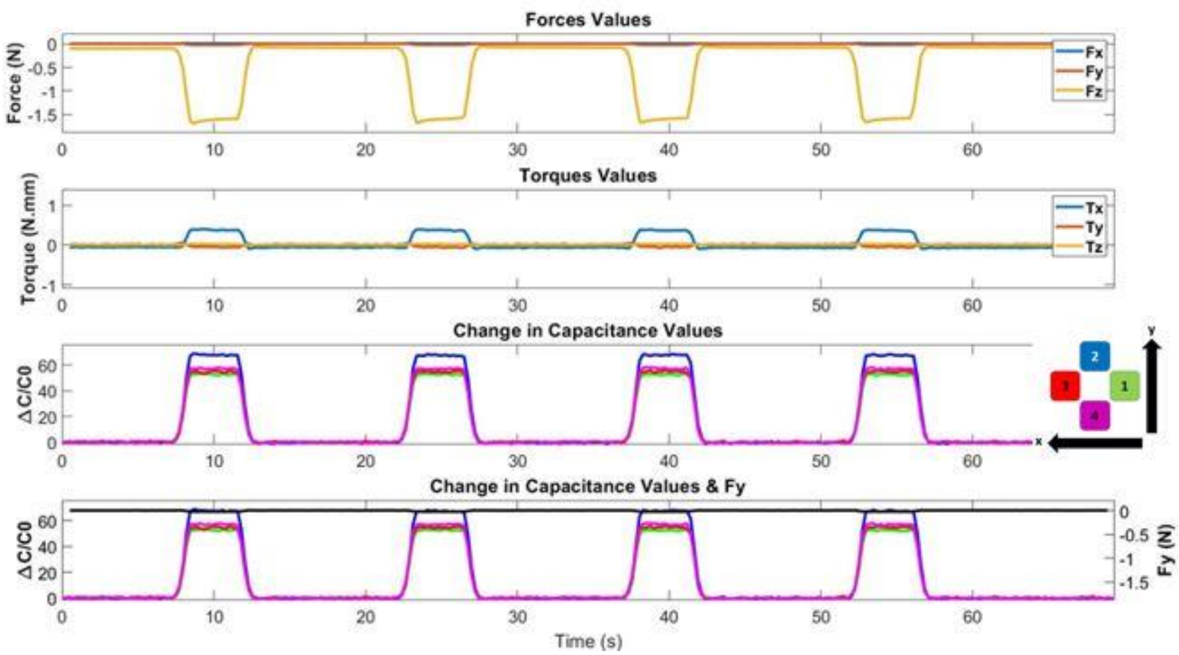

Figure 3-18: Normal Force Characterization at 30 mm Radius of Curvature with Spherical Indenter, 1.6 N Repeated Normal Force. Axis of curvature is through taxels 2 and 4.

Under a 30 mm applied inner radius curvature, the peak average response of the sensor shifts with each indenter shape examined. The data for each indenter at this radius of curvature is presented in Figure 3-16 (flat indenter), Figure 3-17 (cylindrical indenter), and Figure 3-18 (spherical indenter). The average peak signal difference between the 100 mm and 30 mm inner radius of curvature are presented in Table 3-5. Of the three sets, only the flat indenter experimental setup displayed an increase in peak $\Delta C/C_0$ under a 1.6 N applied force when compared to the same sensor laid flat from approximately 15% to approximately 20%, a 33.34% increase in signal change from the flat sensor peak signal. The cylindrical and spherical indenters decreased in peak average signal, with a large change for cylindrical (34% to 18.4%, an approximate 46% decrease in signal value from the flat sensor) and a much smaller one for spherical (60% to 58%, an approximate 3% decrease in signal value from the flat sensor). This significant compared to the noise experienced by the device (<1%), showing that the decrease in radius does have a noticeable but small effect on the sensor signal for the spherical indenter.

Indenter	100 mm Average Peak Signal ($\Delta C/C_0$)	30 mm Peak Average Signal ($\Delta C/C_0$)
Flat	15	20
Cylindrical	34	18.4
Spherical	60	58

Table 3-5: Peak Average Flexible Sensor Signal Change at 1.6 N Normal Force, 100 mm vs. 30 mm Inner Radius of Curvature

The most likely cause for this increase in sensor signal under the flat indenter is the decreased initial contact surface, as well as the stretching of the upper layer of the sensor. As the contact footprint of the indenter is decreased while force is maintained as the same, the applied pressure to the sensor body is increased. This causes an increase in the sensor displacement which results in the increased signal change observed. The same significant increase is not seen in the other two indenter shapes due to their already low indenter-sensor contact area at 100 mm or flat, meaning this same effect is not emphasized. Instead, the estimated surface contact area decreases but lateral tension is applied to the sensor architecture. This tension 'preloads' the dielectric pillars of the sensor, shifting the sensor area upwards along the stress-strain curve; this can be observed in the gradual upward trend of baselines across the decreasing radii of curvature. As the contact surface area is relatively similar for these the cylindrical and spherical indenters compared to the flat ones, the overall effect is either a dramatic decrease in sensitivity for the cylindrical indenter or a very small change for the spherical indenter.

An additional component of decreasing curvature radius is the increased scattering of peak signal responses for each taxel under the 1.6 N load. Scattering refers to the difference in peak sensor signal at the 1.6 N applied normal force, and is measured in the absolute % difference between peak signals. The flat indenter exhibited minimal scattering under either of the test curvatures, the spherical indenter only exhibited scattering in the 30mm test condition, and the cylindrical indenter had scattering in both test conditions examined. The most likely cause of this is also the contact surface area issue described above; a higher relative contact area would ensure deformation of each taxel in a more uniform manner, while low surface contact area may cause them to behave differently (especially in irregular indenters such as the cylindrical). This differing surface area and force distribution is demonstrated in Figure 3-19, with a theoretical 0.25 mm displacement applied and the 'overlap' area with the sensor plane highlighted. As the normal direction characterization measurements are force-controlled, this lowered surface area also indicates that the spherical indenter may exhibit a sensor response to higher pressures than the flat indenter. A combination of the surface area shape and total size are likely to contribute to these disparate sensor responses.

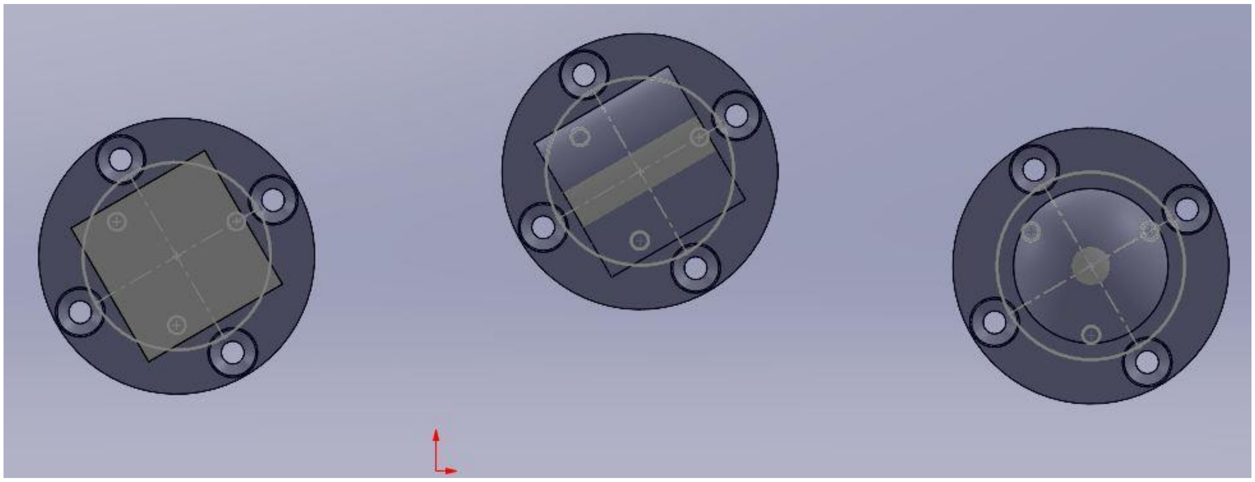

Figure 3-19: Indenter Contact Surface Areas at 0.25 mm Normal Displacement, Indenter-Sensor Contact Area Highlighted in Grey

Due to the vertical spacing between the indenter and the new curvature-imparting mounts for the flexible sensors, the cylindrical and spherical indenter shapes were unable to be characterized at a 10 mm applied curvature. Attempts were made to increase the vertical spacing to allow for the fitting of other indenters, but the constrained time frame imparted by the industry partner disallowed a fuller redesign of the characterization setup. Due to these complications, it was decided that an examination of all three indenters at 100mm and 30mm radii was sufficient to establish trends, and the 10mm radius would only be examined with the flat indenter.

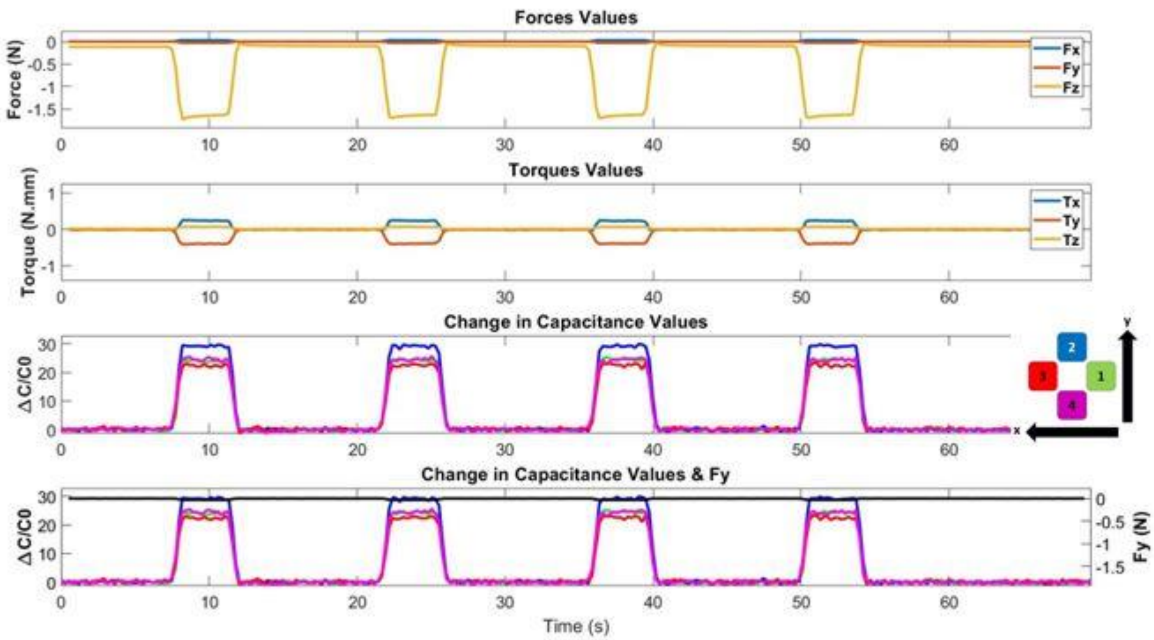

Figure 3-20: Normal Force Characterization at 10 mm Radius of Curvature with Flat Indenter, 1.6 N Repeated Normal Force. Axis of curvature is through taxels 2 and 4.

Characterization done at a 10mm sensor internal radius continued the established trend of the previous flexible sensor characterization. The data collected using the flat indenter at this 10 mm inner radius of curvature is presented in Figure 3-20. The peak $\Delta C/C_0$ signal at 1.6N has increased to approximately 25%, closely following the trend of the previous two flat-indenter measurements. This reinforces the hypothesis that for the large sensor-indenter contact area, highly even flat indenter, increased sensor lateral strain due to stretching increases the relative sensitivity of the flexible sensor to applied normal forces. This furthers the proposal that this lateral strain is thinning the upper layer of the sensor in addition to providing preload to the sensor pillars, and it is predicted that cylindrical and spherical objects would exhibit similar trends with decreased inner radii.

Shear Force Investigation

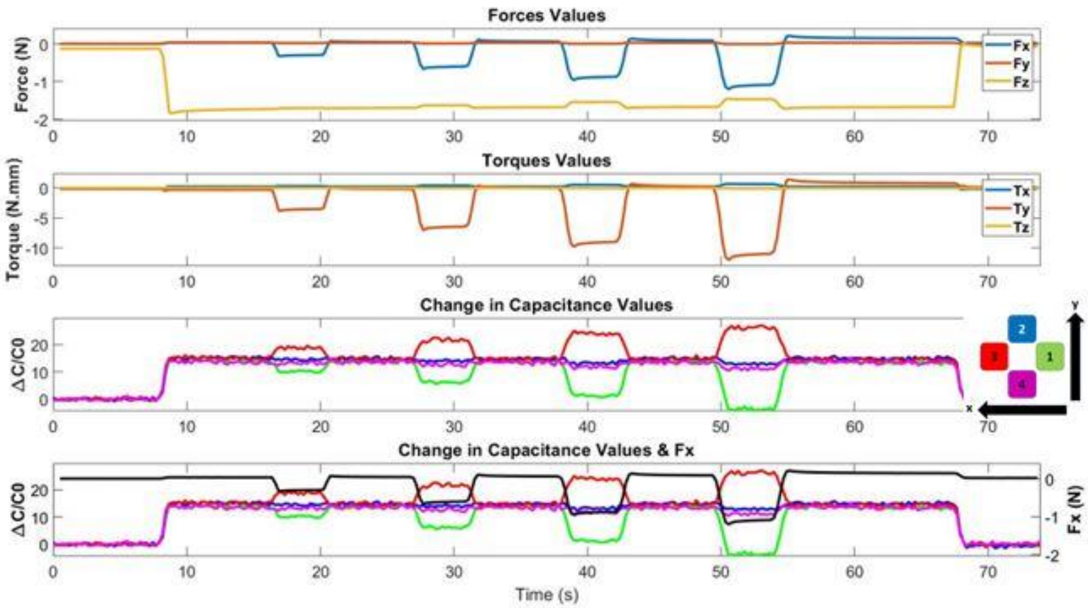

Figure 3-21: Shear Displacement Characterization at 100 mm Radius of Curvature with Flat Indenter, 0.2 mm to 0.8 mm Negative-x Displacement. Axis of curvature is through taxels 2 and 4.

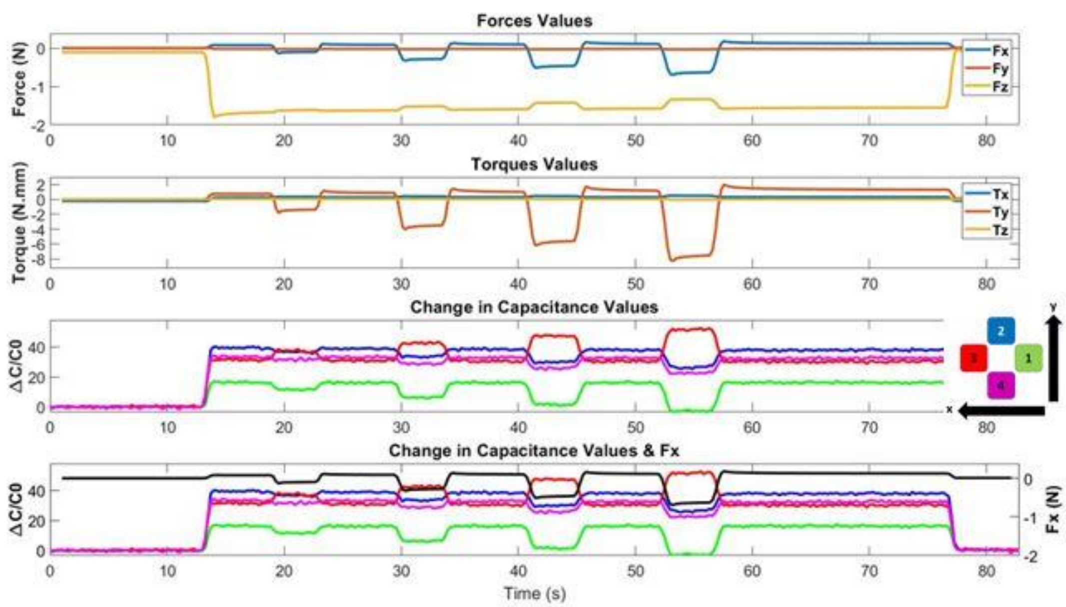

Figure 3-22: Shear Displacement Characterization at 100 mm Radius of Curvature with Cylinder Indenter, 0.2 mm to 0.8 mm Negative-x Displacement. Axis of curvature is through taxels 2 and 4.

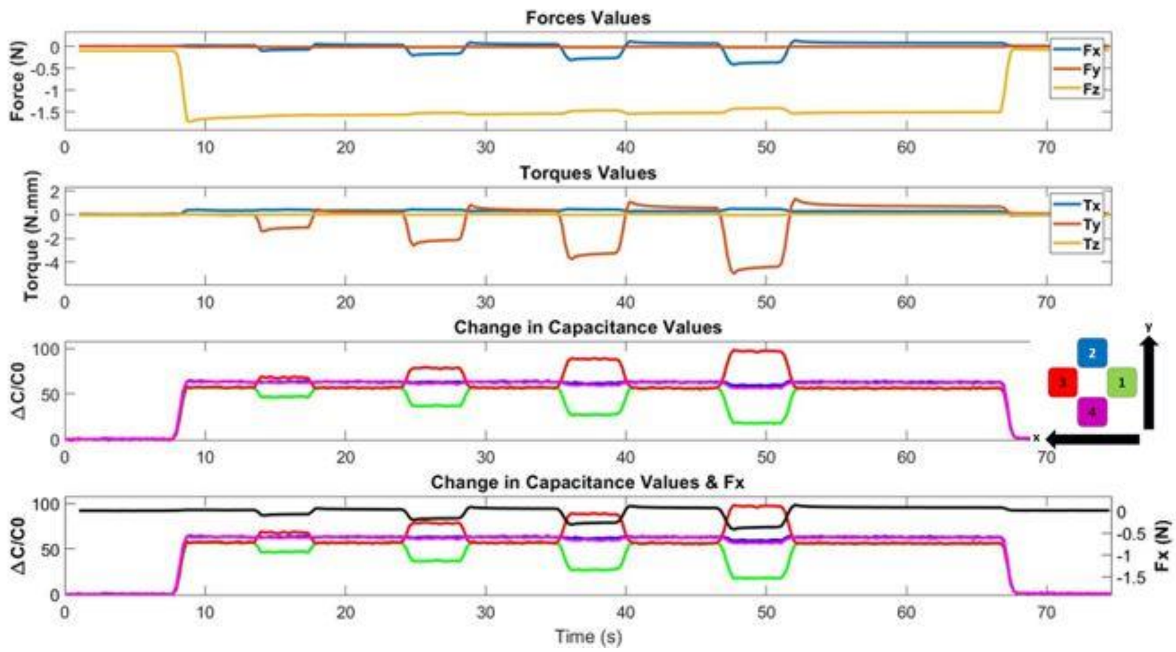

Figure 3-23: Shear Displacement Characterization at 100 mm Radius of Curvature with Spherical Indenter, 0.2 mm to 0.8 mm Negative-x Displacement. Axis of curvature is through taxels 2 and 4.

The indenter used to apply shear displacement in the x-direction has a significant effect on both the peak required force for displacement and the approximate peak sensor signal produced at that displacement. Shear data for each of these indenters is presented in Figure 3-21 (flat indenter), Figure 3-22 (cylindrical indenter), and Figure 3-23 (spherical indenter). The flat indenter required the highest applied force for the displacement, followed by the cylindrical indenter then the spherical one. The $\Delta C/C_0$ values trended inversely to this perceived shear stiffness in the x-direction, with the spherical indenter producing the highest approximate peak signal response by a significant margin (approximately 200% of the cylindrical indenter value). There is also some noticeable crosstalk in the signal response of the sensor, which is most likely due to some physical misalignment of the indenters causing nonuniform pulling on the sensor surface. The cylindrical indenter displayed the highest amount of estimated misalignment based on the shift in baseline $\Delta C/C_0$ clustering, despite best efforts to maintain proper alignment in characterization.

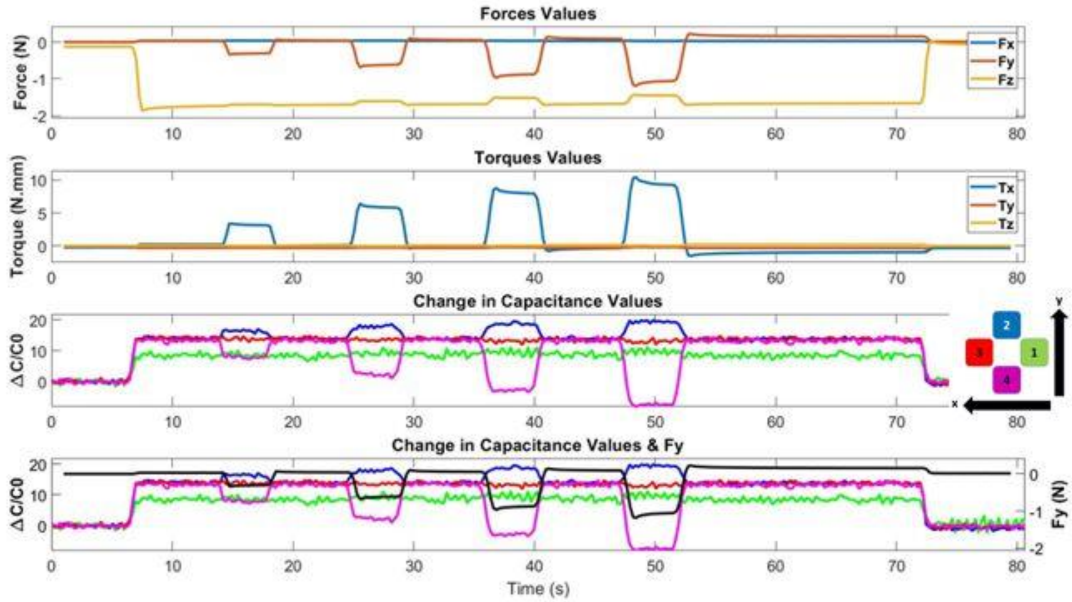

Figure 3-24: Shear Displacement Characterization at 100 mm Radius of Curvature with Flat Indenter, 0.2 mm to 0.8 mm Negative-y Displacement. Axis of curvature is through taxels 2 and 4.

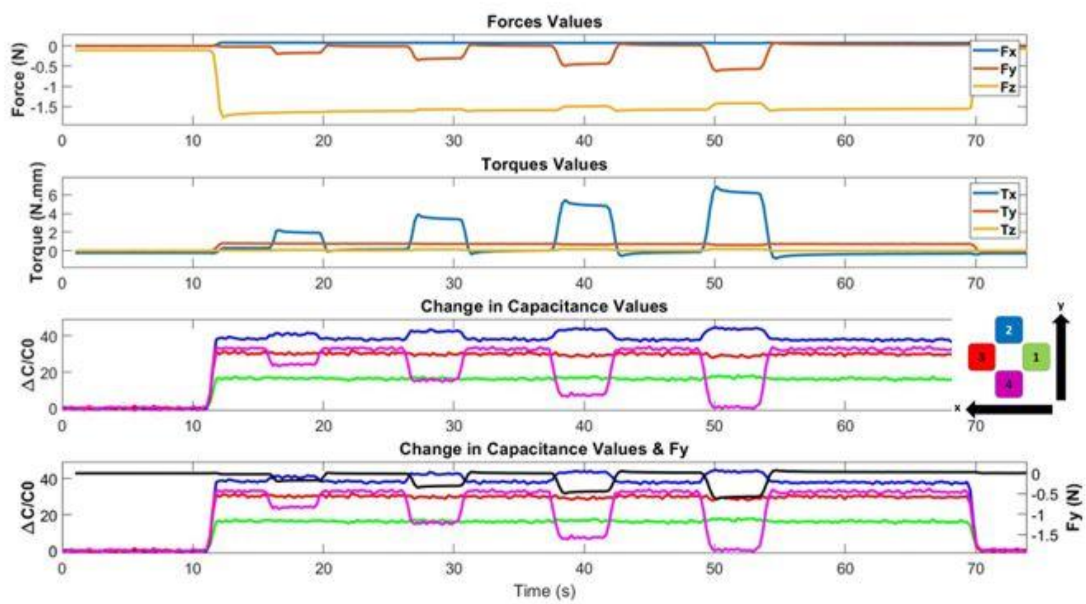

Figure 3-25: Shear Displacement Characterization at 100 mm Radius of Curvature with Cylindrical Indenter, 0.2 mm to 0.8 mm Negative-y Displacement. Axis of curvature is through taxels 2 and 4.

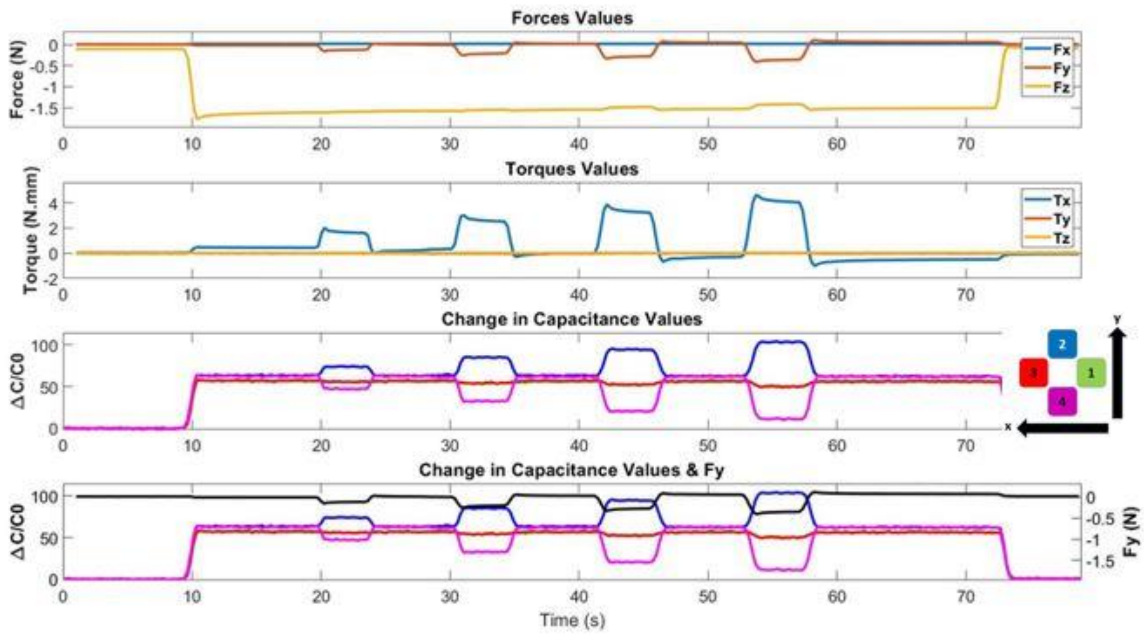

Figure 3-26: Shear Displacement Characterization at 100 mm Radius of Curvature with Spherical Indenter, 0.2 mm to 0.8 mm Negative-y Displacement. Axis of curvature is through taxels 2 and 4.

The y-direction shear application produced a similar trend in shear response values, as shown in Figure 3-24, Figure 3-25, and Figure 3-26. The spherical indenter produced the highest $\Delta C/C_0$ response at 0.8mm displacement by a margin of approximately 20. A notable effect in the y-direction is a consistent mismatch between the two in-line taxels, with one set providing a much larger response than the other (a difference of approximately 3.8x for the flat indenter, and 5.3x for the cylindrical indenter). Apart from this misalignment, each sensor produced a significant and measurable response to shear at each of the 0.2 mm displacement steps. The most likely causes of this major differential in electrode signal response are a difference in pillar or electrode placement on the curvature. While extensive steps are taken in fabrication to ensure all components are aligned, small errors are common due to the hand-fabricated nature of the sensors. While these misalignments generally cause a much less significant effect on the sensor output, the applied curvature is likely amplifying the signal difference due to strain placed on the sensor architecture components. Further testing than what was performed in this thesis is required to verify this, including monitoring of pillar displacement during shear testing and high-zoom examination of sensor alignment to the underlying PCB.

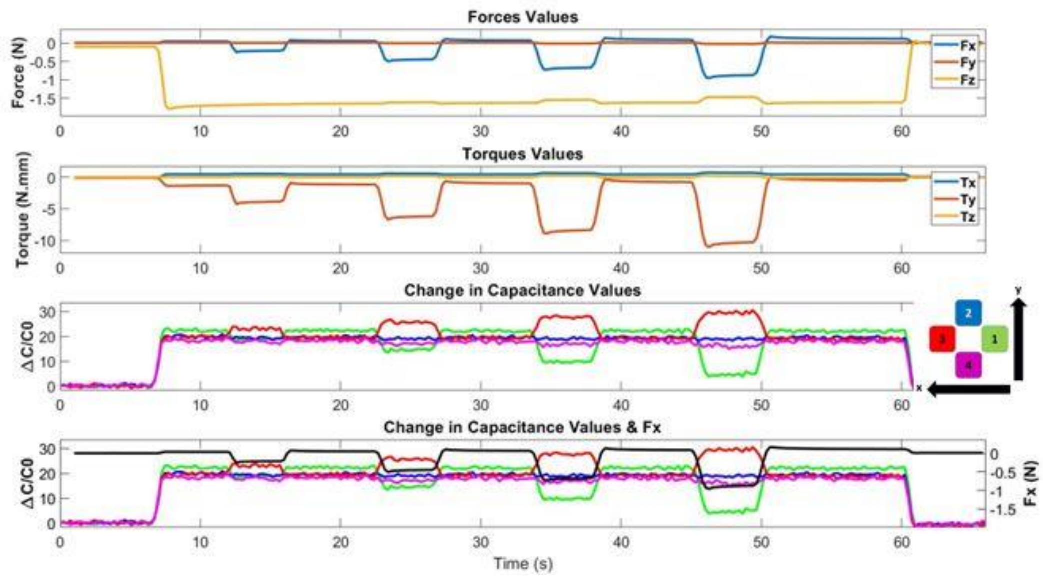

Figure 3-27: Shear Displacement Characterization at 30 mm Radius of Curvature with Flat Indenter, 0.2 mm to 0.8 mm Negative-x Displacement. Axis of curvature is through taxels 2 and 4.

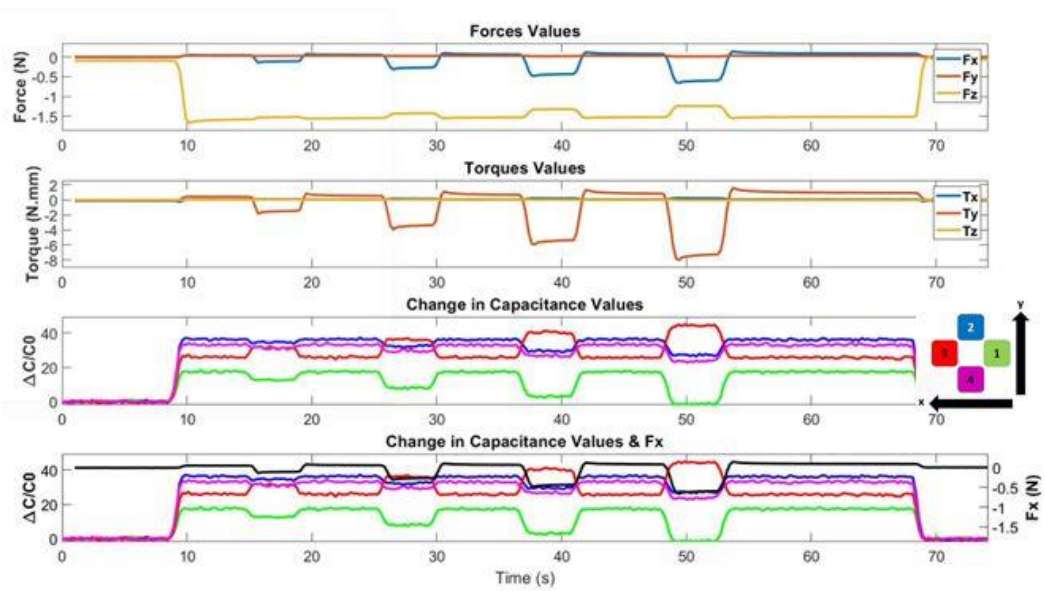

Figure 3-28: Shear Displacement Characterization at 30 mm Radius of Curvature with Cylindrical Indenter, 0.2 mm to 0.8 mm Negative-x Displacement. Axis of curvature is through taxels 2 and 4.

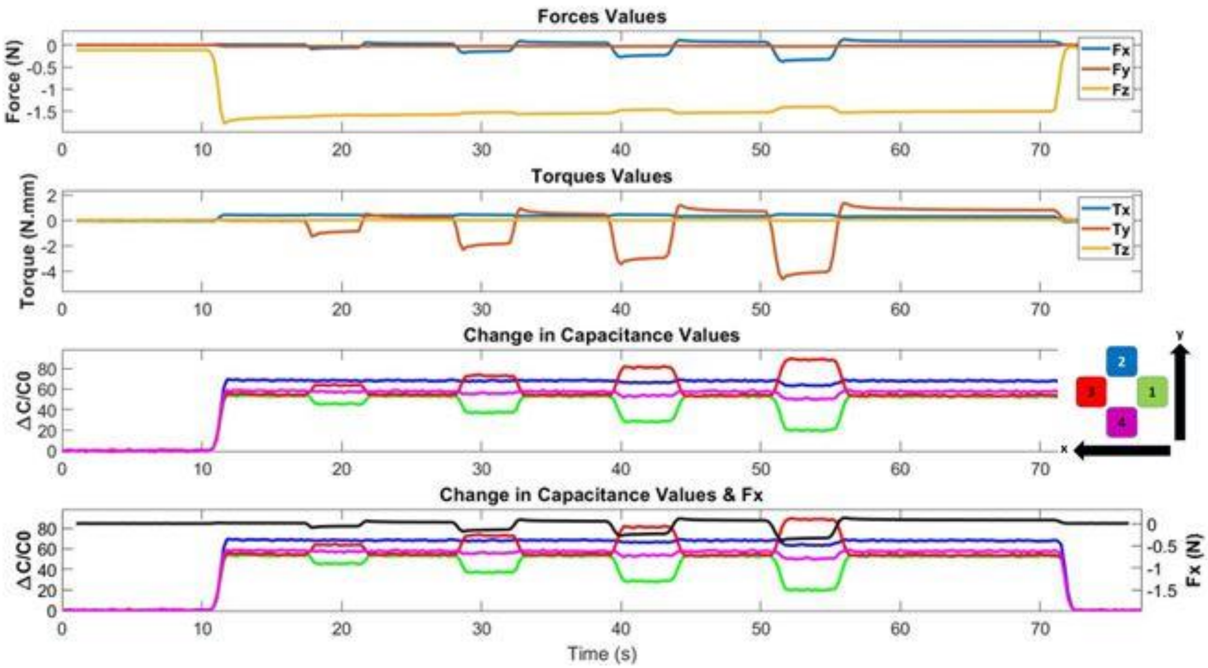

Figure 3-29: Shear Displacement Characterization at 30 mm Radius of Curvature with Spherical Indenter, 0.2 mm to 0.8 mm Negative-x Displacement. Axis of curvature is through taxels 2 and 4.

A decrease in the inner radius of curvature caused varying decreases in the peak approximate sensor $\Delta C/C_0$ response depending on which indenter was used. Shear data collected at a 30 mm inner radius of curvature is presented in Figure 3-27 (flat indenter), Figure 3-28 (cylindrical indenter), and Figure 3-29 (spherical indenter). The flat indenter exhibited the largest change with an approximate 14.85% decrease, followed by the spherical indenter at 12.79% then the cylindrical with 10.52%. This trend was not followed by the shift in force required to reach displacement, as the spherical indenter showed a 40.06% lower force required at the 30 mm inner radius curvature, the flat indenter showed a 27.66% decrease, and the cylindrical indenter retained the highest architecture stiffness compared to the indenters, with an 18.99% decrease in required force for the 0.8mm displacement. The general decrease in both sensor signal and force required for the x-direction shear indicates that the lateral stretching due to the increased outer circumference is significantly affecting the sensor upper layer and dielectric architecture. The most likely cause of this decrease in sensor signal change is the stretching of the upper electrodes, increasing the upper electrode parallel surface area. This increase in area decreases the relative shift in parallel capacitive surface area seen as the sensor is displaced in the x-axis due to shear, potentially without causing any significant change in the baseline capacitance. Force required for displacement is decreased, most likely due to this same stretching effect thinning the upper sensor layer and stretching the dielectric pillars sideways.

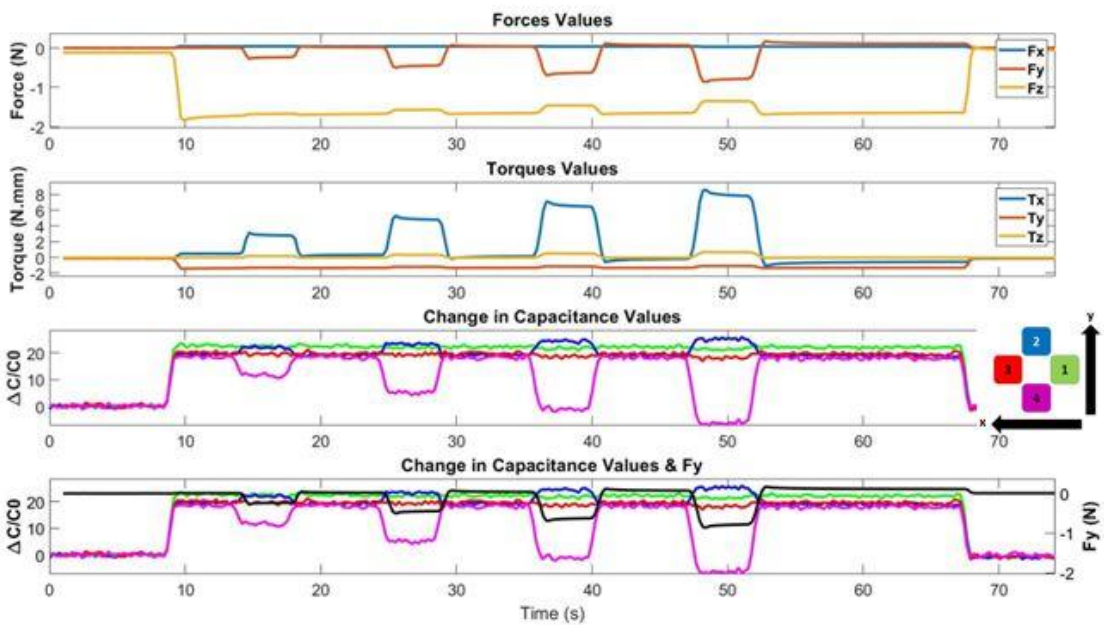

Figure 3-30: Shear Displacement Characterization at 30 mm Radius of Curvature with Flat Indenter, 0.2 mm to 0.8 mm Negative-y Displacement. Axis of curvature is through taxels 2 and 4.

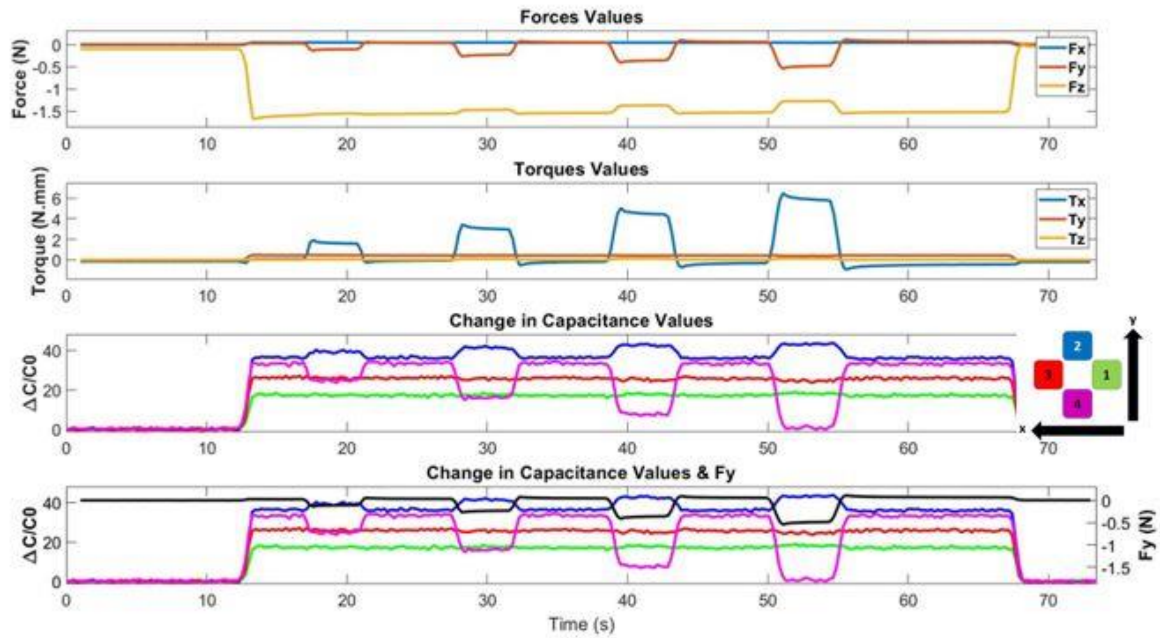

Figure 3-31: Shear Displacement Characterization at 30 mm Radius of Curvature with Cylindrical Indenter, 0.2 mm to 0.8 mm Negative-y Displacement. Axis of curvature is through taxels 2 and 4.

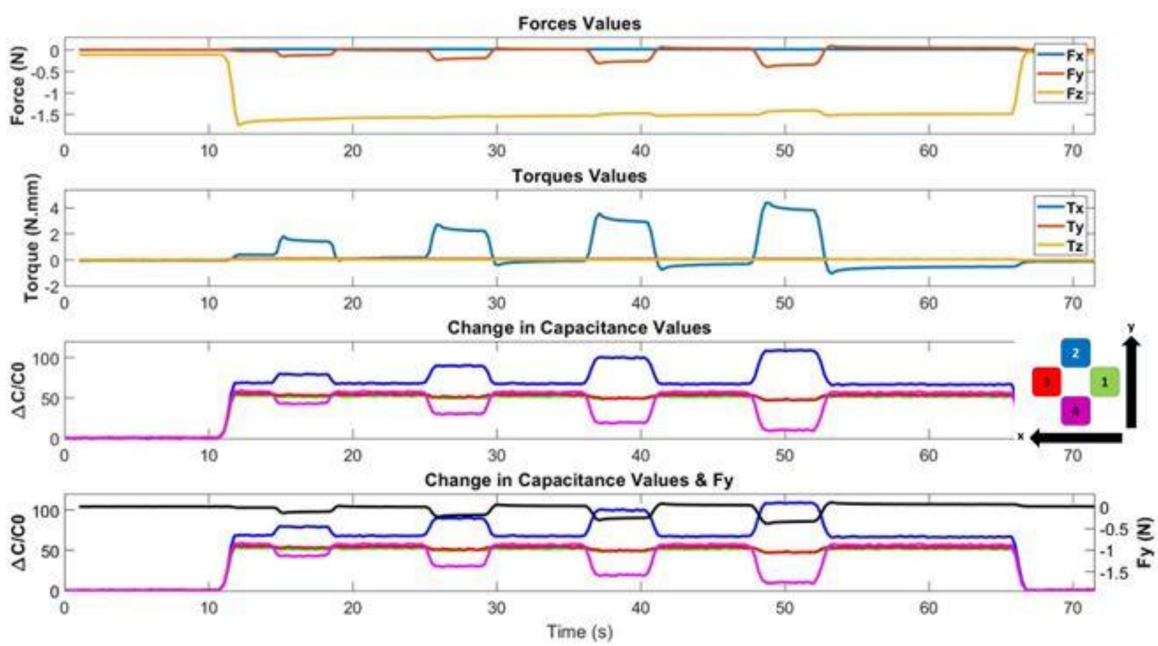

Figure 3-32: Shear Displacement Characterization at 30 mm Radius of Curvature with Spherical Indenter, 0.2 mm to 0.8 mm Negative-y Displacement. Axis of curvature is through taxels 2 and 4.

The sensor response to y-direction shear had a mixed trend of increases and decreases to peak signal at 0.8mm shear displacement, shown in Figure 3-30, Figure 3-31, and Figure 3-32. The flat indenter showed a 14.91% increase in sensor approximate peak signal at 0.8mm displacement with a 36.45% decrease in force required for the displacement, the cylindrical indenter a 3.14% increase in peak signal and 26.47% decrease in required force, and the spherical indenter a 15.59% decrease in peak signal and 15.69% decrease in required force. While the decrease in peak signal from the spherical indenter does not follow the previous pattern established by the x-direction shear measurements, the flat and cylindrical characterization reinforces it. As the sensor is stretched out sideways, the upper electrodes in line with the x-direction shear are stretched in a manner that decreases their overall sensitivity to shear; as this strain is perpendicular to the y direction electrodes, their shape is deformed sideways and shear response is not significantly affected. The force required to reach each shear displacement is still decreased significantly due to this effect, as the strain on the upper layer and pillars thins out the material and better facilitates shear motion. The previously noted imbalance in electrode signal for the in-line electrodes persists in the 30mm characterization, with similar differences between the blue and pink taxels.

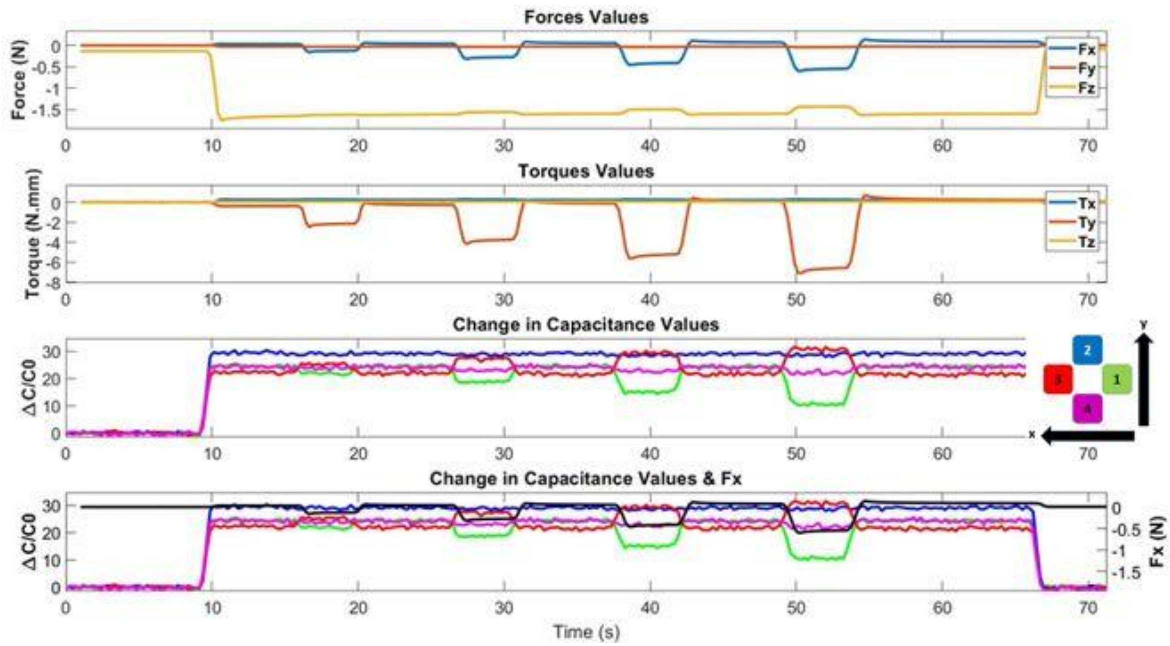

Figure 3-33: Shear Displacement Characterization at 10 mm Radius of Curvature with Flat Indenter, 0.2 mm to 0.8 mm Negative-x Displacement. Axis of curvature is through taxels 2 and 4.

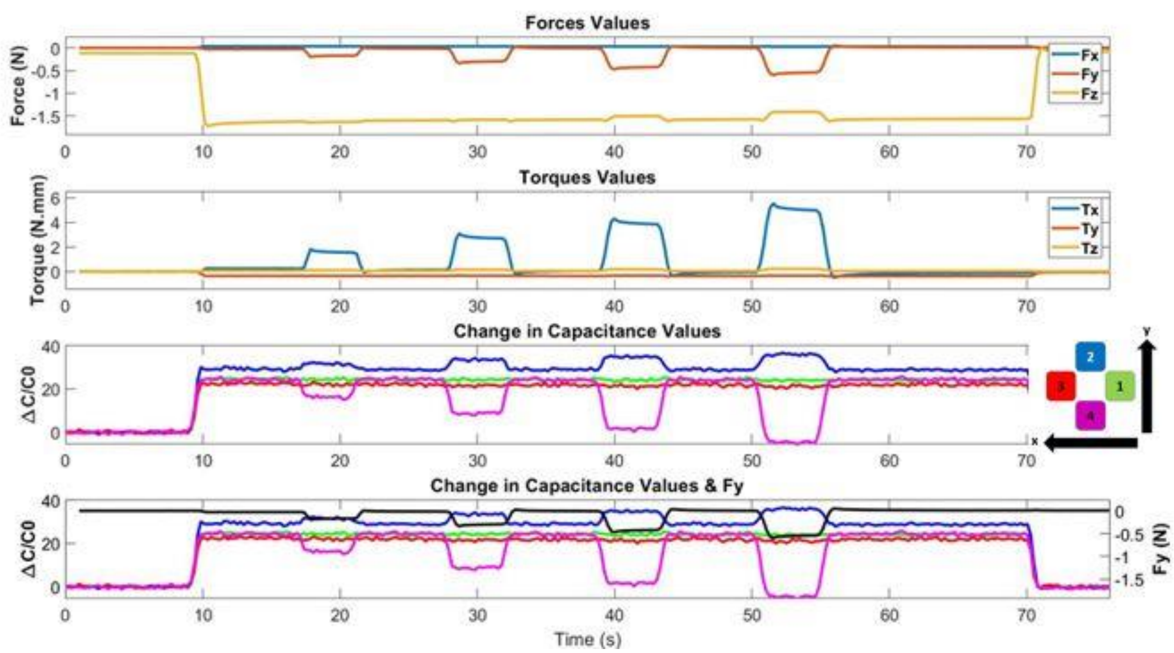

Figure 3-34 Shear Displacement Characterization at 10 mm Radius of Curvature with Flat Indenter, 0.2 mm to 0.8 mm Negative-y Displacement. Axis of curvature is through taxels 2 and 4.

A decrease in sensor inner radius from 30 mm to 10 mm further shifted both the peak sensor $\Delta C/C_0$ and peak force required at 0.8 mm for the flat indenter, shown in Figure 3-33 and Figure 3-34. The force required in the x-direction remained very similar, increasing by approximately 0.32%. This indicates that the lateral strain effect on stiffness in the perpendicular direction to the curvature seen at 30 mm is somewhat saturated, resulting in drastically reduced changes in the remaining 20 mm change in inner radius. Conversely, the force required in the y-direction and the sensor peak signal change for either direction at 0.8mm displacement has continued to increase significantly. Despite the minor increase in force required, the x-direction peak sensor signal response accelerated to a 42.26% decrease from the 30mm value, approximately 6% more change than the 100mm to 30mm radius change. The y-direction shear experienced a significant further increase in peak sensor signal and decrease in force required, comparable to the difference seen between the 100mm and 30mm radii. An approximate 24.41% decrease in force required was observed, with a 19.29% increase in the peak sensor signal.

The overall results of shear testing at different inner radii of curvature, with each indenter used, are presented in Table 3-6.

Sensing Conditions (Indenter, Curvature Radius (mm))	**Sensor Force Direction**	**Approximate Peak ΔF at 0.8 mm displacement (N)**	**Approximate Peak $\Delta C/C_0$ at 0.8 mm displacement (%)**
Flat, 100	Negative x	1.187	11.11
Cylinder, 100	Negative x	0.695	21.95
Sphere, 100	Negative x	0.4181	41.06
Flat, 100	Negative y	1.188	21.195
Cylinder, 100	Negative y	0.6267	31.645
Sphere, 100	Negative y	0.3976	50.98
Flat, 30	Negative x	0.8587	9.46
Cylinder, 30	Negative x	0.563	19.64
Sphere, 30	Negative x	0.2506	35.81
Flat, 30	Negative y	0.755	24.356
Cylinder, 30	Negative y	0.4608	32.6376
Sphere, 30	Negative y	0.3352	43.03
Flat, 10	Negative x	0.4958	9.49
Flat, 10	Negative y	0.5707	29.094

Table 3-6: Curved Sensor Shear Characterization Peak Force and Peak % Change in Capacitance Results, 100 mm Radius of Curvature to 10 mm Radius of Curvature

Flexible Sensor Characterization Curves

Characterization curve plots may also be calculated using the shear data obtained from the flexible sensor. By plotting the calculated shear of the sensor found using Equation 1 against the measured shear imparted on the sensor, a relationship may be established between sensor signal response and actual shear. The major motivation behind these plots is the development of an equation which allows for the separation of pressure and shear, and conversion of capacitive signals to usable information. In addition, the characterization curve plots allow for further verification of independence between x- and y-direction shear forces. The characterization curves presented here are calculated using the data obtained with the flat indenter at varying radii of inner curvature.

Characterization Curves, *x*-direction

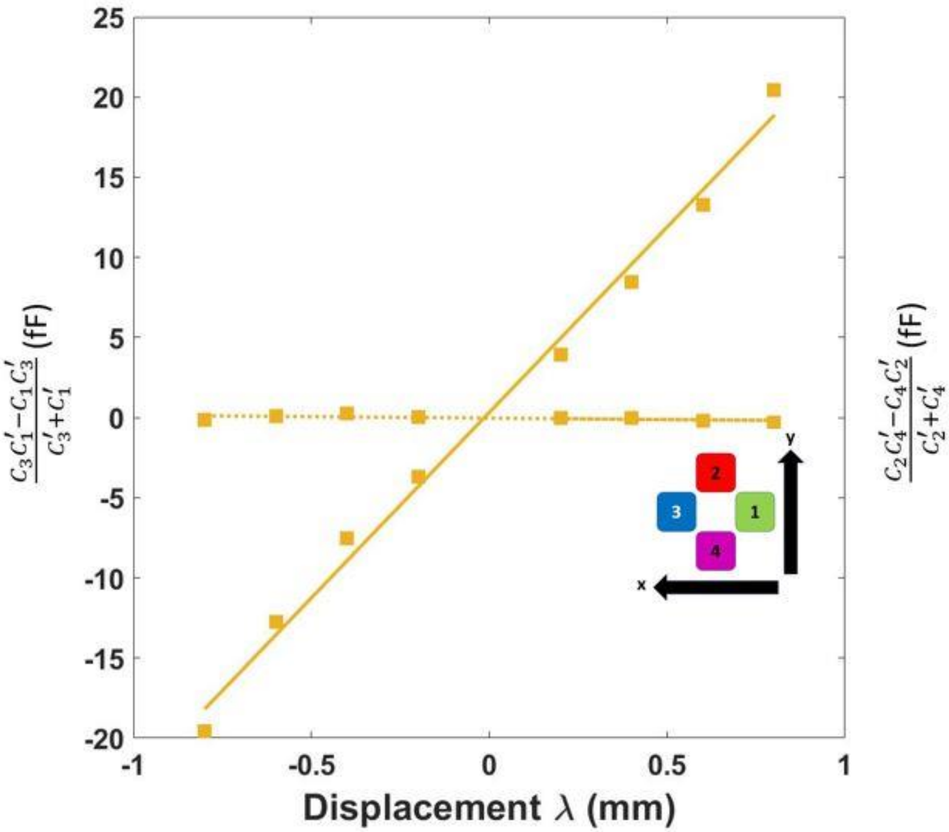

Figure 3-35: Demonstration of x-Direction Shear Performance of Flexible Sensor with 100 mm Radius of Curvature, including Separation of X (Solid Best-Fit Line) and Y (Dotted Best-Fit Line) Shear Responses. Shear Displacement is Plotted vs. the Differential Capacitance in the X and Y Directions (Left, X Difference, Right, Y Difference).

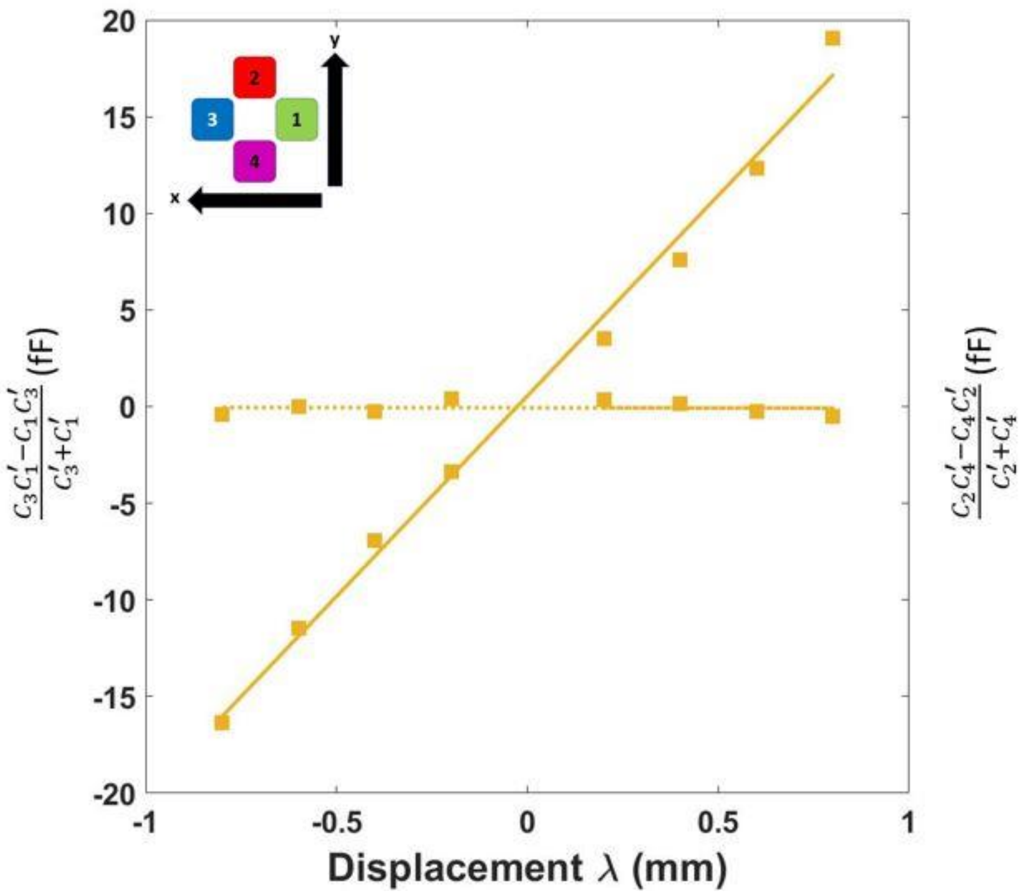

Figure 3-36: Demonstration of x-Direction Shear Performance of Flexible Sensor with 30 mm Radius of Curvature, including Separation of X (Solid Best-Fit Line) and Y (Dotted Best-Fit Line) Shear Responses. Shear Displacement is Plotted vs. the Differential Capacitance in the X and Y Directions (Left, X Difference, Right, Y Difference).

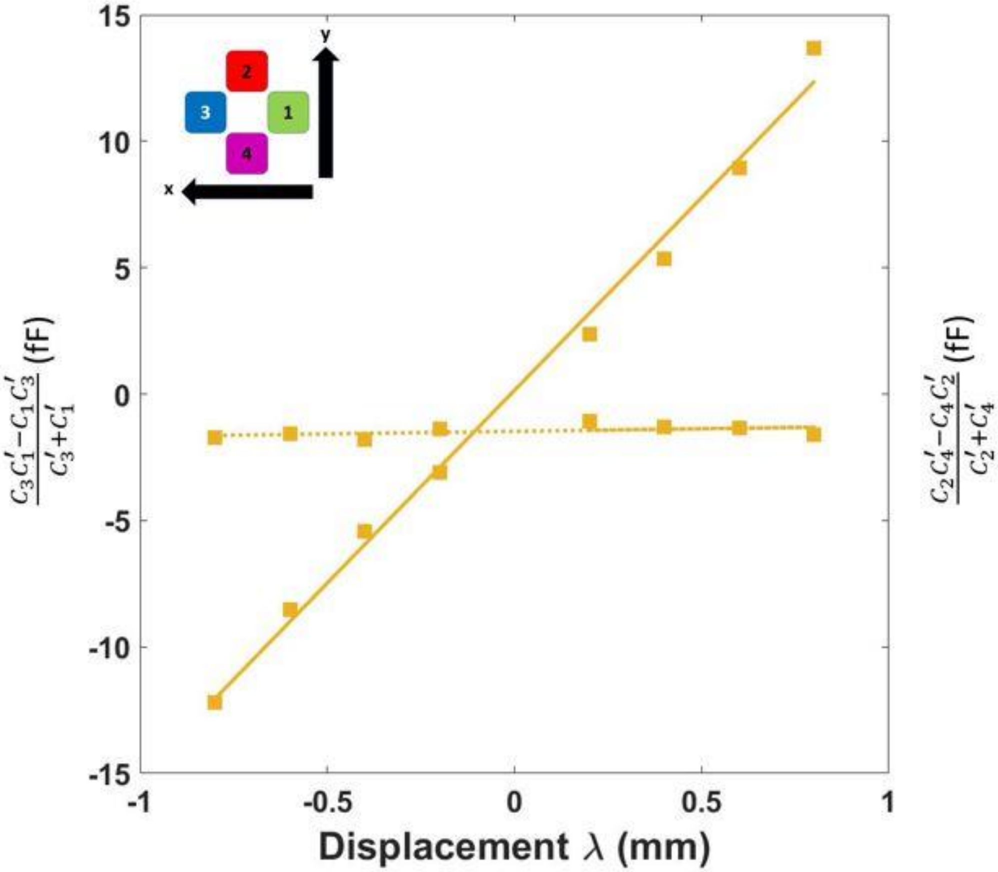

Figure 3-37: Demonstration of x-Direction Shear Performance of Flexible Sensor with 10 mm Radius of Curvature, including Separation of X (Solid Best-Fit Line) and Y (Dotted Best-Fit Line) Shear Responses. Shear Displacement is Plotted vs. the Differential Capacitance in the X and Y Directions (Left, X Difference, Right, Y Difference).

The x-direction characterization curves shown in Figure 3-35-Figure 3-37 generally show a strong relationship between sensor signal and applied shear in the x-direction at each radius of curvature. Each radius of curvature shows a mostly flat shear response in the y-direction and a mostly linear relationship in the x-direction. This indicates that flexing does not introduce significant nonlinearities into the sensor signal in the x-direction, confirming sensor function despite applied curvature. However, a shift is seen in the general trends for the x-direction signal throughout the radii examined. Values calculated using Equation 1 between taxels 1 and 3 at 0.8 mm applied shear follow a negative trend as shown in Table 3-7, with an approximate shift of -6.73 pF in the positive-x direction and 7.39 pF in the negative-x direction.

Radius of Curvature (mm)	Shear Displacement (mm)	Calculated Shear Value
100	0.8	20.42
30	0.8	19.04
10	0.8	13.69
100	-0.8	-19.58
30	-0.8	-16.35
10	-0.8	-12.19

Table 3-7: Calculated Shear Values for x-Direction Characterization Curve Plots

Characterization Curves, *y*-direction

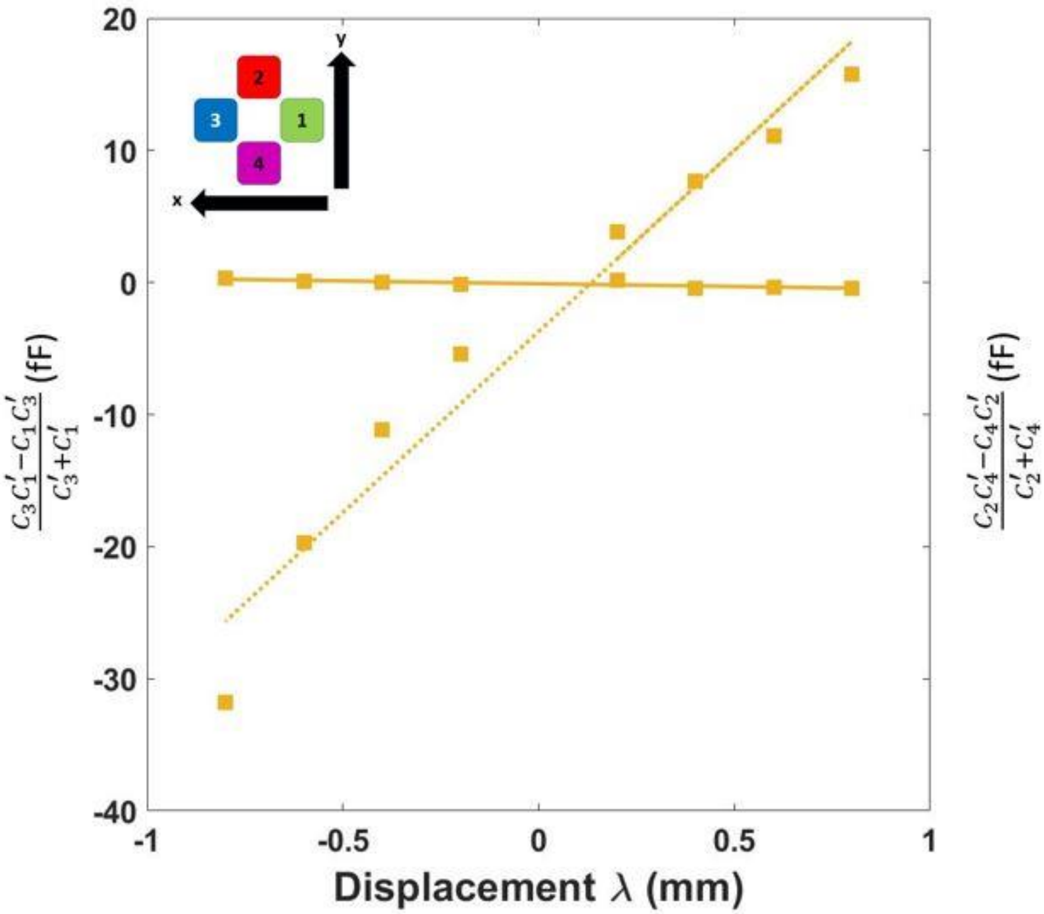

Figure 3-38: Demonstration of y-Direction Shear Performance of Flexible Sensor with 100 mm Radius of Curvature, including Separation of X (Solid Best-Fit Line) and Y (Dotted Best-Fit Line) Shear Responses. Shear Displacement is Plotted vs. the Differential Capacitance in the X and Y Directions (Left, X Difference, Right, Y Difference).

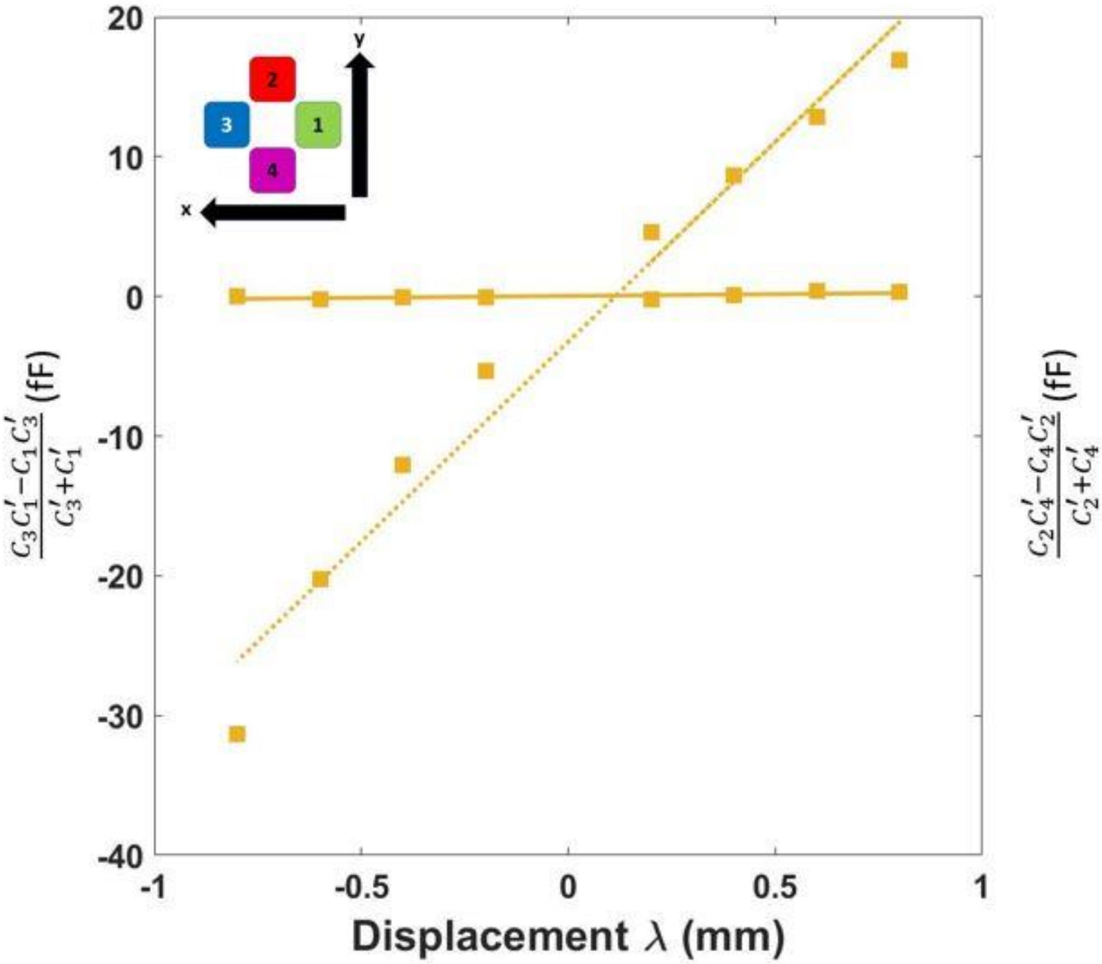

Figure 3-39: Demonstration of y-Direction Shear Performance of Flexible Sensor with 30 mm Radius of Curvature, including Separation of X (Solid Best-Fit Line) and Y (Dotted Best-Fit Line) Shear Responses. Shear Displacement is Plotted vs. the Differential Capacitance in the X and Y Directions (Left, X Difference, Right, Y Difference).

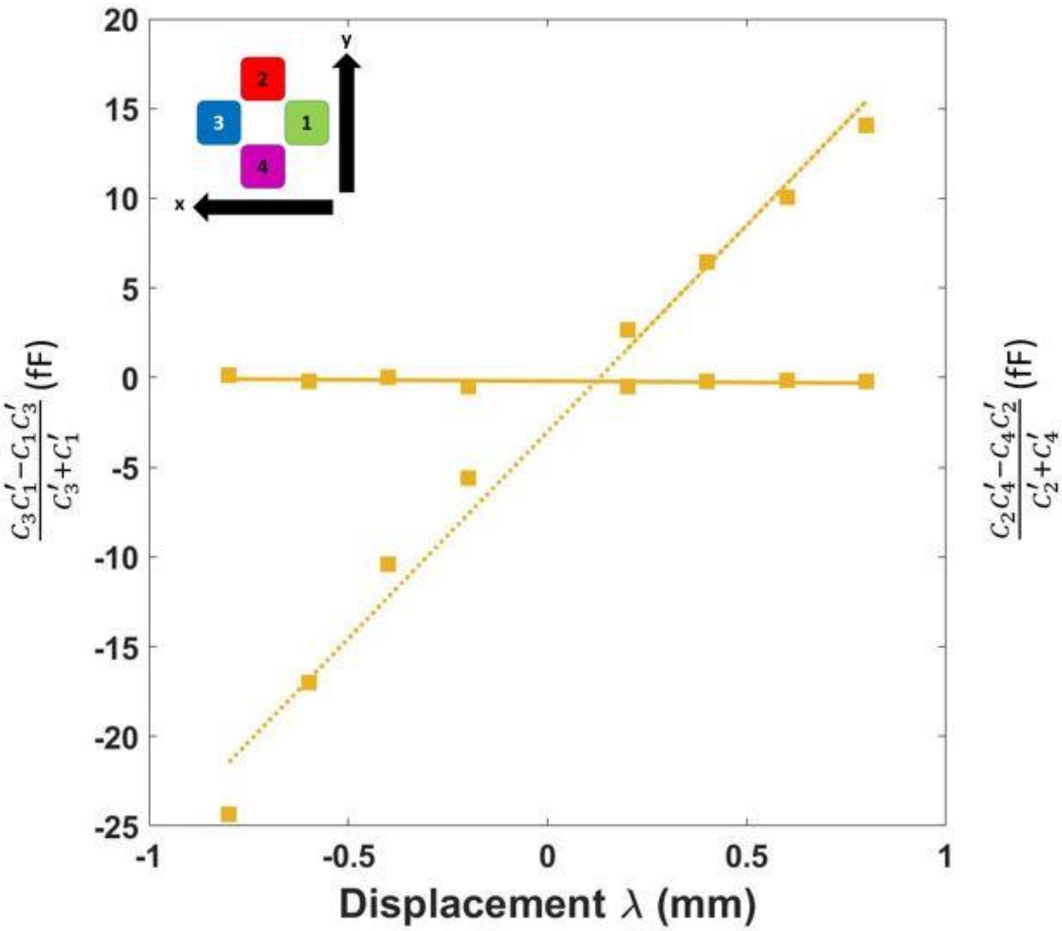

Figure 3-40: Demonstration of y-Direction Shear Performance of Flexible Sensor with 10 mm Radius of Curvature, including Separation of X (Solid Best-Fit Line) and Y (Dotted Best-Fit Line) Shear Responses. Shear Displacement is Plotted vs. the Differential Capacitance in the X and Y Directions (Left, X Difference, Right, Y Difference).

The y-direction characterization curves shown in Figure 3-38-Figure 3-40 display a clear separation of the in-line and out-of-line shear taxels, with only small variations from zero signal in the out-of-plane taxels. However, the in-line taxels in the y-direction display a significant nonlinearity at all curvatures in the negative shear direction. This can be observed by the general curvature shape as well as the peak calculated values as shown in Table 3-8, where the +0.8 mm shear displacement produces approximately 46%-58% of the -0.8 mm shear displacement calculated value. It is expected that this strong nonlinearity shares a cause with the significant discrepancy in taxel $\Delta C/C_0$ observed in the flexible sensors in the y-direction at various radii of curvature. A similar decreasing trend in calculated shear values with radius of curvature as the *x*-direction characterization curves was observed in the Figure 3-38-Figure 3-40, with the exception of an increase in peak calculated value in the positive-*y* shear direction at 30 mm.

Radius of Curvature (mm)	Shear Displacement (mm)	Calculated Shear Value
100	0.8	15.72
30	0.8	16.88
10	0.8	14.04
100	-0.8	-33.95
30	-0.8	-31.29
10	-0.8	-24.35

Table 3-8: Calculated Shear Values (Using Equation 1) for y-Direction Characterization Curve Plots

The curvature observed in the characterization curved response to *y*-direction is most likely a result of the shear displacement being along the axis of curvature, rather than perpendicular to it. This effect is also seen in the $\Delta C/C_0$ data displayed in Figure 3-24, Figure 3-30, and Figure 3-34 where one taxel exhibited a much more dramatic change in signal in response to the applied shear. The most likely hypothesis for the significant deviations from the *y*-direction best fit lines in Figure 3-38-Figure 3-40 is a misalignment between the flat indenter used and the curved sensor surface. It is probable that the decreased surface area of the curved sensor and the increased tension on the sensor surface due to the curvature exacerbate any misalignments that may be present. An alternative but not exclusive explanation for the unevenness in sensor values is the asymmetry in sensor components between the two sides of the device in the *y*-direction. By design of the sensor, all of the leads leave on the bottom of the sensor body, near taxel 4. With the curvature of the sensor, there may be some unanticipated warping of the material in response to shear which may be reflected in the taxel signal disparity.

One factor observed in the characterization curves that is shared between both the x- and y-direction measurements is a decrease in signal sensitivity at tighter radii of curvature, reflected in lesser peak values in one or both positive and negative shear directions. A maximum peak calculated value decrease of approximately 38% was observed in the x-direction and 28% in the y-direction. The most likely mechanism behind this decrease is the increased overall surface tension of the flexible sensor as the radius of curvature is decreased. Additionally, as the curvature radius is decreased, the contact area between the sensor and the flat indenter used will also decrease for the same vertical displacement. This means that a larger indenter displacement is needed to result in the same applied normal force, which is used as a repeatable baseline for the shear measurement start point. While this starting force is regulated, the change in normal displacement may be affecting the shear sensitivity of the sensor.

Conclusions

Based on the data collected from these characterization experiments, the new flexible sensor design is sufficiently functional to mark a milestone in the development of the sensors towards real-world robotics applications. A flexible PCB fabricated out of copper and double-sided tape was integrated into the existing sensor architecture, allowing for persistent and reliable function in curvatures with radii of 100 mm to as small as 10 mm. This flexibility will allow the sensors to potentially be implemented in a variety of human-mimetic sensing applications, such as placement in nursing robot human-interface areas, prosthetic hands, or biomimetic robotic joints. It was identified that the curvature imparted to the sensor has a significant effect on both the sensor baseline signal and the overall response to pressure and shear. This means the sensor will require some calibration or other firmware accommodation for applied curvature in its current state, and will require further work in the future to limit the effect.

In addition, the basic indenter shape was found to significantly impact the response of the sensor in terms of both sensor $\Delta C/C_0$ and force required for a given shear displacement. It was found that each indenter shape produced different signal patterns, which shifted based on the applied curvature to the sensor. This represents another area of the flexible sensor which requires further investigation if the sensor signal is expected to be even across object shapes. However, if the sensor response may be ‘tuned’ to the different object shapes, the indenter effect may be used as a design advantage. Regardless, the new sensor design allows for the consistent measurement of contact forces despite the general shape of the object being contacted.

Chapter 4: High Dynamic Range Sensor

Another component identified for further development on the base sensor used is the working range. The previously designed sensors exhibited a sensing range of approximately 0.1-15 N for normal force. This range is identified as insufficient to appropriately match the sensing of human skin, a specification basis of tactile sensing in robotics [51]. In particular, the human hand skin tactile sensing the sensor aims to emulate generally separates the force into four different categories [52]. The sensor this work builds off of only has one distinct force sensing modality throughout its overall range, so this work aims to increase the distinct regions to two, either low-force pressure and shear or high-force pressure. This chapter presents a version of the sensor previously designed by *Sarwar et al.* capable of force measurement in the approximate range of 0.05-50 N noncontinuous, with two distinct force sensing ranges for applied normal forces.

To increase the operating range of the sensor while still keeping it firmly within the skin-like range, two approaches to the dielectric structure were explored in this thesis. These approaches are displayed in Figure 4-1, either A) a two-electrode layer design or B) a four-electrode layer design. The goal of either approach was to create a dynamic structure in one sensor footprint that provides two distinct dielectric stiffness modalities. This is done to maintain high sensitivity in the sensor while creating a region that is still noticeably compressible under very large force; architectures that are weaker to applied force by definition have a lower overall Young's Modulus, therefore reaching a 'maximum compression' point where the sensor capacitive signal ceases to respond measurably to force. The structural Young's Modulus is controlled in these architectures through both the volume ratio of Ecoflex^{TM} to air, and through the overall shape of the dielectric pillars; it has been found that pyramid pillars produce more sensitive elastomer-based devices than square pillars, which is used to maximize the low-force range in both sensing design types [44].

Each of these two approaches are viable for the development of a sensor with a wide dynamic range, but have their own unique difficulties to work through. The primary point of difficulty for the single-layer sensor design is complexity in fabrication, as the sensors are fabricated with a mold-based process that limits the shapes available for these designs. The double-sensor design requires more complex hardware due to the additional electrodes, and has greatly increased height due to sequential dielectric pillar layers. An additional design was considered but not pursued for this thesis involving a parallel or interspersed sensor design with laterally positioned low-force and high-force regions. This design was not thoroughly considered in this thesis as horizontal space was identified as more valuable in sensor design than vertical space for the industry application.

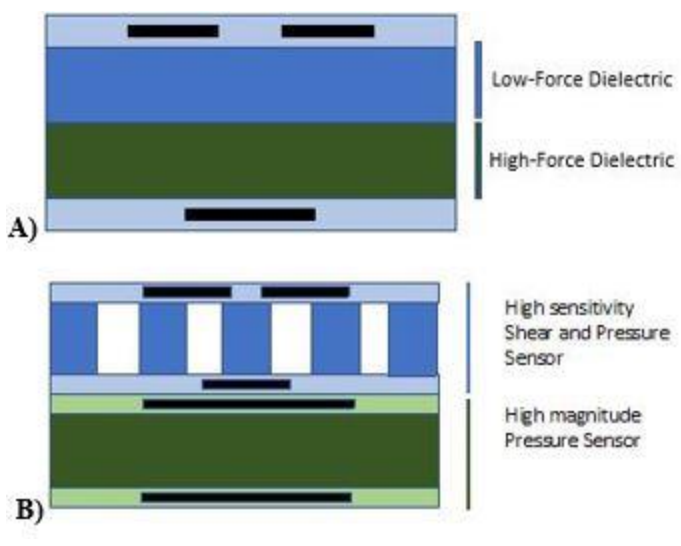

Figure 4-1: High-Force Sensor Design Concepts, A) Single-Layer Four-Taxel Configuration, B) Two-layer Six-Taxel Configuration

Sensor pressure and shear response was tested using the setup described previously, specifically a combination of a load cell, 3-axis low-force stage, and single-axis high-force stage.

The data collected from the sensor experiences small human error due to a variety of factors; low-force human error is primarily due to small misalignment of the sensor and unevenness in the sensor surface, and high-force human error is primarily due to the manual control of the high-force stage. These two force rangers are separated due to limitation of the characterization setup used, as there was no suitable setup readily available that could provide both the force range and z-axis stroke length required for force application in the 10-50 N range. These tests were done on a basic 4-taxel architecture which only measures pressure and shear to simplify the analysis and better isolate the dielectric architecture. For all tests in this section the sensor was mounted on a 3D printed frame made out of PLA, which provided both an enclosed area for the attached PCB and a staging surface for the sensor.

Each sensor design described in this section was characterized with both a set of low-force pressure and shear measurements and a high-force pressure only measurement. For each set of characterization data acquired, an initial normal force of 0.1 N was applied to reduce the effect of any small surface abnormalities on the sensor signal recorded and provide a stable and repeatable starting point for all of the measurements done. The low force characterization consists of one set of repeated applied normal force readings from the initial start point of 0.1 N to a final force of 1.6 N across a 14x14 mm area for a total pressure of approximately 8.16 kPa, in addition to shear displacements between 0.2 and 0.8 mm in the x- and y-directions. High force characterization tests were done using a manually-controlled stage to achieve peak forces of 50 N over a 45-60s period of time. Due to the high expected compression at these peak forces inhibiting shear function and limitation in the characterization setup, no shear testing is done at higher forces than 1.6 N.

Single-Layer Design

The first approach to increase the dynamic force range is through introduction of novel dielectric architectures to the original base sensor. These new designs utilize non-uniform vertical cross sections to enhance both the low-force sensitivity and high-force range. The upper part of each architecture is designed to be softer than the original base sensor, while the lower portion is stiffer than the original. This is primarily done by adjustment of the elastomer-air ratios of each component of the dielectric pillar shape, with a lower ratio for the upper portion and greater ratio for the lower one. The upper portion of the pillar is the focal point of the single-layer design; the upper limit of the high force range was found in preliminary experimentation to require the maximal footprint allowed by the sensor fabrication process in the lower pillar portions, so they were not varied in design.

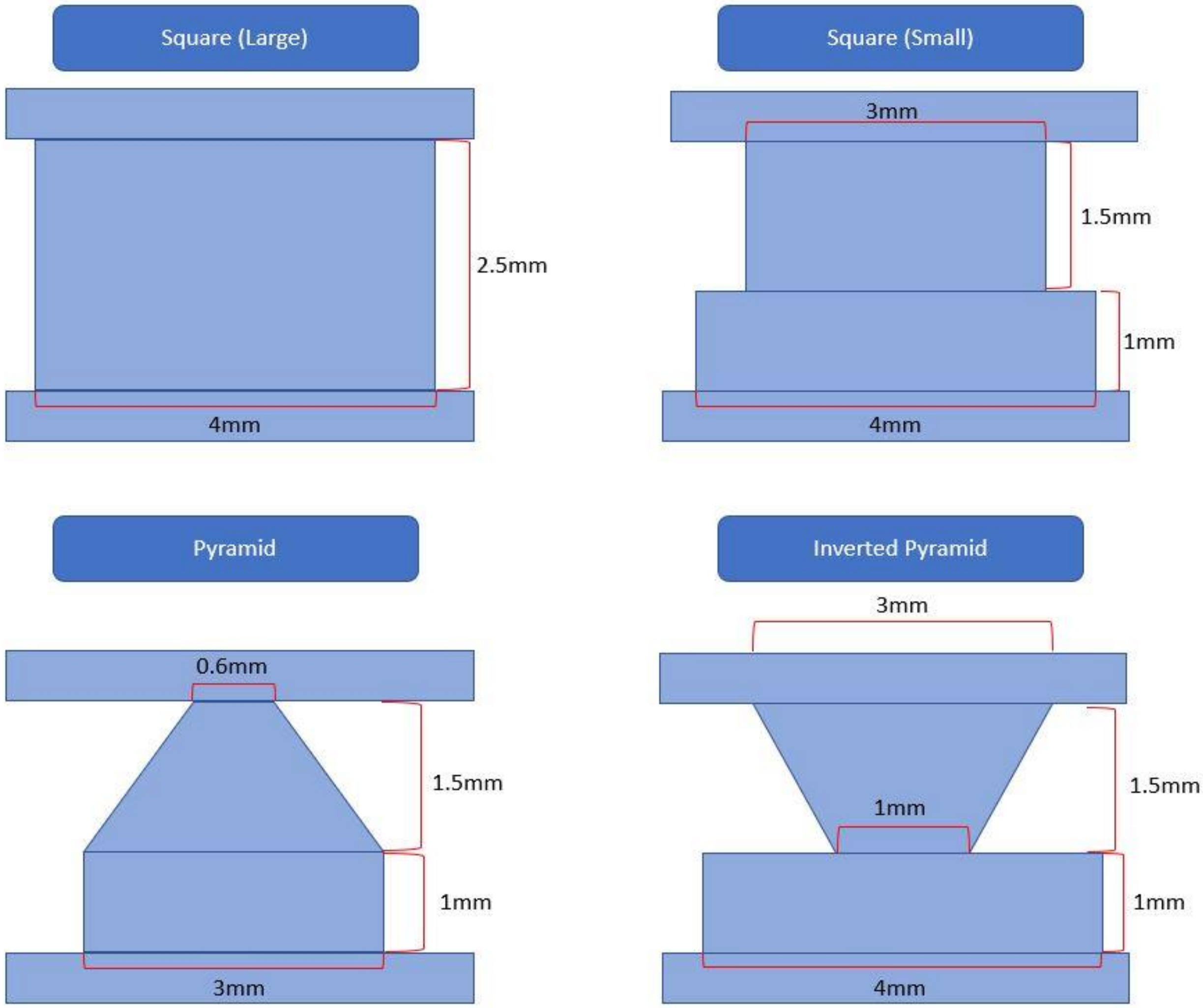

Figure 4-2: Single Layer High Normal Force Range Sensor Architecture Diagrams for Architectures Examined (Large Square, Small Square, Pyramid, Inverted Pyramid)

The architectures tested for the single layer high-range sensor are displayed in Figure 4-2, from left to right: large square, small square, pyramid, and inverted pyramid. This design allows for three major stages of normal force compression while maintaining the skin-like upper layer in the sensors designed by *Sarwar et al.* These layers are light initial touch, in which only the upper electrode-carrying portion of the sensor is displaced and the detection is analogous to light touch detection through fine hairs at the skin surface. As normal force is increased into the estimated 0.1-15 N range, each architecture will move into a moderate force range in which the upper architecture is engaged but the lower architecture is not deformed. Finally, in the estimated large force range of 15-50 N, the upper architecture will become completely compressed and the majority of force-induced deformation will be transferred to the stiffer lower architecture.

Initial high-force tests were performed up to 40 N of applied force for verification of satisfactory architecture performance for each of the four designs considered. This initial point was chosen due to the rapid increase in stiffness of the Ecoflex^{TM} structure in the >40 N range caused by both architectures reaching relatively full compression. This rapid increase caused concerns with the characterization setup, as sharp increases in force could easily damage the load cell or attached stage components. The response of each architecture to 40 N of applied normal force is shown in Figure 4-3; each architecture performed satisfactorily up to this initial 40N range, moving them all forwards into low-force pressure and shear testing.

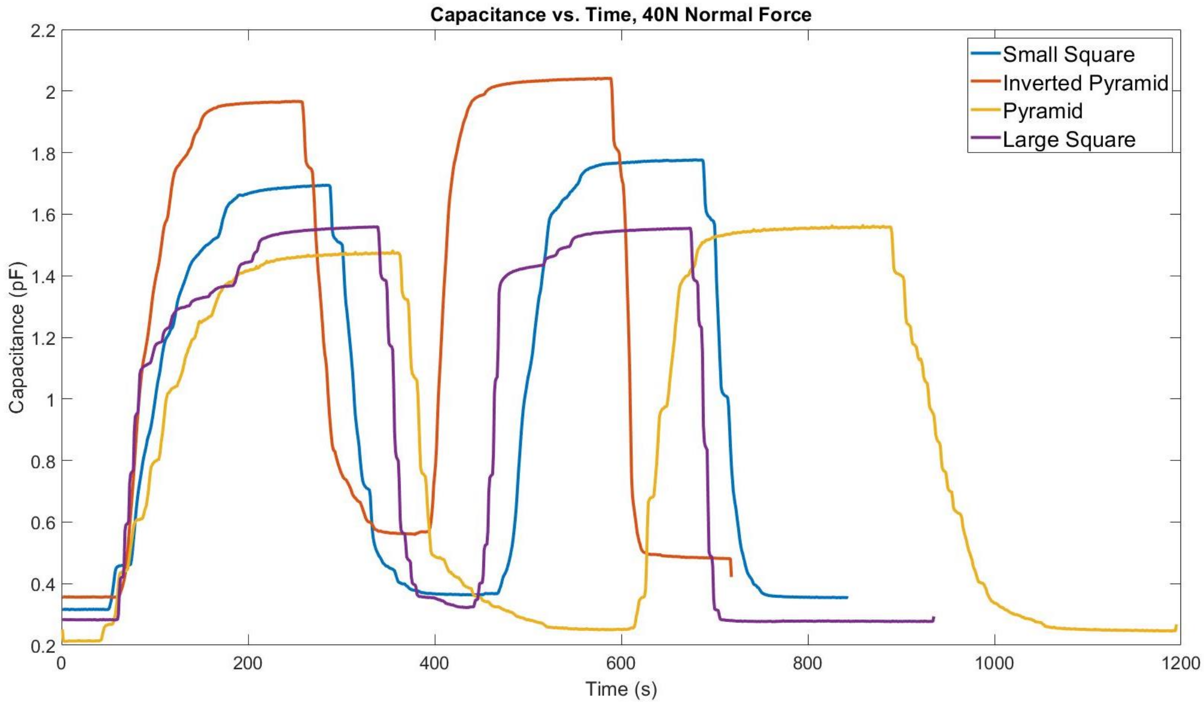

Figure 4-3: Test Architecture Capacitive Response Comparison at 40 N Applied Force, 4-Taxel Average

Given the satisfactory result of each architecture considered at the 40 N test force, the next stage in characterization for the single layer high-range sensor was low-force sensitivity to pressure and shear. Pressure was tested by applying an initial force of 0.1 N to minimize the minimal-force compression effect in the top layer, then repeated sequences of 1.6 N peak force. Shear was tested by applying a 1.6 N normal force to each sensor, then applying sequentially increasing lateral displacements. Sensitivity was assessed by peak sensor signal for each architecture, with the measured sensitivity being directly correlated to the capacitive signal change on applied force. Shear was tested in all directions (+/- x and y); for brevity, only a single direction is presented in this chapter for each sensor, and the others are included in Appendix C

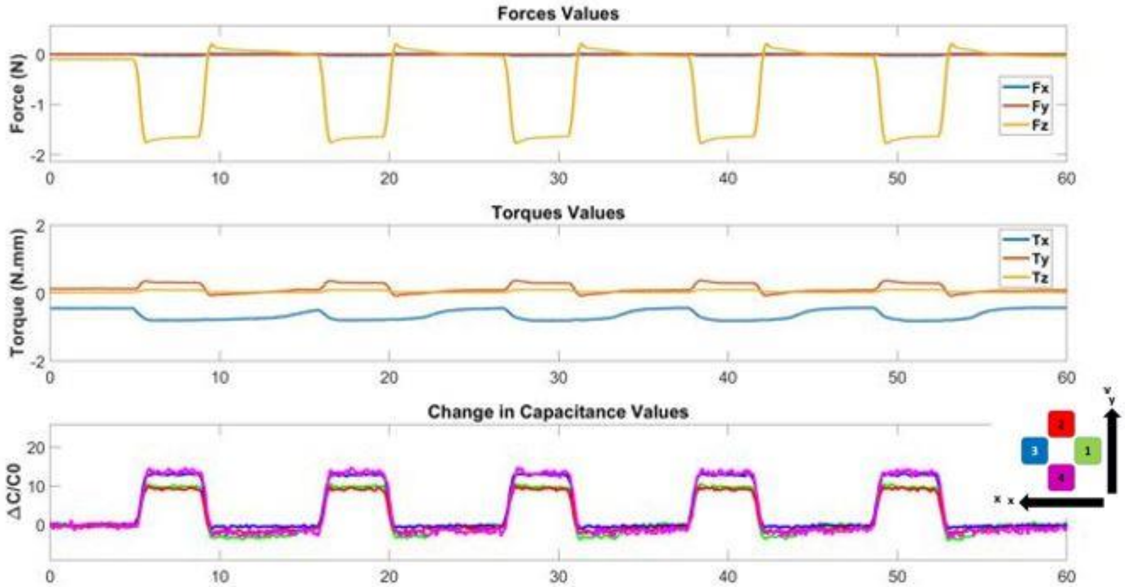

Figure 4-4: Large Square Pillar Single Layer High Normal Force Range Sensor, 1.6 N Repeated Applied Normal Force

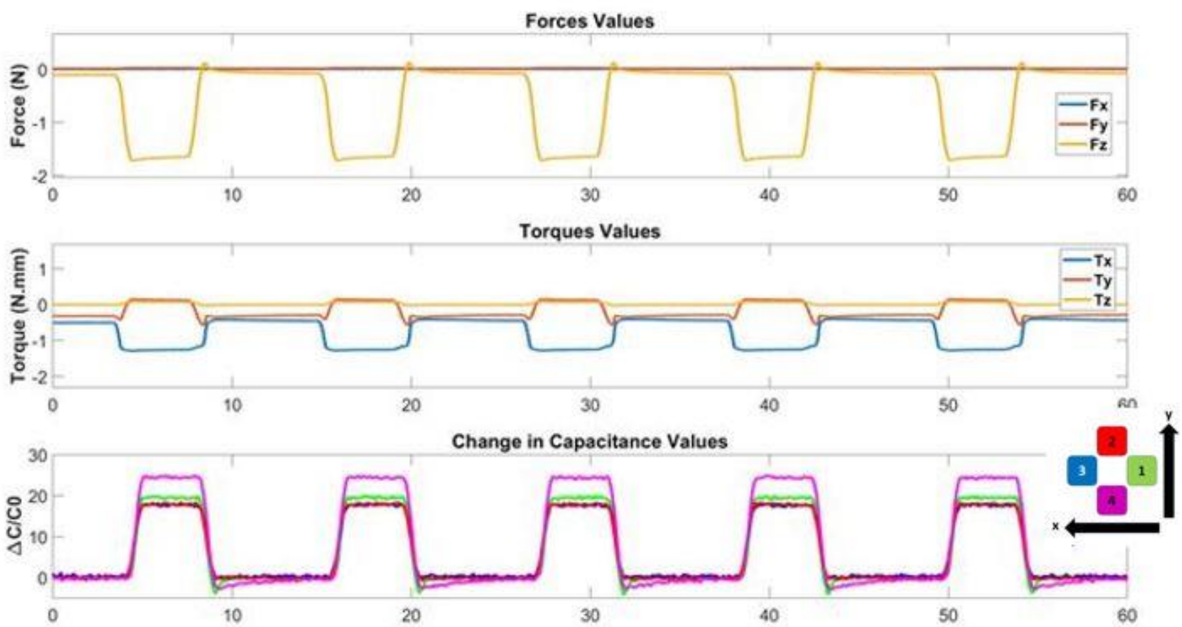

Figure 4-5: Small Square Pillar Single Layer High Normal Force Range Sensor, 1.6 N Repeated Applied Normal Force

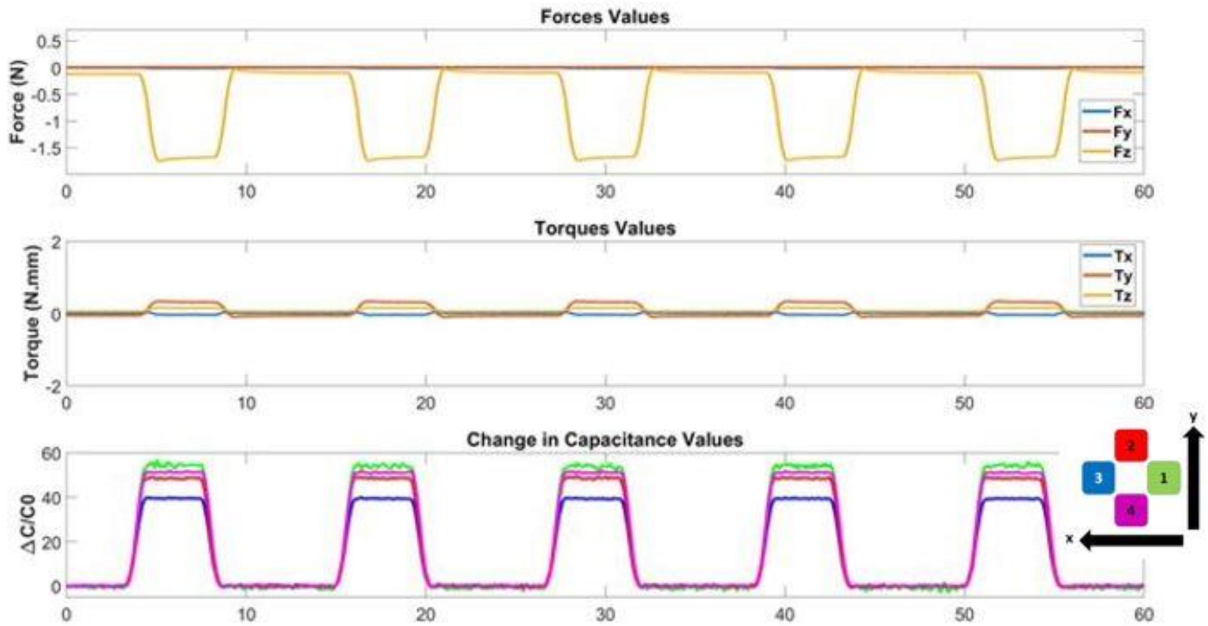

Figure 4-6: Pyramid Pillar Single Layer High Normal Force Range Sensor, 1.6 N Repeated Applied Normal Force

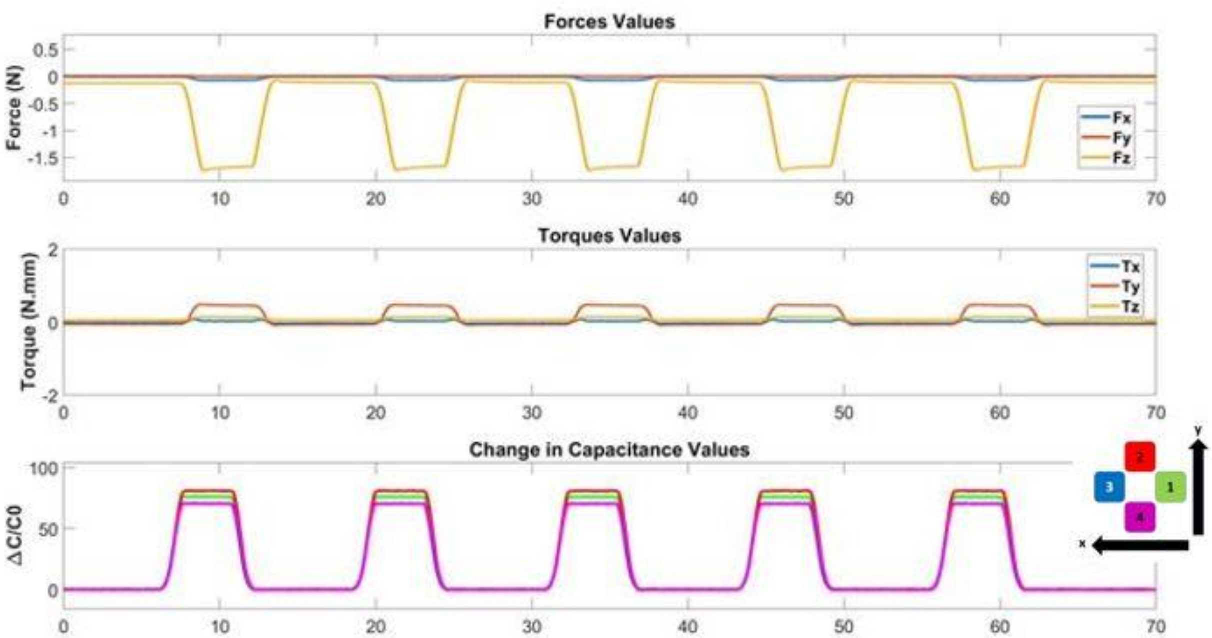

Figure 4-7: Inverted Pyramid Pillar Single Layer High Normal Force Range Sensor, 1.6 N Repeated Applied Normal Force

The sensor responses to 1.6 N of applied normal force for each single layer high-range architecture tested are shown in Figure 4-4 (large square), Figure 4-5 (small square), Figure 4-6 (pyramid), and Figure 4-7 (inverted pyramid). The inverted pyramid upper architecture provided the greatest signal sensitivity to applied force, followed closely by the pyramid architecture. Sensor electrode design, characterization setup components, and overall pillar design were kept consistent besides the shape of the upper dielectric pillar to isolate it as the main factor controlling normal force sensitivity of the architecture. From the data presented in Table 4-1, the inverted pyramid was found to be the most sensitive architecture as defined by $\Delta C/C_0$, with an average value of approximately 46.56/N, while pyramids also provided a relatively overall high sensitivity at approximately 30.17/N. These values at 1.6 N were over double either square architecture, so the pyramidal upper architectures were highlighted for their greatly enhanced low-force pressure response.

Sensor Upper Architecture	Average Signal at 1.6 N Normal Force (%$\Delta C/C_0$)
Large Square	11.36
Small Square	19.77
Pyramid	48.27
Inverted Pyramid	74.5

Table 4-1: Average Peak Signal of Single Layer High Normal Force Range Sensors at 1.6 N Applied Normal Force over Four Cycles

It is notable that the pressure applied and signal response are consistent across each of the five 1.6 N steps for each sensor architecture, indicating little in the way of creep or other unwanted viscoelastic effects. These effects have been noted by previous work on similar sensors by *Sarwar et al.*, with sensors experiencing noticeable creep within up to the first 1-3 normal force cycles depending on the sensor dielectric architecture design. In those sensors, the baseline signals seen in all sensor taxels tend to increase across steps as viscoelastic effects limit the recovery of the dielectric pillars at the zero-force point. The most likely hypothesis for this lack of creep is the dual-layer pillar design allowing for better force absorption and bounce-back in the overall architecture. In previous sensors, the base layer of the sensor was thin (<0.75 mm total) and stiff due to proximity to both the stiffer carbon black-Ecoflex™ electrode layer and the rigid PCB. This forces the Ecoflex™ layers of the dielectric to get closer to full compression at low forces, increasing the time to revert to the initial position in between steps. In the new two-stage architecture the lower portion of the pillars prevents this from occurring, allowing force to be spread through the facets of the architecture in a manner that better facilitates sensor recovery post-compression for low forces.

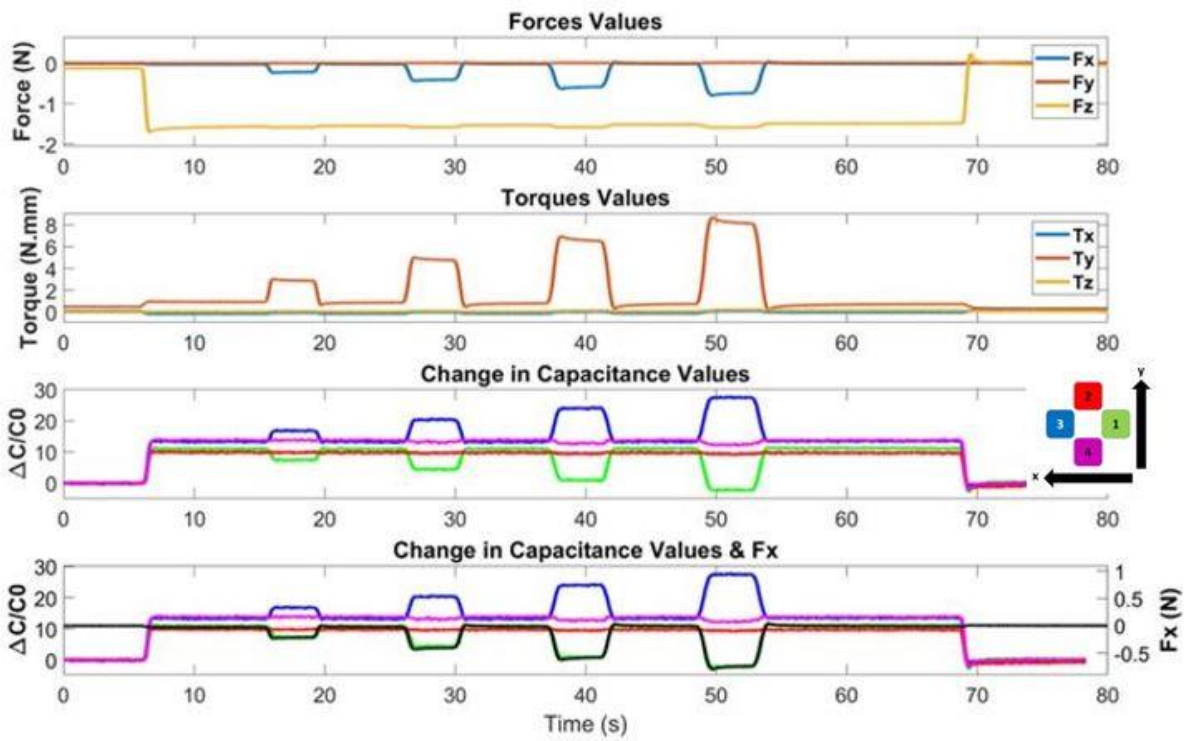

Figure 4-8: Large Square Pillar Single Layer High Normal Force Range Sensor, Negative x-Direction 0.2 mm to 0.8 mm Applied Shear Displacement

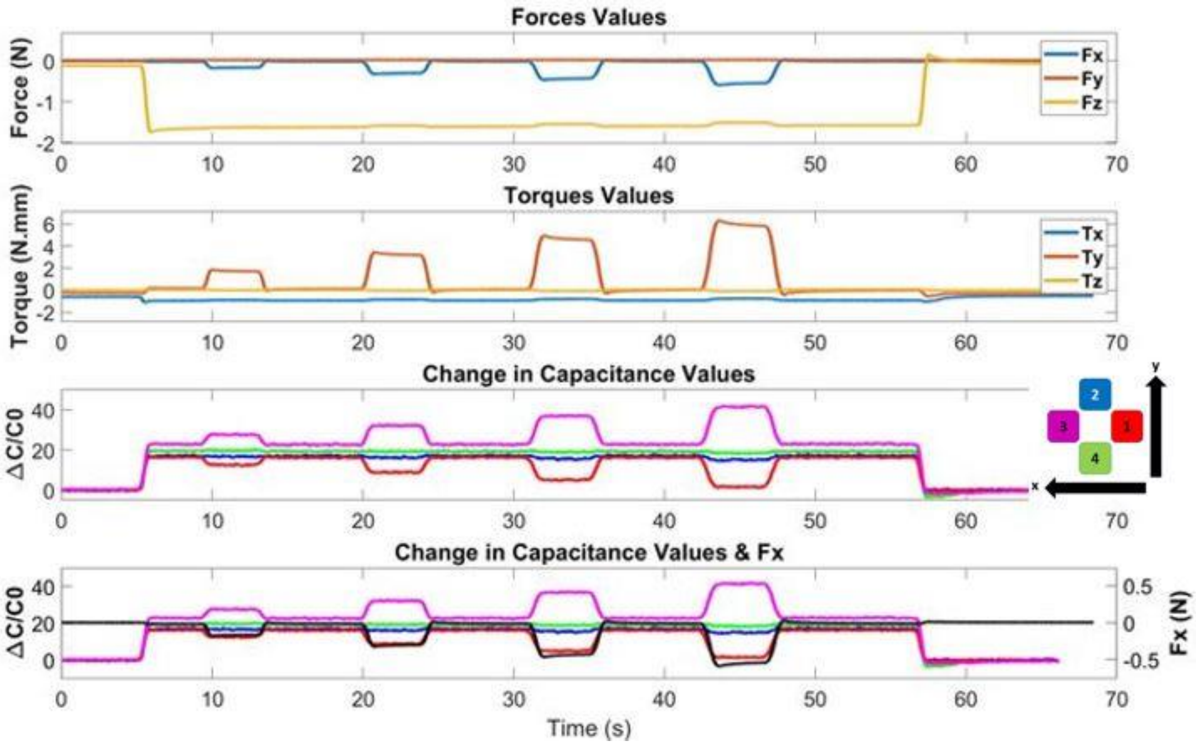

Figure 4-9: Small Square Pillar Single Layer High Normal Force Range Sensor, Negative x-Direction 0.2 mm to 0.8 mm Applied Shear Displacement

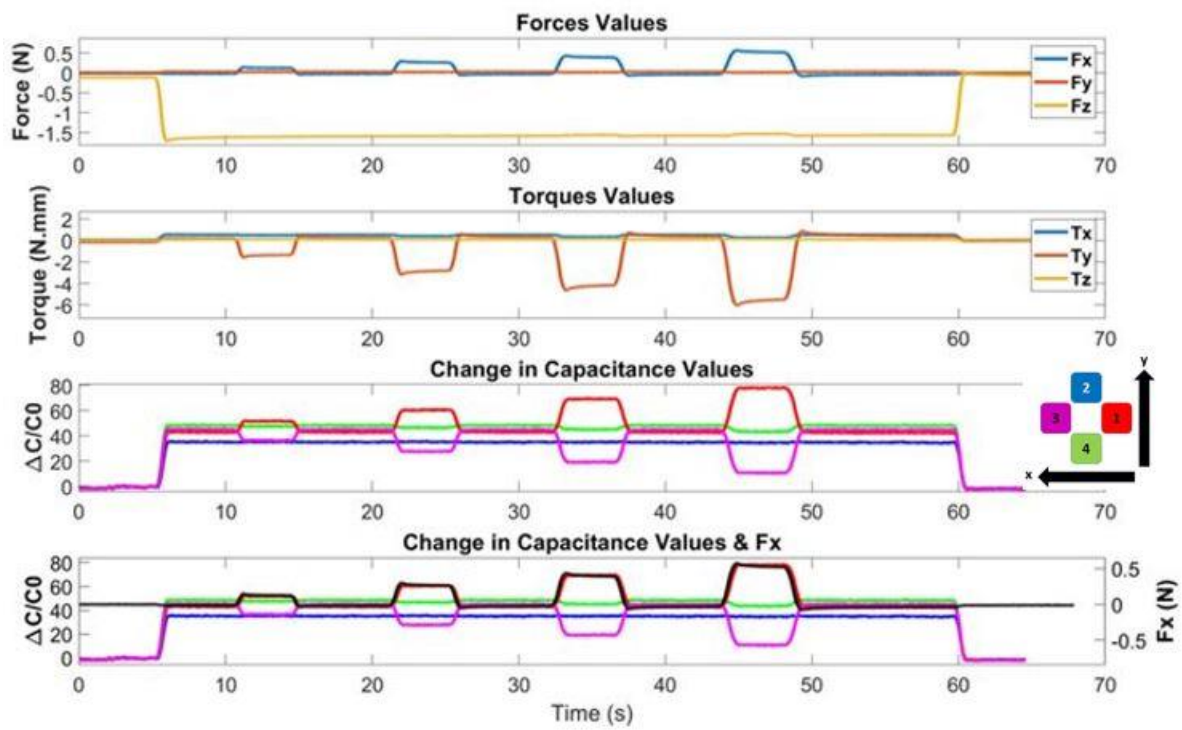

Figure 4-10: Pyramid Pillar Single Layer High Normal Force Range Sensor, Positive x-Direction 0.2 mm to 0.8 mm Applied Shear Displacement

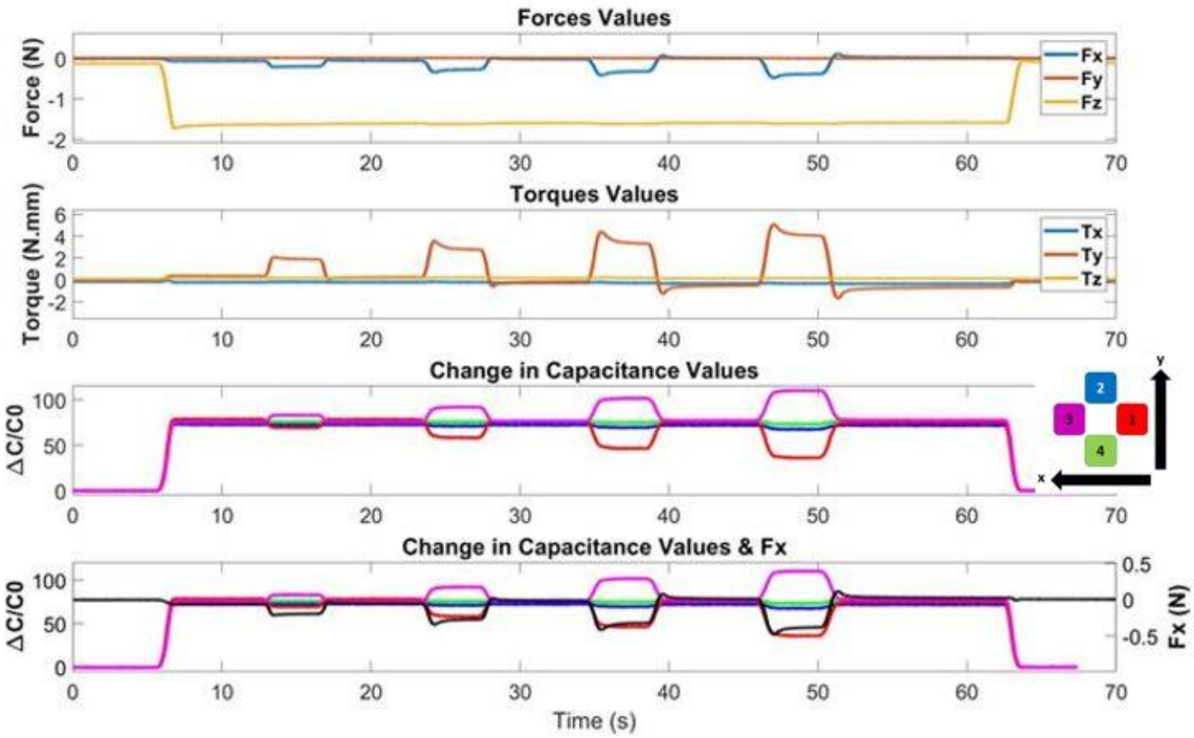

Figure 4-11: Inverted Pyramid Pillar Single Layer High Normal Force Range Sensor, Negative x-Direction 0.2 mm to 0.8 mm Applied Shear Displacement

Shear response is assessed in a similar manner, with estimated overall sensitivity provided by maximal sensor response to a given shear displacement. In addition, as shear application is displacement-controlled rather than force-controlled in these experiments, force at maximum displacement is used as a contributor to overall architecture sensitivity. As with the pressure testing described above, the only parameter changed across sensors tested was the upper layer of the dielectric architecture. All architectures were tested at four different applied displacements in 0.2 mm increments from 0.2 mm to 0.8 mm using a 14x14 mm square indenter. This shear characterization is done in the +/- x and y directions, but due to data symmetry and for brevity only one axis is presented in this chapter; the rest are considered in the discussions presented here, but are presented in Appendix C.

The pyramid and inverted-pyramid architectures displayed the highest signal sensitivity to shear forces as shown in Table 4-2, similar to the findings for pressure sensitivity described above and the characterization data presented in Figure 4-8-Figure 4-11. A sensitivity of approximately 56.4/mm was observed in the pyramid architecture and 40.7/mm for the inverted-pyramid architecture at the maximal shear displacement of 0.8 mm. These values are over double the sensitivities observed in either square-based architecture tested, showing that the either pyramid architecture is a good candidate for further examination in the high-force sensor design. The pyramid-based architectures also tended to show a lower required force to reach the 0.2-0.8 mm range, with a maximum force of approximately 0.4 N needed to reach 0.8 mm shear displacement for the inverted-pyramid architecture compared to approximately 0.7 N needed for the large square architecture.

Sensor Upper Architecture	Average Signal at 0.8mm Applied Shear (%$\Delta C/C_0$)
Large Square	10.59
Small Square	19.04
Pyramid	45.12
Inverted Pyramid	32.54

Table 4-2: Average Signal Change in Single Layer High Normal Force Range Sensor at 0.8 mm Applied Shear Displacement

Two mechanisms are most likely to be the explanations for the increased sensitivity to shear in the pyramid architectures compared to the square ones. The first is a volume-sensitivity relationship, where decreased elastomer volume leads to increased sensitivity due to the architecture having a higher overall structural compliance to applied forces. This increased compliance is due to the increased volume of free-moving air present in the dielectric architecture which provides no structural support. If the dielectric architecture general shape is held approximately the same while elastomer volume is decreased, it is expected that the stiffness of the overall elastomer body to both pressure and shear will decrease. While the pillar cross-sectional shape does play a role in determining overall pillar stiffness to applied shear forces, it is expected that architectures with higher volumes of elastomer material will have a higher equivalent Young's Modulus.

The second proposed mechanism for increased susceptibility to shear force is a 'tipping effect'. Theoretical approaches to the sensor signal calculations assume an idealized displacement model for the dielectric architectures, in which the pillars and electrodes shift laterally with negligible vertical or circular displacement. This has previously been a workable assumption for square and X-shaped architectures employed by *Sarwar et al.* [27], but is likely to not be properly applicable to the novel designs with non-uniform cross sections being examined. The pyramid-based architectures have angled edges to reduce overall elastomer volume while maintaining structural integrity. These angles result in a significant difference between the footprint of the top and bottom of the pyramidal pillar section, compared to the monotonic cross-section of the square pillars. Both the pyramid and inverted-pyramid designs may localize the material strain of the pillars when sheared, and introduce a tipping or tilting action to the shear displacement, pulling vertically on the top and bottom electrode layers of the overall sensor. As capacitive sensors are responsive to changes in plate separation distance, this 'tipping effect' may be inadvertently bringing the sensor electrodes closer together vertically, adding 'sensitivity' to these signals that is not fully representative of the shear displacement and increasing the overall signal observed.

Single-Layer High Range Sensor Characterization Curves

Characterization curves are used to further examine the shear response of the single layer high-range dielectric architectures. The pyramid and inverted pyramid architectures are chosen for characterization curve analysis as they exhibited significantly higher sensitivity to shear compared to the small square and large square architectures. These characterization curves compare the calculated shear to the actual shear imparted by the characterization apparatus. An ideal characterization curve displays a linear relationship in the in-plane taxels which has a x-intercept at zero, with the out-of-plane taxels exhibiting no change from zero.

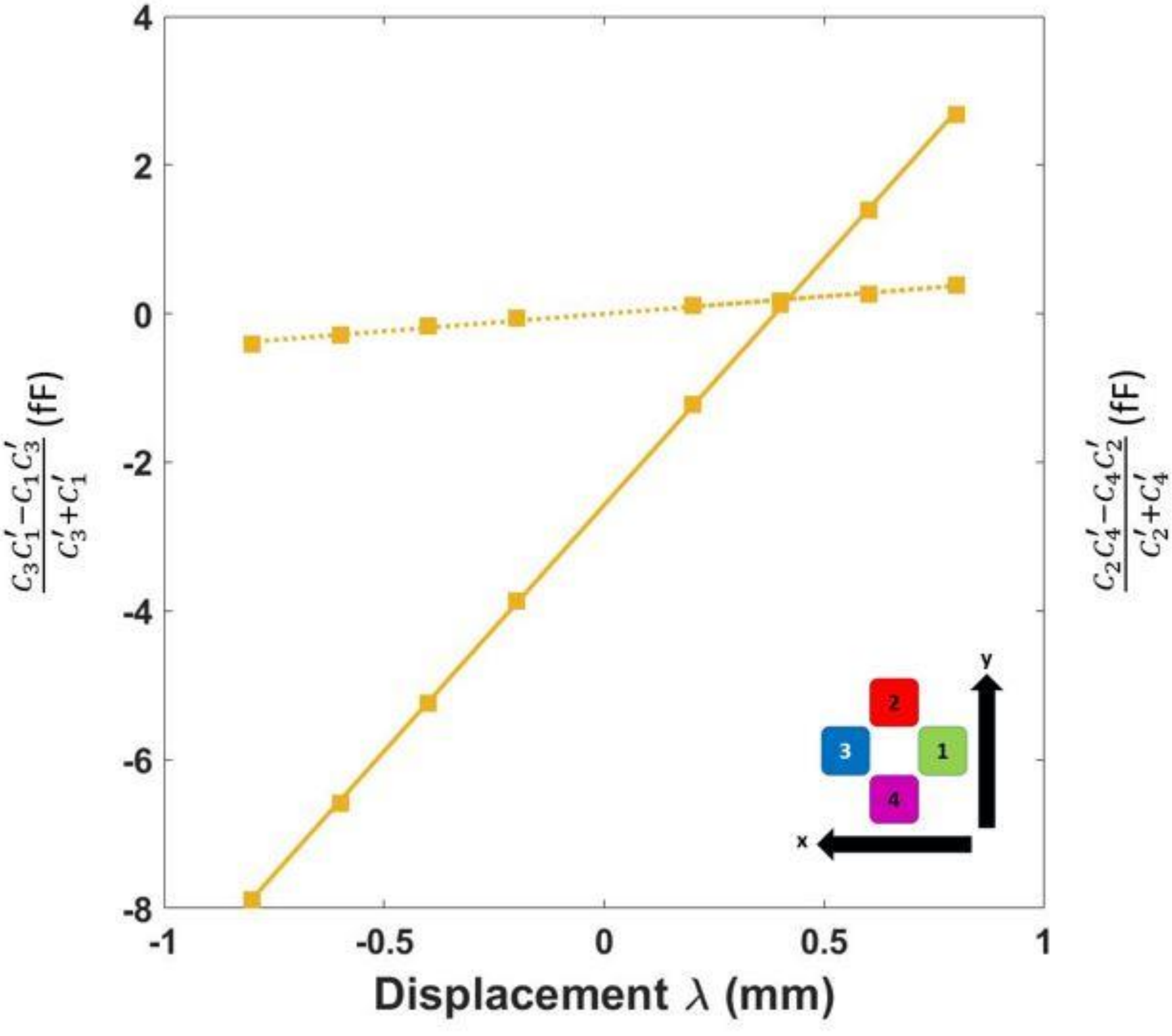

Figure 4-12: Demonstration of x-Direction Shear Performance of High-Range Pyramid Pillar Sensor, including Separation of X (Solid Best-Fit Line) and Y (Dotted Best-Fit Line) Shear Responses. Shear Displacement is Plotted vs. the Differential Capacitance in the X and Y Directions (Left, X Difference, Right, Y Difference).

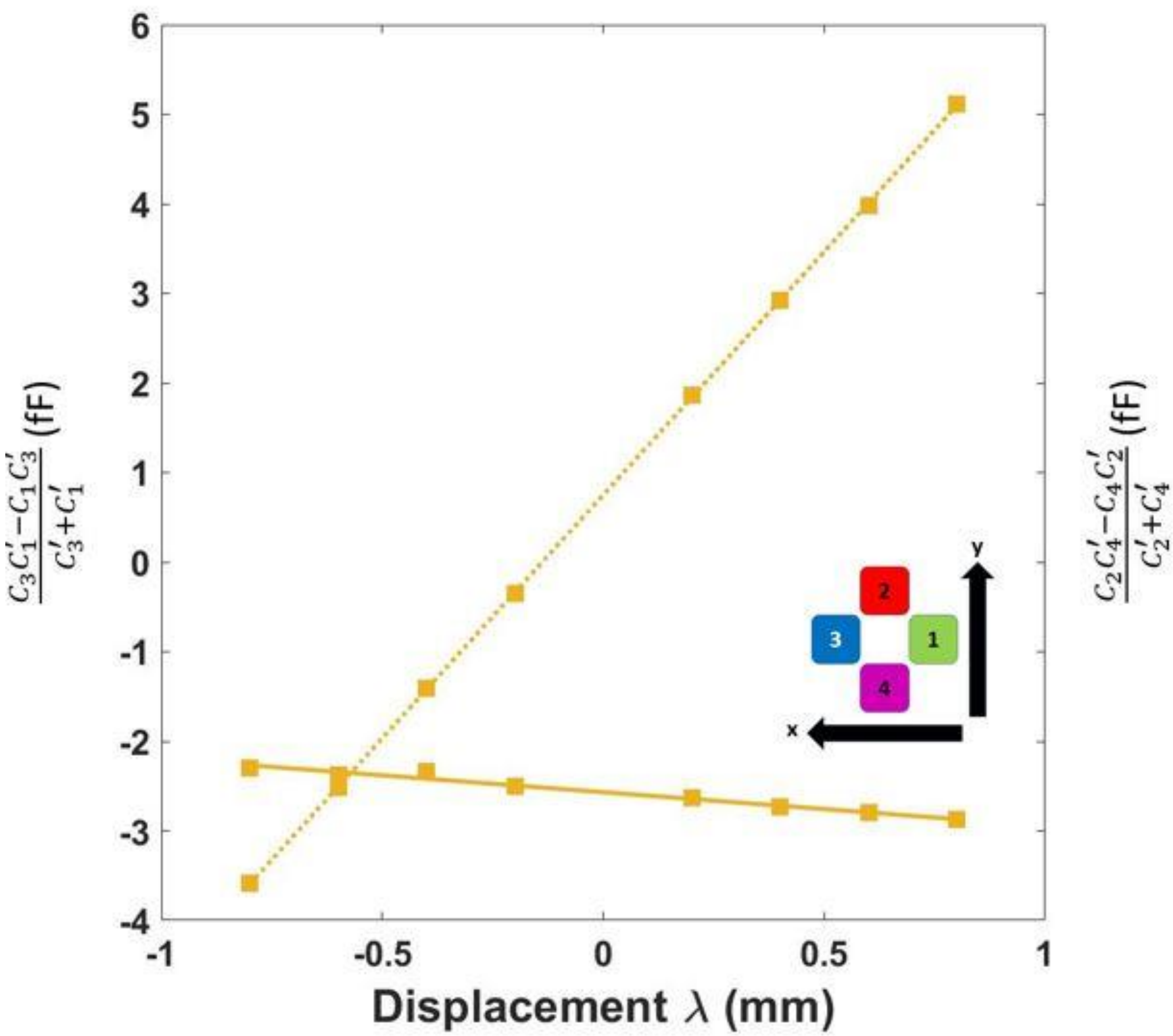

Figure 4-13: Demonstration of y-Direction Shear Performance of High-Range Pyramid Pillar Sensor, including Separation of X (Solid Best-Fit Line) and Y (Dotted Best-Fit Line) Shear Responses. Shear Displacement is Plotted vs. the Differential Capacitance in the X and Y Directions (Left, X Difference, Right, Y Difference).

The pyramid pillar dielectric exhibits a highly linear shear response in both the *x*- and *y*-directions, demonstrating a highly predictable shear response. The shear response for the out of axis taxels also produce a relatively flat response to the applied shear, displaying minimal signal overlap and a strong differentiation between shear directions. A notable component of these characterization curve plots is a significant offset at a shear of zero for the in-axis taxels in the *x*-direction, and both the in-axis and out-of-axis taxels for the *y*-direction. In particular, the *x*-axis taxels, 1 and 3, have a x-intercept of approximately -2.5 pF when either in- or out-of-axis. The most likely cause for this offset in calculated shear values is a disparity in C_0 values, as the offset is present in the *x*-direction regardless of shear behavior. This may be due to an uneven compression response of the dielectric, due to the differing cross-sectional-areas of the dielectric pillars. As the architectures are compressed, any lateral shifting or uneven distribution of force to the pillar-pillar intersection may cause an unexpected change in the measured capacitance values. Overall, disregarding the offset, the pyramid pillar dielectric exhibits a well differentiated, reasonably linear response to applied shear.

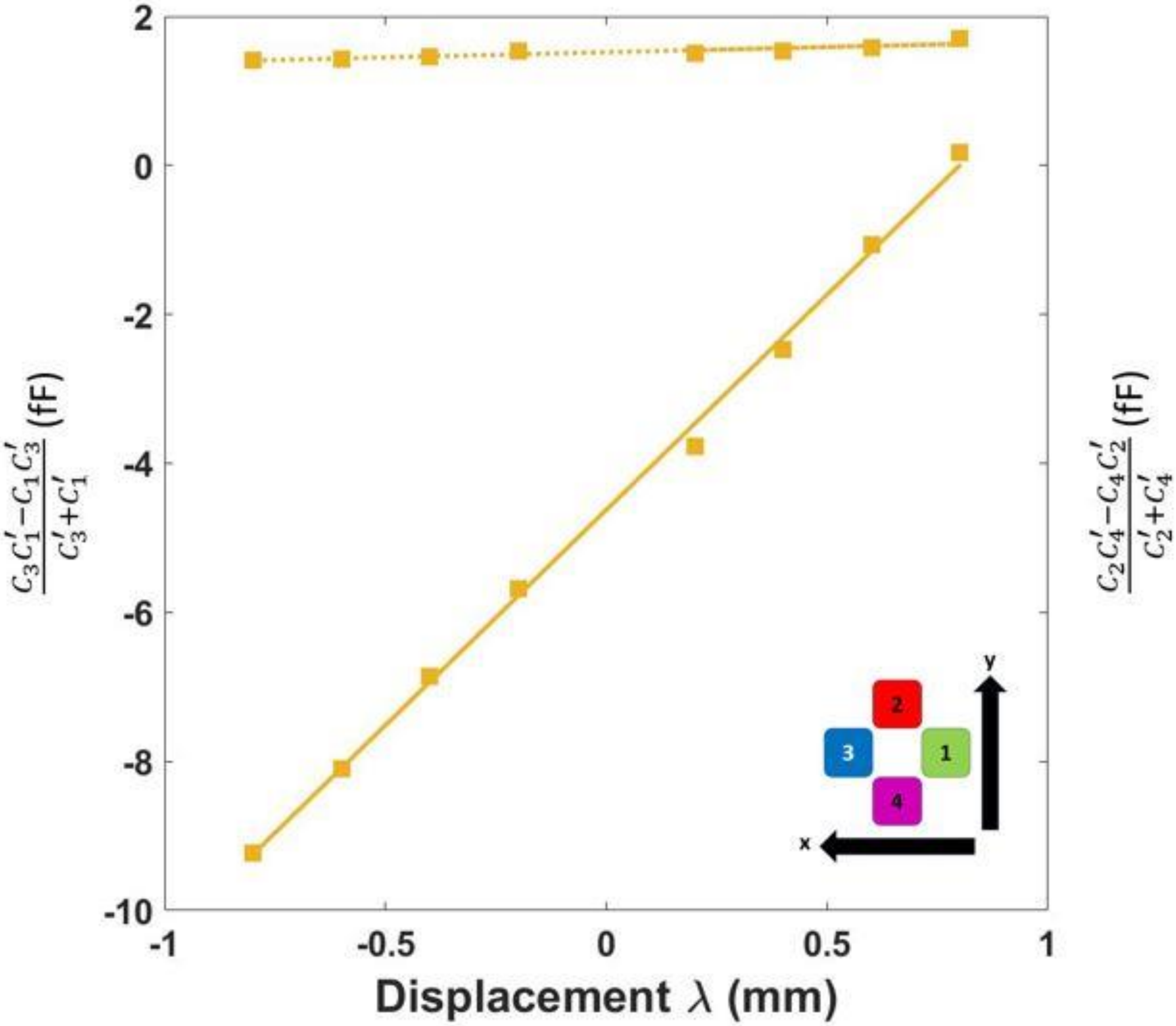

Figure 4-14: Demonstration of x-Direction Shear Performance of High-Range Inverted Pyramid Pillar Sensor, including Separation of X (Solid Best-Fit Line) and Y (Dotted Best-Fit Line) Shear Responses. Shear Displacement is Plotted vs. the Differential Capacitance in the X and Y Directions (Left, X Difference, Right, Y Difference).

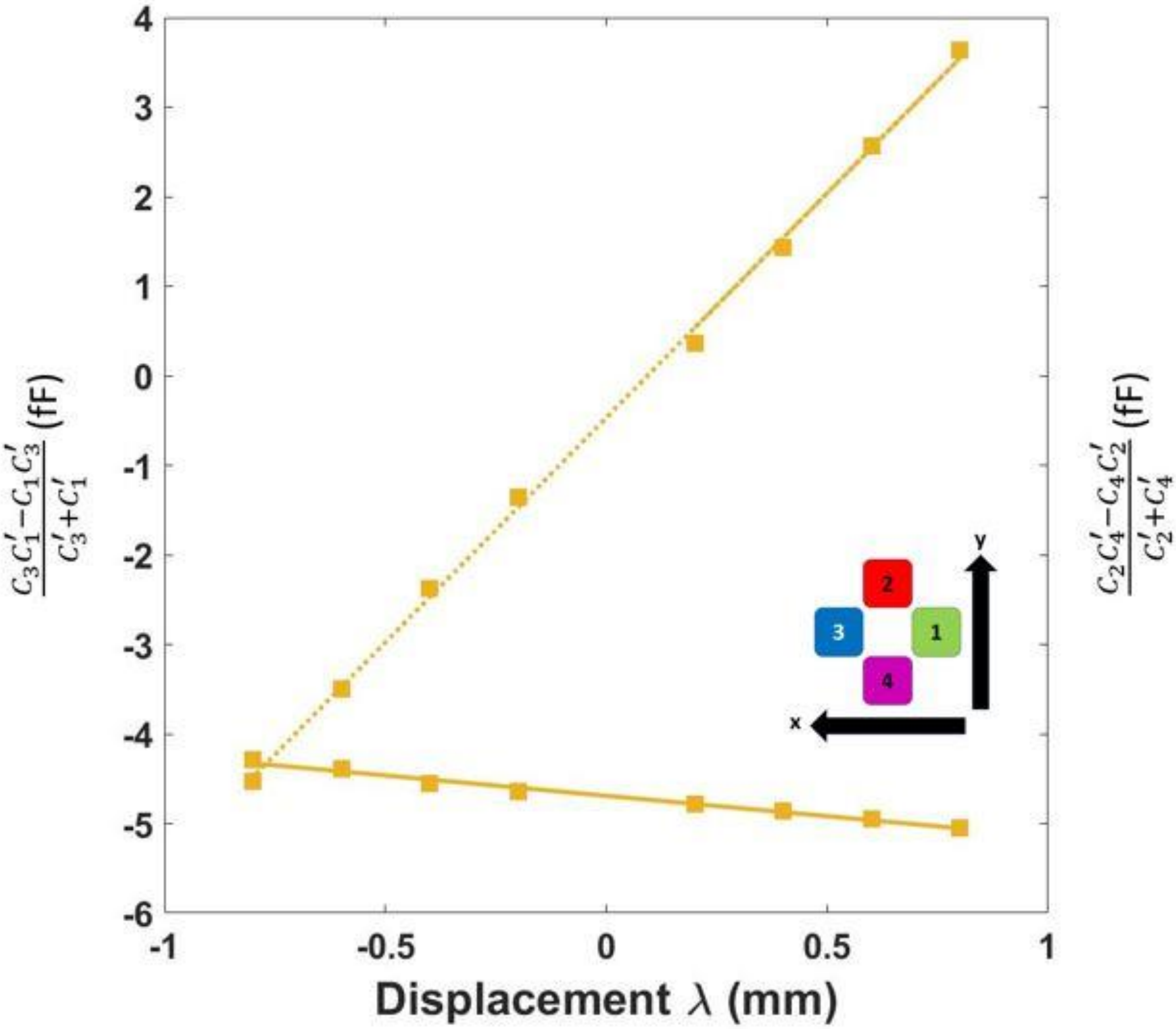

Figure 4-15: Demonstration of y-Direction Shear Performance of High-Range Inverted Pyramid Pillar Sensor, including Separation of X (Solid Best-Fit Line) and Y (Dotted Best-Fit Line) Shear Responses. Shear Displacement is Plotted vs. the Differential Capacitance in the X and Y Directions (Left, X Difference, Right, Y Difference).

The inverted pyramid dielectric design displays a strong linear response to shear in both the *x*- and *y*-directions as shown in Figure 4-14 and Figure 4-15, but experiences the same offset issue as seen in the pyramid architecture. In the *x*-direction shear a significant amount of offset is displayed in the in-line taxels, with a relatively smaller offset exhibited by the out-of-line taxels. This offset may be the result of small inconsistencies in pillar compression due to the normal force exerted prior to the application of shear. The dielectric pillars for these sensors are composed of two shapes with relatively different cross-sectional profiles, which may cause uneven compression due to applied normal force or shear. This uneven compression is a likely reason behind the significant offset seen in the single-layer sensors which is not visible in other sensors with conventional dielectric designs. Overall, the inverted pyramid pillar architecture exhibits a strong response and directional differentiation to applied shear.

Double-Layer Design

The second approach to incorporating high-range force sensing into the existing architecture is a two-tiered architecture. In this design, the sensor is divided into two fully distinct portions: a highly sensitive upper layer for detection of low-force pressure and shear in the 0-15 N normal force range, and a stiffer lower layer for high-force measurements in the 15-50 N normal force range. The upper sensor design employs a five-electrode pressure and shear sensing design, with one lower and four upper measuring electrodes. The lower sensor is a simple two-electrode parallel plate capacitor which only measures normal force by means of plate separation distance. These electrode designs are shown in Figure 4-16, with the orange representing the more sensitive low-force and shear sensing portion and the green representing the high-force pressure only region. As light forces are applied, the upper architecture will be primarily engaged and act as a normal sensor; due to the large difference in stiffness between the upper and lower layer, these forces will not significantly deform the lower sensor. As the applied normal force increases, the upper sensor will become fully compressed and cease proper function, and the lower sensor will become engaged. This lower sensor will then measure the forces applied to the overall sensor, up to the maximum examined force of 50 N.

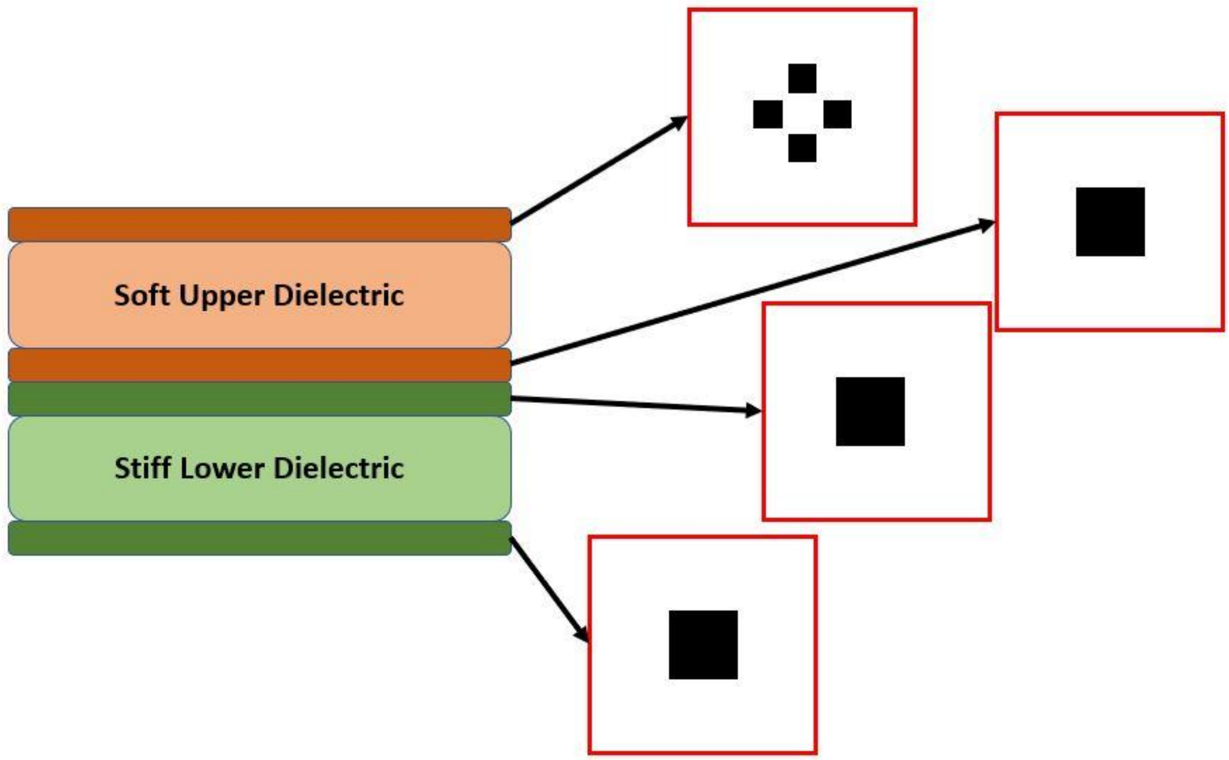

Figure 4-16: Two Layer High Normal Force Range Sensor Electrode Diagram

One difficulty experienced with this two-layer high force range architecture is the structural integrity of the middle layer. Initial data obtained from the sensor device showed a ‘trace following’ effect, in which all of the electrodes experienced similar signal changes regardless of shear direction. The most likely cause for this is a ‘twisting’ effect in the midsection of the sensor, where two layers of electrodes are stacked inside of a relatively thick layer of elastomer. As the sensor is sheared, these electrodes may be experiencing vertical displacement in addition to the expected horizontal displacement. This twisting can be observed at the edges of the sensor under applied shear as well; the fixed top and bottom of the sensor as a whole in addition to the highly soft material cause the dielectric pillars to exert pulling forces on the horizontal layers, causing the material to dip down in the front of the shear direction, and curl up at the rear of the shear direction. The effect can be observed in Figure 4-17, where each electrode signal responded in a similar but not identical manner despite one being out of plane to the shear displacement and another which was expected to increase as a result of the shear force applied. The major influential factor from this twisting is the decrease of electrode area regardless of shear direction, as a curl up or dip down will reduce the parallel-facing areas.

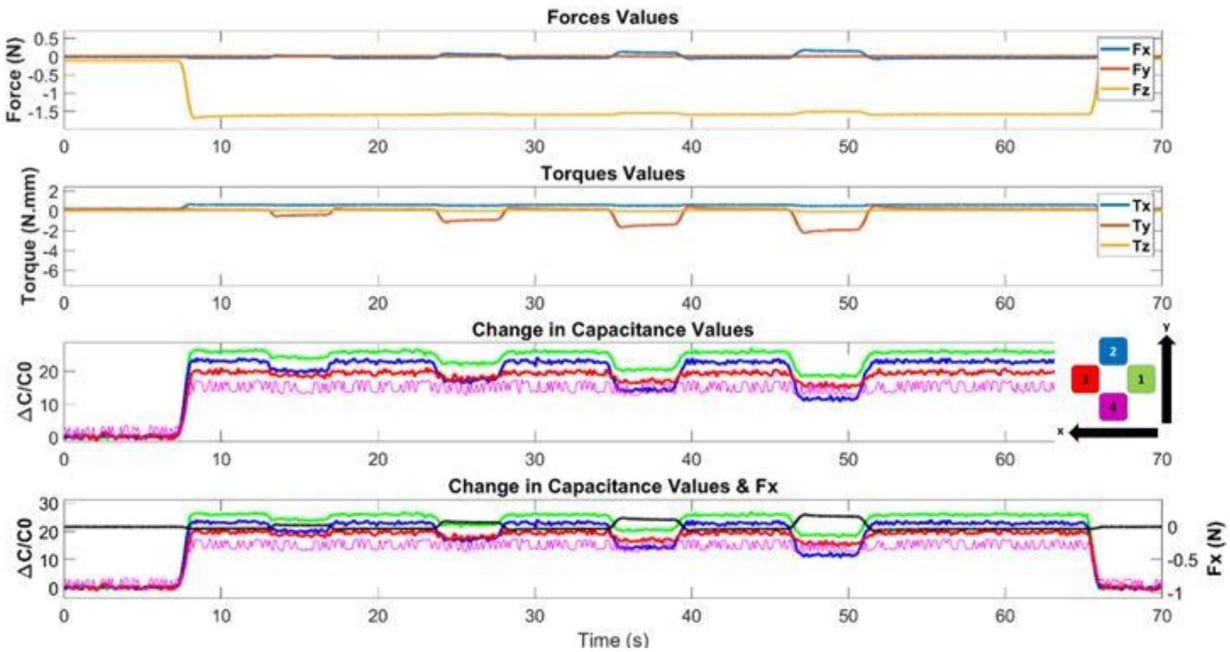

Figure 4-17: Two Layer High Normal Force Range Sensor Twisting Effect Causing 'Trace Following'. One Taxel (Pink) Was Found to Have a Connection Error which Would Not Affect Other Electrodes

To accommodate this twisting effect, the middle layer of the sensor is replaced with a polyamide-based flexible PCB manufactured by PCBWay [53], as shown in Figure 4-18. This change preserves the overall flexible nature of the sensor, while providing a more rigid interlayer to prevent whole-soft-body effects such as twisting from inhibiting overall sensor function. The flexible PCB is then connected to the rigid sensor body via header pins, which replace the otherwise-used soldered crimp connections previously described. All of the following data presented for the two-layer sensor is collected using this new architecture design, which is not expected to have a meaningful effect on the output of the sensors.

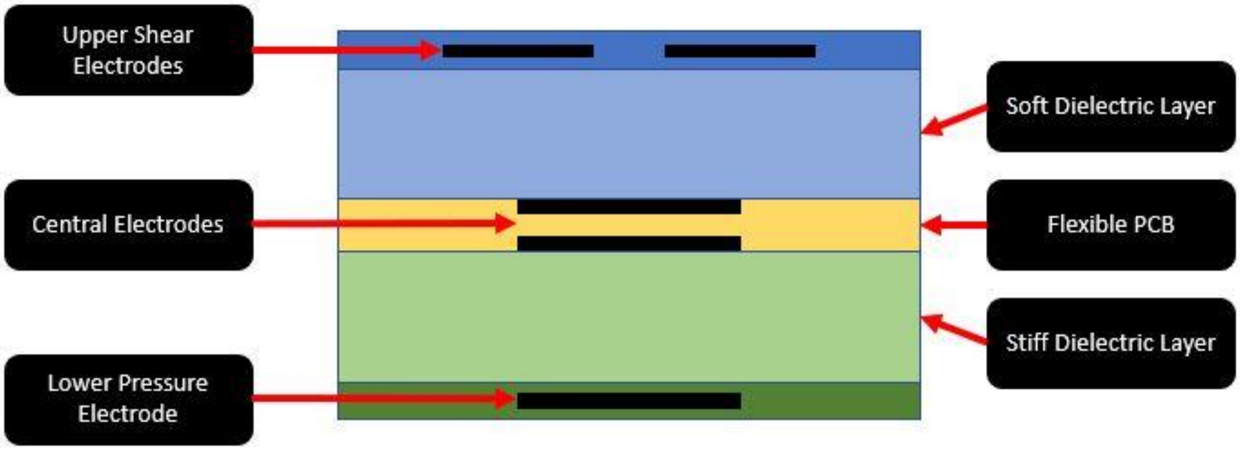

Figure 4-18: Double Layer High Range Sensor Layer Diagram with Central Flexible PCB Integrated

The upper sensor is required to have maximized sensitivity to pressure and shear forces, as the separation of upper and lower sensors is a high priority for this design. Based on the results of the single-layer high range sensor design described above, inverted-pyramid pillars were chosen as the default design for the two-layer sensor design. The lower sensor pillars are also based on the single-layer sensor design lower pillar portions, consisting of square pillars with a maximized cross-sectional surface area as allowed by the fabrication technique used. The information gathered from the single-layer high range sensors previously described is used to inform the design of this two-layer design, so no significant iteration was done regarding the dimensions or overall shape of the dielectric architectures. These two layers are fabricated using the same mold-based method described previously for fabrication of the single-layer sensors, with the two individual sensors attached using a thin layer of Ecoflex™ 00-30 in lieu of the final PCB attachment step for the upper layer.

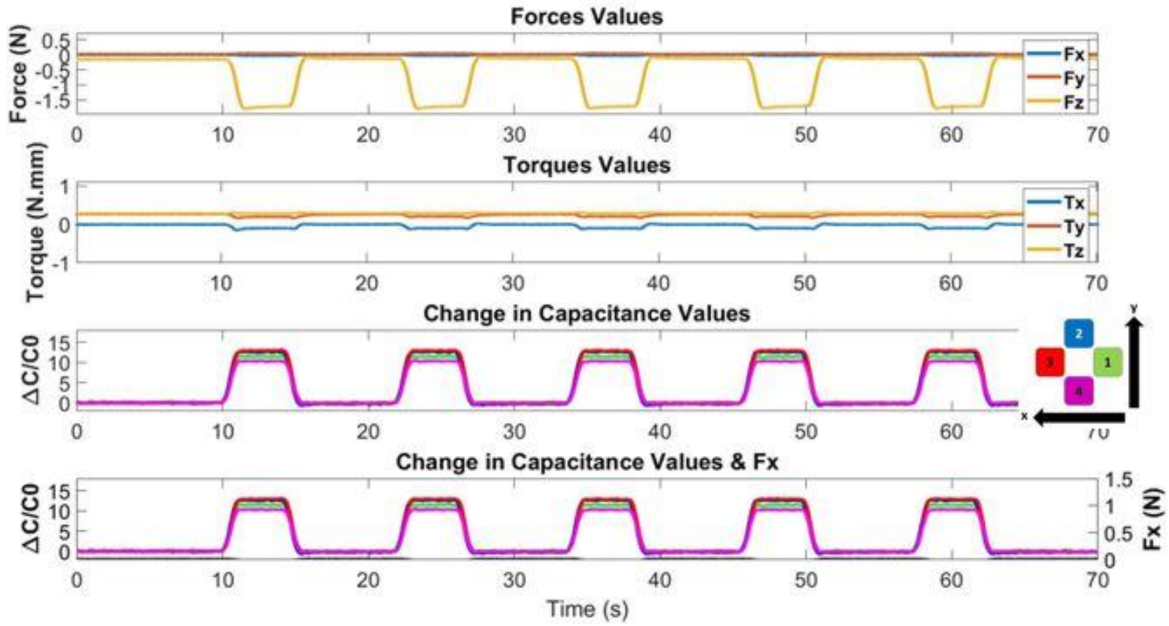

Figure 4-19: Two Layer High Normal Force Range Sensor, 1.6 N Repeated Applied Normal Force

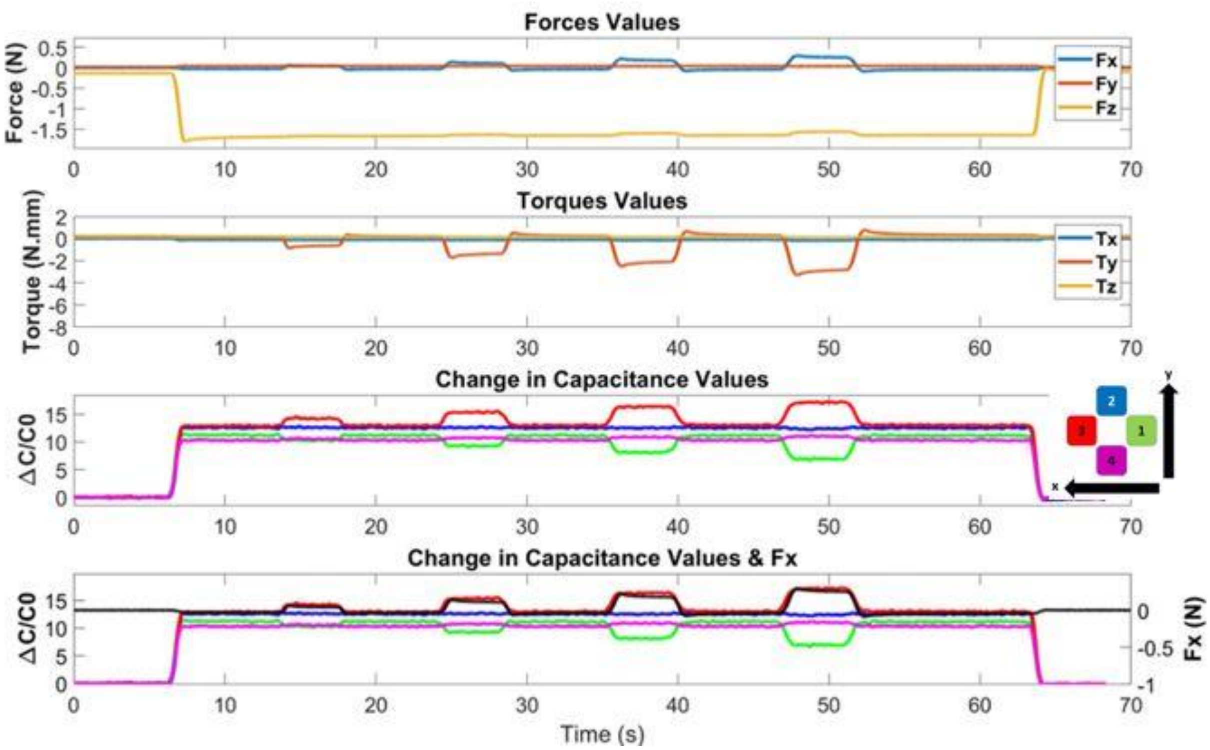

Figure 4-20: Two Layer High Normal Force Range Sensor, Positive x-Direction 0.2 mm to 0.8 mm Applied Shear Displacement

Compared to the single-layer high range designs, the two-layer version has a greatly decreased sensitivity to both pressure and shear forces. Normal force characterization results are shown in Figure 4-19, and shear characterization results in Figure 4-20. The normal force signal response was approximately 7.5/N under the 1.6 N normal force applied in testing, much less than the sensitivity exhibited by either the pyramid or inverted-pyramid single layer architecture. This holds true for the shear sensitivity as well, which have a maximal signal change of approximately 6.25/mm at 0.8 mm shear displacement, with an associated shear force of approximately 0.4 N. This is over an order of magnitude lower than the single-layer design $\Delta C/C_0$ despite being in approximately the same force range and the same displacement.

The most likely reason for this highly decreased sensitivity to both pressure and shear compared to the single-layer design is the double-electrode stacking. The architecture is designed to provide as much of a stiffness differential between the top and bottom architectures as allowable by the fabrication process, based on the knowledge previously acquired by the author regarding pillar stiffness in the single-layer design. However, due to the very soft nature of the Ecoflex™ material used, some coupling is inevitable between the top and bottom sensor layers. As the upper sensor is displaced by the low applied force, some portion will spread into the stiffer lower sensor, causing it to displace as well. This displacement 'leeching', shown in Figure 4-21, in response to force will decrease the $\Delta C/C_0$ observed in the upper sensor despite the force range being similar for a given shear displacement, leading to a sensor that is much less effective in the low-force range compared to the single-layer designs previously described. The major reason this effect is not seen in the single-layer high range sensors is due to the shared electrodes, where low and high forces are observed on the same basic architecture; in the two-layer design, these electrode patterns are split which leads to a more distributed capacitive response to force.

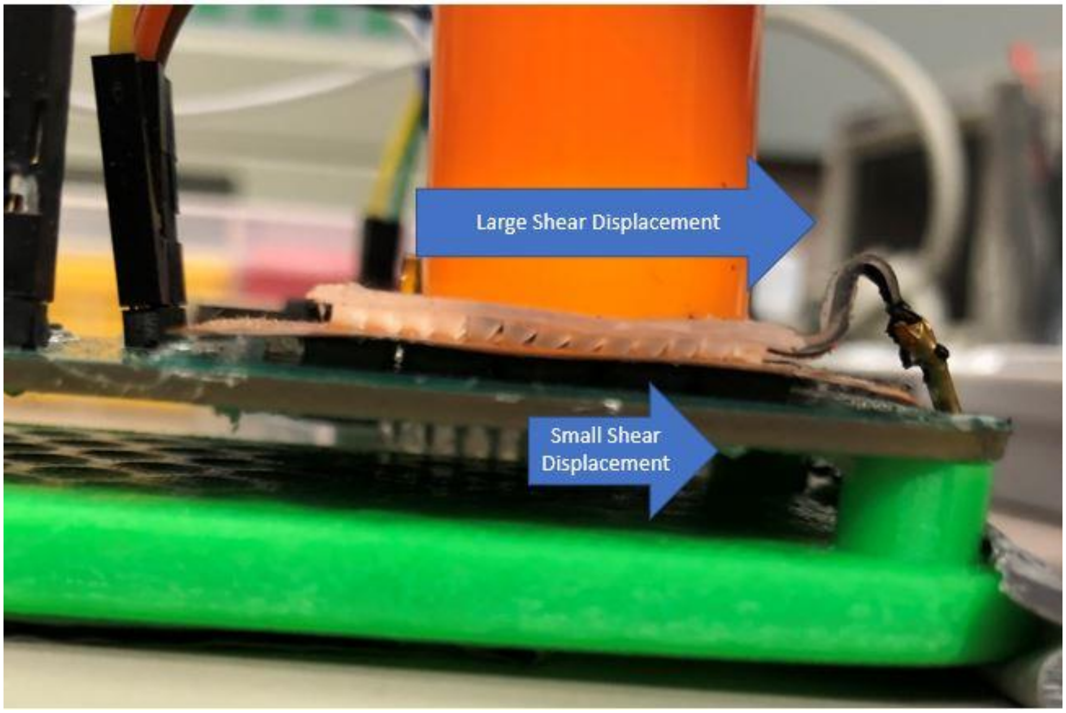

Figure 4-21: Two Layer High Normal Force Range Sensor Shear Displacement 'Leeching' Effect, Lower Shear Displacement Occurring Due to Application of Upper Layer Shear

Low-Force Characterization Conclusions

These low-force characterization results were used to inform which designs to explore at higher force ranges, up to the 50 N maximum normal force specified. The parameters used to determine which architectures to pursue for final high-force testing are sensitivity in the normal force and shear directions, defined as the $\Delta C/C_0$ /N (normal force) or $\Delta C/C_0$/mm (shear displacement). Both the pyramid and inverted-pyramid architectures for the single layer sensor design were determined to be a sufficient improvement on the sensitivity of the original architecture presented by *Sarwar et al.*, and were therefore selected for further experimentation at high force.

High Dynamic Range Characterization

High normal force characterization up to 50 N was done using the characterization setup described in Chapter 2, which provided the required force using a manually-controlled coarse z-axis stage. This characterization was done by Austin Weir, an undergraduate research assistant, under the direct supervision and guidance of the author. As outlined above, only high-force testing of the single-layer design is tested, with both the pyramid and inverted pyramid dielectric architectures. Due to the manual control of this high-force characterization setup by means of a hand-turn knob on the side of the stage, the applied force is not as smooth as what is expected of the low-force characterization. Each architecture is characterized by gradually raising the stage until 50 N is achieved, then holding the device at that normal force for approximately 15 seconds to observe any creep or similar effects with may be prominent at this force.

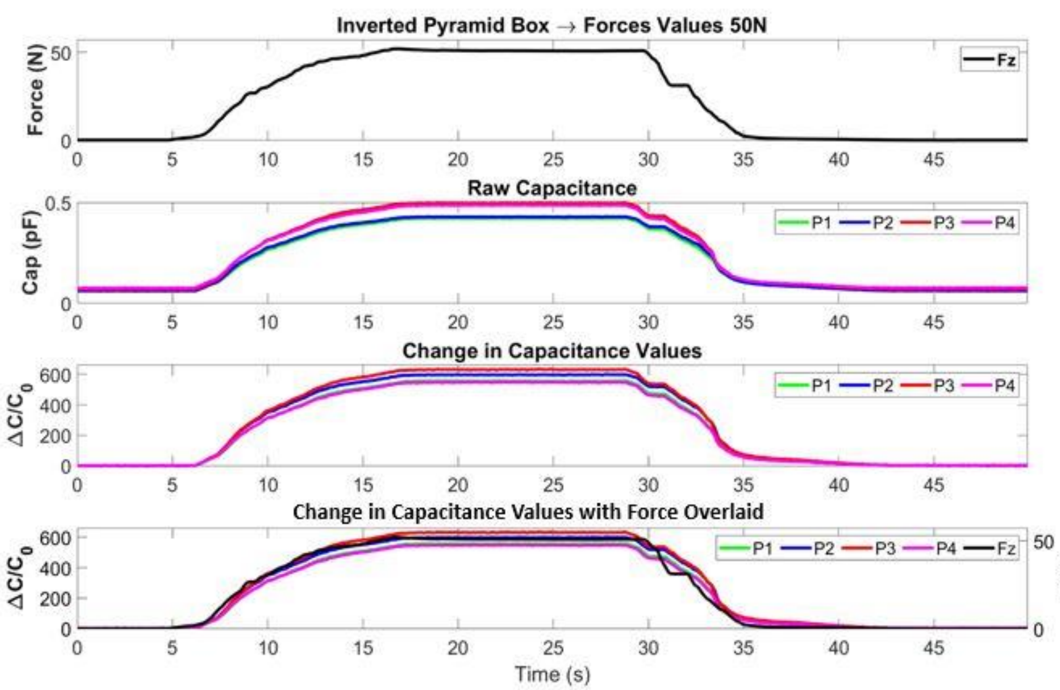

Figure 4-22: Inverted Pyramid Pillar Single Layer High Normal Force Range Sensor, 50 N Applied Normal Force

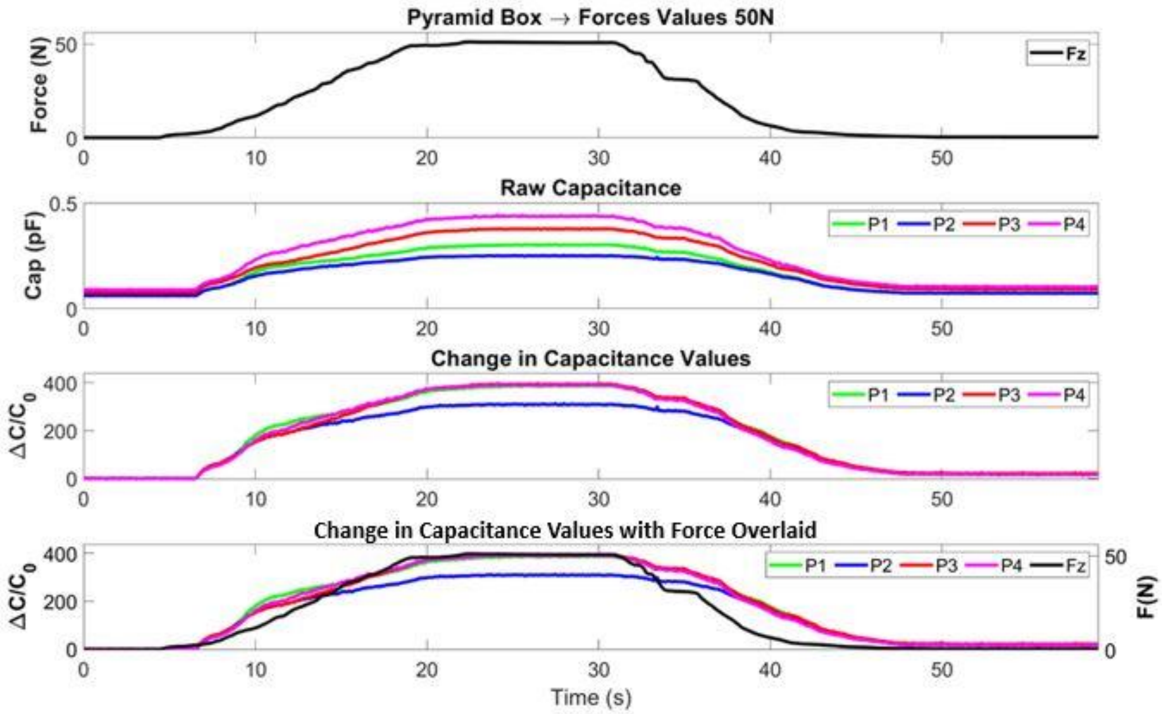

Figure 4-23: Pyramid Pillar Single Layer High Normal Force Range Sensor, 50 N Applied Normal Force

Both the pyramid and inverted pyramid exhibited sufficient sensitivity to and function under high forces up to 50 N, shown in Figure 4-22 and Figure 4-23. The pyramid single layer high range sensor produced a sensor $\Delta C/C_0$ of approximately 391.5 and the inverted pyramid high range sensor approximately 630.3. At these high force ranges a significant reduction in signal response related to applied force is observed. This is expected, as the incompressible viscoelastic dielectric would begin to become more displacement-saturated as the dielectric air gaps become filled. The inverted pyramid experienced a drop in overall signal response normalized to force from 46.56/N (1.6 N applied force) to 12.61/N (50 N applied force). The pyramid architecture saw a similar drop in the same normalized signal response, from 30.17/N (1.6 N applied force) to 7.83/N (50 N applied force). This reinforces the approach of the sensor towards an upper force saturation limit, a major design concern for the high-range sensors as the Ecoflex™ material is very soft.

Due to the limitations of the characterization setup described in Chapter 2, the displacement required for this 50 N applied force is unavailable. This limits the ability to assess the true force saturation of either sensor, as a stress-strain curve may not be established for the higher force range. Due to this difficulty the viability of the sensor at forces up to 50 N will be established by means of examining the force and capacitance curves. Strong mapping between applied force and capacitive response would indicate continued sensor function even at the high forces tested. The nonuniform application of force due to the manually controlled stage aids in establishing this relationship, as strong conformation and response to irregularities establishes the sensor's ability to detect unusual contacts even at the high forces explored.

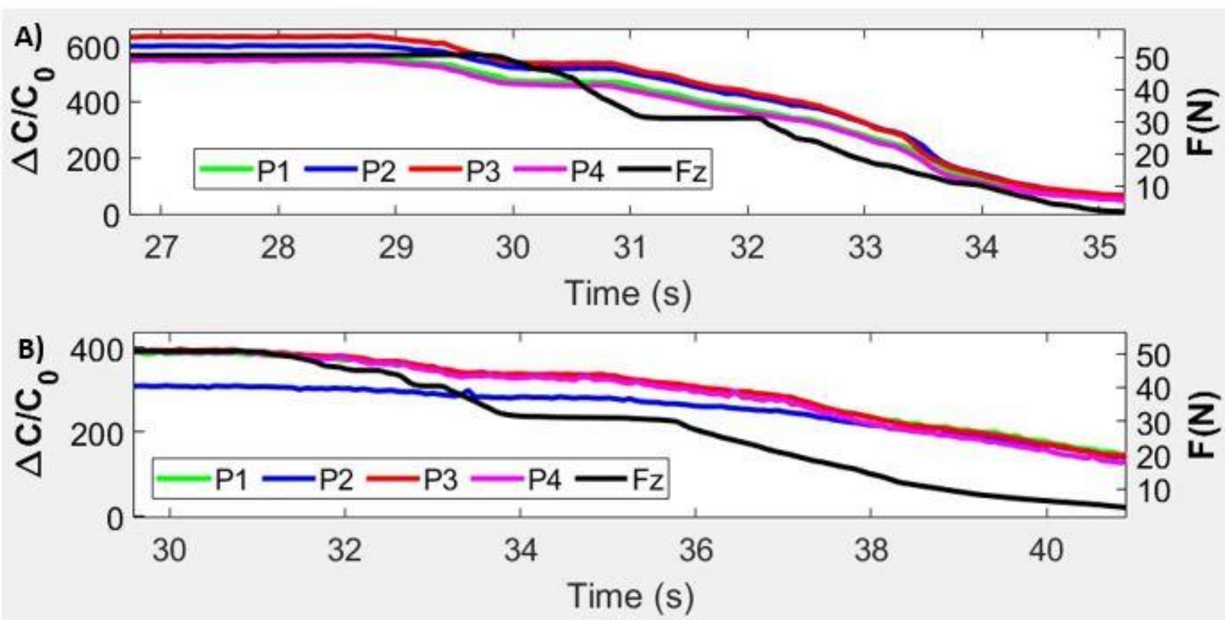

Figure 4-24: High Force Range Sensor Capacitance-Force Following Effect at Release of High Force, A) Inverted Pyramid Sensor, B) Pyramid Sensor

It can be seen in the declining curve of the 50 N applied force that both architectures display a reasonable, but slightly damped, capacitive response to the irregularities in descending force. In the inverted pyramid descending force shown in Figure 4-24 A), a small slope change occurs directly after the descent from 50 N begins, followed by a plateau region before the force reduction resumes. These two components of the curve are visible in the capacitive response of each sensor, with a distinct plateau preceded by a two-stage slope down from the peak signal observed in each taxel. This effect is observed in the pyramid sensor as well in Figure 4-24 B), with two distinct ‘bumps’ in the descending force mirrored by similar artifacts in the capacitive response.

It was observed during characterization that the sensor became much stiffer to force beginning at approximately 35 N, which persisted up until the 50 N maximum force achieved. This indicates the existence of the third proposed sensor modality discussed earlier in this thesis, in addition to the two lower-force modalities explored by *Sarwar et al.* This third ‘mode’ of the dielectric layer represents full compression into the air gaps introduced into the dielectric layer, sharply increasing the stiffness of the sensor as a whole. As the Poisson’s ratio of Ecoflex^{TM} is very close to 0.5 [54], it is expected that the pillars will expand to fill the air gap at approximately the same rate as they are compressed vertically. This will increase the perceived stiffness of the sensor, creating a nonlinear ramping-up of force required for a given normal displacement at higher forces.

Conclusions

Based on the results of the high force range sensor presented in this chapter, the novel nonuniform pillar design facilitates the fabrication of soft, flexible pressure and shear sensors capable of measuring high forces. These sensors allow for a wide range of normal force measurements in addition to sub-mm shear displacements, while preserving the skin-like designs from *Sarwar et al.* These designs increase the maximum force measurable by the sensor from 15 N to 50N, and the minimum detectable force from 0.1 N to approximately 0.05 N. These new designs primarily trade fabrication complexity for this increased functionality, using more complex architectures than previously fabricated sensors. The parameters met for these sensors was sufficient for the industry partner of the project to mark another milestone in the development of the sensors.

Two designs were explored to achieve this increased sensing range. The first is a 'single-layer' design with one set of upper and lower electrodes, using a novel nonuniform architecture design to produce an additional range of normal force stiffness alongside the two ranges seen in the previously fabricated sensors. The second design uses two sets of electrode pairs to create a stacked 'two-layer' sensor, in which the upper sensor has a much softer dielectric layer and the bottom sensor has a very stiff dielectric. Both designs combine Ecoflex™ dielectric architectures that were found to be either softer or stiffer, such as pyramids for the former and large cross-sectional area squares for the latter. The exploration conducted in this chapter found the single-layer design to be most promising in terms of ability to sense both low (1.6 N) and high (50 N) forces, while the double-layer design had very low signal response at forces up to 1.6 N. A novel dielectric architecture combining a pyramid (upper portion) and large square (lower portion) design was found experimentally to produce the most sensitive single-layer device at both low normal and shear, and high normal forces.

Chapter 5: Conclusions and Future Work

Summary of Work Done

In this thesis, two major improvements to a flexible, stretchable pressure and shear sensor design previously described by *Sarwar et al.* were proposed. The first improvement to the base sensor design was the integration of a novel flexible PCB to act as the base of the device, allowing for full functionality on curvatures with a radius of 100 mm-10 mm. The second proposed improvement was a novel sensor architecture which allowed for measurement of normal forces between 0.05-50 N, while maintaining low-force shear sensing functionality. These sensors are designed for the end goal of implementation in biomimetic robotic limbs or at human-device interfaces of medical robotics. Presented in this thesis are three sensor designs that fulfill these goals, one flexible sensor for the first objective and two high force range sensors for the second objective. The flexible sensor provided a set of twelve sensing taxels (4 pressure and shear combined, 8 pressure-only), and the high-range sensor provided four pressure and shear combined taxels with the ability to expand to include 8 additional pressure sensing taxels. These novel sensor designs were identified as sufficient to mark a new milestone in device development by the project's industry partner.

Additional work was conducted aside from these two primary established goals. The characterization setup outlined previously in work by *Sarwar et al.* was updated with several new components. These include a metal frame design designed by Bertille Dupont, a manually controlled high force stage augmentation, and a laser diode alignment system designed by an undergraduate research assistant Austin Weir and the author. These two improvements combined ensured more stable and consistent measurement results, although not all error due to characterization setup factors could be eliminated. Additionally, a previously documented issue with sensor electrode material breakdown over time which adversely affected conductivity was explored. This exploration involved testing various nanomaterial additives to the traditionally used carbon black-Ecoflex^{TM} material over a period of 238 days to monitor change in resistance over time. Carbon nanofibers in a Dragon Skin^{TM} FX-Pro host was found to stabilize the conductive material to a conductive decrease of less than 10% per year and a significant reduction in starting resistance.

Future Work

The work presented in this thesis paves the way for a wide variety of future work regarding implementation into biomedical robotics. The main motivation for the sensors presented in this thesis is an eventual integration into human mimetic robotics requiring touch sensing, such as upper limb prosthetics or biomedical human-interfacing robots. While significant progress was made on the sensor device in this stage of development, there are several components which require more future work:

Flex, High-Range Sensor Integration: Presented in this thesis are two novel sensor developments for the flexible pressure and shear sensor, both a flexible PCB system integration and novel high force range architecture. Since these two components were designed in parallel, they were not integrated during the work presented in this thesis. Both the ability to maintain flexibility while PCB-mounted and to measure a wide force range are important for the future use of these sensors in the desired application, so the integration of the two designs is a key component of future work. This would involve incorporating the novel dielectric architectures for high force into the flexible-PCB design, then characterizing these sensors at a variety of different curvatures. The primary anticipated difficulty with these sensors is the increased height of the novel high-force dielectrics, which will create potential difficulties in function at small curvature radii.

Practical Testing of High-Conductance Material: To isolate the effect of the novel materials on sensor electrode durability over time and facilitate consistent testing, the materials were examined in a non-sensor environment. In this investigation, materials were identified that are promising for extending the conductive lifespan of the sensors. What remains is to test these materials in practice with sensors to confirm continued function over long periods of time.

Array Implementation: The sensors currently fabricated operate independently, with each sensor unit having a dedicated PCB and microcontroller attached. A key component for practical implementation of the sensor is the ability to place multiple sensors in close proximity, as areas such as prosthetic hands have very limited space for placement of sensors and microcontrollers. This work would involve developing a multi-sensor PCB with multiple sensors in parallel, and an updated microcontroller architecture capable of handling more data channels at once. An example of an array-oriented sensor system is shown in Figure 5-1, with 2*x*1 sensor layout.

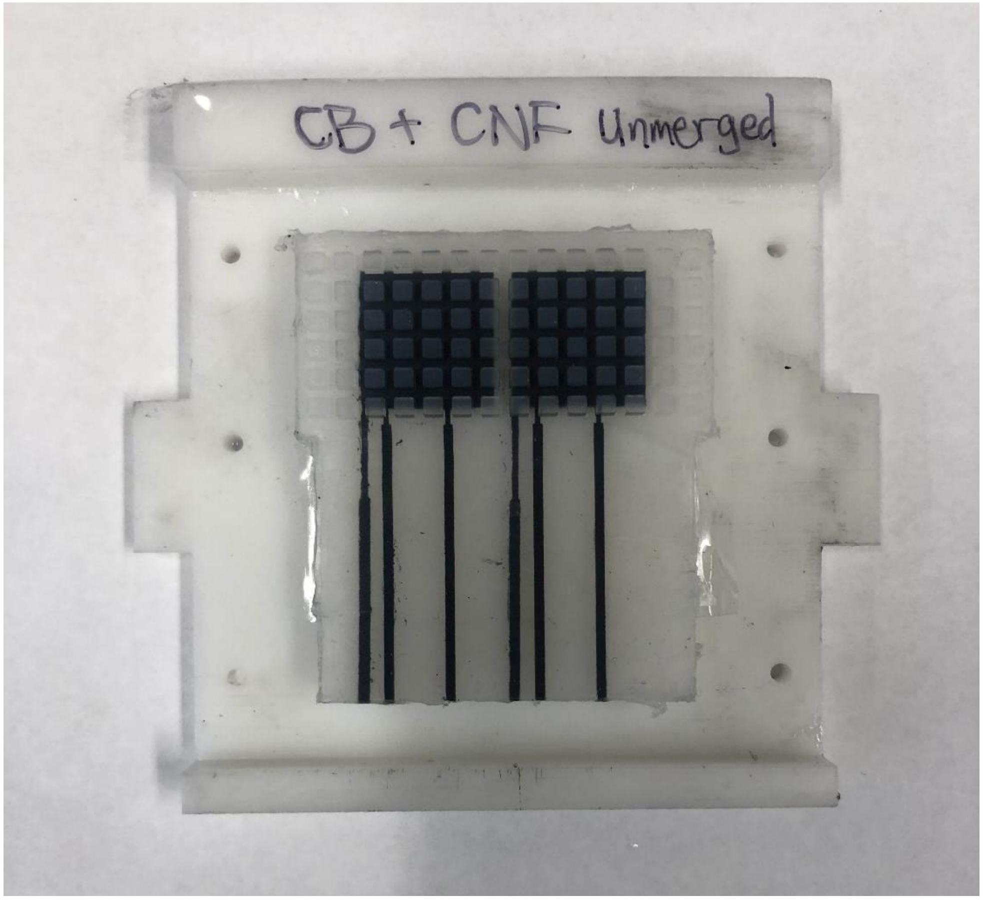

Figure 5-1: Example 2x1 12-Taxel Pressure and Shear Sensor Array Prototype

Real-World Indenter Testing: In Chapter 3, it was established that the response of a sensor mounted to a curved surface varies significantly based on the shape of the indenter used. The indenters chosen for this characterization (flat, cylindrical, and spherical) were intended to represent a variety of real-world objects which a sensing skin may encounter. This indicates that in practical applications, a sensing skin employing a device similar to the one described in this thesis may have difficulty differentiating between force and indenter shape. More work is required in the future to alleviate this issue, as the sensor will ideally be able to sense imparted force regardless of the shape of the object.

Overall, the work presented in this thesis outlines the potential for the flexible combined pressure and shear sensor design to be implemented as an artificial touch-sensing skin in applications such as prosthetics and human-interface medical robotics. Further work is required to develop the sensor into these applications, but the device is promising for these devices. Once further developed, the sensor could allow for pressure and shear sensory feedback in upper limb prosthetic users, medical robotics, and a wide variety of other applications.

References

[1] A. K. Hemal and M. Menon, “Robotics in Genitourinary Surgery,” doi: 10.1007/978-3-319-20645-5.

[2] R. S. Dahiya and M. Valle, “Robotic tactile sensing: Technologies and system,” *Robot. Tactile Sens. Technol. Syst.*, vol. 9789400705791, pp. 1–245, Jan. 2014, doi: 10.1007/978-94-007-0579-1.

[3] J. Jørgensen, K. B. Bojesen, and E. Jochum, “Is a Soft Robot More ‘Natural’? Exploring the Perception of Soft Robotics in Human–Robot Interaction,” *Int. J. Soc. Robot. 2021*, no. 3, pp. 1–19, Mar. 2021, doi: 10.1007/S12369-021-00761-1.

[4] D. Silvera-Tawil, D. Rye, and M. Velonaki, “Artificial skin and tactile sensing for socially interactive robots: A review,” *Rob. Auton. Syst.*, vol. 63, no. P3, pp. 230–243, Jan. 2015, doi: 10.1016/J.ROBOT.2014.09.008.

[5] A. P. Gerratt, H. O. Michaud, and S. P. Lacour, “Elastomeric Electronic Skin for Prosthetic Tactile Sensation,” *Adv. Funct. Mater.*, vol. 25, no. 15, pp. 2287–2295, Apr. 2015, doi: 10.1002/ADFM.201404365.

[6] R. S. Dahiya, G. Metta, M. Valle, and G. Sandini, “Tactile sensing-from humans to humanoids,” *IEEE Trans. Robot.*, vol. 26, no. 1, pp. 1–20, Feb. 2010, doi: 10.1109/TRO.2009.2033627.

[7] Y. Lee, J. Park, A. Choe, S. Cho, J. Kim, and H. Ko, “Mimicking Human and Biological Skins for Multifunctional Skin Electronics,” *Adv. Funct. Mater.*, vol. 30, no. 20, p. 1904523, May 2020, doi: 10.1002/ADFM.201904523.

[8] D. Purves *et al.*, *Neuroscience*, 2nd ed. Sunderland: Sinauer Associates, 2001.

[9] M. L. Hammock, A. Chortos, B. C.-K. Tee, J. B.-H. Tok, and Z. Bao, “25th Anniversary

Article: The Evolution of Electronic Skin (E-Skin): A Brief History, Design Considerations, and Recent Progress,” *Adv. Mater.*, vol. 25, no. 42, pp. 5997–6038, Nov. 2013, doi: 10.1002/ADMA.201302240.

[10] R. Sun *et al.*, “Stretchable Piezoelectric Sensing Systems for Self-Powered and Wireless Health Monitoring,” *Adv. Mater. Technol.*, vol. 4, no. 5, p. 1900100, May 2019, doi: 10.1002/ADMT.201900100.

[11] X. Pu, S. An, Q. Tang, H. Guo, and C. Hu, “Wearable triboelectric sensors for biomedical monitoring and human-machine interface,” *iScience*, vol. 24, no. 1, p. 102027, Jan. 2021, doi: 10.1016/J.ISCI.2020.102027.

[12] M. Ramuz, B. C.-K. Tee, J. B.-H. Tok, and Z. Bao, “Transparent, Optical, Pressure-Sensitive Artificial Skin for Large-Area Stretchable Electronics,” *Adv. Mater.*, vol. 24, no. 24, pp. 3223–3227, Jun. 2012, doi: 10.1002/ADMA.201200523.

[13] B. J. Kim, C. A. Gutierrez, and E. Meng, “Parylene-Based Electrochemical-MEMS Force Sensor for Studies of Intracortical Probe Insertion Mechanics,” *J. Microelectromechanical Syst.*, vol. 24, no. 5, pp. 1534–1544, Oct. 2015, doi: 10.1109/JMEMS.2015.2420043.

[14] C. A. Gutierrez and E. Meng, “Impedance-based force transduction within fluid-filled parylene microstructures,” *J. Microelectromechanical Syst.*, vol. 20, no. 5, pp. 1098–1108, Oct. 2011, doi: 10.1109/JMEMS.2011.2160935.

[15] C. M. Boutry *et al.*, “A hierarchically patterned, bioinspired e-skin able to detect the direction of applied pressure for robotics,” 2018.

[16] S. Li *et al.*, “Physical sensors for skin-inspired electronics,” *InfoMat*, vol. 2, no. 1, pp. 184–211, Jan. 2020, doi: 10.1002/INF2.12060.

[17] Y. Luo *et al.*, “Flexible Capacitive Pressure Sensor Enhanced by Tilted Micropillar

Arrays," *ACS Appl. Mater. Interfaces*, vol. 11, no. 19, pp. 17796–17803, May 2019, doi: 10.1021/ACSAMI.9B03718.

[18] R. B. Mishra, N. El-Atab, A. M. Hussain, and M. M. Hussain, "Recent Progress on Flexible Capacitive Pressure Sensors: From Design and Materials to Applications," *Adv. Mater. Technol.*, vol. 6, no. 4, p. 2001023, Apr. 2021, doi: 10.1002/ADMT.202001023.

[19] B. Zhuo, S. Chen, M. Zhao, and X. Guo, "High Sensitivity Flexible Capacitive Pressure Sensor Using Polydimethylsiloxane Elastomer Dielectric Layer Micro-Structured by 3-D Printed Mold," *IEEE J. Electron Devices Soc.*, vol. 5, no. 3, pp. 219–223, May 2017, doi: 10.1109/JEDS.2017.2683558.

[20] E. P. Scilingo, F. Lorussi, A. Mazzoldi, and D. De Rossi, "Strain-sensing fabrics for wearable kinaesthetic-like systems," *IEEE Sens. J.*, vol. 3, no. 4, pp. 460–467, Aug. 2003, doi: 10.1109/JSEN.2003.815771.

[21] A. Hu, K. Shaikh, and C. Liu, "Super flexible sensor skin using liquid metal as interconnect," *Proc. IEEE Sensors*, pp. 815–817, 2007, doi: 10.1109/ICSENS.2007.4388525.

[22] "uSkin SENSOR — XELA Robotics." https://xelarobotics.com/en/uskin-sensor (accessed Sep. 05, 2021).

[23] "BioTac® Product Manual," 2018.

[24] C. Pang *et al.*, "A flexible and highly sensitive strain-gauge sensor using reversible interlocking of nanofibres," *Nat. Mater.*, p. 29, 2012, doi: 10.1038/NMAT3380.

[25] M.-Y. Cheng, C.-L. Lin, Y.-T. Lai, and Y.-J. Yang, "A Polymer-Based Capacitive Sensing Array for Normal and Shear Force Measurement," *Sensors 2010, Vol. 10, Pages 10211-10225*, vol. 10, no. 11, pp. 10211–10225, Nov. 2010, doi: 10.3390/S101110211.

[26] N. T. Nguyen *et al.*, “Transparent stretchable capacitive touch sensor grid using ionic liquid electrodes,” *Extrem. Mech. Lett.*, vol. 33, p. 100574, Nov. 2019, doi: 10.1016/J.EML.2019.100574.

[27] M. S. us Sarwar, “Soft capacitive sensors for proximity, touch, pressure and shear measurements,” University of British Columbia, 2019.

[28] J. Park, I. You, S. Shin, and U. Jeong, “Material Approaches to Stretchable Strain Sensors,” *ChemPhysChem*, vol. 16, no. 6, pp. 1155–1163, Apr. 2015, doi: 10.1002/CPHC.201402810.

[29] P. Kalla, S. Boppud, S. Adinarayana, and M. A. Prakash, “Polyurethane Elastomer—A Low-Cost Artificial Epidermal Skin,” pp. 681–692, 2019, doi: 10.1007/978-981-13-7643-6_56.

[30] B. Li, A. K. Fontecchio, and Y. Visell, “Mutual capacitance of liquid conductors in deformable tactile sensing arrays,” *Appl. Phys. Lett.*, vol. 108, no. 1, p. 013502, Jan. 2016, doi: 10.1063/1.4939620.

[31] S. H. Kim, S. Jung, I. S. Yoon, C. Lee, Y. Oh, and J.-M. Hong, “Ultrastretchable Conductor Fabricated on Skin-Like Hydrogel–Elastomer Hybrid Substrates for Skin Electronics,” *Adv. Mater.*, vol. 30, no. 26, p. 1800109, Jun. 2018, doi: 10.1002/ADMA.201800109.

[32] Y. Zhang *et al.*, “Carbon nanotubes/acetylene black/Ecoflex with corrugated microcracks for enhanced sensitivity for stretchable strain sensors,” *J. Mater. Sci. Mater. Electron. 2020 3117*, vol. 31, no. 17, pp. 14145–14156, Jul. 2020, doi: 10.1007/S10854-020-03969-5.

[33] M. S. Sarwar *et al.*, “Soft Artificial Skin for Detecting Approach, Contact and Shear,”

Manuscript. 2021.

[34] K. Liu *et al.*, “Artificial Sensitive Skin for Robotics Based on Electrical Impedance Tomography,” *Adv. Intell. Syst.*, vol. 2, no. 4, p. 1900161, Apr. 2020, doi: 10.1002/AISY.201900161.

[35] S. Salminger *et al.*, “Current rates of prosthetic usage in upper-limb amputees – have innovations had an impact on device acceptance?,” *https://doi-org.ezproxy.library.ubc.ca/10.1080/09638288.2020.1866684*, 2020, doi: 10.1080/09638288.2020.1866684.

[36] L. Resnik *et al.*, “Advanced Upper Limb Prosthetic Devices: Implications for Upper Limb Prosthetic Rehabilitation,” 2012, doi: 10.1016/j.apmr.2011.11.010.

[37] D. Giovanelli and E. Farella, “Force Sensing Resistor and Evaluation of Technology for Wearable Body Pressure Sensing,” *J. Sensors*, vol. 2016, 2016, doi: 10.1155/2016/9391850.

[38] T. Agcayazi, Y. Menguc, and S. Reese, “Skin in the Game: A Tunable Interface-Quality Sensor for Human-Coupled Accessories,” *IEEE Sensors Lett.*, vol. 4, no. 9, Sep. 2020, doi: 10.1109/LSENS.2020.3011864.

[39] L. C. Smail, C. Neal, C. Wilkins, and T. L. Packham, “Comfort and function remain key factors in upper limb prosthetic abandonment: findings of a scoping review,” *https://doi-org.ezproxy.library.ubc.ca/10.1080/17483107.2020.1738567*, 2020, doi: 10.1080/17483107.2020.1738567.

[40] LlamosiArtémis and ToussaintSéverine, “Measuring Force Intensity and Direction with a Spatially Resolved Soft Sensor for Biomechanics and Robotic Haptic Capability,” *https://home.liebertpub.com/soro*, vol. 6, no. 3, pp. 346–355, Jun. 2019, doi:

10.1089/SORO.2018.0044.

[41] E. A. Biddiss and T. T. Chau, “Upper limb prosthesis use and abandonment: A survey of the last 25 years:,” *http://dx.doi.org/10.1080/03093640600994581*, vol. 31, no. 3, pp. 236–257, Jun. 2016, doi: 10.1080/03093640600994581.

[42] F. Cordella *et al.*, “Literature Review on Needs of Upper Limb Prosthesis Users,” *Front. Neurosci.*, vol. 0, no. MAY, p. 209, 2016, doi: 10.3389/FNINS.2016.00209.

[43] “Ecoflex™ Series, Super-Soft, Addition Cure Silicone Rubbers | Smooth-On, Inc.” https://www.smooth-on.com/product-line/ecoflex/ (accessed Aug. 08, 2021).

[44] W. Deng *et al.*, “Microstructure-Based Interfacial Tuning Mechanism of Capacitive Pressure Sensors for Electronic Skin,” *J. Sensors*, vol. 2016, 2016, doi: 10.1155/2016/2428305.

[45] “Staples Copier Transparency Film, 8-1/2" x 11", 100/Pack | staples.ca.” https://www.staples.ca/products/368095-en-staples-copier-transparency-film-8-12-x-11-100pack (accessed Aug. 03, 2021).

[46] H. F. Posada-Quintero, N. Reljin, C. Eaton-Robb, Y. Noh, J. Riistama, and K. H. Chon, “Analysis of Consistency of Transthoracic Bioimpedance Measurements Acquired with Dry Carbon Black PDMS Electrodes, Adhesive Electrodes, and Wet Textile Electrodes,” *Sensors (Basel).*, vol. 18, no. 6, Jun. 2018, doi: 10.3390/S18061719.

[47] B. A. Reyes *et al.*, “Novel electrodes for underwater ECG monitoring,” *IEEE Trans. Biomed. Eng.*, vol. 61, no. 6, pp. 1863–1876, 2014, doi: 10.1109/TBME.2014.2309293.

[48] J. Zhu, H. Wang, and Y. Zhu, “A flexible piezoresistive carbon black network in silicone rubber for wide range deformation and strain sensing,” doi: 10.1063/1.5006523.

[49] E. Enríquez, J. de Frutos, J. F. Fernández, and M. A. de la Rubia, “Conductive coatings

with low carbon-black content by adding carbon nanofibers," *Compos. Sci. Technol.*, vol. 93, pp. 9–16, Mar. 2014, doi: 10.1016/J.COMPSCITECH.2013.12.021.

[50] A. S. Haidyrah, P. Sundaresan, K. Venkatesh, S. K. Ramaraj, and B. Thirumalraj, "Fabrication of functionalized carbon nanofibers/carbon black composite for electrochemical investigation of antibacterial drug nitrofurantoin," *Colloids Surfaces A Physicochem. Eng. Asp.*, vol. 627, p. 127112, Oct. 2021, doi: 10.1016/J.COLSURFA.2021.127112.

[51] H. Yousef, M. Boukallel, and K. Althoefer, "Tactile sensing for dexterous in-hand manipulation in robotics—A review," *Sensors Actuators A Phys.*, vol. 167, no. 2, pp. 171–187, Jun. 2011, doi: 10.1016/J.SNA.2011.02.038.

[52] J. Dargahi and S. Najarian, "Human tactile perception as a standard for artificial tactile sensing—a review," *Int. J. Med. Robot. Comput. Assist. Surg.*, vol. 1, no. 1, pp. 23–35, Jun. 2004, doi: 10.1002/RCS.3.

[53] "China PCB Prototype & Fabrication Manufacturer - PCB Prototype the Easy Way." https://www.pcbway.com/ (accessed Aug. 23, 2021).

[54] Seongpil An, D. Jin Kang, and A. L. Yarin, "A blister-like soft nano-textured thermo-pneumatic actuator as an artificial muscle," *Nanoscale*, vol. 10, no. 35, pp. 16591–16600, Sep. 2018, doi: 10.1039/C8NR04181D.

Appendices

Appendix A: Characterization Setup Component Specifications

Stage	Max *z* Range (mm)	Max *x*, *y* Range (mm)	Max Load (kg)
NanoMax 300 3-axis	4	4	1
BoliOptics SG02201211	120	N/A	20

Table A-1: Characterization Setup Stage Displacement Ranges, Max Load Specifications

	Force Sensing Range			Force Sensing Resolution	
Load Cell	F_x, F_y (N)	F_z (N)	T_x, T_y, T_z (Nmm)	F_x, F_y, F_z (N)	T_x, T_y, T_z (Nmm)
ATI SI-50-0.5	50	70	500	1/80	1/16

Table A-2: ATI SI-50-0.5 Load Cell Force and Torque Specifications

Appendix B: Curved Surface Characterization Data

This appendix presents shear data from the flexible combined pressure and shear sensor presented in Chapter 3. This shear is applied in one of either the +/- *x* or +/- *y* direction, to align applied force with the direction of the taxels. For all data presented in this appendix, the color scheme is used for the sensor central shear taxel orientation matches Figure B-1. The inner curvature radii tested are 100 mm, 30 mm, and 10 mm.

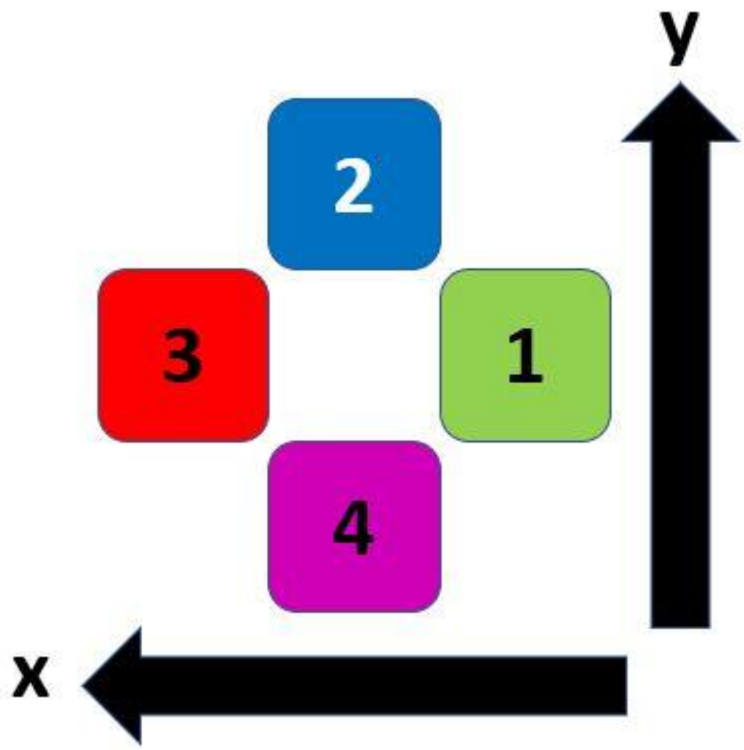

Figure B-1: Taxel Orientation for Curved Sensor Shear Characterization

Positive *x*-shear, 100 mm Inner Radius of Curvature

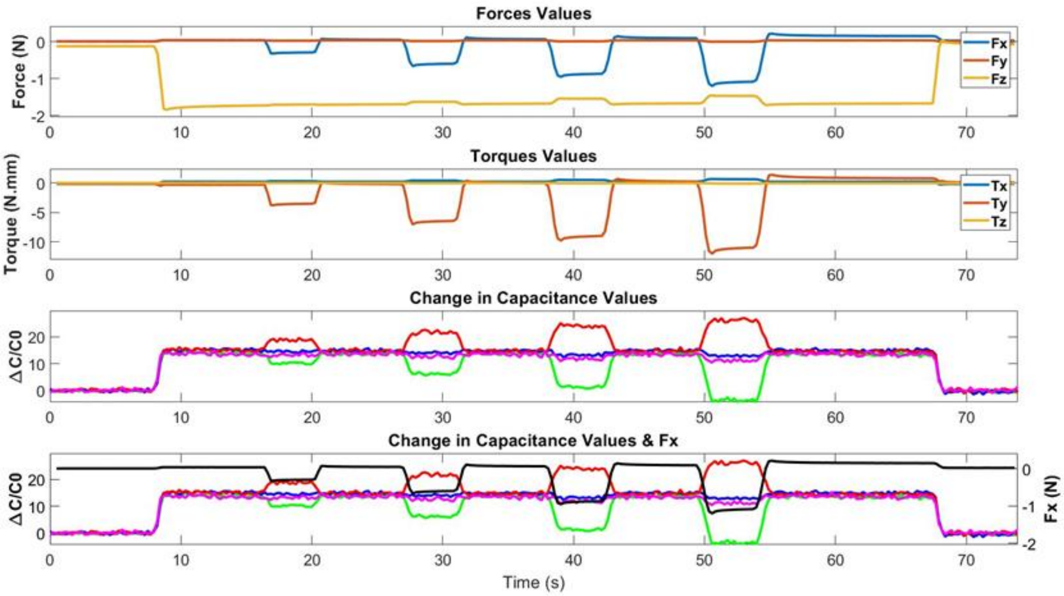

Figure B-2: Shear Displacement Characterization at 100 mm Radius of Curvature with Flat Indenter, 0.2 mm to 0.8 mm Positive-x Displacement

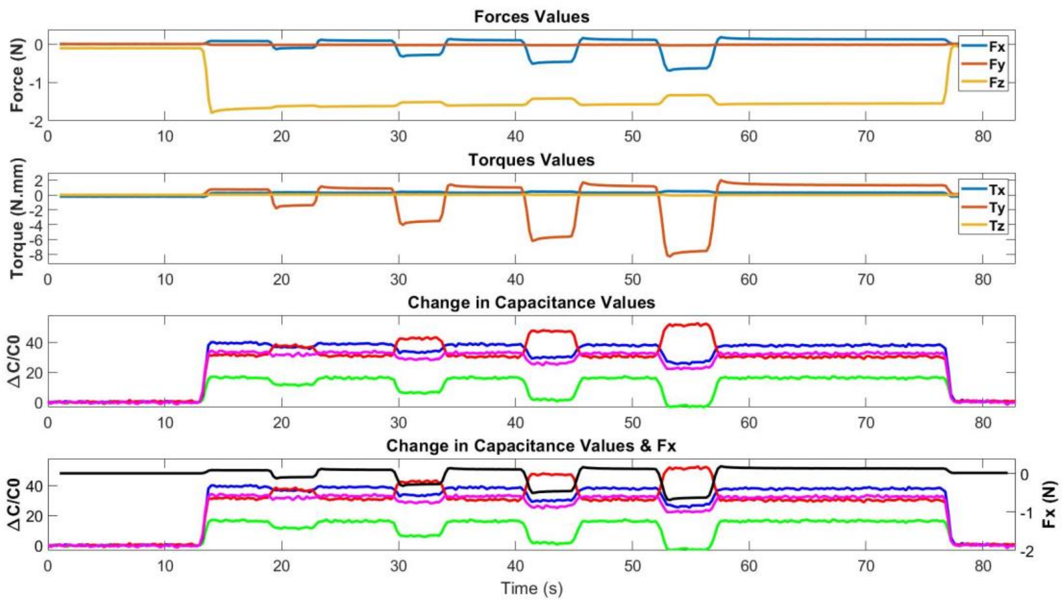

Figure B-3: Shear Displacement Characterization at 100 mm Radius of Curvature with Cylinder Indenter, 0.2 mm to 0.8 mm Positive-x Displacement

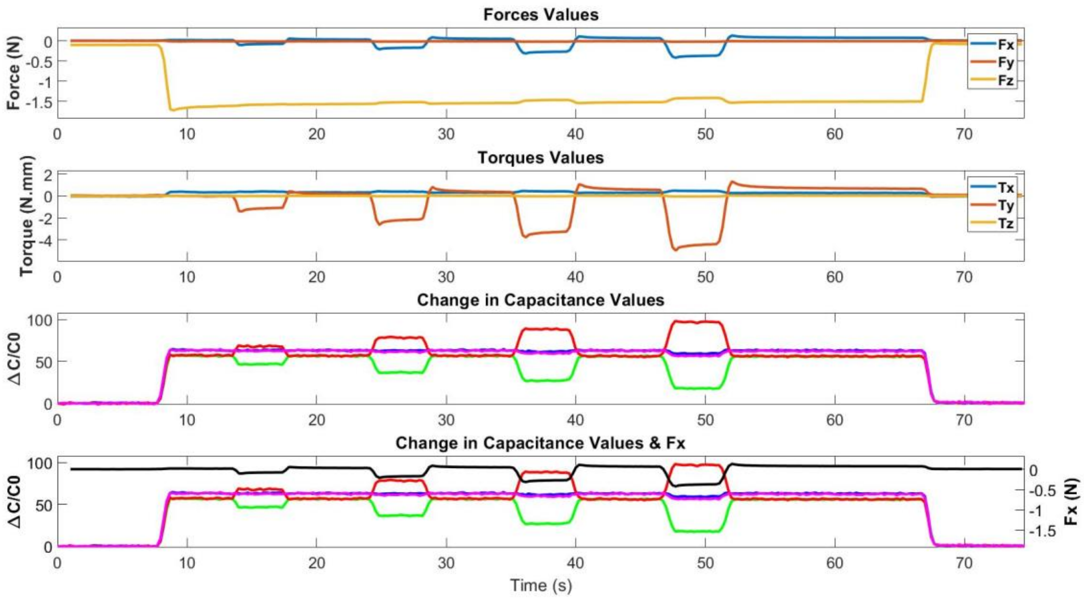

Figure B-4: Shear Displacement Characterization at 100 mm Radius of Curvature with Sphere Indenter, 0.2 mm to 0.8 mm Positive-x Displacement

Negative *x*-shear, 100 mm Inner Radius of Curvature

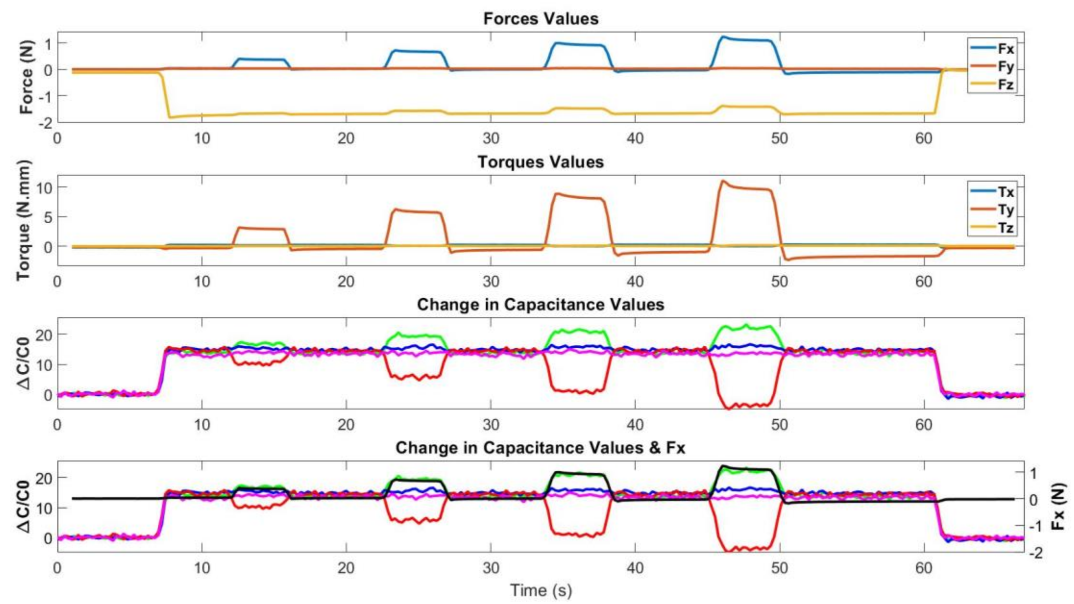

Figure B-5: Shear Displacement Characterization at 100 mm Radius of Curvature with Flat Indenter, 0.2 mm to 0.8 mm Negative-x Displacement

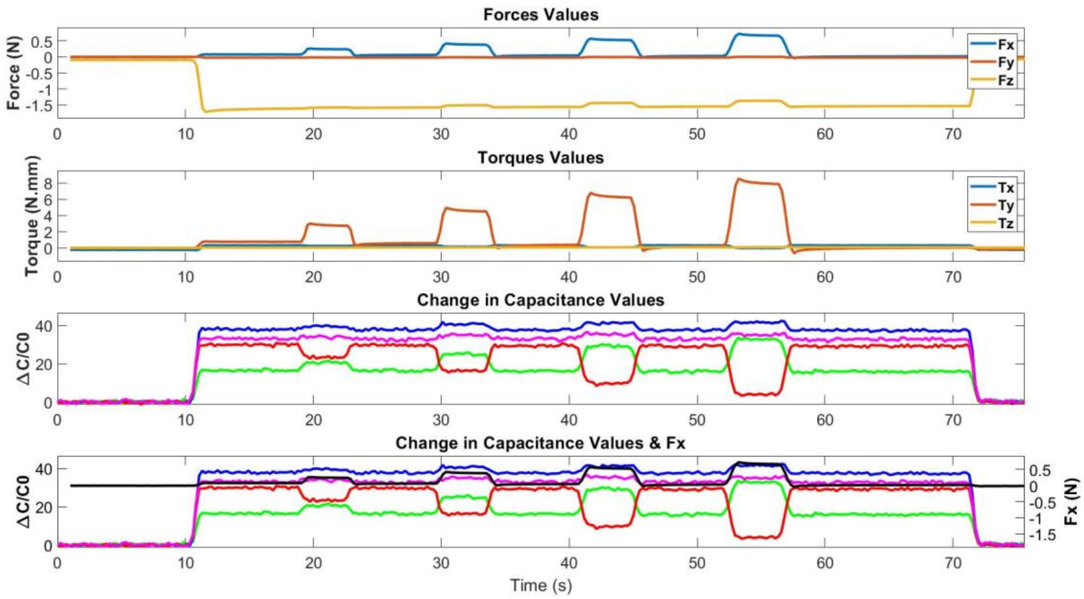

Figure B-6: Shear Displacement Characterization at 100 mm Radius of Curvature with Cylindrical Indenter, 0.2 mm to 0.8 mm Negative-x Displacement

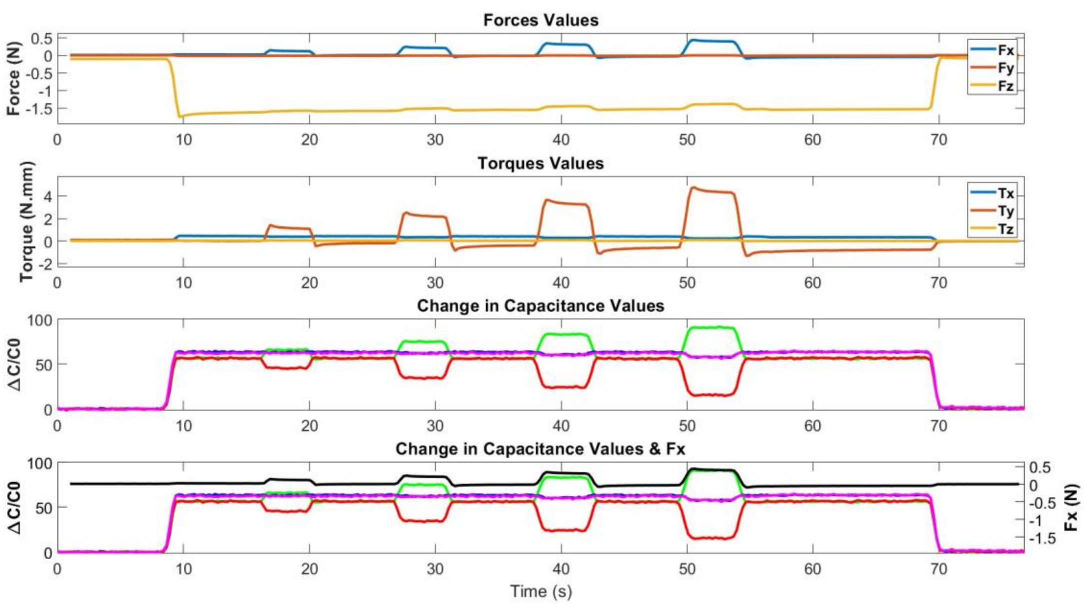

Figure B-7: Shear Displacement Characterization at 100 mm Radius of Curvature with Spherical Indenter, 0.2 mm to 0.8 mm Negative-x Displacement

Positive *y*-shear, 100 mm Inner Radius of Curvature

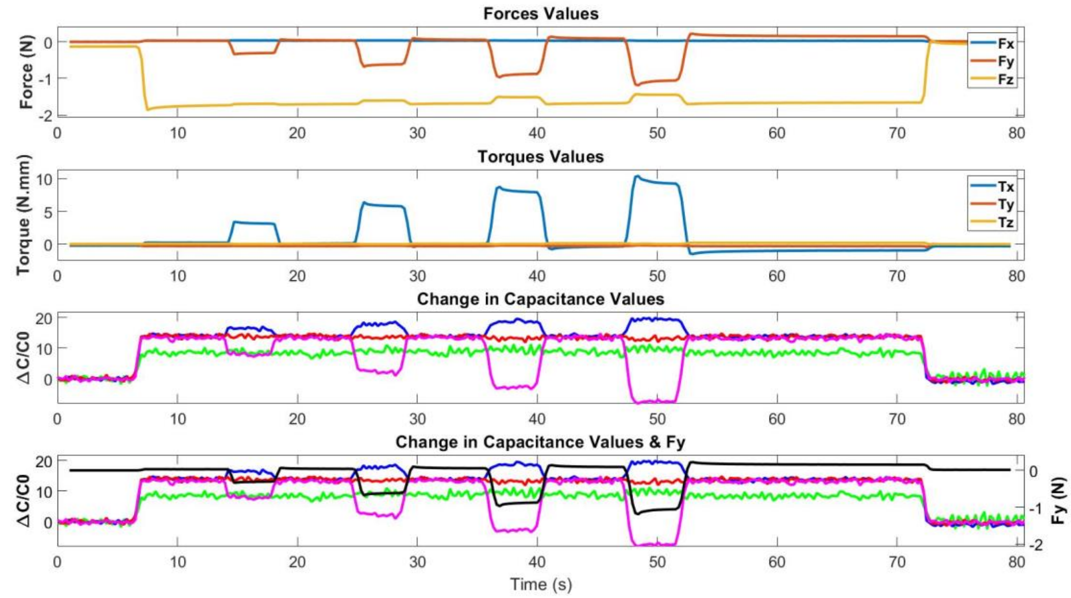

Figure B-8: Shear Displacement Characterization at 100 mm Radius of Curvature with Flat Indenter, 0.2 mm to 0.8 mm Positive-y Displacement

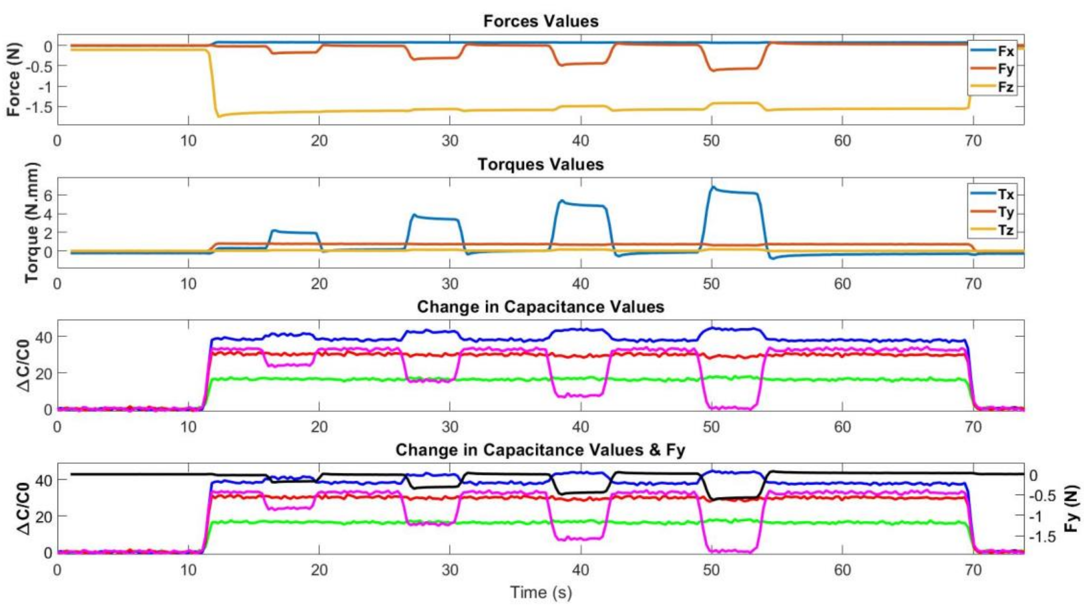

Figure B-9: Shear Displacement Characterization at 100 mm Radius of Curvature with Cylinder Indenter, 0.2 mm to 0.8 mm Positive-y Displacement

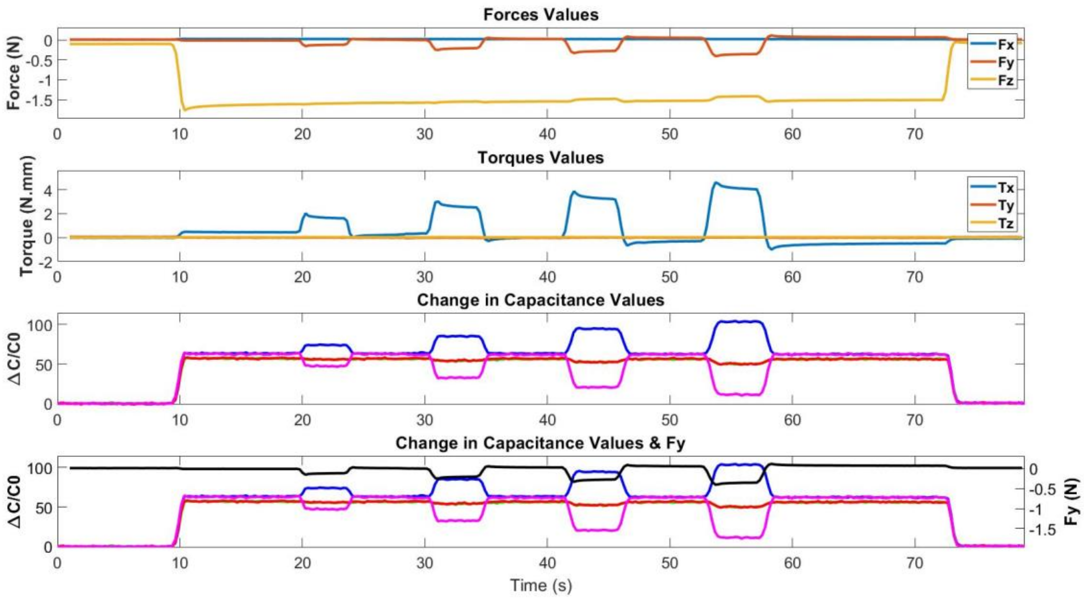

Figure B-10: Shear Displacement Characterization at 100 mm Radius of Curvature with Sphere Indenter, 0.2 mm to 0.8 mm Positive-y Displacement

Negative *y*-shear, 100 mm Inner Radius of Curvature

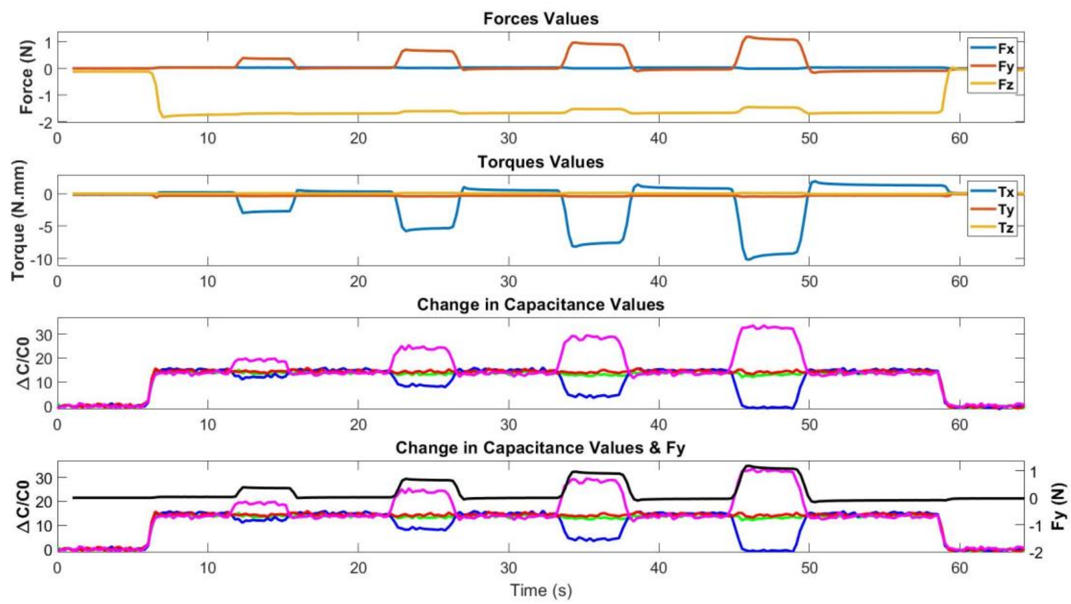

Figure B-11: Shear Displacement Characterization at 100 mm Radius of Curvature with Flat Indenter, 0.2 mm to 0.8 mm Negative-y Displacement

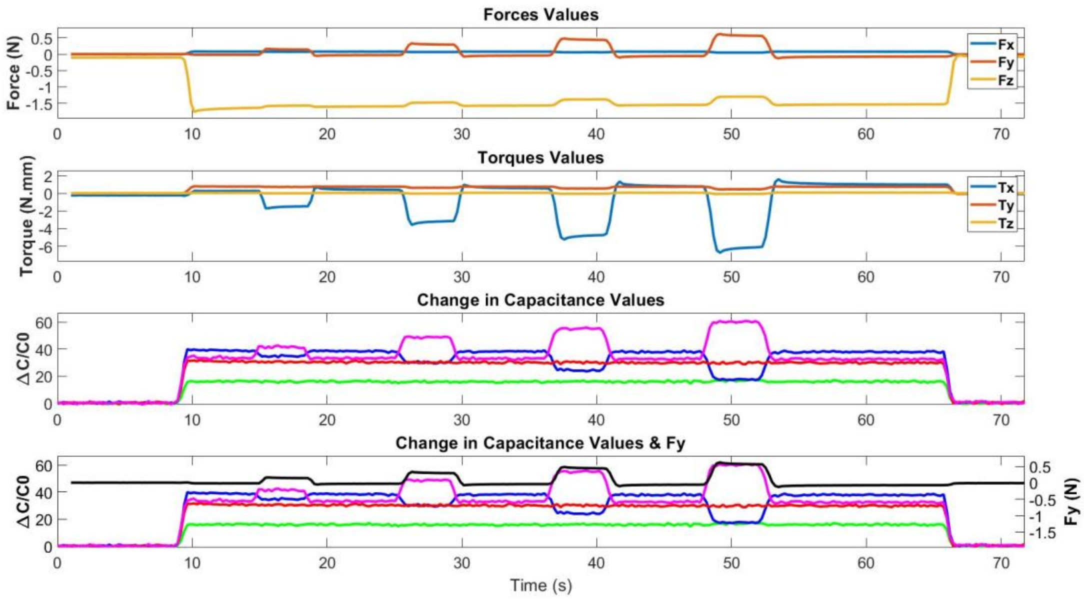

Figure B-12: Shear Displacement Characterization at 100 mm Radius of Curvature with Cylinder Indenter, 0.2 mm to 0.8 mm Negative-y Displacement

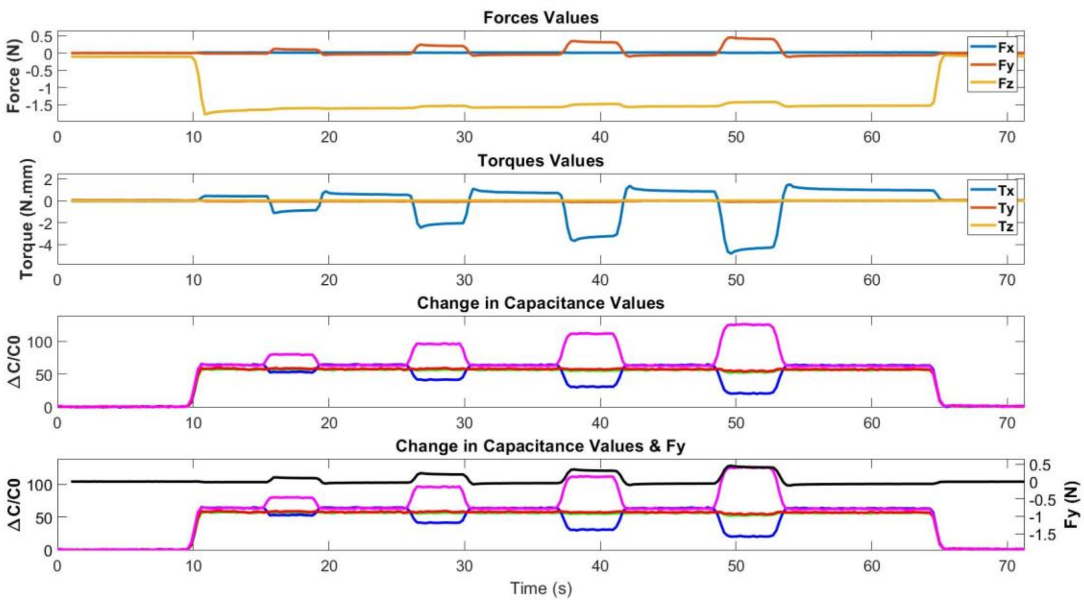

Figure B-13: Shear Displacement Characterization at 100 mm Radius of Curvature with Sphere Indenter, 0.2 mm to 0.8 mm Negative-y Displacement

Positive *x*-shear, 30 mm Inner Radius of Curvature

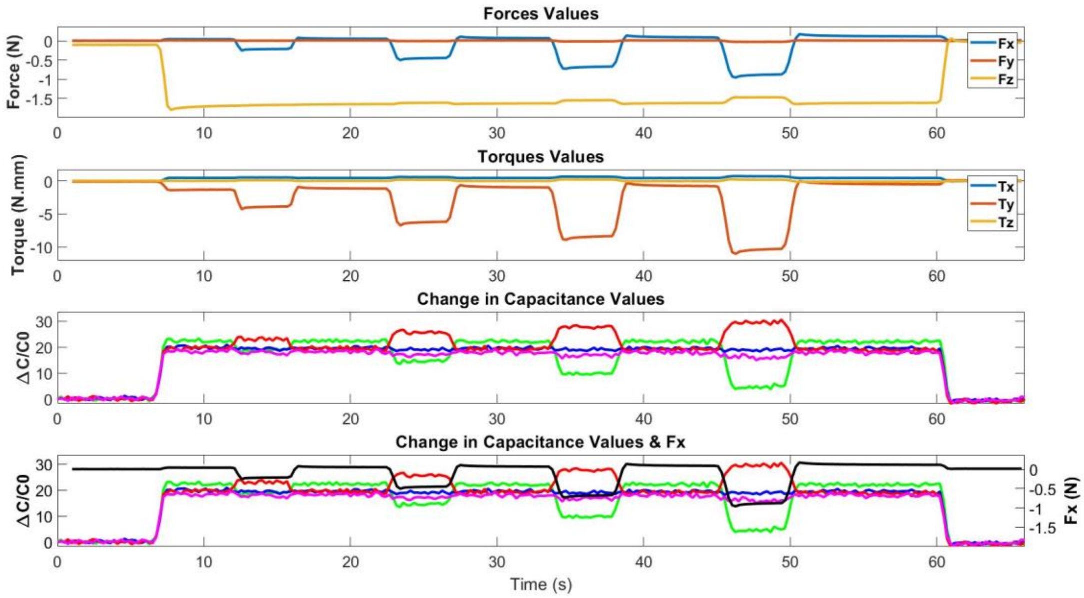

Figure B-14: Shear Displacement Characterization at 30 mm Radius of Curvature with Flat Indenter, 0.2 mm to 0.8 mm Positive-x Displacement

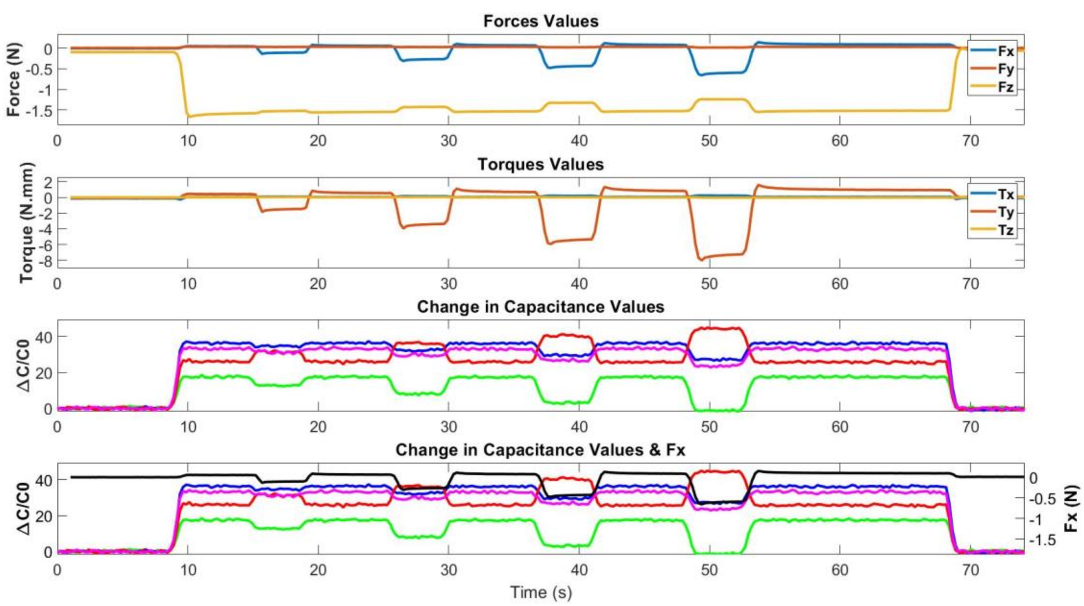

Figure B-15: Shear Displacement Characterization at 30 mm Radius of Curvature with Cylinder Indenter, 0.2 mm to 0.8 mm Positive-x Displacement

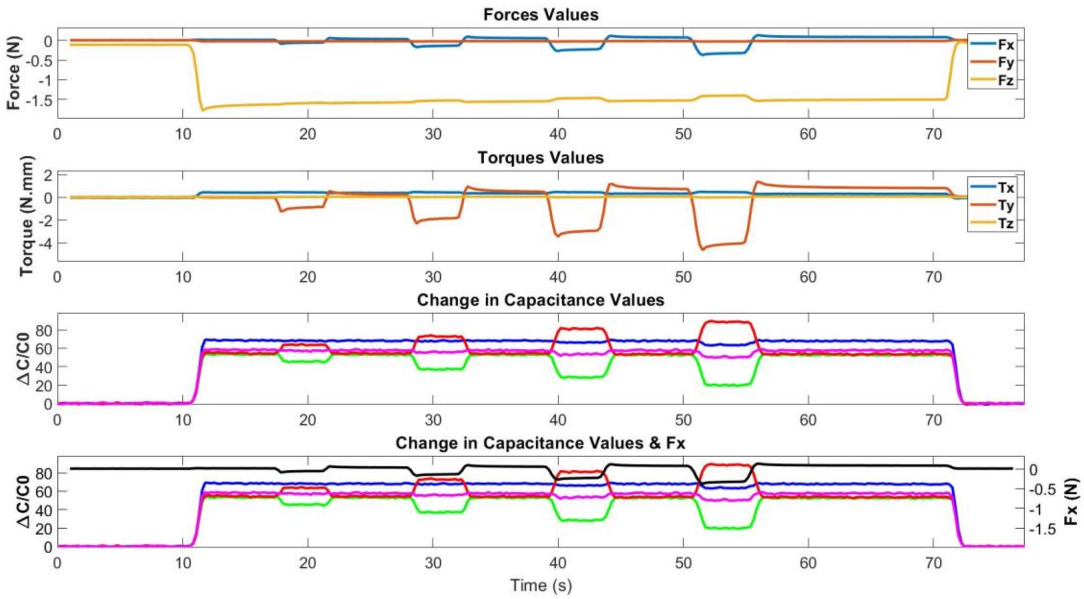

Figure B-16: Shear Displacement Characterization at 30 mm Radius of Curvature with Sphere Indenter, 0.2 mm to 0.8 mm Positive-x Displacement

Negative *x*-shear, 30 mm Inner Radius of Curvature

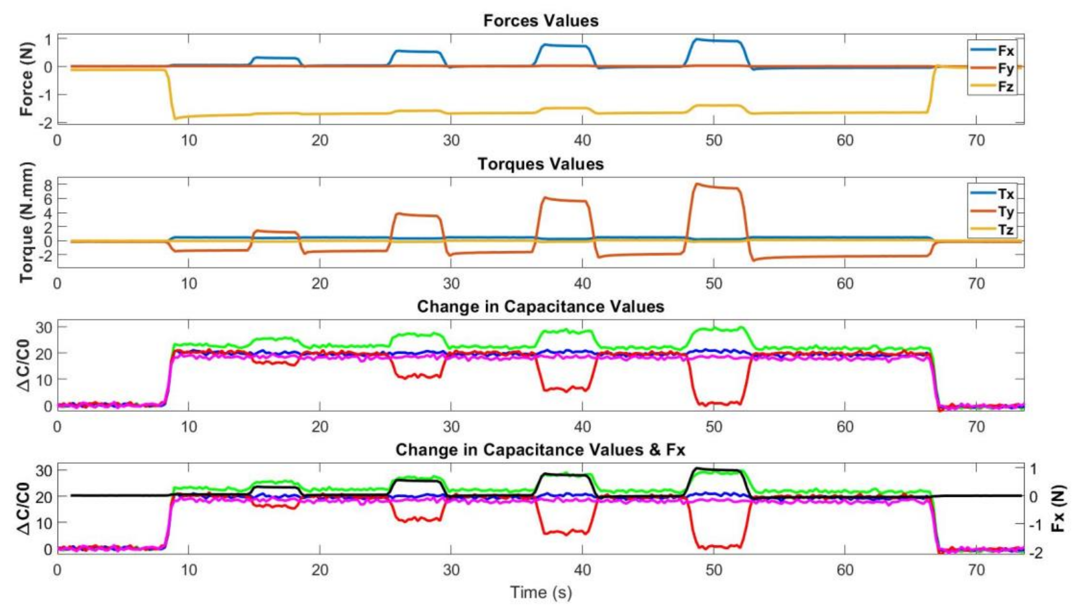

Figure B-17: Shear Displacement Characterization at 30 mm Radius of Curvature with Flat Indenter, 0.2 mm to 0.8 mm Negative-x Displacement

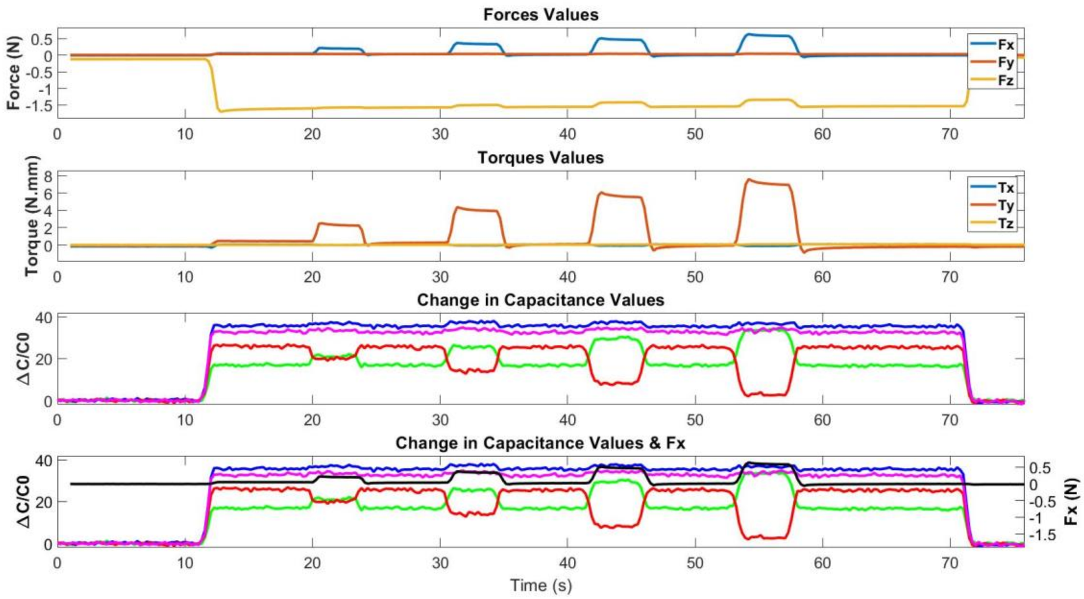

Figure B-18: Shear Displacement Characterization at 30 mm Radius of Curvature with Cylinder Indenter, 0.2 mm to 0.8 mm Negative-x Displacement

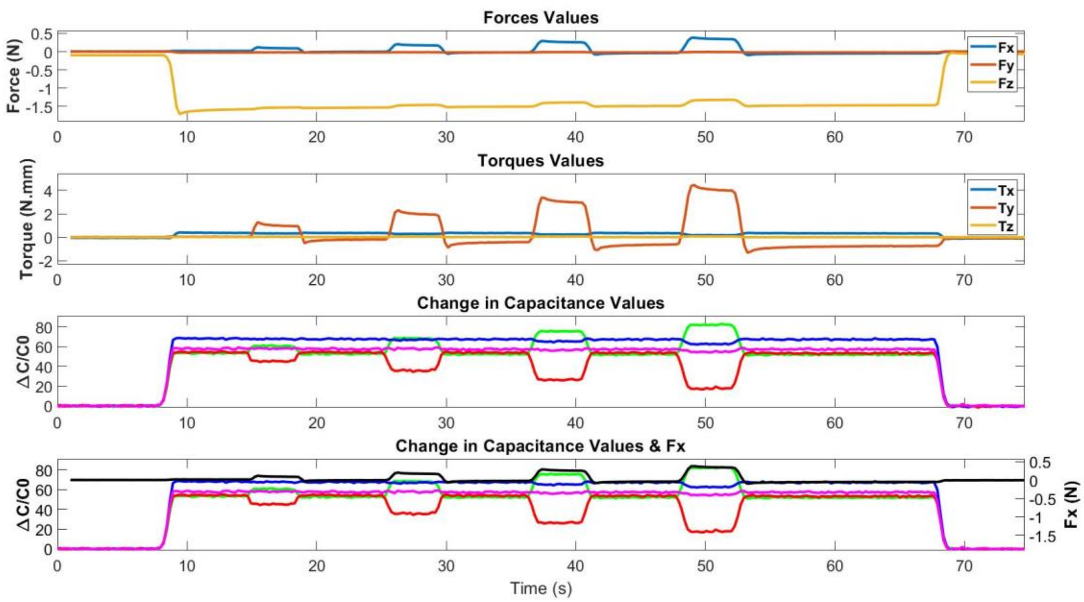

Figure B-19: Shear Displacement Characterization at 30 mm Radius of Curvature with Sphere Indenter, 0.2 mm to 0.8 mm Negative-x Displacement

Positive *y*-shear, 30 mm Inner Radius of Curvature

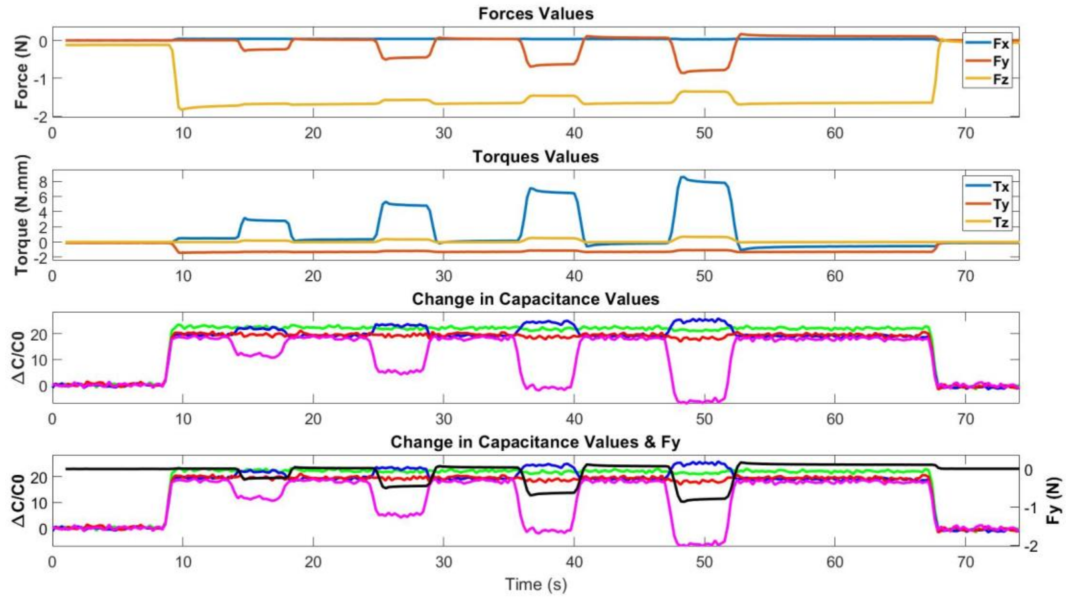

Figure B-20: Shear Displacement Characterization at 30 mm Radius of Curvature with Flat Indenter, 0.2 mm to 0.8 mm Positive-y Displacement

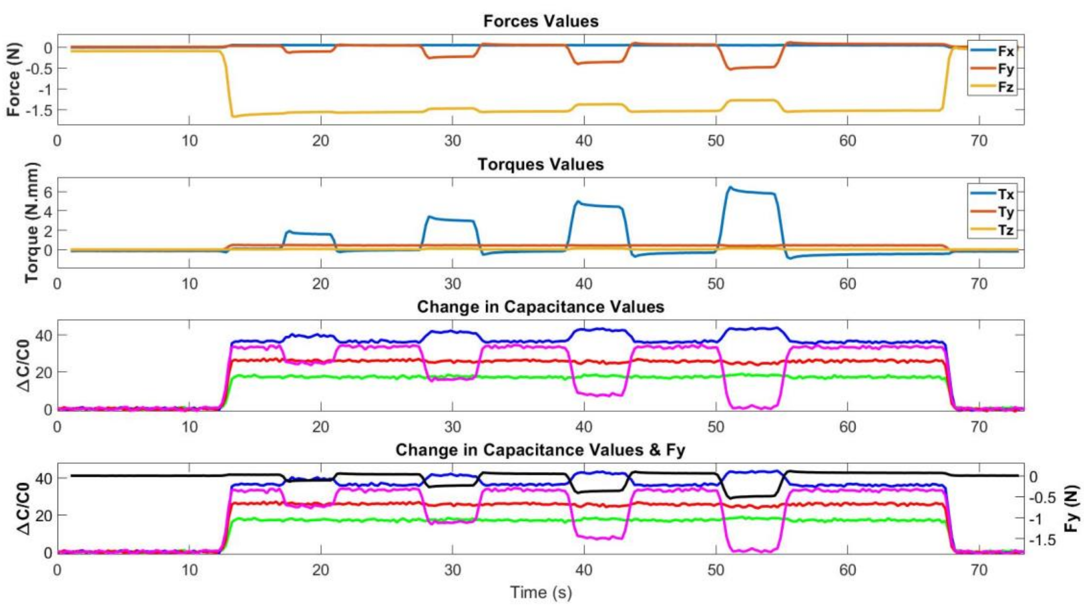

Figure B-21: Shear Displacement Characterization at 30 mm Radius of Curvature with Cylinder Indenter, 0.2 mm to 0.8 mm Positive-y Displacement

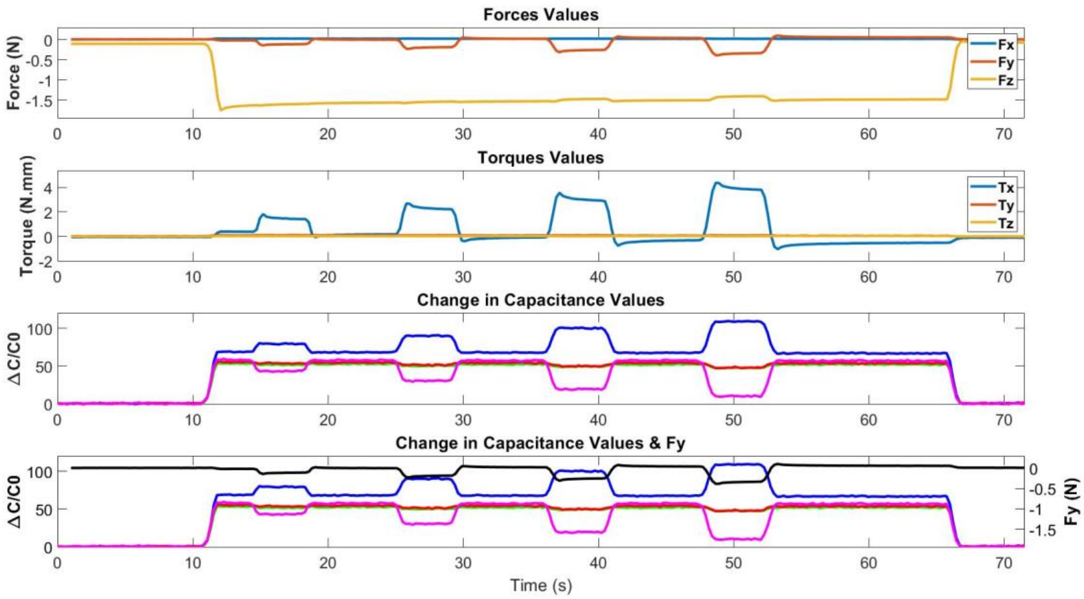

Figure B-22: Shear Displacement Characterization at 30 mm Radius of Curvature with Sphere Indenter, 0.2 mm to 0.8 mm Positive-y Displacement

Negative *y*-shear, 30 mm Inner Radius of Curvature

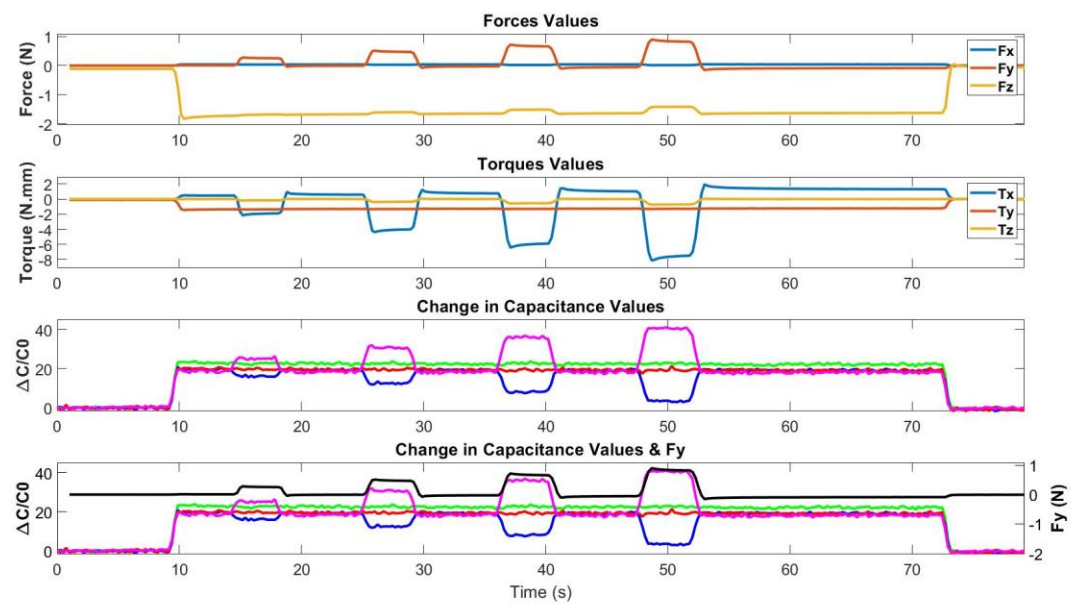

Figure B-23: Shear Displacement Characterization at 30 mm Radius of Curvature with Flat Indenter, 0.2 mm to 0.8 mm Negative-y Displacement

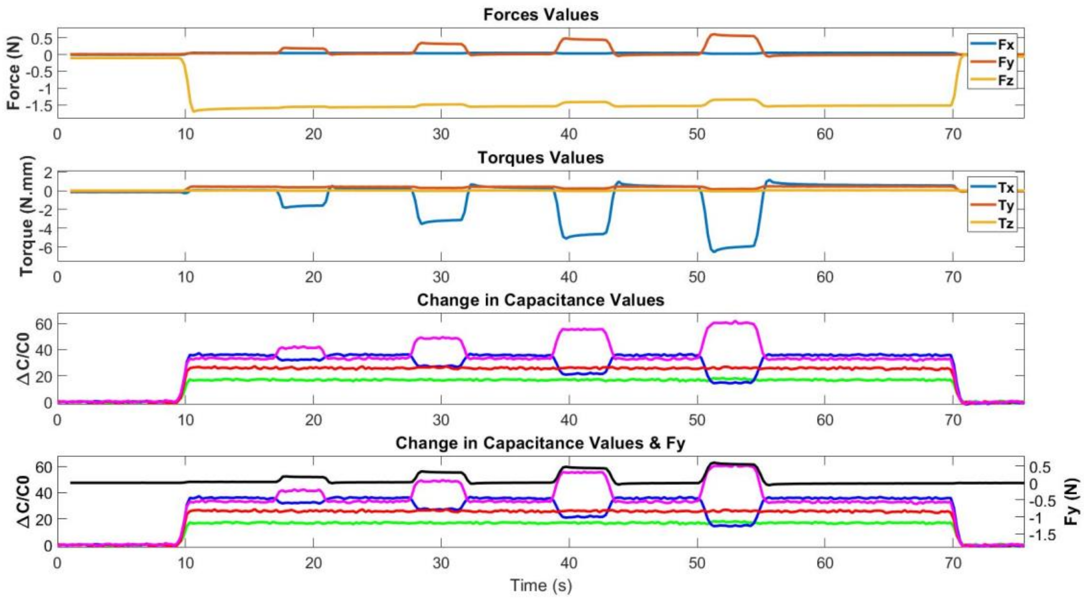

Figure B-24: Shear Displacement Characterization at 30 mm Radius of Curvature with Cylinder Indenter, 0.2 mm to 0.8 mm Negative-y Displacement

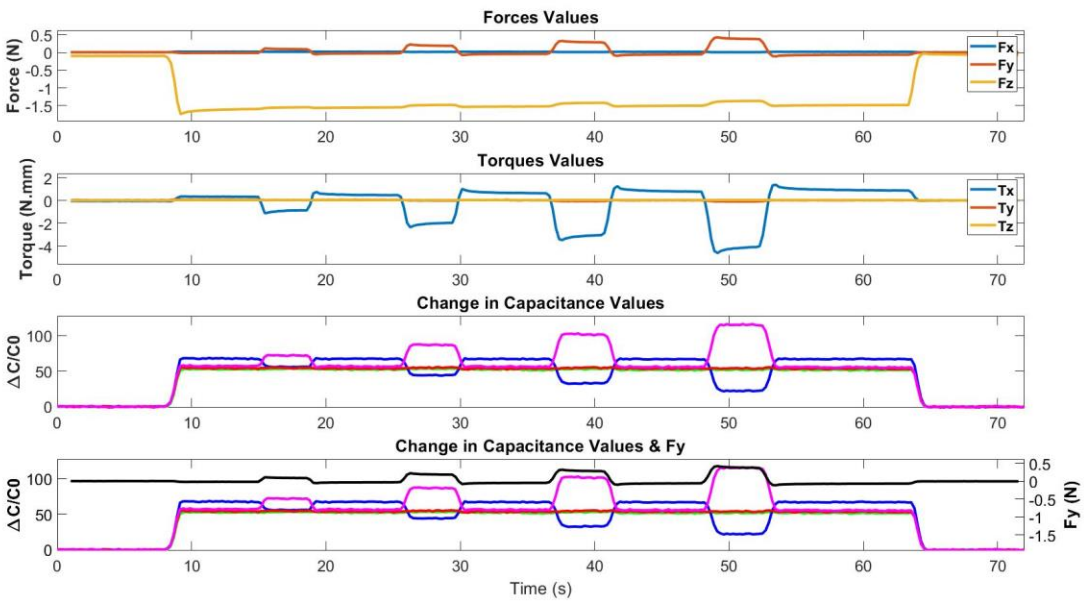

Figure B-25: Shear Displacement Characterization at 30 mm Radius of Curvature with Sphere Indenter, 0.2 mm to 0.8 mm Negative-y Displacement

Positive *x*-shear, 10 mm Inner Radius of Curvature

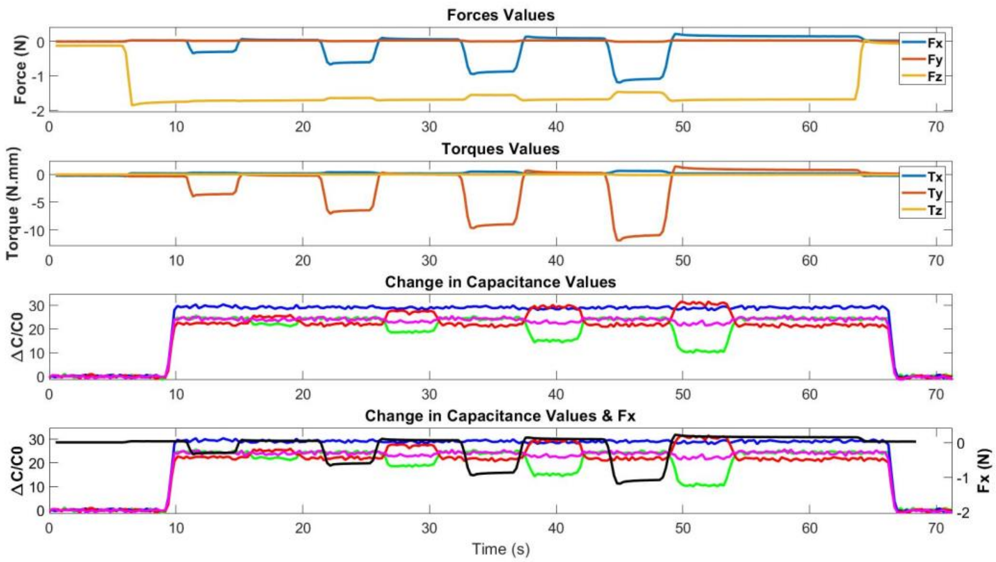

Figure B-26: Shear Displacement Characterization at 10 mm Radius of Curvature with Flat Indenter, 0.2 mm to 0.8 mm Positive-x Displacement

Negative *x*-shear, 10 mm Inner Radius of Curvature

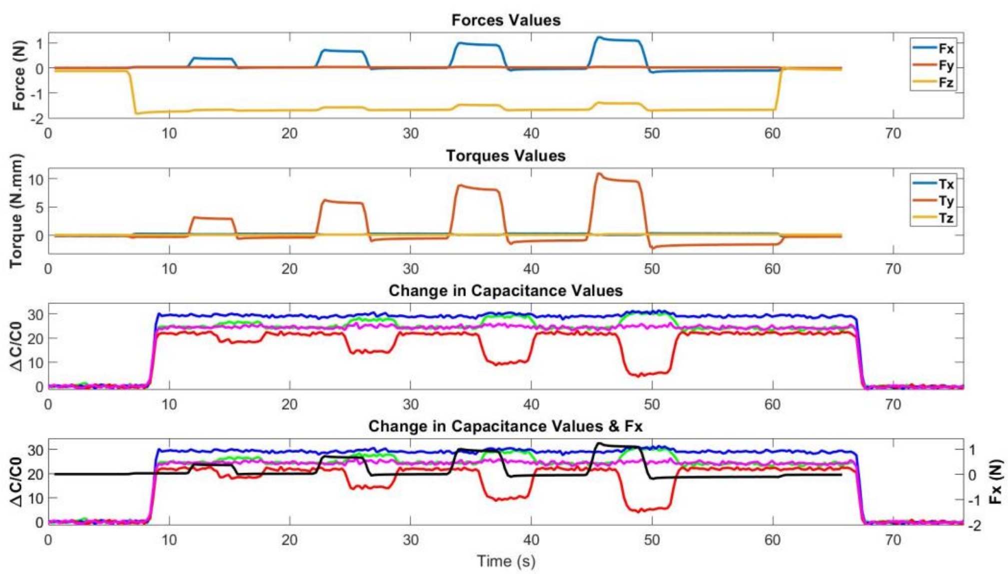

Figure B-27: Shear Displacement Characterization at 10 mm Radius of Curvature with Flat Indenter, 0.2 mm to 0.8 mm Negative-x Displacement

Positive *y*-shear, 10 mm Inner Radius of Curvature

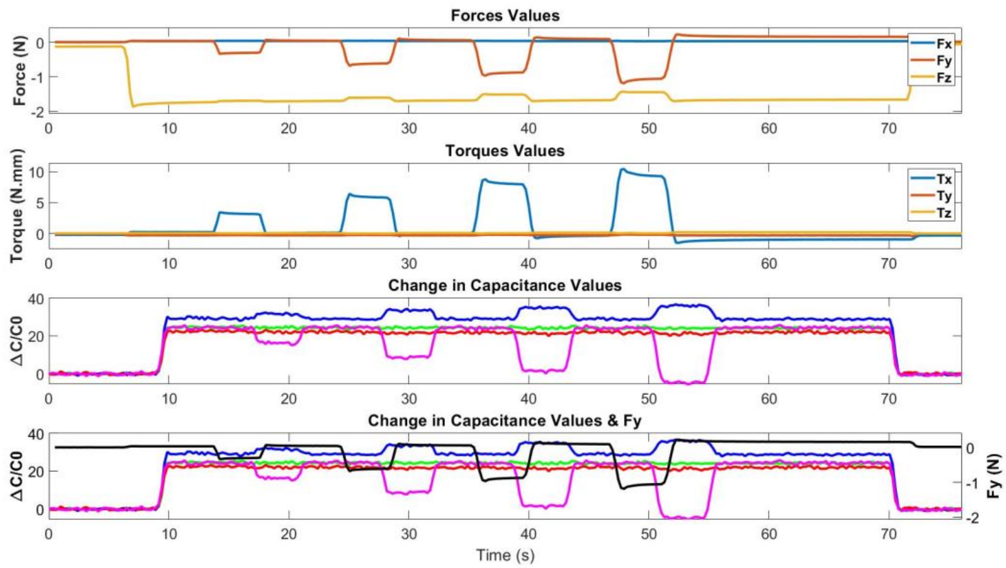

Figure B-28: Shear Displacement Characterization at 10 mm Radius of Curvature with Flat Indenter, 0.2 mm to 0.8 mm Positive-y Displacement

Negative *y*-shear, 10 mm Inner Radius of Curvature

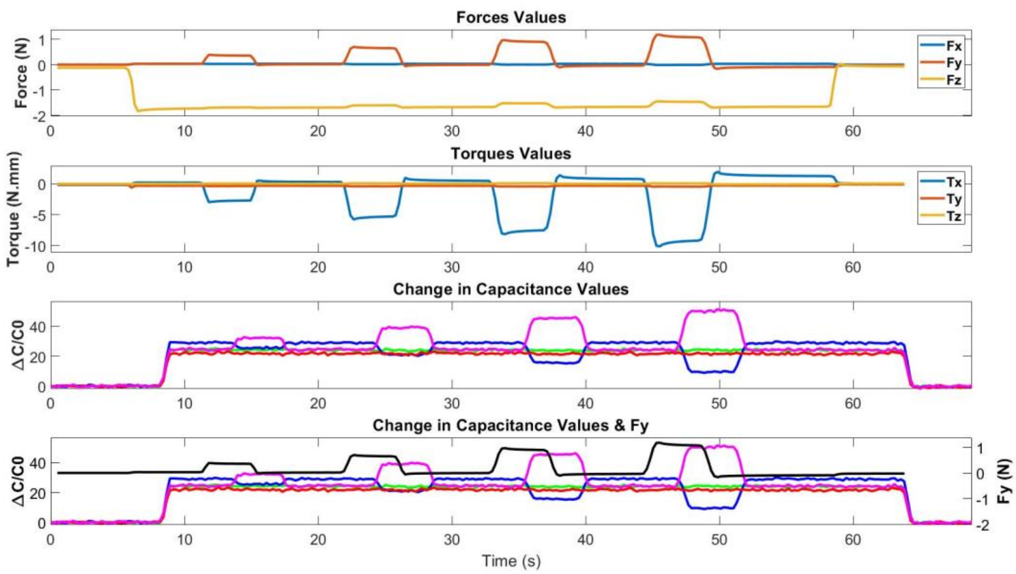

Figure B-29: Shear Displacement Characterization at 10 mm Radius of Curvature with Flat Indenter, 0.2 mm to 0.8 mm Negative-y Displacement

Appendix C: High Force Range Sensor Shear Data

The data presented in this appendix is from the low-normal-force (1.6 N normal force) characterization of the high force range architectures presented in Chapter 4. These sensors utilize dielectric architectures designed to function similarly to the sensors previously developed by *Sarwar et al.* at low normal forces (<12 N), while maintaining normal force sensing function up to a maximum force of 50 N. The electrode color coding for the shear portion of these sensors is presented in Figure C-1, with the *x*- and *y*-directions indicated.

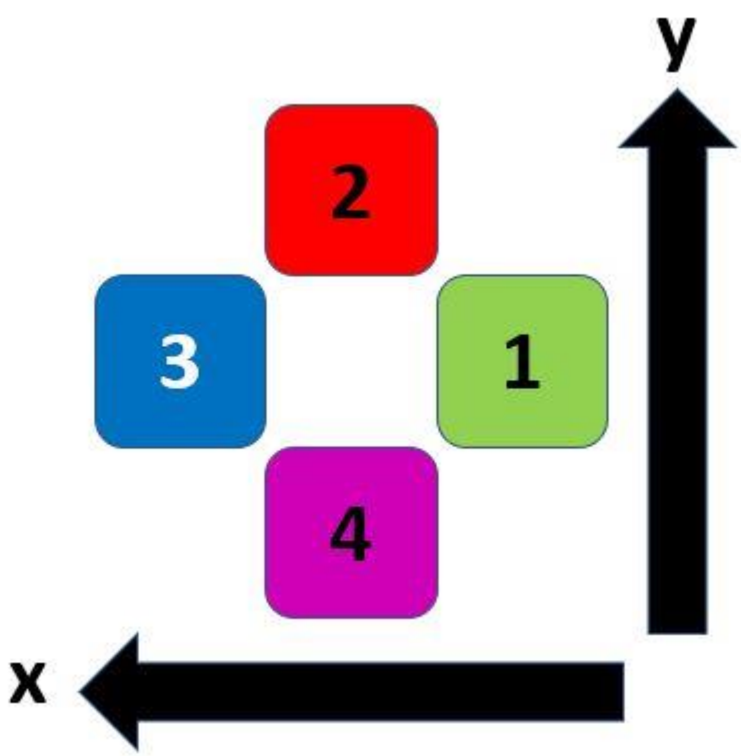

Figure C-1: Taxel Orientation for High Normal Force Range Sensor Characterization

Large Square Architecture

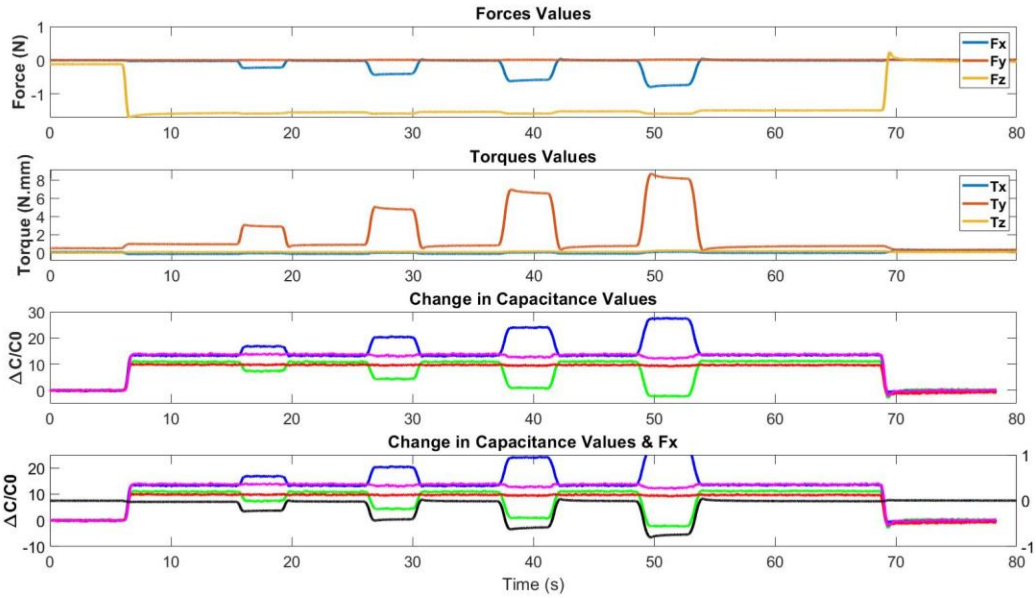

Figure C-2: Shear Displacement Characterization with Large Square Architecture, 0.2 mm to 0.8 mm Positive-x Displacement

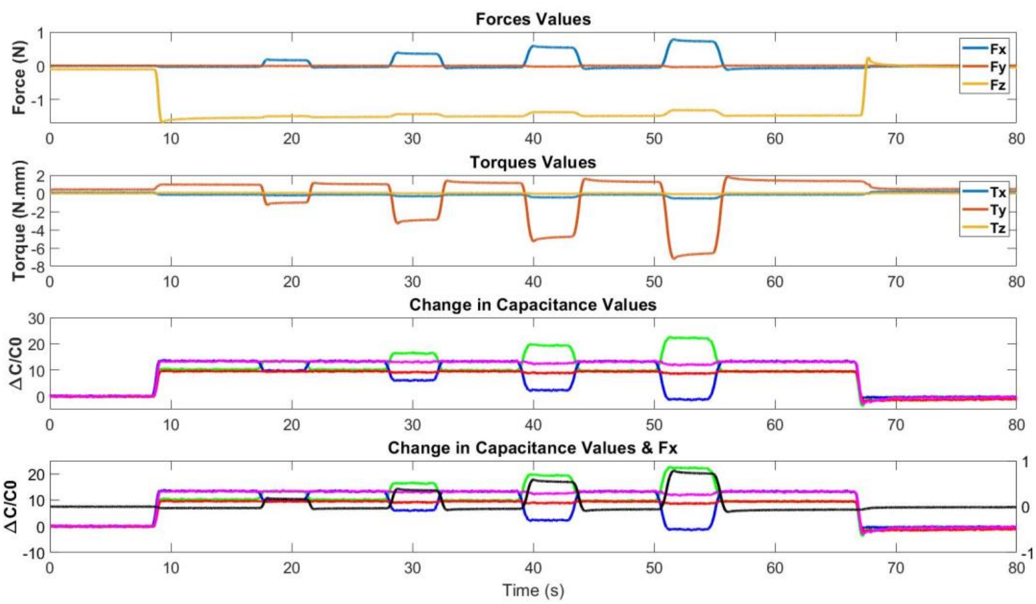

Figure C-3: Shear Displacement Characterization with Large Square Architecture, 0.2 mm to 0.8 mm Negative-x Displacement

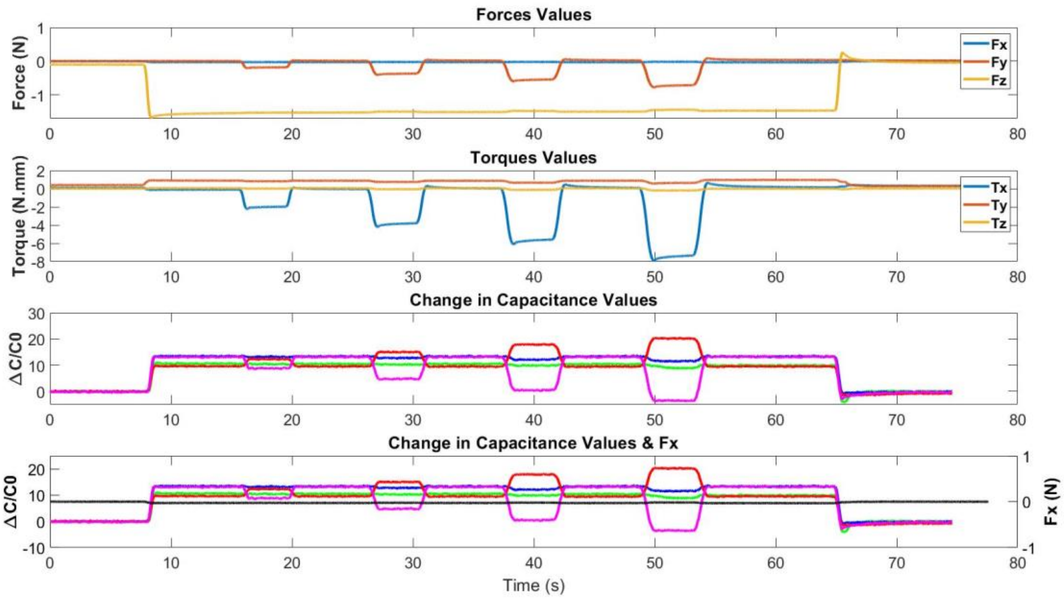

Figure C-4: Shear Displacement Characterization with Large Square Architecture, 0.2 mm to 0.8 mm Positive-y Displacement

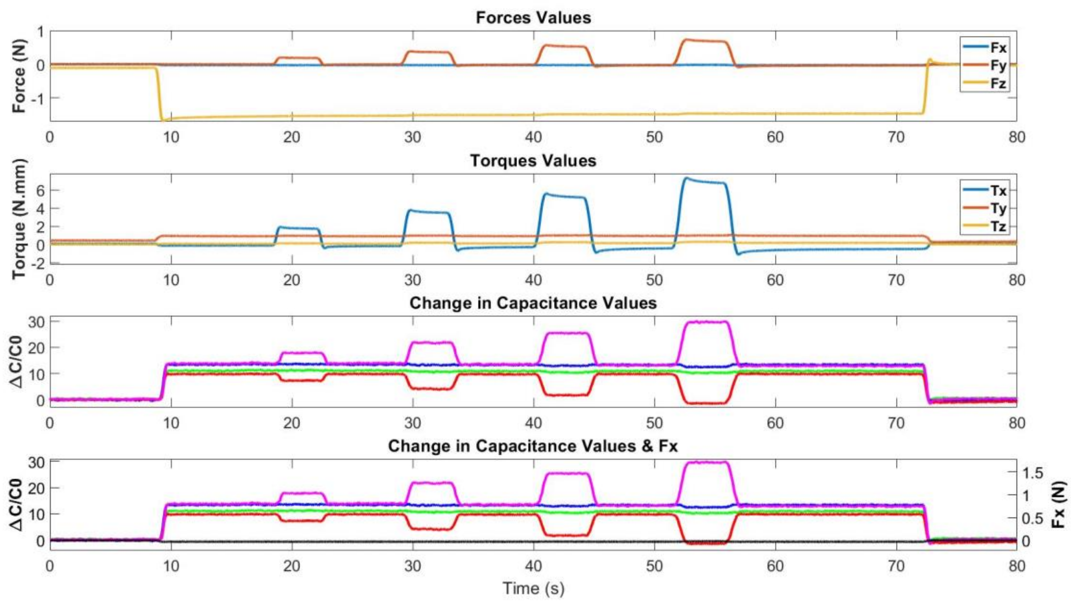

Figure C-5: Shear Displacement Characterization with Large Square Architecture, 0.2 mm to 0.8 mm Negative-y Displacement

Small Square Architecture

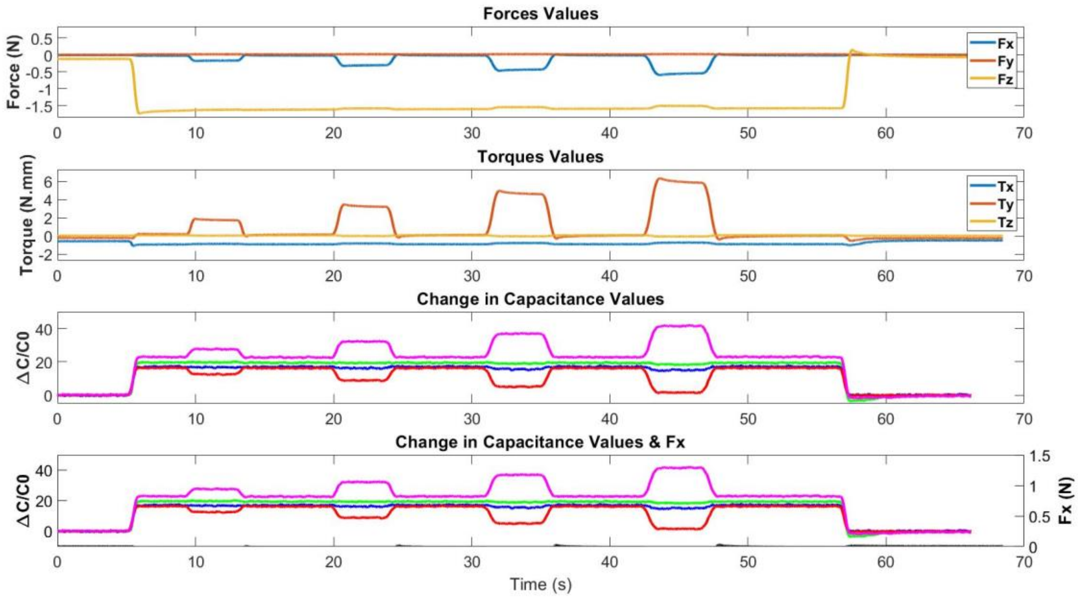

Figure C-6: Shear Displacement Characterization with Small Square Architecture, 0.2 mm to 0.8 mm Positive-x Displacement

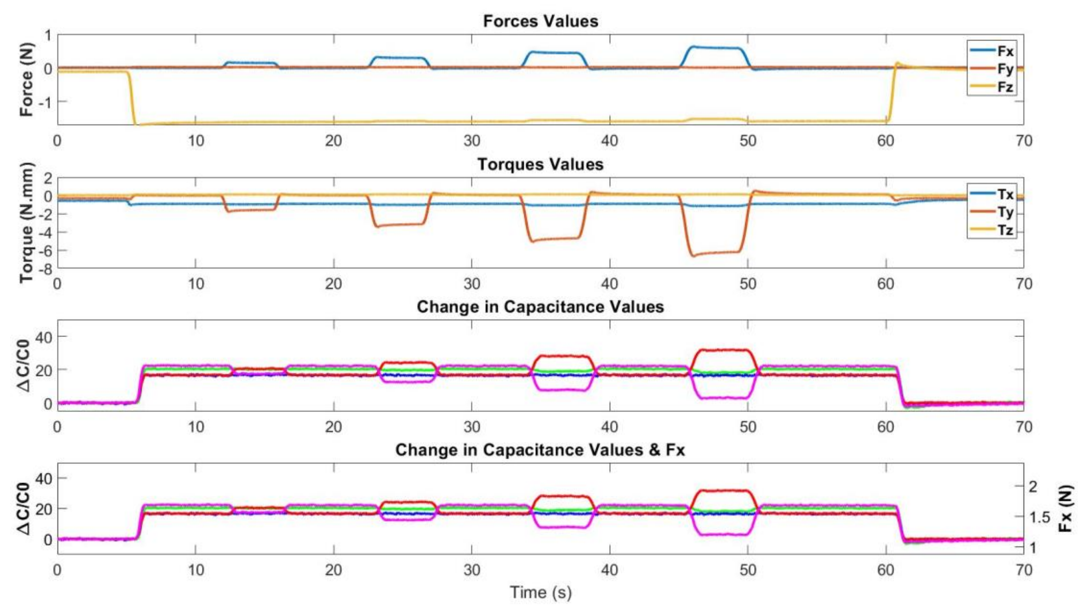

Figure C-7: Shear Displacement Characterization with Small Square Architecture, 0.2 mm to 0.8 mm Negative-x Displacement

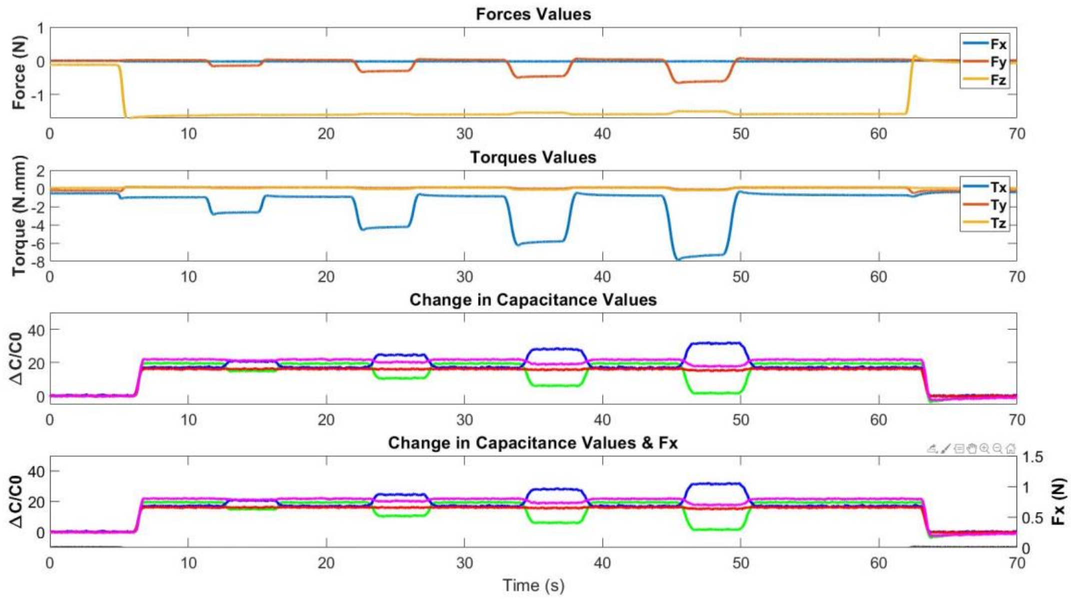

Figure C-8: Shear Displacement Characterization with Small Square Architecture, 0.2 mm to 0.8 mm Positive-y Displacement

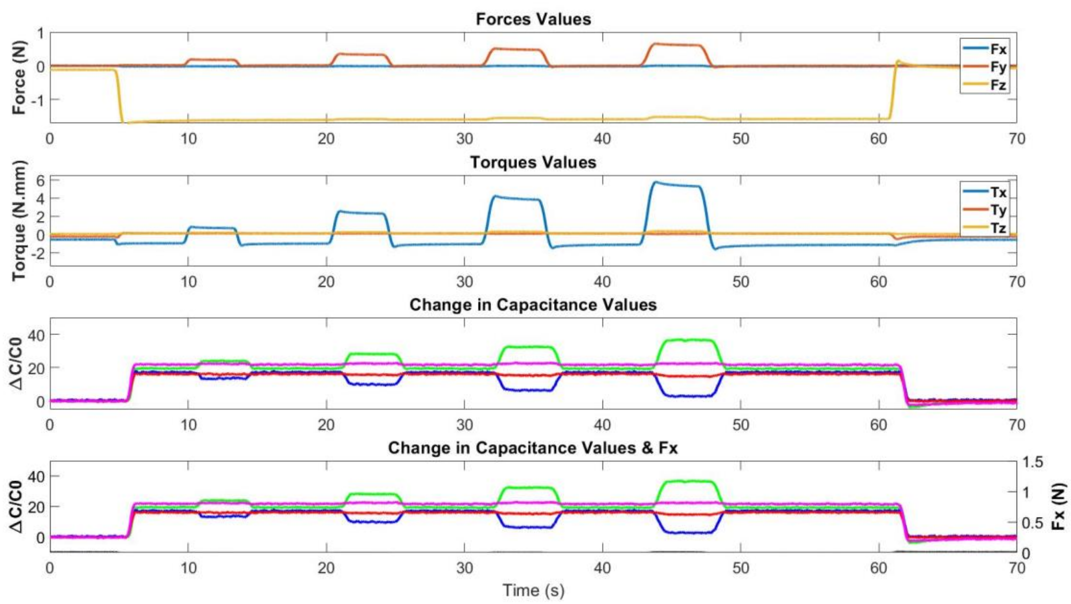

Figure C-9: Shear Displacement Characterization with Small Square Architecture, 0.2 mm to 0.8 mm Negative-y Displacement

Pyramid Architecture

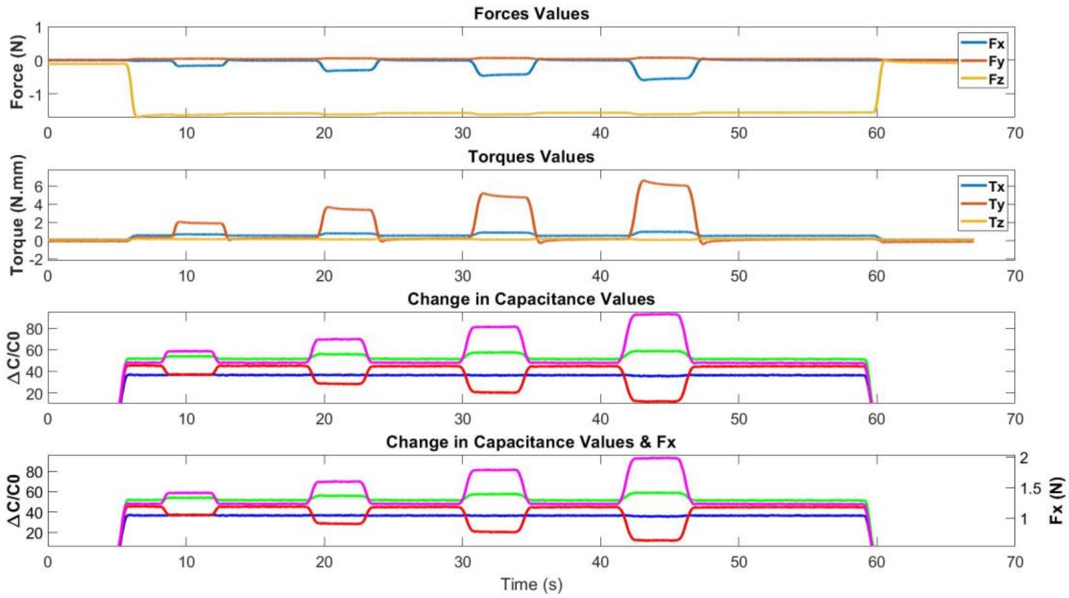

Figure C-10: Shear Displacement Characterization with Pyramid Architecture, 0.2 mm to 0.8 mm Positive-x Displacement

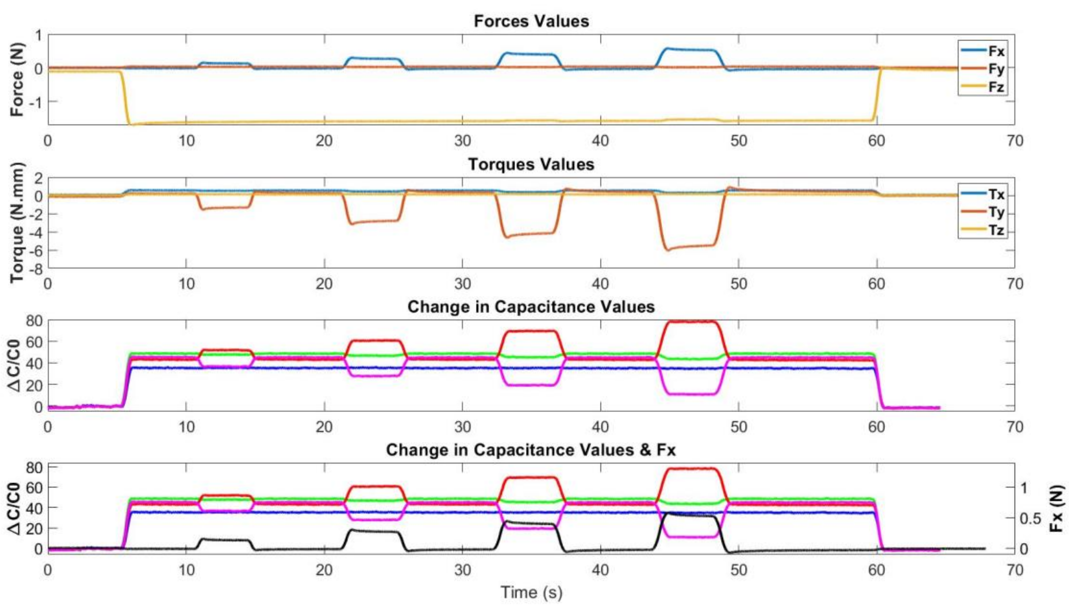

Figure C-11: Shear Displacement Characterization with Pyramid Architecture, 0.2 mm to 0.8 mm Negative-x Displacement

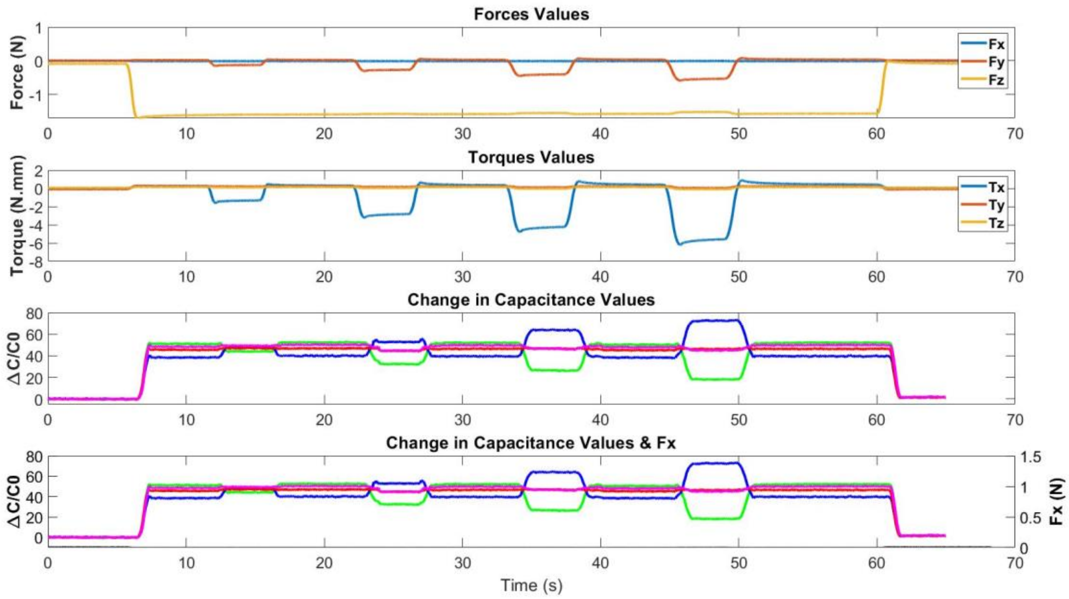

Figure C-12: Shear Displacement Characterization with Pyramid Architecture, 0.2 mm to 0.8 mm Positive-y Displacement

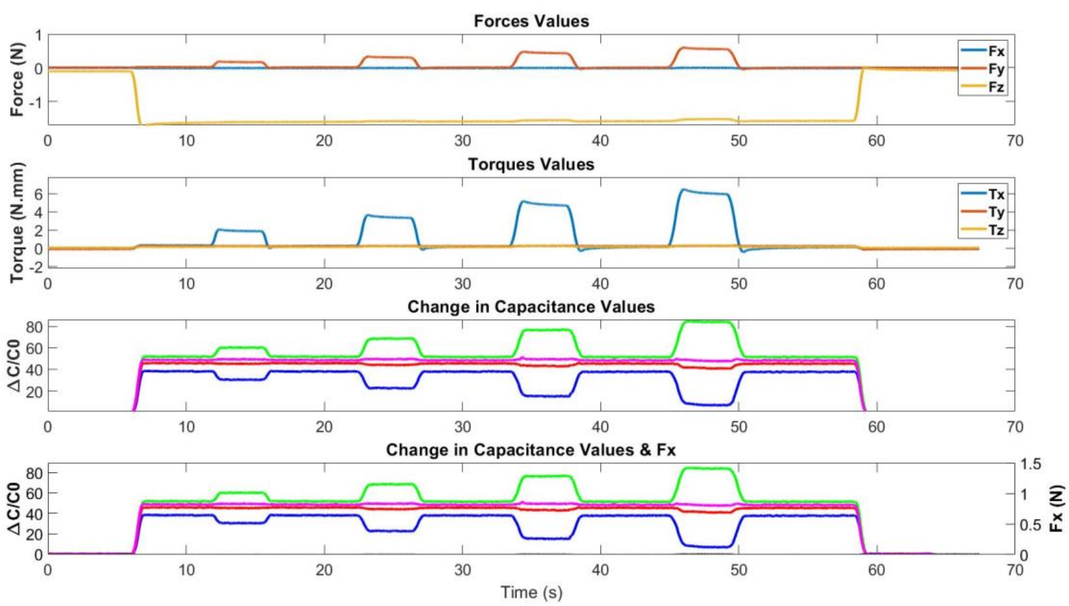

Figure C-13: Shear Displacement Characterization with Pyramid Architecture, 0.2 mm to 0.8 mm Negative-y Displacement

Inverted Pyramid Architecture

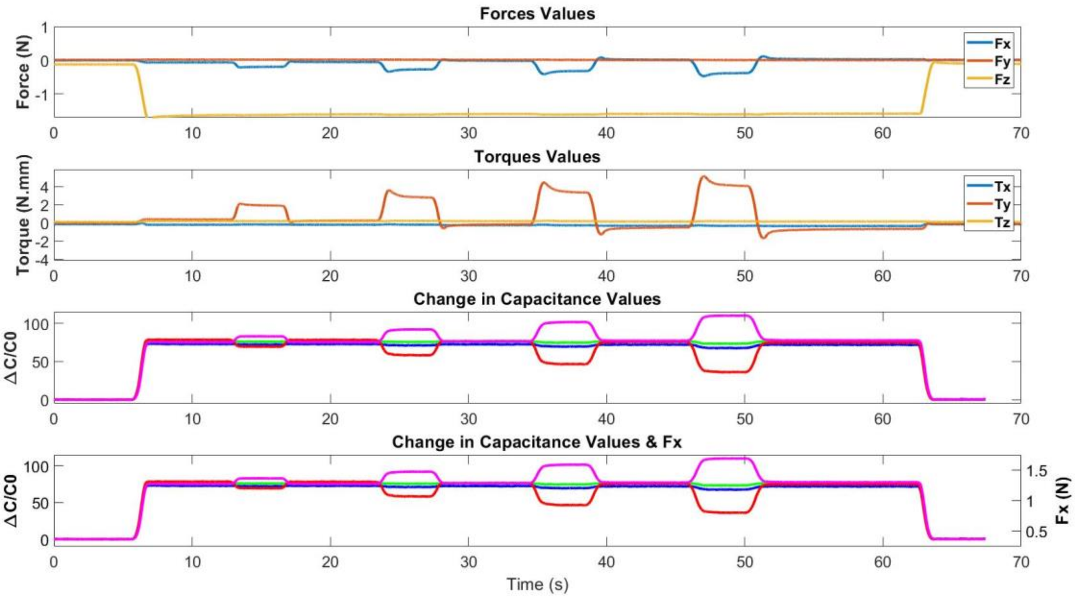

Figure C-14: Shear Displacement Characterization with Inverted Pyramid Architecture, 0.2 mm to 0.8 mm Positive-x Displacement

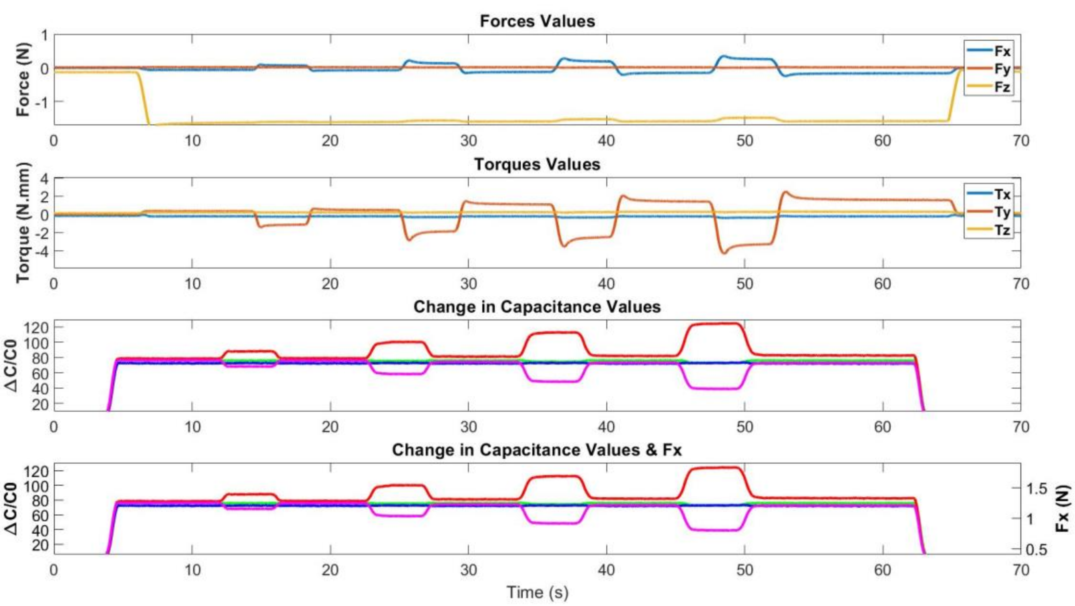

Figure C-15: Shear Displacement Characterization with Inverted Pyramid Architecture, 0.2 mm to 0.8 mm Negative-x Displacement

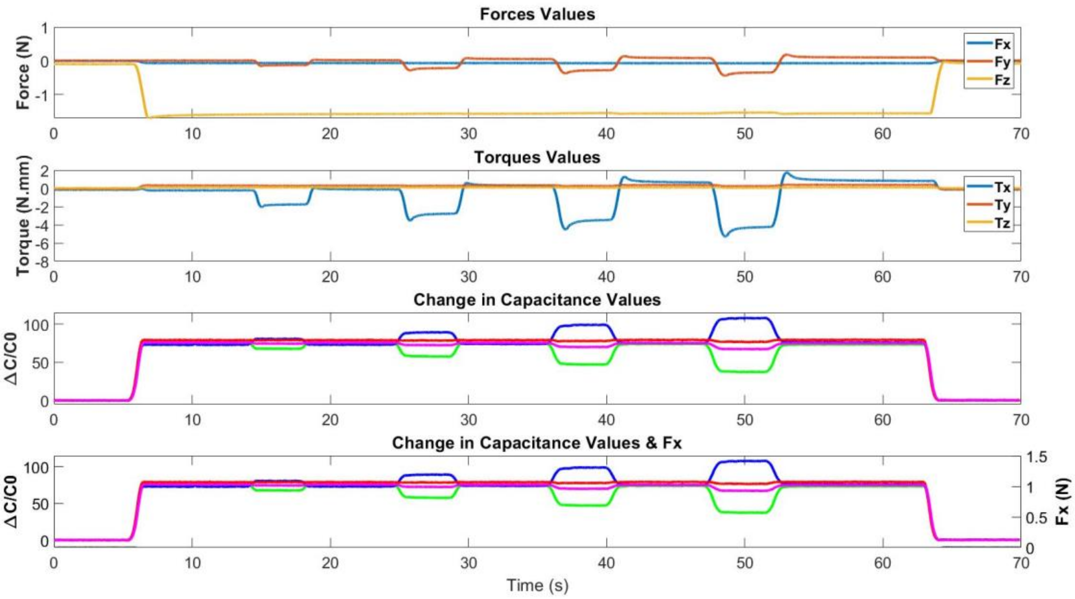

Figure C-16: Shear Displacement Characterization with Inverted Pyramid Architecture, 0.2 mm to 0.8 mm Positive-y Displacement

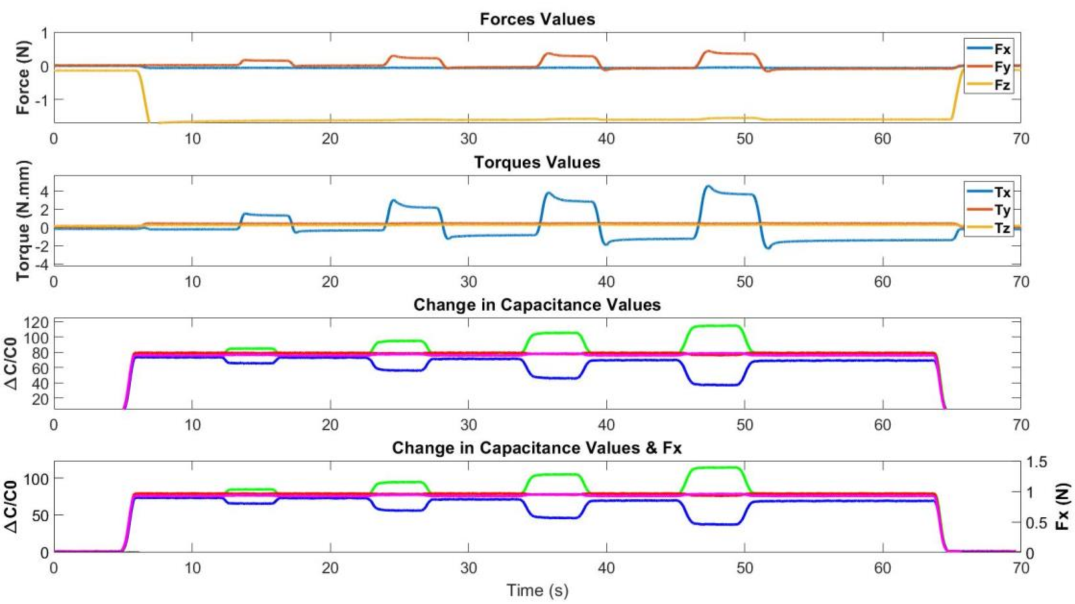

Figure C-17: Shear Displacement Characterization with Inverted Pyramid Architecture, 0.2 mm to 0.8 mm Negative-y Displacement